THE UNIVERSITY of EDINBURGH

Title	Infrared and millimeter-wave spectroscopic study of the DR21 outflow
Author	Garden, Rognvald Peebles
Qualification	PhD
Year	1986

Digitisation Notes:

- pages 17, 235 missing from original

AN INFRARED AND MILLIMETER-WAVE SPECTROSCOPIC STUDY OF THE DR21 OUTFLOW

Rognvald Peebles Garden

Presented for the Degree of Doctor of Philosophy

at the University of Edinburgh

October 1986

This Thesis has been composed by
me and the work described in it
is my own except where specifically
acknowledged in the text.

THE DR21 MOLECULAR JETS

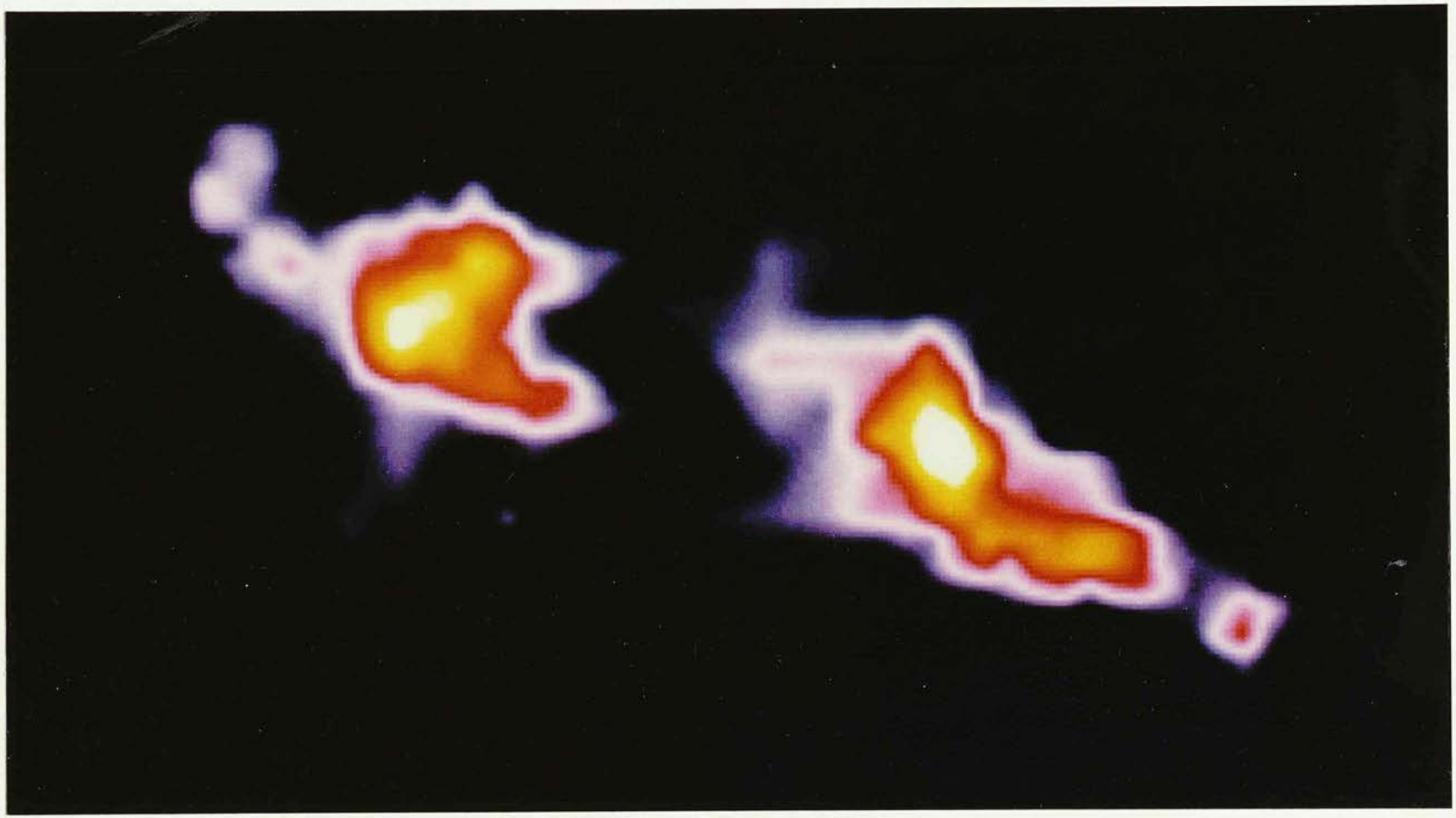

measured in H_2 v=1-0 S(1) line emission using an 18" beam.

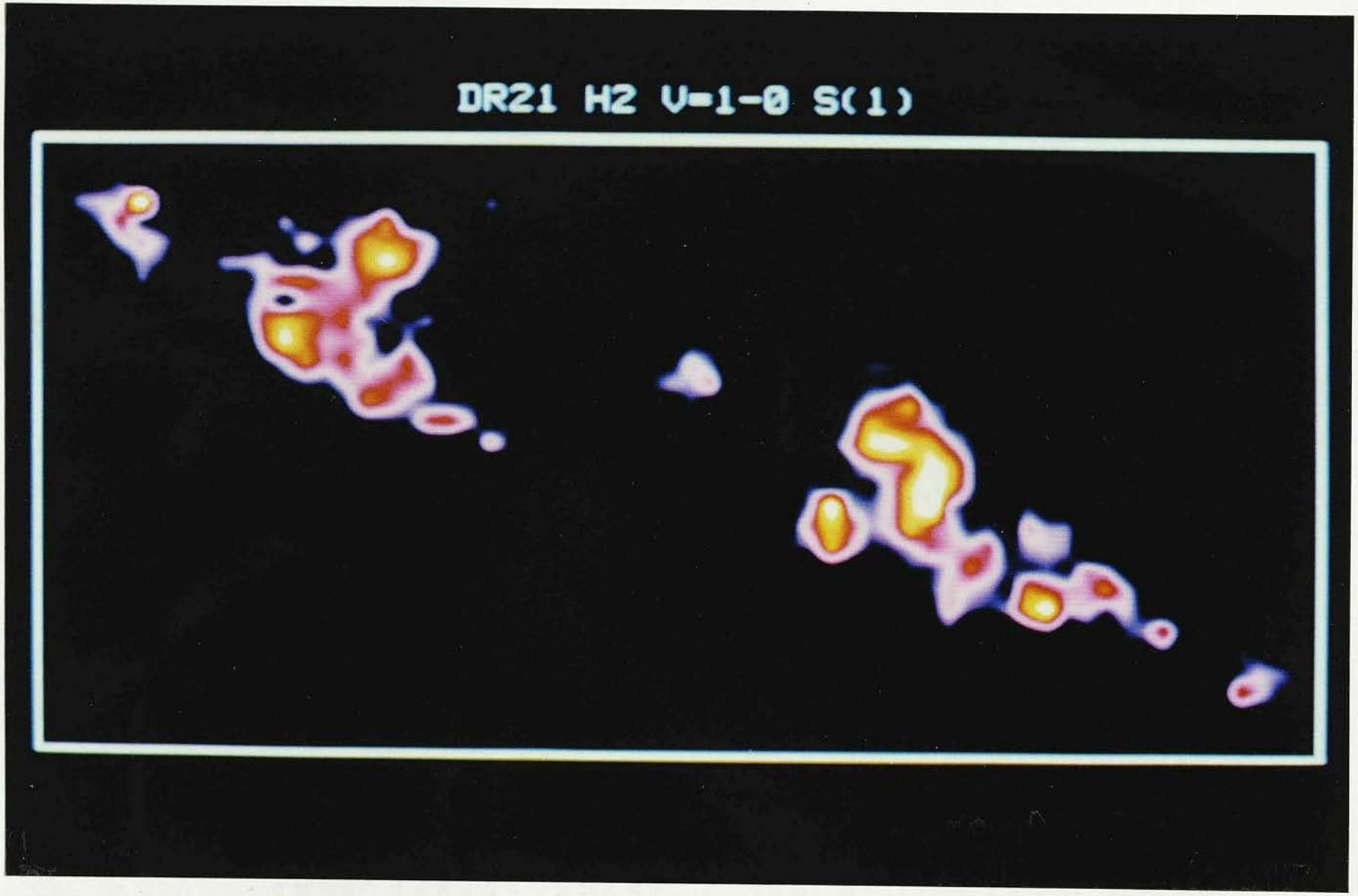

measured in H_2 v=1-0 S(1) line emission using a 6" beam

ABSTRACT

In this thesis, new high-angular resolution infrared and millimeter-wave spectroscopic observations of the enigmatic outflow activity associated with the luminous DR21 star-forming region are presented and discussed. The intent is to use these observations to undertake a detailed investigation of the physical nature of the central driving engine and the related dynamical processes involved in collimating the hypersonic outflow gas.

In the infrared, large-scale mapping and high-spectral resolution profile measurements of the vibrational H_2 v=1-0 S(1) line are used to investigate the morphology and kinematic structure of the hot, dense gas that is collisionally excited behind fast shocks. The H_2 emission delineates a highly-collimated pair of bipolar jets that extend over a projected distance of ~ 5 pc, centred on the DR21 molecular cloud core; this is undoubtedly the most luminous (in H_2 line emission) and extended galactic outflow source yet discovered. Furthermore, the H_2 line profiles at certain locations within the jets possess high-velocity wings that extend to beyond 100 kms^{-1} from the DR21 rest velocity. These observations pose interesting dynamical consequencies as at such high velocities H_2 should be entirely dissociated.

In an attempt to derive the mass distribution and velocity structure of the molecular gas participating in the outflow, and hence the driving force and associated mechanical luminosity, detailed observations were also undertaken at millimeter-wavelengths in the CO J=1-0 and CS J=1-0, J=2-1 lines. It is found that the DR21 outflow is considerably more massive and energetic than any other outflow source studied to date. Another feature unique to the DR21 region is the discovery of extended high-velocity CS emission that is dynamically associated with the outflow lobes and extends to a distance of ~ 3 pc from the cloud core; this component presumably originates from ambient gas that has been swept up and compressed by the outflow. The high-velocity CS may be overabundant by 2 orders of magnitude, in good agreement with current numerical models of post-shock chemistry.

The CS observations further reveal the existence of an extremely massive, slowly rotating disc of high-density neutral gas that surrounds the central outflow source. It is most probable that the large momentum flux in outflow material derives from efficient mass-loss from the surface of this disc, mediated via a centrifugally propelled, magneto-hydrodynamic wind. An additional confinment mechanism is required to collimate the outflow at large distances from the flow origin. If this confinment is primarily pressure driven, then sudden changes in the ambient cloud pressure could induce a succession of oblique shocks within the outflow that may give rise to the periodic clumpy structure that characterizes the H_2 emission-line jets. Other consequencies of the pressure-confinment mechanism are discussed and a broad resemblance to extragalactic radio jets is remarked upon.

TABLE OF CONTENTS

Chapter 1 INTRODUCTION TO THE THESIS

Large-scale mapping of the distribution of rotational carbon monoxide (CO) emission in the galaxy has provided concrete evidence in favour of the notion that a major fraction of interstellar molecules are assembled into gravitationally bound condensations, appropriately termed, Giant Molecular Clouds (GMCs) (Scoville & Solomon 1975; Gordon & Burton 1976; Cohen & Thaddeus 1977; Solomon & Sanders 1979). The physical conditions characteristic of a typical GMC have, in turn, been deduced from extensive millimeter-wave observations of molecular rotational line emission, at higher angular and spectral resolutions, mainly in the J=1-0 transitions of ^{12}CO, ^{13}CO (Dickman, 1979) and, in some instances, $C^{18}O$ (Frerking, Langer & Wilson 1982). As a result of these observations it is now believed that the GMCs are probably the most massive objects in the galaxy, containing between 10^4 - 10^7 M_0 of molecular gas, with linear dimensions extending from 10 - 100 pc, and are among the coolest objects known in the Universe, with kinetic temperatures often below 10 K. The physical states of these clouds and the rate at which they evolve depend on the heating and cooling of matter composed almost entirely of molecular hydrogen (H_2). As a guide for comparison with the observations presented in this thesis, the physical properties currently thought to characterize a typical GMC within our own galaxy are summarized in Table[1.1].

Within a GMC there may be several core regions of enhanced CO excitation temperature, these sub-condensations usually being intimately associated with currently forming and/or recently formed stars (Elmegreen & Lada 1976,1977; Blitz 1980; Ho, Martin & Barrett 1981). In general, any luminous object within the core region of a GMC will be observable only in

TABLE 1.1 :

BASIC PHYSICAL PROPERTIES OF GIANT MOLECULAR CLOUDS (GMCs)

LARGE SCALE CLOUD :

dust/gas = 0.01 (by mass)

visual optical depth, $\tau_V = 1.08\ A_V \approx 20 - 100$

$n(H_2) = 500 - 2{,}000\ cm^{-3}$

diameter = 2R = 10 - 100 pc

mass = $10^4 - 10^7\ M_0$, typically $10^5\ M_0$

kinetic temperature of gas, $T_k = 10 - 20$ K

All of luminosity will emerge in far-infrared or submillimeter.

CORE REGIONS :

$n(H_2) = 10^4 - 10^6\ cm^{-3}$

diameter < 4 pc

mass = $100 - 10^4\ M_0$

$T_k = 40 - 100$ K

Active star formation may be in progress.

i.e. IR sources
OH, H_2O masers
young stars (T Tauri)
compact HII regions
molecular outflows

the infrared since all the radiation will, ultimately, be degraded to infrared photons through absorption and re-emission by dust grains mixed in with the high-density gas (Stahler, Shu & Tamm 1980 & 1986). The core regions, being characterized by dust temperatures, T_d = 30-100 K, are strong 10, 20, 50 and 100 μm infrared continuum sources, whilst the GMC, as a whole, will radiate predominantly in the 300 μm region due to its lower average dust temperatures, T_d = 10-20 K.

If star formation has continued for longer than 10^5 yr, then, in all probability, the most massive stars will have evolved to their nuclear hydrogen buring phase, thus leading to the generation of abundant ionizing radiation, accompanied by the immediate formation of an ultra-compact radio continuum and recombination-line nebula. Multi-frequency radio continuum and near-infrared Brackett alpha HI recombination-line observations are thus extremely useful as indirect tracers of recent high-mass star formation within dense cloud cores. More importantly, if both radio and infrared observations are available for the same star-forming cloud core, then it is possible to investigate whether the luminosity derives primarily from a single massive star or a cluster of lower-mass stars. If the latter case applies, then such observations can further be used to estimate the luminosity function for the stars in the cluster; a quantity of immense importance for understanding the star formation process and its influence on the initial mass function (Lada & Wilking 1984; Lada 1986).

The most important advance in the observational study of star formation within GMCs has taken place over the last decade and involves the discovery of highly-energetic and organized motions associated with the gas forming the dense cloud cores, as revealed through the ubiquitous observation of anomalously

broad CO line profiles. These flows were first discovered by the observation of extended wings of CO J=1-0 rotational line emission along the line of sight to the Orion Molecular Cloud (Zuckerman, Kuiper & Rodriguez-Kuiper 1976). Mapping of the high-velocity emission regions suggests an anisotropic angular distribution of the red and blue-shifted velocity components (Bally & Lada 1983). Centres of these molecular flows often coincide with bright sources of infrared emission which may represent sites of recent star formation (Downes et al. 1981; also, see Lada 1986, for an excellent review). Since such flows have been observed in both high-mass (e.g. Orion) and low-mass (e.g. T Tauri stars) star formation sites, they may correspond to a universal evolutionary stage between the collapse of the parent molecular cloud and the eventual formation of new stars. Indeed, the occurrence of an energetic mass-loss phase during early stages of the star formation process may play an important, if not decisive, role in fixing the final mass of the young star formed and, on a more global scale, may determine the initial proto-stellar mass function. Depending on their lifetimes, high-velocity molecular outflows can also present the major source of energy and momentum injection into the natal GMCs and may, therefore, help thermalize the cloud medium and prolong the lifetimes of GMCs beyond their predicted free-fall timescales ($\sim 10^6$ yr).

The nature of the energy source responsible for driving these hypersonic motions is presently a complete enigma, but is inevitably associated, in some broad physical sense, with the star formation process itself. Numerous theoretical models have been proposed which attempt to explain this enigmatic phenomenon in terms of a diverse variety of fundamental physical processes, however, the current status of the observations is inadequate to unambiguously differentiate between any of these equally plausible models.

Clearly, because of its fundamental importance to all aspects of star formation and molecular cloud evolution, a deeper understanding of the enigmatic young-stellar outflow phenomenon is perhaps one of the most important quests bestowed upon infrared, millimeter and radio observers at this moment in time. As a consequence of the nature of the star formation process (takes place in the optically opaque cores of dense molecular clouds), advancements in this exciting new field of galactic astronomy rely heavily upon the accumulation of both line and continuum observations at wavelengths longer than 1 μm.

The observations presented in this thesis where motivated by the desire to improve upon existing observations by undertaking a detailed investigation of one particular outflow source, DR21, using information derived from infrared, millimeter and radio line/continuum observations. The rationale was that these detailed observations would supply important new constraints governing the physical nature and time evolution of the poorly understood young-stellar outflow phenomenon.

CHAPTER 2 BACKGROUND TO THE H_2 MOLECULE

2.1 PROPERTIES OF THE H_2 MOLECULE

The properties of diatomic molecules are treated in detail by Herzberg (1950). Here, only those notations and concepts directly related to the molecular hydrogen (H_2) molecule will be briefly reviewed.

Fig.[2.1.1] shows an energy level diagram of the H_2 molecule. Each electronic state has a series of vibrational levels (with vibrational quantum numbers v) and each of these breaks up into a rotational fine structure (with rotational quantum numbers J). Since H_2 is a homonuclear molecule, electric dipole transitions can only occur between different electronic states. The transitions from the electronic ground state $X\,^1\Sigma_g^+$ to the $B\,^1\Sigma_u^+$ and $C\,^1\Pi_u$ states are known as the Lyman and Werner bands with wavelengths in the far ultraviolet region (912 - 1108 Å). Transitions are labelled by giving the upper and lower vibrational quantum number, v, and by R(J), Q(J) or P(J), if the rotational quantum number, J, of the lower state changes by 1, 0, -1, respectively. Accurate wavelengths and corresponding spontaneous transition probabilities, A, for the different spectral lines can be found in the literature (Allison & Dalgarno 1970, Cartwright & Drapatz 1970).

In contrast to the overtone electronic states, electric and magnetic dipole transitions between different vibrational-rotational levels of the electronic ground state are forbidden, but electric quadrupole transitions may occur. These quadrupole transitions are labelled by the upper and lower vibrational quantum number, v, and by S(J), Q(J) or O(J), if the rotational quantum number, J, of

FIGURE 2.1.1 (a) Electronic Energy Levels of H_2

Schematic potential energy curves of the low lying electronic states of H_2 are shown (after Field et al. 1966). States with total electronic orbital angular momentum, $\Lambda = 0$, 1, or 2 are Σ, π, or Δ states. The subscripts g or u and superscripts + or - indicate the symmetry properties of the electronic wave function and the value of $2S + 1$ is a left superscript to the term symbol, where S is the total electronic orbital angular momentum. The total energy is plotted against internuclear distance. The electronic states involved in the Lyman and Werner band transitions are indicated for the convenience of the reader.

(b) Vibration-Rotation Energy Levels of H_2

The vibration-rotation energy levels in the ground electronic state and the v=1-0 Q(3), S(1), O(5) transitions are shown. (The vibrational quantum numbers are indicated by v and the rotational quantum numbers are indicated by J′, J′′, and J′′′.)

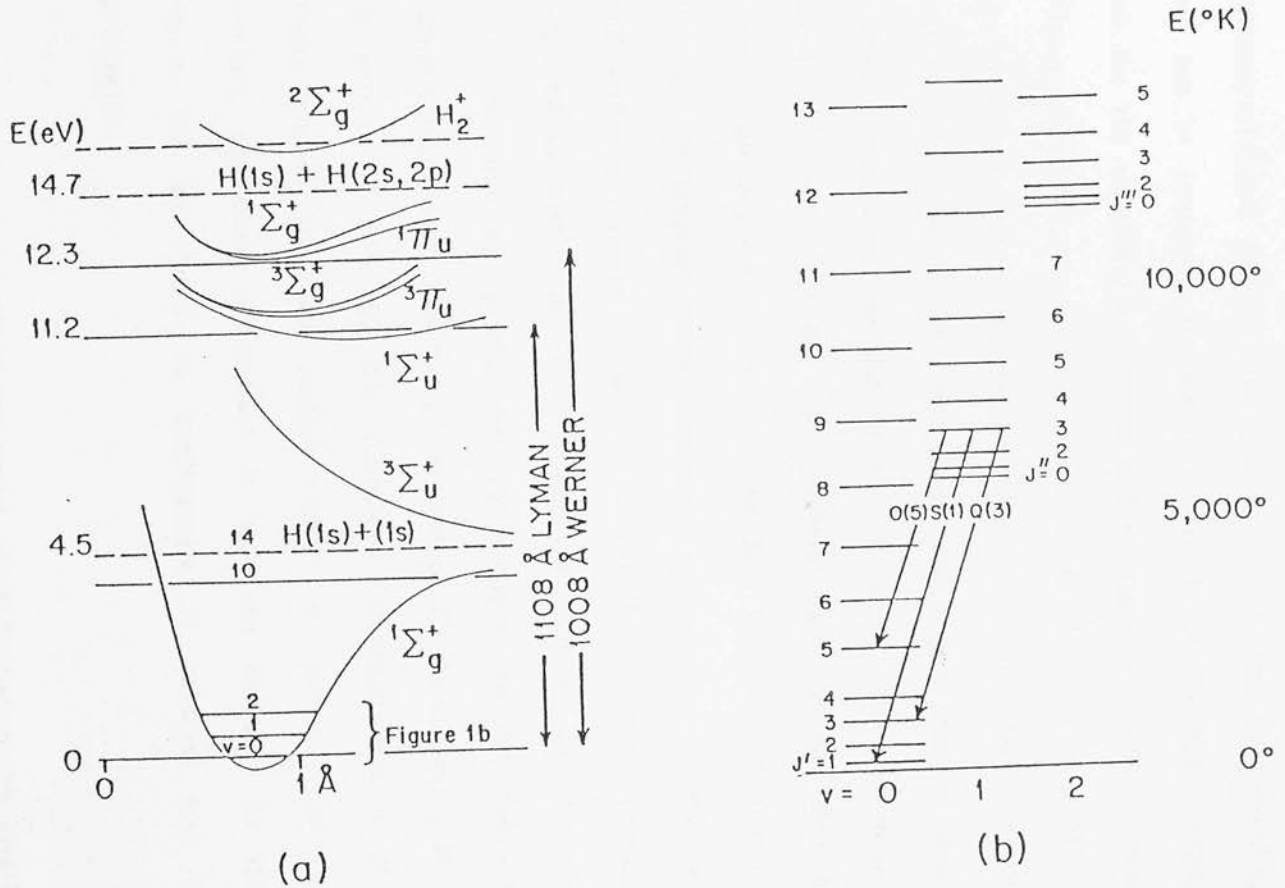

FIGURE 2.1.1 : see previous page for description.

the lower state changes by 2, 0 or -2, respectively. 0-0 transitions are forbidden. The strongest vibrational-rotational lines with $\Delta v = 1$ occur around 2 μm in the near-infrared region, while pure rotational lines (in the $v = 0$ state) lie between 3 and 28 μm. Empirical measurements and theoretical calculations of vibrational-rotational energy levels (up to $v = 4$) and corresponding transition values can be found in Dabrowski (1984). In Appendix[1], tables are given which list the wavelengths, energies and spontaneous transition values of many of the strongest H_2 quadrupole transitions in the near-infrared window (1-5 μm). Because H_2 has a very small moment of inertia, the rotational levels are widely spaced, i.e. excitation temperatures reach a few hundred degrees even for the lowest levels. Thus, the vast majority of the H_2 molecules in the interstellar medium will freeze into the lowest energy state and can therefore only be detected in the ultra-violet electronic resonance lines through absoption against a background continuum source. Localized excitation mechanisms such as UV photon pumping followed by cascade through the vibrational-rotational levels of the ground electronic state or collisional excitaion at high molecular densities and temperatures are prerequisites for emission in the near-infrared lines. Prominent radio lines (like the 21 cm line of H) do not exist, only very weak lines around 50 and 500 Khz (ultra-fine structure) due to the interaction between nuclear spin and nuclear rotation are present (Field et al. 1966). Therefore, the direct observation of molecular hydrogen in the interstellar medium has to reside on spectroscopy at infrared and far-ultraviolet wavelengths.

As a result of possessing two nuclei which happen to be identical fermions, H_2 exists in two different forms, ortho-H_2 and para-H_2 (Herzberg 1950). Ortho-H_2, in which the nuclear proton spin projections are parallel, consists of nuclear triplet states characterized by odd-J rotational quantum numbers only. In

para-H_2, the nuclear spin projections are antiparallel, thus the symmetry laws of quantum mechanics allow only singlet states, and the molecule is characterized by even-J rotational levels only. Following the usual rules governing angular momentum stastistics, the stastistical weight, g, of a level, J, in the ground state is 3(2J+1) for odd J (ortho-H_2) and (2J+1) for even J (para-H_2). Since the exothermicity of the formation reaction of H_2 exceeds the relative energy spacing of the even and odd states, then the probability that the forming molecule will end up in odd or even-J form is simply proportional to the 3:1 relative statistical weights of the respective states (Reeves & Harteck 1979). Ortho-para interchange via radiative or simple collisional processes is striktly forbidden (Dalgarno, Black & Weisheit 1973, Dalgarno 1975, Reeves & Harteck 1979). Dalgarno (1975) has shown that, at the temperatures and densities characteristic to the cool interstellar medium, practically all of the H_2 present will be in the lowest J rotational states of the lowest vibrational state : J=0 for para-H_2 and J=1 for ortho-H_2. The energy deficit beween these two lowest states roughly correseponds to 170 K. Therefore, at low temperatures one would expect a net conversion of ortho-H_2 to para-H_2, that is, the ortho-para ratio in the interstellar medium should be in the range between 3:1 and 0:1.

Infrared observations of vibrational H_2 line emission towards the Orion high-velocity outflow (Davis et al. 1986) show that the empirical ortho-para ratio is indeed 3:1 for a shock-excited source. However, of more importance, are the recent observations of Hasegawa et al. (1987) which clearly show that this ratio is of order 1:1 in the UV fluoresced H_2 emission-line source associated with the bright reflection nebula, NGC2023. The exciting possibility thus arises that further observations of the H_2 ortho-para ratio in a wide variety of astrophysical environments may facilitate a new probe of the physical and chemical processes that occur within and around dense molecular clouds.

2.2 EXCITATION OF INFRARED H_2 LINE EMISSION

Molecular hydrogen can be excited to produce infrared line emission either by interaction with ultra-violet (UV) radiation or by collisional shock heating. The physical processes involved in these two excitation mechanisms will now be discussed, as they bear direct relevance to the interpretation of the observational data presented in Sec.[4.2] of this thesis.

2.2.(a) NON-THERMAL EXCITATION

After absorption of a photon, an atom or molecule will usually cascade back through a variety of states, reaching levels which could not be populated by direct radiative transitions from the ground state. This indirect excitation of low-lying levels by photon absorption is termed "photon pumping" or "fluorescence". The excitation of the H_2 molecule via fluorescence with UV photons was first introduced as a possible mechanism for stimulating abundant vibrational H_2 line emission by Black & Dalgarno (1976). The basic physical processes underlying the UV fluorescence mechanism can be summarized as follows.

Under normal interstellar conditions H_2 molecules are almost entirely concentrated into the lowest (v=0) vibrational level of the ground electronic state, X (see Fig.[2.1.1]). These low-excitation H_2 molecules can absorb an ultraviolet photon, in the Lyman or Werner bands (912 - 1108 Å), and jump to any vibrational level of the excited electronic states B or C, with $\Delta J = 1$. The molecule then spontaneously decays back down to any vibrational level, v, of the ground electronic state, X. Transitions to levels with $v > 14$ (or with $J > 5$

for v = 14) lead to dissociation of the molecule, accounting for approximately 11% of the total Lyman and Werner band absorptions. The remaining 89% of the absorptions end up in bound vibrational levels of the electron state, X, from where they continue to cascade down in a series of rotational-vibrational transitions to v = 0. Typically, for every cascading molecule, there is a 1 to 3% probability that it will "flow" through a particular channel in the v = 1-0 band, such as S(1) (Black & Dalgarno). At low densities and UV fluxes, the radiative cascade is entirely determined by the product of the "cascade entry matrix" (the fraction of pumped H_2 that enters the ground electronic state in level vJ) with the "cascade efficiency arrays" (which describe the cascade lines that result per unit population rate of level vJ).

Hollenbach & Shull (1977) describe how the observed intensity, and hence the column density, of a specific line can be related to the local UV pumping rate. The analysis assumes that most of the pumped H_2 lines lie on the square-root portion of the curve of growth, and that extinction by dust is negligible. In essence, the calculation involves a simple multiplication of the pump rate by the product of the fraction of pumped H_2 that passes through a level vJ and the radiative lifetime of that level. Complications arise, however, in the dense environment of a cool molecular cloud as the UV absorption rate is then significantly reduced by dust absorption and line self-shielding (Shull 1978b). The relative intensities of several near-infrared H_2 lines, as predicted by the Black & Dalgarno (1976) model, are compared with those predicted by other line excitation mechanisms (see below), in Table[4.2.1b].

A severe limitation of the Black & Dalgarno (1976) analysis is that their model applies only for the case of low interstellar densities ($n(H_2) = 10^3$ cm^{-3}) and thus cannot be used to predict emission line ratios under normal molecular

cloud conditions where densities are high. Noting this limitation, Shull (1978a,b) extended the work of Black & Dalgarno to the case where the UV flux is high, and included multiple pumping and other density sensitive effects, finding a similar distribution in v but a spread to higher J values. Others (London 1978, Tielens & Hollenbach 1985a,b) have developed more elaborate cloud models to include the effect of a region of photodissociation advancing into the cloud ahead of an expanding HII region. Overall, the main astrophysical quantities which affect the population of the (v,J) levels are found to be the UV pumping rate, the UV extinction of the dust associated with the gas (which competes for H_2 pumping photons) and the density and temperature of the gas (for the gas can redistribute the population by collisional processes). In the high UV photon flux case, the important variable is the gas density, as the strength of the fluorescence is almost independent of the UV flux owing to an interesting saturation phenomenon (Shull 1978a,b).

Webster (1986) has illustrated how the fluorescence mechanism populates the different magnetic substates for a given (v,J) differently thus resulting in polarized emission; the cascade process and collisional redistribution will, however, tend to lower the degree of polarization.

Resonance fluorescence of H_2 molecules via interaction with Lyman alpha/beta line photons, for example within or close to luminous HII regions, provides yet another route for populating the vibrational states (Raymond et al. 1981; Schwartz, Dopita & Cohen 1985).

2.2.(b) THERMAL EXCITATION

This second mode of excitation involves the collisional excitation of H_2 in the hot, dense gas following the propagation of a strong shock wave through a molecular cloud. The high efficiency of the conversion of kinetic to thermal energy in these molecular shocks can result in rapid cooling via strong infrared H_2 line emission. The potentially large column densities of thermally excited H_2 associated with these shocks further explains why this particular mode of excitation has dominated the observational scene over the past decade (Shull & Beckwith 1982).

The first models attempting to describe the passage of a strong shock within a typical molecular cloud environment ($n(H_2) > 10^3$ cm^{-3}) were constructed using simple hydrodynamical codes. Under these crude assumptions, the passage of a strong shock-wave can be modelled as an impulsive event in a single-fluid medium. As shown by Field et al. (1968), the shock separates into four distinct zones; (i) the pre-shock zone, (ii) the region where the translational motion is excited, (iii) the region where vibrational, rotational and fine-structure states are excited, and (iv) the region where the post-shock gas is radiatively cooled. The application of hydrodynamical shock models to explain the H_2 emission observed toward the Orion outflow was pioneered by Kwan (1977), Hollenbach & Shull (1977), and London et al. (1977). These models, which assume plane-parallel shocks and steady-state conditions, are characterized primarily by two parameters: the preshock density n_0, and the shock velocity V_S. For a hydrodynamic shock, collisional dissociation of H_2 becomes important for $V_S >$ 25 kms^{-1}, if $n_0 > 10^5$ cm^{-3} (Hollenbach & McKee 1980). For $V_S <$ 25 kms^{-1}, region (i) is negligible and region (ii) collapses to form an infinitesimally thin discontinuity in the translational temperature, T, and density, n.

The critical density, n_{crit}, required for thermal population of the H_2 levels can be readily calculated by noting that the collisional de-excitation rate of a level must be greater than the corresponding spontaneous decay rate. As the spontaneous decay rates increase with increasing vibrational quantum number (see Appendix[1]), a strong upper limit on the post-shock density required for theramization of the H_2 levels can be derived by considering the specific case of the v=2-1 S(1) transition. Consequently, the above defined condition can be expressed as, $n(H,H_2).g_{21}(H,H_2) > A_{21}$, where, $n(H,H_2)$ is the density of a specific species (neutral or molecular), $g_{21}(H,H_2)$ is the collisional de-excitation rate for the same species and A_{21} is the corresponding spontaneous decay rate. Using the values given by Hollenbach & McKee (1979), critical densities of, $n(H) > 4\times10^3$ and $n(H_2) > 3\times10^5$ cm^{-3}, are calculated for collisions with atomic or molecular hydrogen, respectively. These two values are significantly different and clearly emphasize the point first made by Kwan (1977) that partial dissociation of H_2, thus increasing n(H), can be very effective for thermalizing the molecule at only moderate densities. For pre-shock densities, $n_0 > 10^5$ cm^{-3}, region (iii) may, therefore, also be treated as a discontinuity, in which a thermal population of rotational and vibrational levels is produced.

Fortunately, modelling of the H_2 line intensities does not require the use of complex radiative transfer codes as the H_2 quadrupole lines are optically thin for column densities, $N(H_2) < 10^{25}$ cm^{-2}, because of their low A-values; observed values for $N(H_2)$ are typically $< 10^{20}$ cm^{-2}. The post-shock temperature in region (iii) is therefore given by the usual adiabatic jump approximation

$$T_S = 2 \frac{[\ \gamma - 1\ ]}{[\ \gamma + 1\ ]^2} \frac{\mu_0 V_S^2}{k} \approx 3080\ K \left[\frac{V_S}{10\ kms^{-1}}\right]^2 \qquad (2.2.1)$$

where, μ_0, is the mean molecular weight (=2.36) and, γ, is the adiabatic index (=9/7 for three translational, two vibrational and one rotational degree of freedom).

An approximation to the emission intensity expected from a plane-parallel shock, viewed plane-on, can be derived as follows. The intensity of a transition from level i to level j can be written as

$$I_{ij} = f_i\ N(H_2)\ A_{ij}\ E_{ij}\ /\ (4\pi) \qquad (2.2.2)$$

where, A_{ij}, is the spontaneous emission rate (s^{-1}), E_{ij}, is the transition energy, $N(H_2)$ is the total column density (cm^{-2}) of H_2 molecules, and, f_i, is the fraction of H_2 in the upper state. A characteristic cooling time, t_c, after which the gas is assumed to fall rapidly to zero temperature, can also be introduced

$$t_c = \frac{[\ \gamma\ ]}{[\ \gamma - 1\ ]} \frac{k\ T_S}{f_i\ A_{ij}\ E_{ij}\ \epsilon_{ij}} \qquad (2.2.3)$$

where, ϵ_{ij}, is the ratio of the total cooling rate to the rate in the line (ij). Further noting that the total column density of H_2 molecules through the post-shock layer is given by, $N(H_2) = n_0\ V_S\ t_c$, then sustitution of eqns.(2.2.1) & (2.2.3) into eqn.(2.2.2) gives the desired result

$$I_{ij} = \frac{\mu_0\ n_0\ V_S^3}{4\ \pi\ \epsilon_{ij}} \frac{[\ 2\gamma\ ]}{[\ \gamma + 1\ ]^2} \qquad (2.2.4)$$

One thus arrives at the well-known result that the power per unit area of the shock front radiated in the H_2 line is directly proportional to the product of n_0 and V_S^3. This simple proportionality, relating the H_2 line intensity with the pre-shock density and shock velocity, is the fundation underlying all shock interaction codes, and will be employed frequently in the interpretation of the H_2 observations, to be presented in Sec.[4.2].

The purely hydrodynamical analysis described above is, unfortunately, severely limited in its applicability to the real physical conditions expected to pertain within dense molecular clouds. Primarily, the influence of magnetic fields can introduce new physics into the problem, such as ambipolar diffusion, which will significantly alter the physical and dynamical structure of the shocks. This has been clearly explicated by Mullan (1971) and Draine (1980), who find that if the fractional ionisation, X_{io}, in the pre-shock gas is low (i.e. $X_{io} < 5\times10^{-7}$), then magnetic fields may alter substantially the structure of shock waves and in particular may lead to lower levels of excitation and dissociation in the shocked gas than in the non-magnetic counterparts (Draine, Roberege & Dalgarno 1983).

Draine (1980) defines a critical preshock magnetic field strength, B_{crit}, which separates two distinct classes of shock wave structure; B_{crit} depends on V_S, n_0 and X_{io}. When the component of the pre-shock magnetic field perpendicular to the shock velocity, $B_{0\perp}$, is less than B_{crit}, then neutral-neutral collisions dominate the momentum transfer in the shock. As a result, the gas is suddenly accelerated and heated in the shock front over a length scale short compared with characteristic cooling lengths. The shock front can therefore be treated as a nonradiative discontinuity or "jump"; Draine terms such structure

"J-type" shocks. Shocks in interstellar molecular gas are J-type for shock velocities, V_S > 40-50 kms-^{1} (McKee, Chernoff & Hollenbach 1984). These shocks are therefore dissociative and radiate strongly at UV and optical wavelengths. The strongest infrared lines generated by J-type shocks are usually fine structure lines, such as [OI] 63 μm and [SiII] 38 μm; emission in H_2O and OH lines can also become important coolants at high pre-shock densities (n_0 > 10^7 cm-^{3}). H_2 reformation on grains may occur further downstream from the hot shock front, in the cooler recombination region. This process can elevate the gas temperature and may give rise to weak H_2 line emission at velocities significantly shifted relative to the cloud rest velocity. The neutral temperature, density and flow velocity profiles of a J-type shock are schematically shown in Fig.[2.2.1a].

When, B_{crit} > $B_{0\perp}$, then the acceleration of the neutral gas is due to collisions with charged particles (ions, electrons and grains). For sufficiently strong magnetic fields, compressive (magnetosonic) waves can propagate upstream of the shock thus helping to smooth out any sudden discontinuities, resulting in an interaction length scale which is long compared to the characteristic cooling length. Draine terms such structure "C-type" shocks since the structure parameters are continuous variables. The theoretical modelling of C-type shocks is rather complicated as relative interactions in a four-fluid medium must be treated. In contrast to J-type shocks, C-type shocks exist only in magnetized, weakly ionized molecular gas and, as a consequence of the lower excitation conditions, radiate primarily at infrared wavelengths.

The important observational effects of magnetic fields on shocks are (i) to lower the peak temperature of the neutral gas, (ii) to lower the compression of the gas whilst it is radiating, (iii) to heat the molecules over a much larger

range of velocities, and (iv) to increase the critical velocity for dissociation, V_s < 40-50 kms^{-1} (Hollenbach 1982). The intensity of H_2 line emission in C-type shocks is typically an order of magnitude stronger than in J-type shocks (Chernoff, Hollenbach & McKee 1982; Draine & Roberge 1982). The C-type shock structure, of the neutral component, is shown schematically in Fig.[2.2.1b].

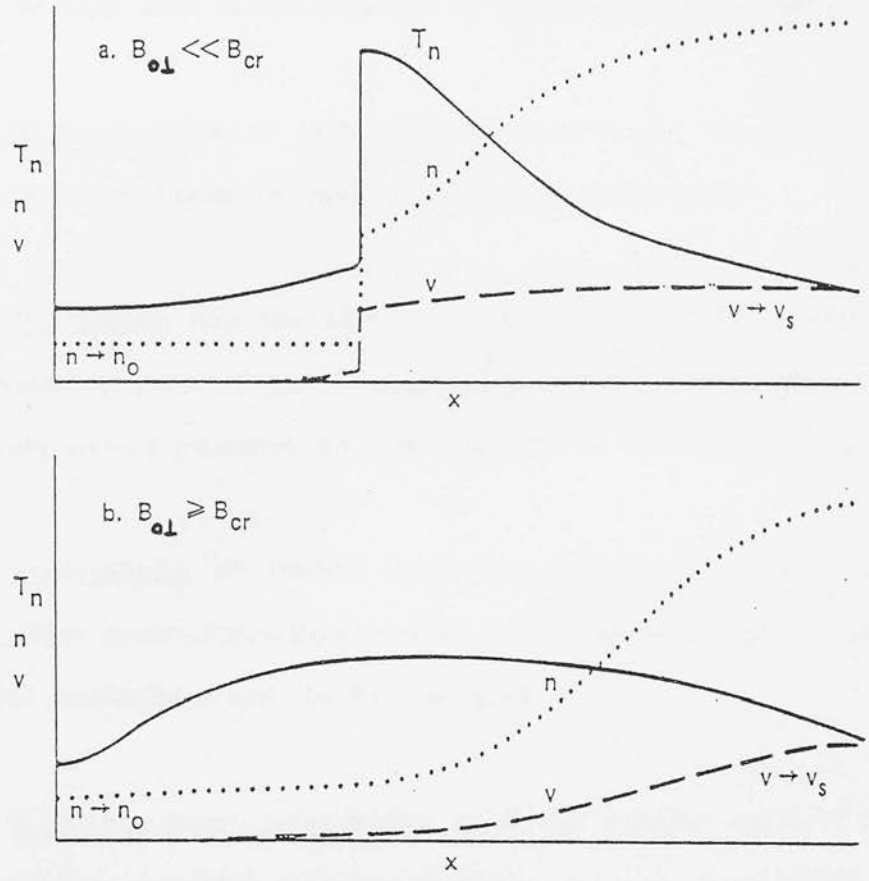

FIGURE 2.2.1 : A schematic plot of the neutral temperature, Tn (solid line), neutral density, n (dotted line), and neutral flow velocity, v (dashed line), in the rest frame of the preshock gas. In (a), a J-type shock with a sharp discontinuity and a high T(max) is seen; in (b), a C-type shock is pictured with reduced T(max) but a substantially greater column density of warm gas, emitting over a wider range of v and lower values of n.

CHAPTER 3 OBSERVATIONAL STRATEGY OF THIS WORK

3.1 THE OBSERVATIONAL GOALS

The main goals of this work can be broadly outlined as follows:

(a) To survey regions of recent star formation for H_2 line emission in order to find prime candidates for more detailed observational study.

(b) To illustrate how the infrared H_2 line emission can be used as a highly advantageous probe of the dynamics, energetics and morphology of high-velocity outflow activity associated with star formation in dense molecular clouds.

(c) To investigate the physical relationship between the infrared vibrational H_2 and other density/temperature sensitive millimeter-wave molecular emissions with spatial displacement over the outflow region.

(d) To gain a better understanding of (i) the physical origin of the mass-loss phenomenon associated with star formation and (ii) the processes involved by which the injected energy and momentum is mediated to the surrounding ambient cloud medium. Of particular interest in this regard, is an investigation of the physics underlying the collimation/confinment mechanisms that lead to the formation of anisotropic (bipolar) outflows, or jets, within dense molecular cloud environments.

(e) To highlight the potential of collaborative infrared and millimeter-wave studies, preferably at comparable angular resolution, as an important new

technique for probing the detailed microstructure of hypersonic molecular flows. This technique is applicable to any region where dense molecular gas is shocked by impact with a supersonic flow.

The purpose of this thesis is to present a detailed infrared and millimeter-wave spectroscopic study of the extremely violent outflow activity associated with luminous star formation internal to the DR21 molecular cloud. From the appearance of the "quick-look" spectroscopic maps of the seven outflow sources (OMC2, NGC6334, W51, W49, GL691, NGC1333 and DR21) observed during the preliminary H_2 v=1-0 S(1) emission-line survey, it was immediately obvious that the DR21 H_2 source would prove the most interesting for further study; being considerably brighter, larger in angular extent and morphologically more interesting than any of the other outflow sources mentioned above. Furthermore, at that time (1983), a number of observations had already been published which unambiguously prove the enigmatic nature of this dynamically active region. In particular, the DR21 source was already known to possess a far-infrared luminosity (Harvey et al. 1977), CO profile widths (Dickel et al. 1978) and extended H_2 line emission analogous in nature to those previously observed in association with the extremely interesting and well studied Orion outflow source. It was therefore without reservation that I decided to focus all future effort in undertaking as detailed a study as possible of the fascinating DR21 star-forming region.

3.2 A DESCRIPTION OF THE OBSERVING TECHNIQUES

By analogy with the Orion outflow source (Beckwith at al. 1978), it is most likely that the infrared H_2 emission-line regions associated with other molecular

clouds are similarily characterized by extended, diffuse emission which may not necessarily coincide with other previously identified indicators of star-formation activity. It is thus good observational strategy to execute searches for such emission with instruments accomodating large beam sizes; once the main areas of interest are well defined on a global scale, only then is the application of higher-angular resolution advised. Appropriately, I always adopted a standard practice of commencing with the lowest angular and spectral resolution available (typically, a 20 arcsec beam and 1% CVF), then carefully progressed to higher resolution, the final outcome depending upon the time available and the underlying brightness of the source in question.

For the line intensity measurements, the circular variable filter (CVF) gives good results for sources in which the line-to-continuum ratio is large, otherwise, if the continuum comprises a significant fraction of the line emission then a Fabry-Perot interferometer (FP), of low resolution (i.e. 100 kms^{-1}), was used in order to increase the available line equivalent width. At higher velocity resolution, the line may be partially resolved, resulting in a decrease of the line-to-continuum ratio. Consequently, a velocity resolution higher than 100 kms^{-1} was employed only when line profile information was desired.

The problem of chopping the secondary mirror and beam-switching the telescope between the signal and sky reference positions in regions of larger emission extent than the chop throw, was solved using a variety of standard and some not-so-standard techniques. The specific observing mode chosen varied from object to object depending on the anticipated line strengths and an "a priori" knowledge of the emission-line distribution and the existence of other emission components which may further confuse the H_2 mapping observations (ie. the location of bright stars or luminous HII regions).

The various observing methods employed to obtain the infrared data presented in this thesis were as follows:

(a) DUAL-BEAM CHOPPING: This is the most commonly used method at infrared wavelengths were thermal background fluctuations dominate over most other potential noise sources. Consequently, it is the best method to use if the source size is smaller than the chop throw (for UKIRT, this is a maximum of 4 arcmin), if the observations are made under background-limited conditions (i.e. at wavelengths above 2.4 μm through a CVF), if weather conditions are poor, or if scattered moonlight is a problem. It is therefore preferable to default to this well-proven method when at all possible. All of the long-baseline CVF spectra and velocity-resolved H_2 line profiles presented in this thesis were aquired using this technique.

(b) SINGLE-BEAM CHOPPING: This is a second-best alternative to method (a). If the source size is larger than the maximum chop throw but less than than two chop throws in width then two maps can be made, in the left and right beams, each covering one half of the total source area. These positive and negative images can then be merged at a later date. The major disadvantage here, especially for background-limited conditions, is that any local gradients in the thermal sky emission are not accounted for. The H_2 v=1-0 S(1) emission-line maps of the Orion Molecular Cloud (Fig.[4.2.1]), NGC2023 (Gatley et al. 1986) and the Orion Bright Bar (Hayashi et al. 1986) were made using this method. The excellent quality of these published data, which were made under detector-noise limited conditions, advocates the usefulness and reliability of this method.

(c) FREQUENCY-SWITCHING: This method requires the use of a reasonably high-spectral resolution CVF or FP and works best for strong emission-line sources with little or no continuum emission. Basically, the observations are made without the use of the chopping secondary and without beam-switching. Instead, the optical filter (FP or CVF) is modulated between the wavelength of the emission-line peak and a predefined wavelength lying on an uncontaminated part of the adjacent sky spectrum; the switching frequency was typically 1 Hz. This is the best method to use if one has no "a priori" knowledge of the source morphology or if it is suspected that the souce is relatively bright and very extended. Calibration was found to be good only to the 10% level, hence, this is not a photometric mode but, nonetheless, is highly desirable if approximate results are required quickly. The H_2 v=1-0 S(1) line-intensity map of the DR21 outflow source (Fig.[4.2.2]) was made using the frequency-switching mode in combination with a 100 kms^{-1} resolution FP.

(d) DC : This final observing mode, although used frequently at some infrared observatories, was not proven to be entirely reliable during test observations made using the near-infrared In Sb photometers on UKIRT. Specifically, it was found that observing in DC mode through a large beam (> 10 arcsec) in broad band (J,H,K) was plagued by severe non-linear drifts which could not be properly deconvolved. The DC stability is a strong function of both the entrance aperture diameter and the spectral resolution, and improves greatly with decreasing aperture and increasing spectral resolution. From my somewhat limited experience in this controversial field, it is my opinion that DC observations should be conducted only as a last resort, using the smallest beam size (< 10 arcsec) permitted by the source brightness and using a medium resolution FP in preference to a CVF. Furthermore, accurate and frequent monitoring of the sky emission throughout the observing period are crucial in

order to properly subtract the variable sky emission from the final image at a later date. Unlike the frequency-switching method, which performs automatic and almost instantaneous continuum subtraction, the DC mode requires that two separate maps be made, one in the line and the other in the adjacent continuum; these maps are not time synchronous and consequently necessitate a carefully thought out algorithm for their eventual subtraction. Any attempt to interpolate the sky behaviour over significant periods of time will undoubtedly introduce additional noise thus degrading the photometric quality of the final map. Although several attempts were made, no data of any real astrophysical significance was obtained using the DC method.

Of great benefit to the infrared mapping observations was the recent introduction of reasonably efficient telescope control and data aquisition software at UKIRT (under the supervision of Dr. Ian Gatley). The fast raster mapping capability was especially crucial for the success of many of the infrared observations presented in this thesis. Further improvements in the near future should arise from the introduction of a new generation of wide-field, near-infrared array cameras which are currently being developed by several groups. Their multiplex advantage coupled with efficient telescope rastering and data aquisition software should increase the present data gathering rate by several orders of magnitude. In retrospect, most of the infrared maps presented in this work, which were necessarily constructed using a single element detector, should be significantly extended by employing a 2-D infrared array (camera) to take high-angular resolution images of the brighter emission regions.

Observations conducted at near-infrared wavelengths using a 4 meter mirror facilitate higher angular resolution (effectively down to the seeing limit) than any currently available millimeter-wave dish, however, the infrared observations

are significantly inferior in terms of spectral resolution. The highest spectral resolution currently attainable in the infrared is of order 10 kms^{-1}, whilst millimeter heterodyne receivers are typically configured to have spectral resolutions as high as 0.1 kms^{-1}. In light of this spectral advantage, it is obvious that only by using efficient, low-noise (i.e. SIS) millimeter heterodyne receivers is it possible to probe in detail the kinematic structure of the molecular gas under study.

An extremely-large millimeter telescope (45 meters in diameter) has recently been constructed at the Nobeyama Radio Observatory in Japan; this is the largest millimeter-wave dish yet constructed and is a fine example of progressive planning. This telescope is unique in that its projected beam size on the sky at 115 GHz, the frequency of the J=1-0 transition of the abundant CO molecule, is approximately 15 arcsec and is thus comparable to the larger beam sizes available in the infrared with UKIRT. A direct comparison between the infrared and millimeter observations is therefore straightforward. Appropriately, extensive use of the Nobeyama telescope has been made in order to procure millimeter velocity-channel maps in a variety of density and temperature sensitive molecular emission lines for direct comparison with the near-infrared H_2 data. These studies clearly illustrate why a combination of observations spanning a wide range of frequencies are crucial for formulating an overall perspective of the problem in hand, in this case, an understanding of the importance of mass loss during early stellar evolution.

In total, 80 hours of observing time at the United Kingdom Infrared Telescope was awarded to this project, of which only 50% was of sufficient photometric quality to provide usable data. In contrast, out of the 110 hours of observing time allocated at the Nobeyama Radio Observatory, only 20% of the data was

lost due to poor weather conditions.

3.3 AN OUTLINE OF THE PRESENTATION

The observations are presented in chronological order thus enabling the reader to appreciate the strategy adopted and, hopefully, also the logical manner in which the problem of understanding the nature of the peculiar dynamical motions inherent to the fascinating DR21 region was approached. First, in Sec.[4.2], the preliminary large-scale mapping observations (June 1984) of the DR21/W75S molecular cloud complex in infrared H_2 line emission are described. It was the dramatic appearance of this map (Fig.[4.2.2]) which initially kindled interest in this particular star-froming region, as it clearly reveals the exceptional luminosity, size, and highly-collimated, bipolar morphology of the DR21 molecular outflows. Also in Sec.[4.2], follow-up high-spectral resolution profile measurements (June 1985) of the H_2 v=1-0 S(1) line, taken at several positions along the outflow lobes, are presented; these observations were made in order to supplement kinematic information to the existing line-intensity maps. Having gathered a satisfying quantity of exciting and informative infrared data, it was then (October 1985) deemed profitable to embark upon the next stage of the investigation, which entailed high-angular resolution mapping of the millimeter-wave CO emission using the 45-m telescope belonging to the Nobeyama Radio Observatory. The results of the CO observations are presented in Sec.[4.3]. Finally, in order to form a clearer picture of the role played by the dense core gas for generating and shaping the DR21 bipolar molecular outflows, a return journey was made to Nobeyama (in April 1986), during which time simultaneous observations of the CS J=1-0 and J=2-1 transitions were undertaken, the results of which are presented in Sec.[4.4]. In Chapter 5,

the infrared and millimeter data are combined, thus providing an extensive observational framework on which to discuss the physical state of the high-velocity gas that constitutes the DR21 outflows. In Chapter 6, a variety of theoretical ideas are introduced to investigate different dynamical models that help to constrain the nature of the central driving agent of the hypersonic molecular outflows and the physical processes important for their collimation. Finally, in Chapter 7, an overall review of the current observations is given, and the main conclusions derived from these observations are summarized.

CHAPTER 4 PRESENTATION OF THE OBSERVATIONAL RESULTS

4.1 THE DR21/W75S MOLECULAR CLOUD COMPLEX

The DR21/W75 molecular cloud complex, discovered by Downes & Rinehart (1966) in their 5 Ghz survey of the Cygnus X region, contains several compact HII regions and near infrared sources (Wynn-Williams, Becklin & Neugebauer 1974). Millimeter line observations indicate that there are two molecular clouds within this region, one at V_{lsr} = -3 kms^{-1} associated with DR21 and a second at V_{lsr} = 9 kms^{-1} associated with W75N, which is located approximately 18 arcmin to the north of DR21. The CO line profiles are broad with extended wing structure (FWZI ~ 50-60 kms^{-1}), indicative of high-velocity gas flows, over a 2 arcmin diameter centred on the DR21 cloud core (Dickel, Dickel & Wilson ~~Watson~~ 1978; Phillips et al. 1981; Richardson et al. 1986; Fischer et al. 1985; Garden 1986). Radio continuum interferometric observations at 6 cm (Harris 1973) indicate that the DR21 HII region is itself composed of four separate subcondensations, all of which possess luminosities consistent with those expected from single stars of spectral types O9 to O6. The integrated infrared luminosity of DR21 is 2×10^5 L_0 (Harvey, Campbell & Hoffmann 1977). At mid-infrared wavelengths, DR21 consists of two major components DR21(N) and DR21(S) (Wynn-Williams, Becklin & Neugebauer 1974), superposed on an extended region of diffuse emission showing a prominent east-west asymmetry (Harvey et al. 1986). Genzel & Downes (1977) have detected an H_2O maser near the southern source and suggest that this object may be the dominant outflow centre. Fischer, Righini-Cohen & Simon (1981) have detected an extended source of shock-excited H_2 line emission ~ 90 arcsec east of DR21 with an apparent luminosity of ~ 2 L_0.

Within a 3 arcmin radius of DR21 are two other infrared sources: W75(IRS1) and W75(IRS2) (Wynn-Williams et al. 1974). W75(IRS1) is closely associated with an OH maser, DR21(OH), which have a combined luminosity of ~ 5×10^4 L_0 (Harvey et al. 1977). W75(IRS2) lies within 1 arcmin of the luminous DR21 far-infrared/radio peak, but does not show any local enhancement of mid/far-infrared emission above that expected from the DR21 diffuse component; this source is, however, comparable in brightness to DR21(N) & DR21(S) at 20 μm. H_2 line emission has been detected at the position of W75(IRS1) by Fischer et al. (1981), who measure a S(1) line luminosity of ~ 0.1 L_0.

Despite the plethora of published data concerning the DR21/W75 region and its environs, attempts to understand its detailed structure and kinematics have been hindered by the confused aspect which it presents to us. Since it is situated in a local spiral arm viewed tangentially, spatially separated features are superimposed along the same line-of-sight; such contamination is particularily evident in the CO emission profiles presented in Sec.[4.3]. The most commonly quoted distance to the DR21/W75 molecular cloud complex is 3 kpc; this distance scale is therefore adopted throughout the following discussions. As a word of warning, however, the reader should always be aware of the considerable uncertainty in the assumed distance (1.5 to 3 kpc), especially when assessing the physical arguments presented in Chapter 5 & 6.

4.2 OBSERVATIONS OF INFRARED VIBRATIONAL H_2 LINE EMISSION

4.2.(a) INTRODUCTION TO THE H_2 OBSERVATIONS

Recent developments in near-infrared astronomical technology have made the task of mapping large areas of the sky (tens of square arcmin) in the diffuse line emission of vibrationally-excited H_2 a currently feasible and highly attractive proposition. The large-scale distribution of intensity and velocity width of the H_2 emission obtained from such observations provide a direct probe of the physical state and dynamical structure of the hot component of the molecular-cloud medium in which these lines originate. If more than one H_2 transition is studied, then useful constraints regarding the spatial distribution of excitation and extinction over the region mapped may also be derived (e.g. Beckwith et al. 1983; Beck & Beckwith 1983, Geballe et al. 1986).

Previously, such observations have necessarily been restricted to the central outflow region of the Orion Molecular Cloud, otherwise known as OMC1, where the line intensities are an order of magnitude stronger than any other presently known H_2 emission-line source. As part of our H_2 mapping programme, we (Gatley et al. 1986) have improved upon the previous observations by extending the area mapped to cover a 7 arcmin by 7 arcmin region centred on the Trapezium stellar cluster, as shown in Fig.[4.2.1]. The apparent size of the bright H_2 emission-line region associated with the Orion high-velocity outflow is extremely compact (less than 1 arcmin in diameter), hence, only a limited amount of information can be derived regarding the detailed outflow mophology at the angular resolution employed for this measurement (18 arcsec beam); note that the extended emission is not associated with the high-velocity outflow but

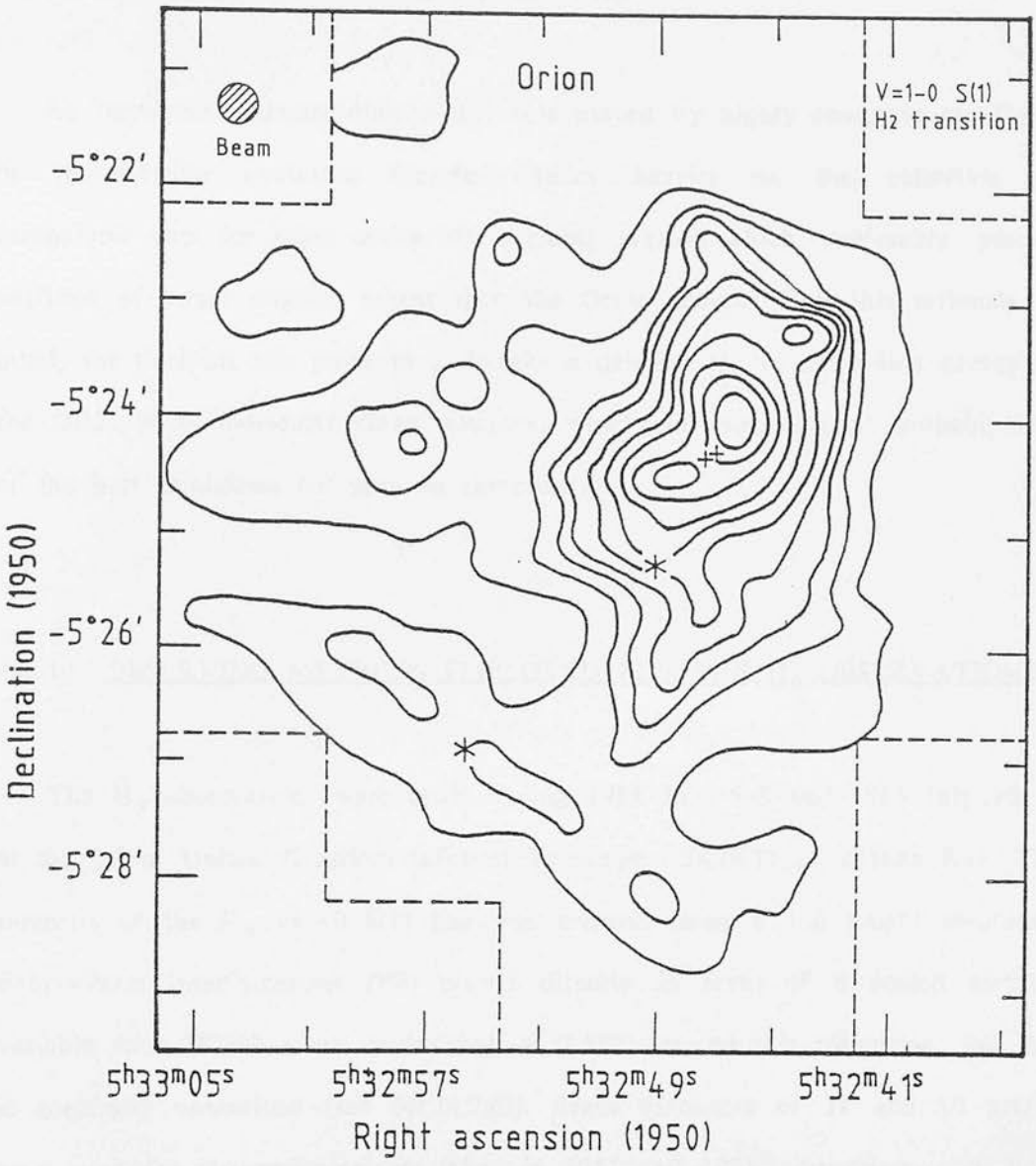

FIGURE 4.2.1 : Contours of H2 line intensity in the Orion region, made using a 100 kms-1 resolution FP and an 18 arcsec beam. Crosses indicate the positions of the infrared objects, BN (upper) and Irc 2 (lower) and the asterisks the positions of the Trapezium cluster star θ^1_C Ori (upper) and the star θ^2_A Ori (lower). The lowest intensity contour corresponds to a flux of 2(-20) W cm-2 and the highest contour to a flux of 2(-18) W cm-2. The measurements were made on a square grid with 15 arcsec spacing. The dashed line indicates the extent of the region mapped.

originates at the ionization fronts which separate the Trapezium HII region from the Orion Molecular Cloud (Hayashi et al. 1985).

An improved understanding of the role played by highly energetic gas flows in young-stellar evolution therefore relies heavily on the collection of comparable data for other active star-forming regions which, preferably, possess outflows of larger angular extent than the Orion source. With this rationale in mind, the decision was made to undertake a detailed H_2 emission-line survey of the DR21/W75S molecular cloud complex, which, in retrospect, is probably one of the best candidates for such an investigation.

4.2.(b) OBSERVING METHODS EMPLOYED FOR THE H_2 OBSERVATIONS

The H_2 observations were made during 1984 July 5-8 and 1985 July 10-14 at the 3.8-m United Kingdom Infrared Telescope (UKIRT) on Mauna Kea. The intensity of the H_2 v=1-0 S(1) line was mapped using a 130 kms^{-1} resolution Fabry-Perot interferometer (FP) placed directly in front of a cooled circular variable filter (CVF) tuned to transmit at 2.122 μm. At this resolution, the line is spectrally unresolved (see Sec.[4.2.d]). Beam diameters of 18 and 10 arcsec were used for the measurements taken in 1984 and 1985, respectively. On both occassions, the line intensity measurements were made by sequentially switching the FP between frequencies near the nominal S(1) line frequency and two absolute reference frequencies chosen to lie on uncontaminated parts of the adjacent atmospheric spectrum; a switching frequency of 1 Hz was used throughout. These observations were made using the telescope in DC mode, for which the chopping-secondary mirror is redundant. Each spectrum thus obtained consisted of three spectral points spaced by 75 kms^{-1}, with a total integration

time of 3 and 10 sec per point for the 18 and 10 arcsec beam observations, respectively. Both maps are half-beam sampled, with sky spectra and absolute pointing checked after every 10 map positions. Relative positions were established by offsetting the telescope from a nearby bright star and are accurate to 2 arcsec. Wavelength calibration of the frequency-switched data was determined by observing the H_2 v=1-0 S(1) line of the bright planetary nebula, NGC 7027. Line flux calibration was obtained by scaling the S(1) line fluxes at the peaks of line emission in the east and west lobes, to those measured with the CVF through the same sized aperture, but this time, using the secondary chopper and beam switching.

CVF scans (0.85% resolution) over a 2.0-2.5 μm interval were taken at the strongest peaks of line emission in both lobes, using 20 and 12 arcsec beams. Flux calibration of these CVF spectra was based on measurements of the 2.1 μm flux density of BS7949, whose K magnitude and temperature were assumed to be +0.11 and 6000 K, respectively.

Higher-spectral resolution v=1-0 S(1) line profiles were also obtained at several positions along the outflow axis in both lobes, where the line intensity showed strong local maxima. These measurements were made using an ambient-temperature, piezoelectric scanning FP of nominal resolution ~ 25 kms^{-1}. The basic instrumental set-up consisted of a collimator feeding parallel light through the FP, followed by a 0.8% blocking filter (CVF) and finally, reimaging the processed light onto a single 0.5-mm square In Sb detector. Both the CVF and In Sb detector were cooled to solid nitrogen temperature. The resultant instrumental profile, measured using a high-pressure argon arc, showed a reasonably symmetric Lorentzian profile with a FWHM ~ 35 kms^{-1}. In this observing mode, where temporal stability and reproducibility are crucial,

chopping of the secondary mirror at 3.5 Hz and telescope beam-switching 130 arcsec N-S was favoured over the DC method. Flux calibration of the profiles was attempted but is not accurate due to the complexities and uncertainties introduced by the overlap of adjacent orders (aliasing) resulting from the inadequate resolution of the CVF; although the CVF is ideally suited as an order sorter for the 100 kms^{-1} resolution FP, it allows approximately four orders to overlap in the case of the higher-resolution FP. Aliasing is not too severe a problem if, as is the case for DR21, the underlying continuum is negligible and no other strong emission lines occur within the FP pass-band. It is therefore expected that the observed line profiles give a good representation of the intrinsic source kinematics.

4.2.(c) APPEARANCE OF THE H_2 EMISSION LINE MAPS

Contour plots displaying the distribution of H_2 v=1-0 S(1) line flux over the DR21 molecular cloud complex, measured using an 18 and 10 arcsec beam, are shown in Figs.[4.2.2] and [4.2.3], respectively. The S(1) intensity contours reveal the existence of an extremely sinuous and elongated region of H_2 line emission oriented roughly E-W, and perpendicular to the N-S major axis of the DR21/W75S/W75N molecular cloud chain (Fig.[5.1.1]). An abrupt break in the continuity of the H_2 line emission, coincident with the DR21 cloud core and associated HII region, bisects the elongated structure into spatially distinct east and west lobes. The emission spans a projected distance of ~ 5 (D/3kpc) pc along the E-W axis, has a maximum breadth of ~ 1 (D/3kpc) pc, and becomes both weaker and narrower with increasing distance from the DR21 cloud core. The east lobe is shorter and appears more compressed than the west lobe and has its brightest peak of S(1) line emission located innermost to the centre. This

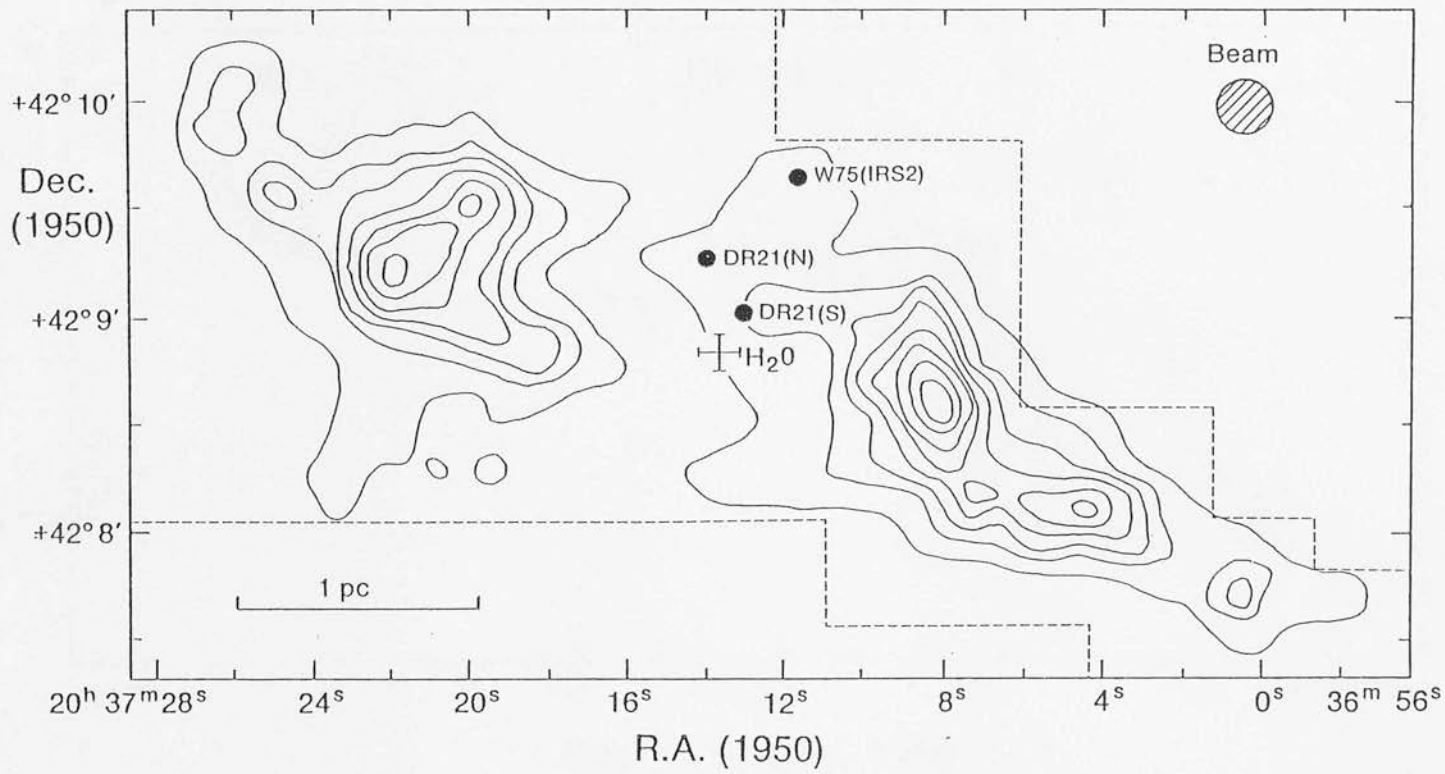

FIGURE 4.2.2 : Intensity contour plot of the DR21 H2 source in the v=1-0 S(1) line using data obtained on a 9 arcsec grid. The first intensity contour level is 2.1(- 12) W cm-2 ster-1 and the subsequent contour level intervals are 1.4(- 12) Wcm-2 ster-1. The dashed line indicates the region mapped, the hatched circle shows the beam size (18 arcsec) and a linear scale, corresponding to a distance of 3kpc, is provided. The positions of the infrared sources DR21(N), DR21(S), W75(IRS2) and the DR21 H2O maser (cross) are indicated.

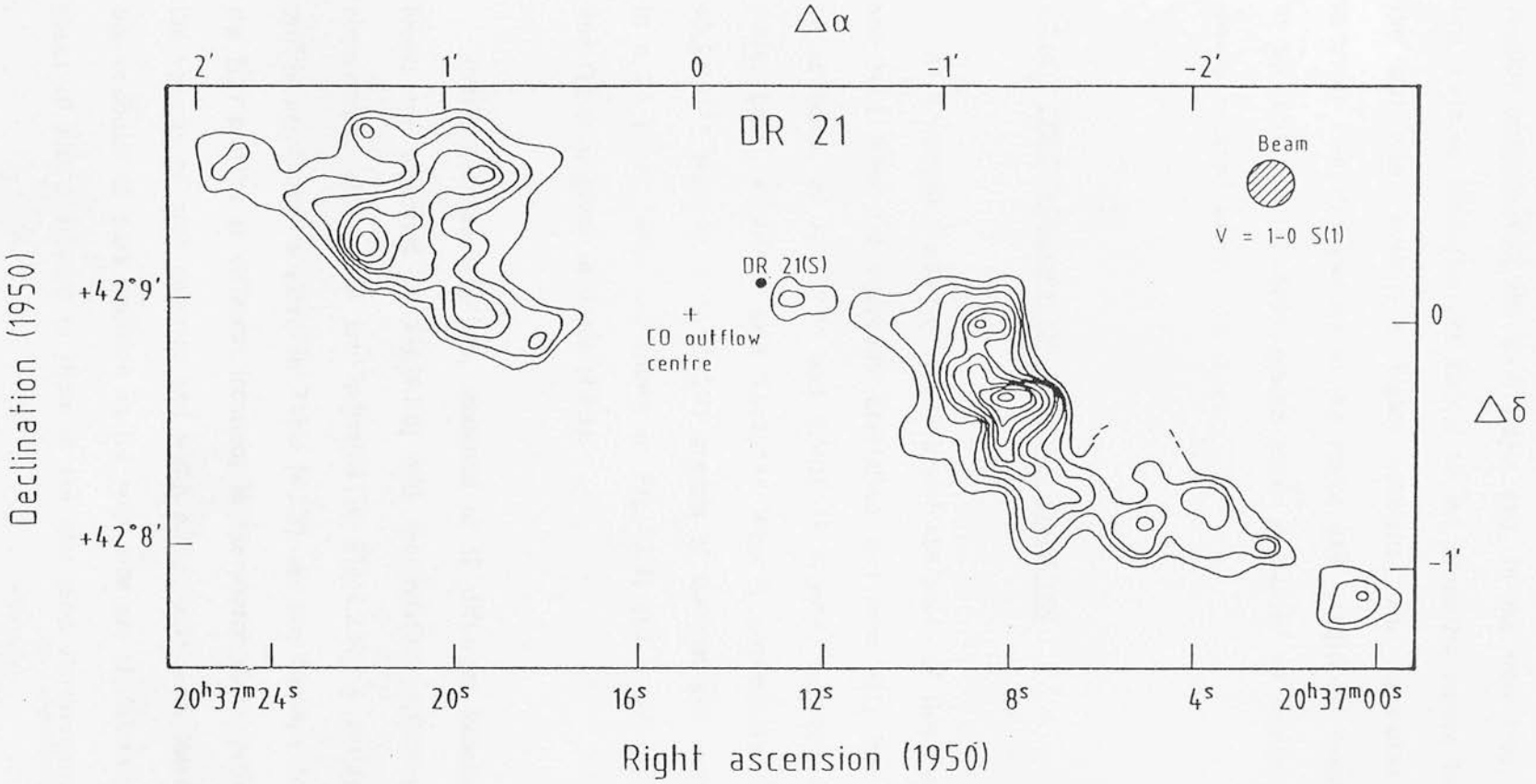

FIGURE 4.2.3 : Contours of H2 v=1-0 S(1) line intensity in the DR21 outflow as measured using a 100 kms-1 resolution FP and a 10 arcsec beam. The lowest intensity contour level is 3.5(- 12). W cm-2 ster-1 and the subsequent contour level intervals are 3.0(- 12) W cm-2 ster-1. The map is sampled on a square grid with 5 arcsec spacing.

eastern peak is broken into at least three subcomponents which form an outwards directed arrow, highly reminiscent of a segmented shell, oriented roughly orthogonal to the E-W major axis. In the west lobe, the peak of S(1) line emission similarily lies closest to the geometric centre but, in contrast to the east lobe, exhibits a highly collimated and somewhat sinuous internal structure elongated parallel to the major axis. Additional smaller-scale structure in the form of regularily spaced peaks or 'knots' of weaker line emission is clearly resolved within both lobes.

4.2.(d) SPECTROSCOPY OF H_2 LINE EMISSION

At a spectral resolution of 130 kms^{-1} the peaks of line emission in the east and west lobes are spectrally unresolved and have S(1) line fluxes, in a 20 arcsec beam, of 8.2×10^{-20} and 9.5×10^{-20} Wcm^{-2}, and for the case of a 12 arcsec beam, 4.7×10^{-20} and 5.6×10^{-20} Wcm^{-2}, respectively (typical errors are $\pm0.5\times10^{-20}$ Wcm^{-2}). K band CVF spectra of the east and west peaks, measured in a 20 arcsec beam, are shown in Fig.[4.2.4] and a list of representative H_2 line fluxes is given in Table [4.2.1].

Profiles of the S(1) line, measured at 12 different locations across the H_2 lobes, are presented in Fig.[4.2.6] and the relative positions at which these observations were made are indicated in Fig.[4.2.5]. A listing of the specific profile parameters is given in Table [4.2.2]. As can be seen from these figures, the S(1) profiles at different locations in the source show distinct differences in the velocity of peak emission and width at half-maximum intensity. On average, the velocities of peak emission in the west lobe are significantly blue shifted by about 10 kms^{-1} relative to those in the east lobe. Furthermore, at the position

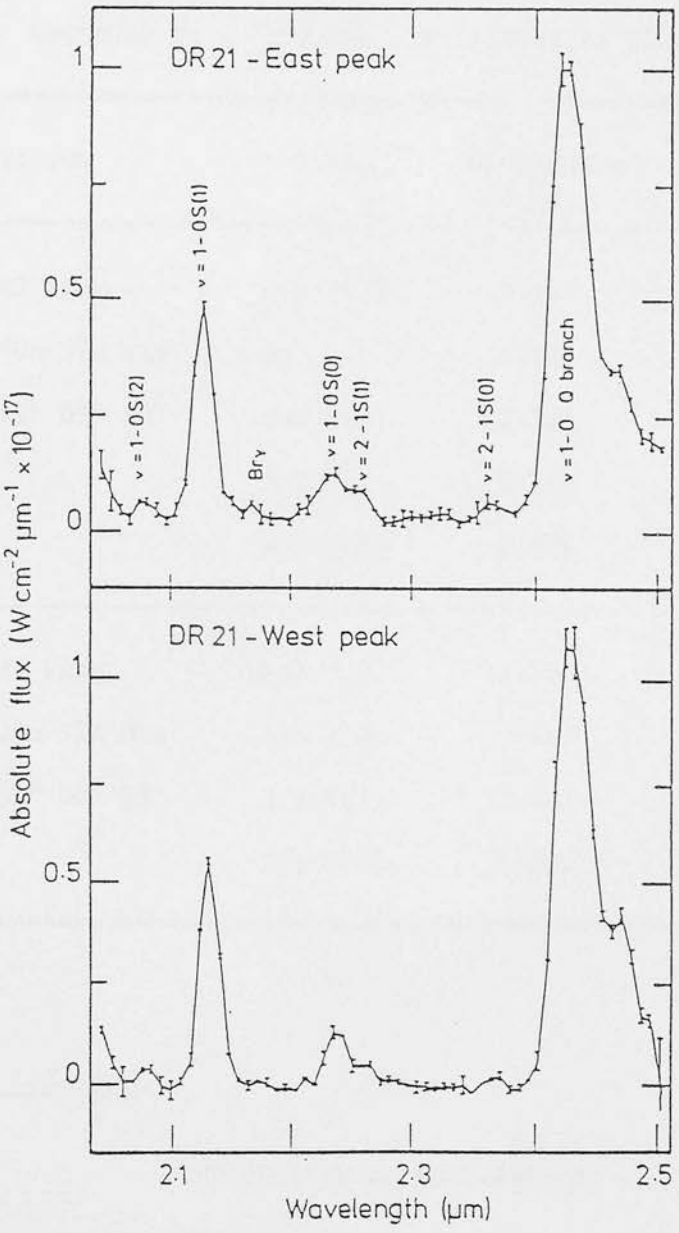

FIGURE 4.2.4 : CVF spectra of the peaks of H2 line emission in the east and west lobes of the DR21 outflow source. Both measurements were made using a beam size of 20 arcsec. The spectral resolution of these measurements is $\lambda/\Delta\lambda$ = 120. The wavelengths of several H2 lines and of HI Brackett gamma are indicated. The positions at which these spectra were taken and the measured line fluxes are tabulated in TABLE[4.2.1].

TABLE 4.2.1a:

OBSERVED DR21 INFRARED LINE FLUXES IN 20 ARCSEC BEAM

POSITION	LINE	WAVELENGTH (μm)	FLUX (1(-21) Wcm-2)
EAST H2 PEAK	1-0 S(1)	2.122	82 (+/- 5)
RA : 20h 37m 22s	Br	2.168	8 (+/- 3)
DEC: 42° 09′ 10"	1-0 S(0)	2.223	19 (+/- 3)
	2-1 S(1)	2.248	13 (+/- 3)
	2-1 S(0)	2.356	8 (+/- 3)
WEST H2 PEAK	1-0 S(1)	2.122	95 (+/- 5)
RA : 20h 37m 08s	1-0 S(0)	2.223	24 (+/- 3)
DEC: 42° 08′ 33"	2-1 S(1)	2.248	10 (+/- 3)
	2-1 S(0)	2.356	8 (+/- 3)

TABLE 4.2.1b :

THEORETICAL H2 LINE RATIOES

MODE OF EXCITATION	$\frac{1\text{-}0\ S(0)}{1\text{-}0\ S(1)}$	$\frac{2\text{-}1\ S(1)}{1\text{-}0\ S(1)}$
UV PUMPED	0.67	0.55
SHOCK	0.22	0.10

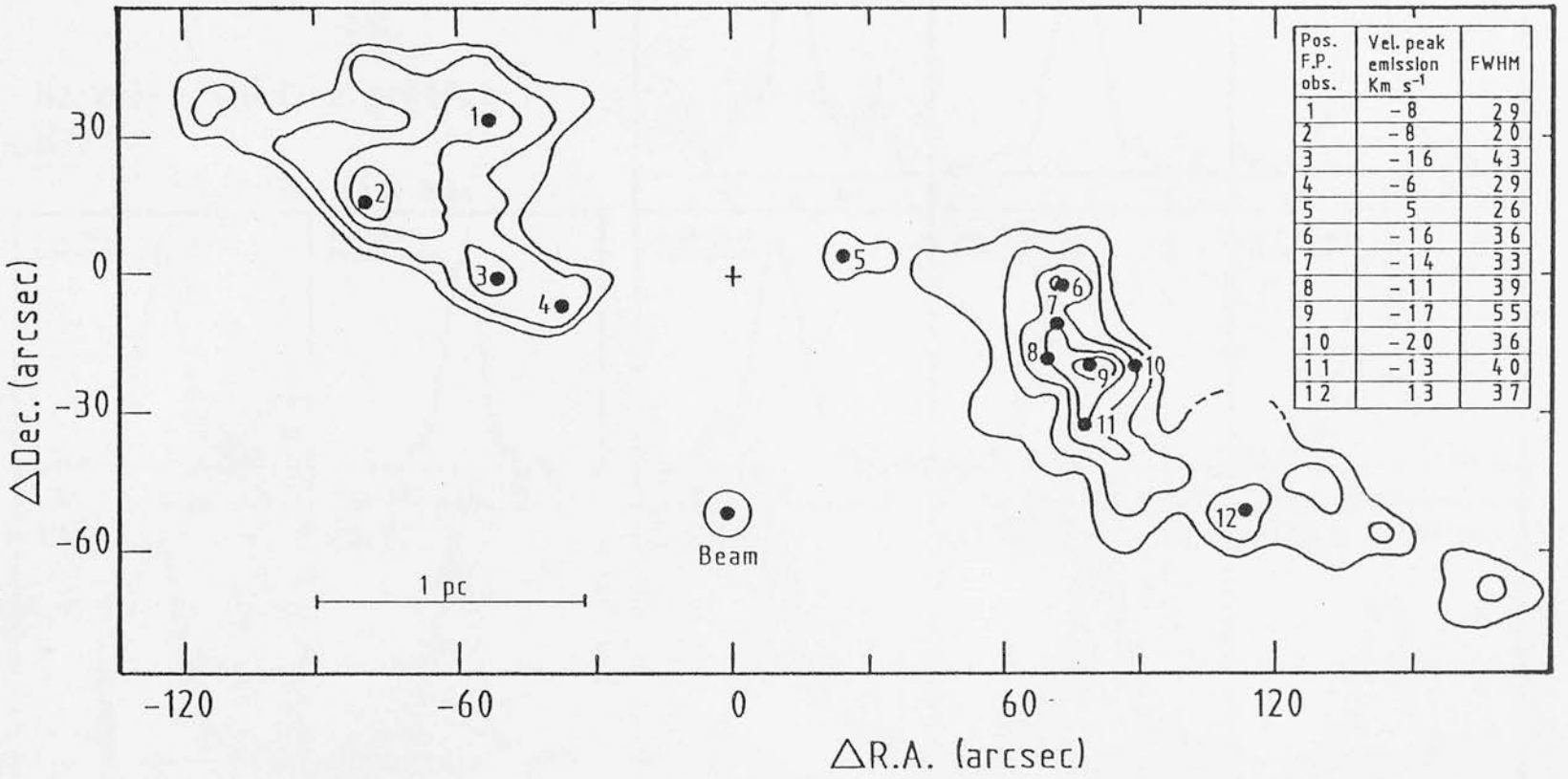

FIGURE 4.2.5 : Positions at which the FP profiles shown in Fig.[4.2.6] were measured. The H2 v=1-0 S(1) intensity contours are taken from Fig.[4.2.3] and the offsets of each position observed are as given in Table[4.2.2].

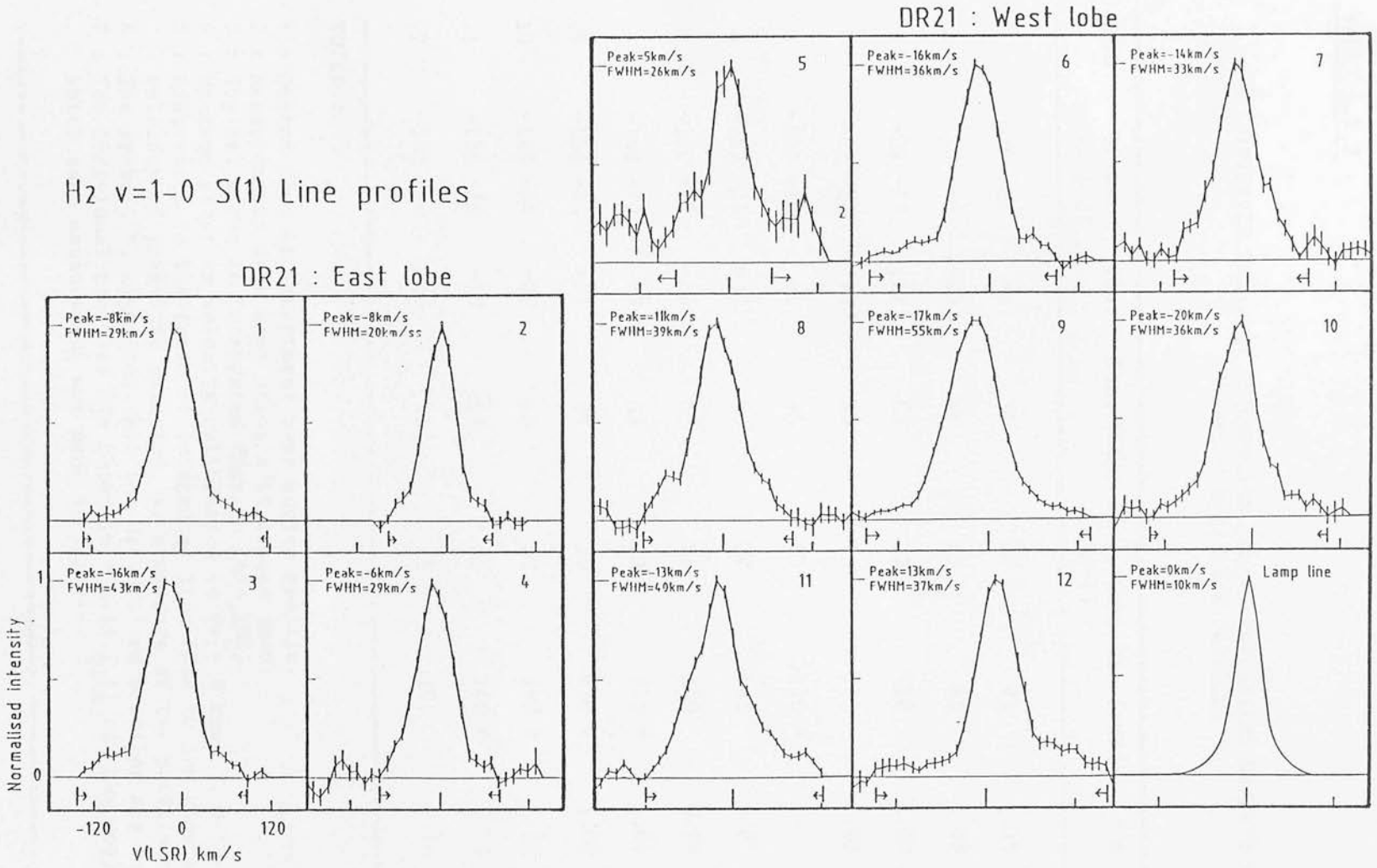

FIGURE 4.2.6 : H2 v=1-0 S(1) line profiles measured using a 35 kms-1 resolution FP with a 10 arcsec beam, at the positions as indicated in Fig.[4.2.5].

TABLE 4.2.2 :

OBSERVED (Obs.) & DECONVOLVED (Dec.) PARAMETERS DERIVED FROM THE H2 v=1-0 S(1) LINE PROFILES

Posn.	Offset (arcsec)	Vlsr	Obs.(FWHM)	Dec.(FWHM) (kms-1)	Dec.(FWZI)	B/R	Flux (Wcm-2s-1)
1	-26 14	-8	52	20	95	1.35	2.9(-20)
2	0 -6	-10	48	15	60	1.05	4.0
3	-28 -23	-17	65	35	110	1.00	2.1
4	-42 -28	-5	53	23	105	1.07	2.0
5	-103 -18	+4	45	23	>140 *	?	0.9
6	-152 -24	-17	63	37	115	0.81	3.6
7	-150 -33	-14	57	26	140	0.94	2.2
8	-148 -42	-8	63	23	175 *	1.07	2.7
9	-158 -44	-21	80	58	230 *	1.02	5.3
10	-165 -44	-22	60	23	140 *	1.32	2.7
11	-156 -56	-19	65	22	160 *	0.71	2.9
12	-192 -74	+16	61	25	105	0.74	3.0

NOTES :

1 : Quoted flux is integrated over entire profile.
2 : Measurements were made using a 10 arcsec beam.
3 : Typical error in integrated flux is (+/- 15%).
4 : Maximum error in velocity calibration is (+/- 5 kms-1).
5 : B/R, which is the ratio of integrated line flux to the blue and red of the velocity of peak-line emission, is a measure of the profile asymmetry.
6 : The symbol, *, signifies that the deconvolved profiles are multi-component.
7 : The individual profiles are shown in Fig.[4.2.6] and the positions at which each measurement was made in Fig.[4.2.5].

of brightest line emission in the west lobe (posn.9, in Figs.[4.2.5] & [4.2.6]) the S(1) profile is exceedingly broad (FWHM > 50 kms^{-1}, FWZI > 200 kms^{-1}) compared to the corresponding profile at the brightest position in the east lobe (posn.2). Fig.[4.2.7], which illustrates a direct comparison of these two profiles, clearly shows that the S(1) line from the west lobe has a broad peak and possessess an extended blue wing, in striking contrast to the eastern lobe profile which is barely resolved and has an emission centroid that lies closer to the rest velocity of the DR21 molecular cloud (V_{lsr} ~ -2.5 kms^{-1}).

It is interesting to compare the width of the broad S(1) profile observed toward the west lobe of the DR21 H_2 source with that of the well-studied, high-velocity H_2 emission in the Orion outflow (Nadeau, Geballe & Neugebauer 1982). In order to facilitate such a comparison, a velocity-resolved S(1) line profile was observed toward Peak 1 in Orion, at a later date, using an instrumental set-up identical to that employed for the DR21 measurements. A comparison of the DR21 and Orion S(1) profiles (Fig.[4.2.8]) shows that both possess similar widths at half-maximum intensity (i.e. ~ 55 kms^{-1}) and are of comparable velocity extent. These observations therefore suggest that the high-velocity H_2 v=1-0 S(1) emission associated with the DR21 molecular jets, is similar in nature to that previously identified with the Orion outflow and, more importantly, that the Orion H_2 source is not truly unique with regard to its ultra-high outflow velocities.

Finally, in order to investigate the full extent of the high-velocity S(1) emission, an attempt has been made to deconvolve the instrumental profile from the observed profiles, thus obtaining a best estimate of the intrinsic source profile. A 1-D maximum-entropy (MEM) deconvolution algorithm was employed (Willingale 1981; Skilling & Bryan 1984; Burton 1986), the results of which are

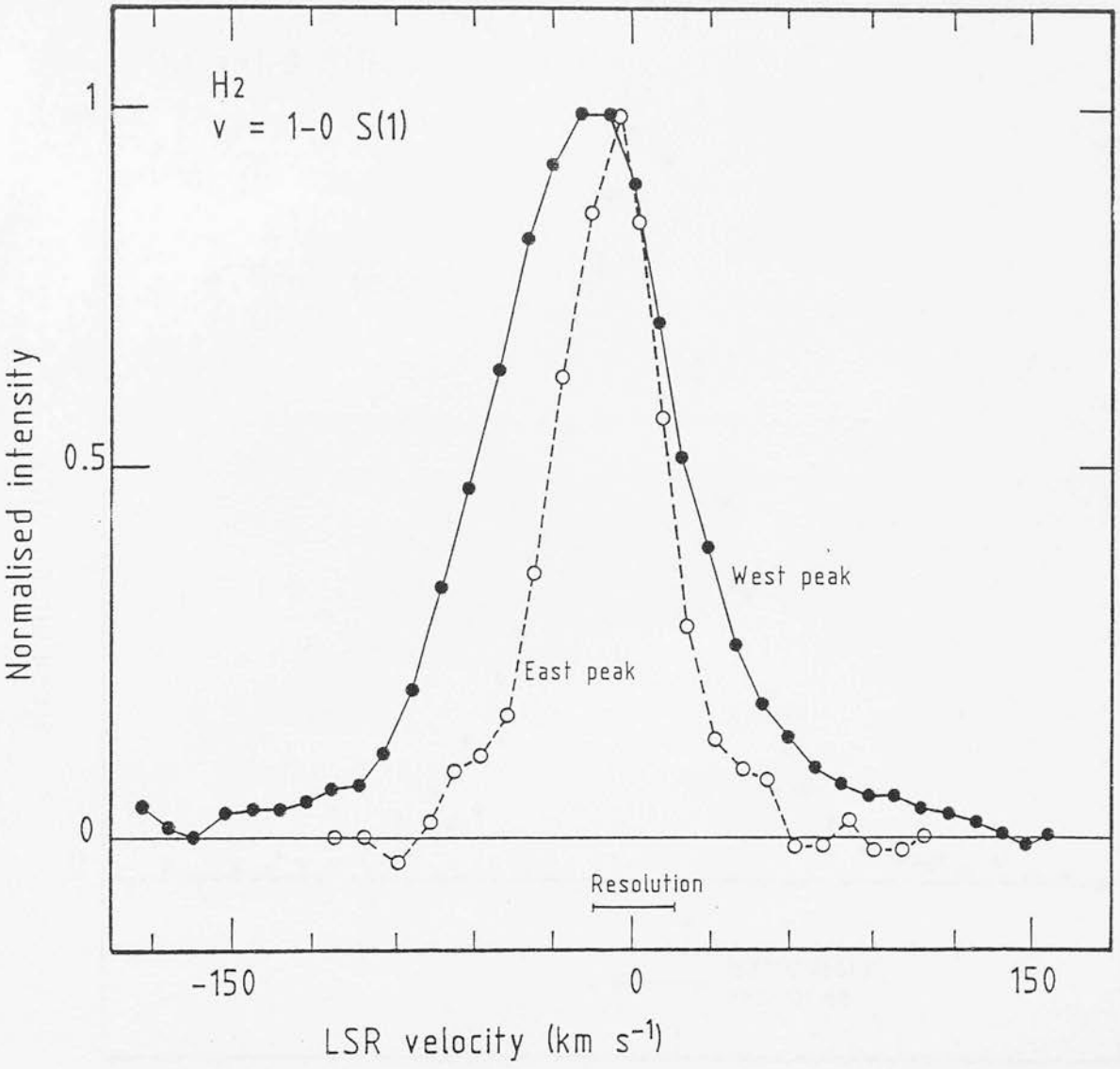

FIGURE 4.2.7 : A comparison of H2 S(1) profiles measured at the peaks of line emission in the east and west lobes of the DR21 outflow source. The velocity resolution is 35 kms-1 and the beam size is 10 arcsec for both measurements.

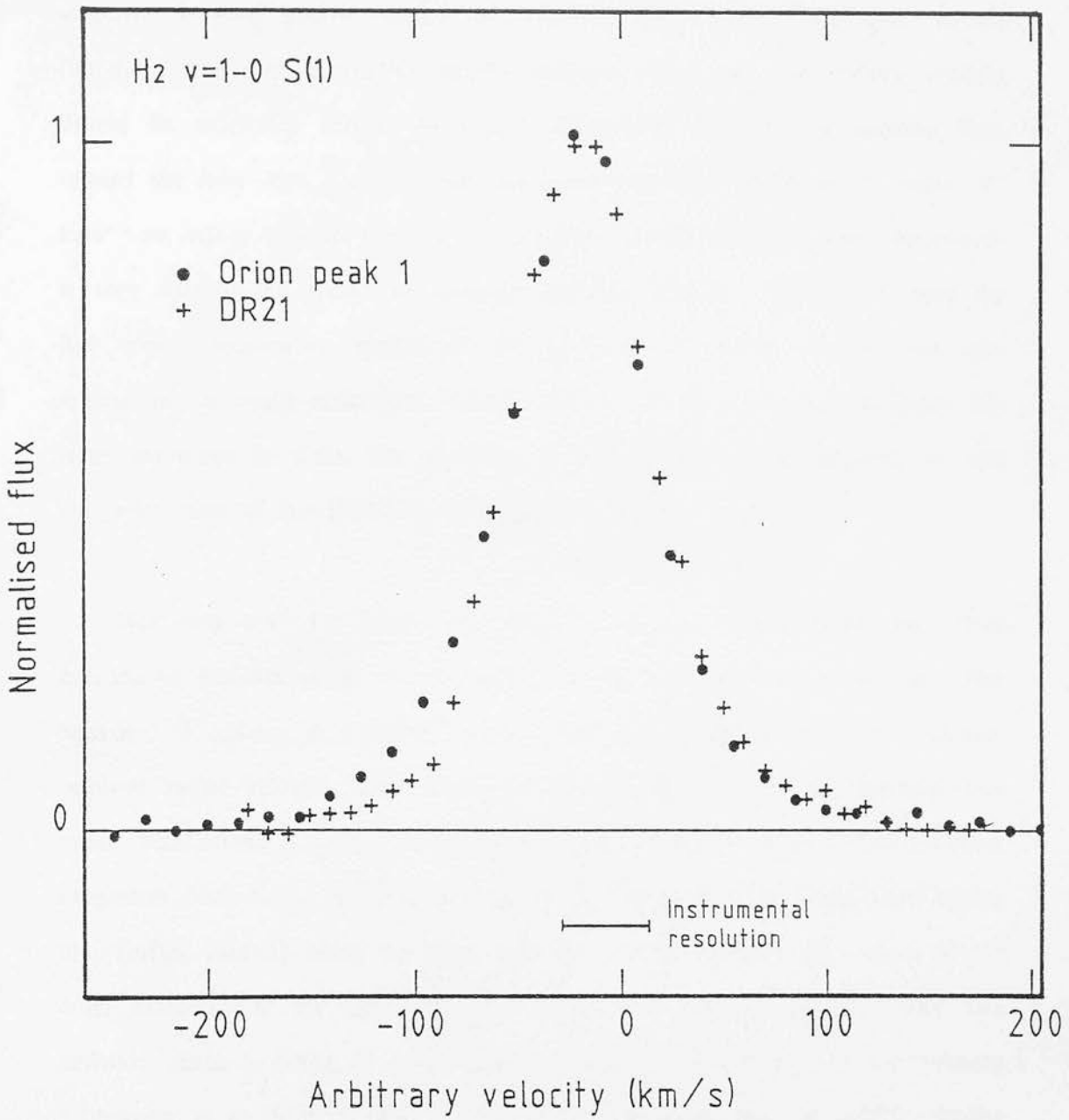

FIGURE 4.2.8 : A comparison of H2 S(1) profiles measured at the west lobe of the DR21 outflow source and at Peak 1 in Orion. The velocity resolution is 35 kms-1 and the beam size is 18 arcsec for both measurements.

displayed in Fig.[4.2.9]. Although the deconvolution method cannot be trusted to give reliable quantitative results, the method does considerably reduce the intensity in the profile wings, as expected for a Lorentzian-type spread function, thus any qualitative results deduced from the deconvolved profiles should be relatively secure. From the deconvolved profiles, it appears that, toward the west lobe, the S(1) line emission extends to velocities of order 100 kms^{-1} on either side of the line core, whilst, toward the east lobe, the profile is very narrow and shows no apparent emission beyond ~ 20 kms^{-1} from the line core. Furthermore, several of the deconvolved profiles in the west lobe appear to be multi-component. These results present convincing evidence for large variations in either the geometry or internal kinematics between the east and west lobes of the DR21 H_2 emission-line source.

Not only does the width and shape of the S(1) line profile vary from position to position across the H_2 lobes, but so does the velocity of peak line emission. A glance at Fig.[4.2.9] shows that these measurements have cleanly resolved radial velocity shifts along the line-of-sight to different emission-line knots. Most notably, in the west lobe the radial velocity of peak line emission progresses from being red-shifted close to the cloud core, to being significantly blue-shifted midway along the lobe, and then shifts redwards once again at the outer extremity of the lobe; the observed shift in radial velocity at peak line emission spans a range of > 30 kms^{-1} whilst the uncertainty in the velocity calibration is at most 5 kms^{-1}. As will be discussed later (Sec.[4.3]), similar radial velocity shifts are also seen in the higher-spectral resolution millimeter-wave CO data and may be interpreted as resulting from periodic excursions of the mean direction of motion of the outflowing material relative to the line-of-sight.

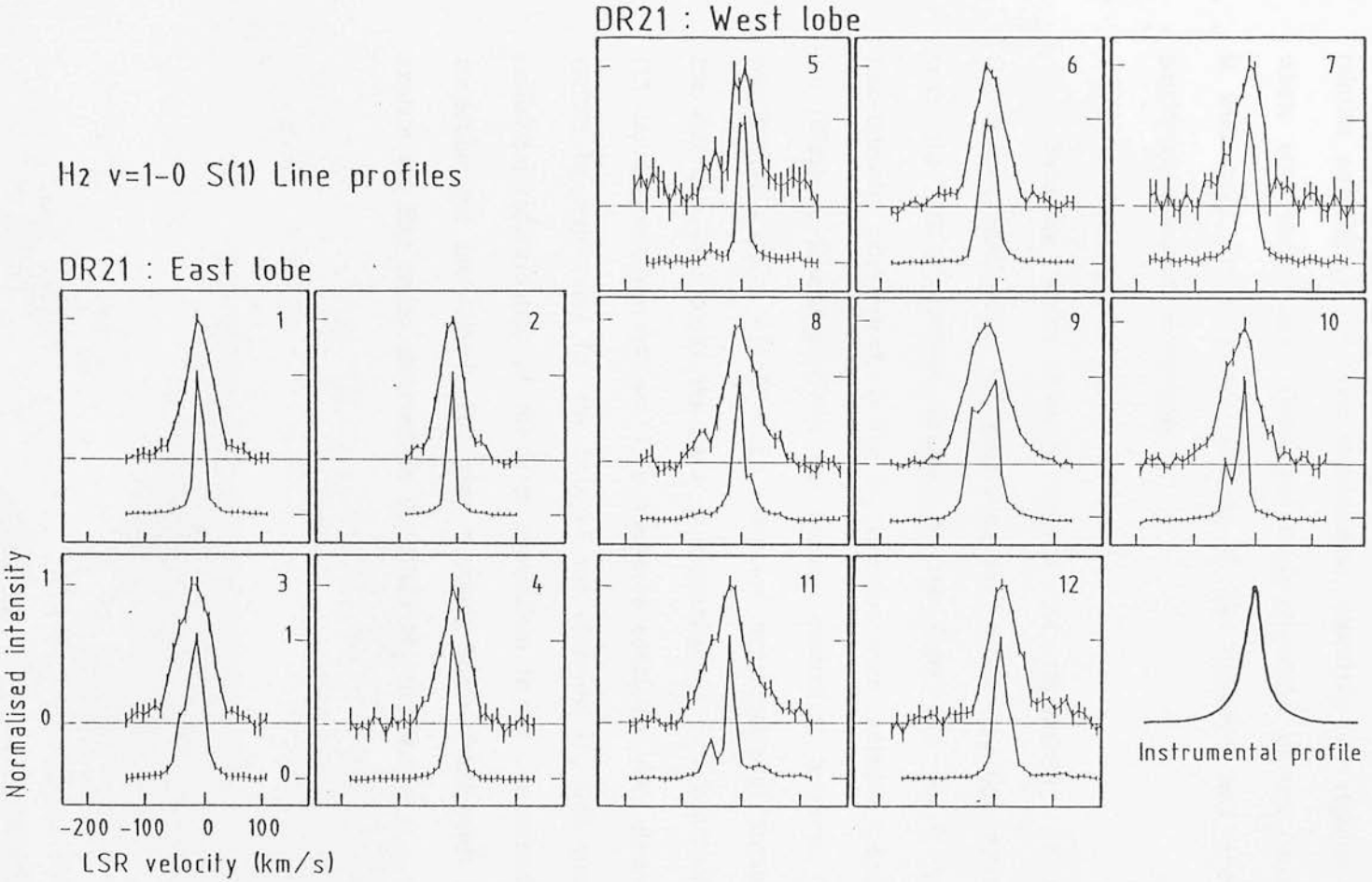

FIGURE 4.2.9 : Observed (top) and deconvolved (bottom) H2 v=1-0 S(1) profiles in the DR21 outflow source. The positions observed are as illustrated in Fig.[4.2.5]. The instrumental resolution is 35 kms-1.

4.2.(e) THE H_2 EXCITATION MECHANISM

Shock pumping and near-ultraviolet pumping are competitive mechanisms for producing vibrationally excited H_2 (see, Sec.[3.2]). A determination of the relative contribution of these mechanisms, especially for regions such as DR21 where both high-velocity flows and large ultraviolet photon fluxes are present, is thus vital for a proper analysis of the dynamics and energetics of the particular excitation mechanism.

Evidence which directly refutes the applicability of the ultraviolet fluorescence mechanism for generating the intense H_2 line emission associated with the DR21 outflow source, derives from the v=1-0 S(1)/v=2-1 S(1) line-intensity ratio which, if the H_2 emission were radiatively excited, would be 1.8 (Black & Dalgarno 1976). For thermal excitation, however, the same ratio would give a value of 10 at an excitation temperature of around 2000 K. At the east and west peaks this ratio is approximately 6.5 (9 dereddened) and 9.5 (13 dereddened), respectively. It is therefore concluded that ultraviolet excitation cannot be responsible for the bulk of the observed H_2 line emission and that collisional redistribution of the level populations in the compressed layers of hot molecular gas immediately following a strong shock front must be invoked to explain the line ratios observed in the DR21 H_2 source.

4.2.(f)

EXTINCTION ESTIMATES DERIVED FROM THE H_2 OBSERVATIONS

For the H_2 line parameter calculations conducted in this section, the energy levels used are those given by Dabrowski (1984), the Einstein A-values are taken from Turner, Kirby-Docker & Dalgarno (1977), and an ortho-para hydrogen ratio of 3 is used (see Sec.[3.1]). For the following analysis, it is further assumed that the H_2 is excited by collisions, as was justified in the preceeding section.

The reddening can be determined from the CVF spectra (Fig.[4.2.5]) by comparing the observed ratio of integrated flux in the v=1-0 Q(1-4) blend to the v=1-0 S(1) line with the corresponding ratio calculated under conditions of zero extinction (~ 1.84 for thermal excitation at T = 2000 K and within the range 2.20-1.76 for 1000 K < T < 3000 K; see Fig.[4.2.10b]). It is important to note, however, that extinction estimates derived using the Q branch are somewhat unreliable as a consequence of telluric absorption and temporal variations thereof by unresolved features within the 2.40-2.45 μm wavelength interval. This is reflected by the large uncertainties in the results. The v=1-0 Q(5) line at 2.455 μm (seen as a feature on the long wavelength side of the Q branch), is not incorporated into the above extinction determination because of its proximity to a strong telluric H_2O line.

The observed Q branch to S(1) line flux ratios from the CVF data, are 3.6 and 3.4 for the east and west peaks, respectively. From the differential extinction between the Q branch (2.41 μm) and the S(1) line (2.12 μm) implied by these ratios, the extinctions at 2.12 μm and V(5500 Å) are derived assuming

the wavelength dependence of the interstellar extinction law as described by Landini et al. (1983) and Rieke et al. (1985), i.e. $A_\lambda \propto \lambda^{-1.85}$. This chosen relation is almost identical to the Van de Hulst No.15 extinction curve. The derived values of $A_{2.12\mu m}$ along the line-of-sight to the east and west lobes of H_2 line emission are then 3.4(±1) and 3.2(±1) mag, respectively. These extinctions are so similar that a mean value of $A_{2.12\mu m}$ = 3.3(±1) mag is taken, which corresponds to a visual extinction of A_V = 33(±10) mag.

4.2.(g)

THE H_2 KINETIC TEMPERATURE, COLUMN DENSITY AND LUMINOSITY

For the case of optically-thin line emission arising from a thermal distribution of excited H_2 molecules, a characteristic rotation-vibration temperature can be readily derived by comparison of the relative intensities of two lines arising from adjacent vibrational levels. The assumption that the emission is optically thin is an excellent one as a column density of ~ 10^{-25} cm^{-2} in hot H_2 molecules is required before the lines become optically thick (cf. Hollenbach & Shull 1977). The column density $N_{v,J}$ of the molecules in the upper level (v,J) of a transition with an observed intensity I is then

$$N_{v,J} = [4 \pi I] / [A h \nu] \qquad (4.2.1)$$

where, A is the Einstein A-value and ν is the frequency of the transition. Additionally, if the level populations are in a Boltzmann distribution, then the column densities $N_{v,J}$ are related to the temperature of the gas by the relation

$$\frac{N_{v,J}}{N(H_2)} = \frac{G(J)}{Z(T)} \exp[-T_{v,J}/T] \qquad (4.2.2)$$

where, $G(J) = (2J+1)g_{spin}$ is the stastistical weight of the level (g_{spin} = 3 for ortho-hydrogen and 1 for para-hydrogen), $T_{v,J}$ is the energy of the upper level in K, Z(T) is the partition function and $N(H_2)$ is the total column density of hot H_2 molecules.

The most easily observable pair of lines, arising from adjacent vibrational levels, are the v=1-0 S(1) and the v=2-1 S(1) lines, the ratio of the intensities of which, using eqns.(4.2.1) & (4.2.2), can be expressed as follows

$$\frac{I_{v=1-0}}{I_{v=2-1}} = 0.738 \exp(5594/T_{vib}) \times 10^{-(A_{2.12\mu m}-A_{2.25\mu m})/2.5} \qquad (4.2.3)$$

Substituting into this equation the v=1-0 S(1) and v=2-1 S(1) line fluxes given in Table [4.2.1] and using a differential extinction of $(A_{2.12\mu m}-A_{2.25\mu m})$ = 0.33 mag, based on the Q branch to S(1) line flux ratio, excitation temperatures between the v=1 and v=2 energy levels of 2250(±350) and 1950(±350) K are calculated for the east and west peaks, respectively. It is henceforth assumed that an excitation temperature of 2000 K, which is consistent with both of the above temperatures and similar to that found for the Orion H_2 source (Beckwith et al. 1983), is applicable over the entire extent of the observed H_2 line emission.

Having estimated the temperature of the gas from which the bulk of the H_2 line emission originates, it is now possible to calculate the overall luminosity measured in H_2 line emission. First, however, it is necessary to calculate an appropriate value for the partition function Z(T) at 2000 K. The value of Z(T)

can be computed for the vibrational and rotational energy levels in the ground electronic state by evaluating the sum

$$Z(T) = \sum_{v=0}^{v=14} \sum_{J=0}^{J=J_{max}} G(J).\exp[-T_{v,J}/T] \qquad (4.2.4)$$

This summation was evaluated numerically using values for $T_{v,J}$ calculated from the empirical constants of Fink et al. (1965) and with J_{max} chosen such that, $G(J_{max}).\exp(-T_{v,Jmax}/T)$ was less than 10^{-4}. This numerical technique gives the following results: Z(1000 K) = 25, Z(2000 K) = 52 and Z(3000 K) = 88. As is discussed in Herzberg (1945), the partition function can also be expressed analytically with little loss in accuracy. Employing the simple harmonic-oscillator, rigid-rotator approximation, the internal partition function $Z_{int}(T)$ can be expressed as a product of the rotational $Z_{rot}(T)$ and vibrational $Z_{vib}(T)$ parts

$$Z_{int}(T) = Z_{rot}(T).Z_{vib}(T)$$

$$\sim 2\ (T/T_{rot}).[1-\exp(-T_{vib}/T)] \qquad (4.2.5)$$

where, the rotational and vibrational molecular constants, T_{rot} (= 87.5 K) and T_{vib} (= 6330 K) are taken from Huber & Herzberg (1979). A plot of Z(T) versus T, calculated using the harmonic oscillator approximation, is shown in Fig.[4.2.10a]. Clearly, the analytical and numerical predictions are in adequate agreement. For the remainder of this work a partition function, Z(2000 K) = 50, will therefore be adopted.

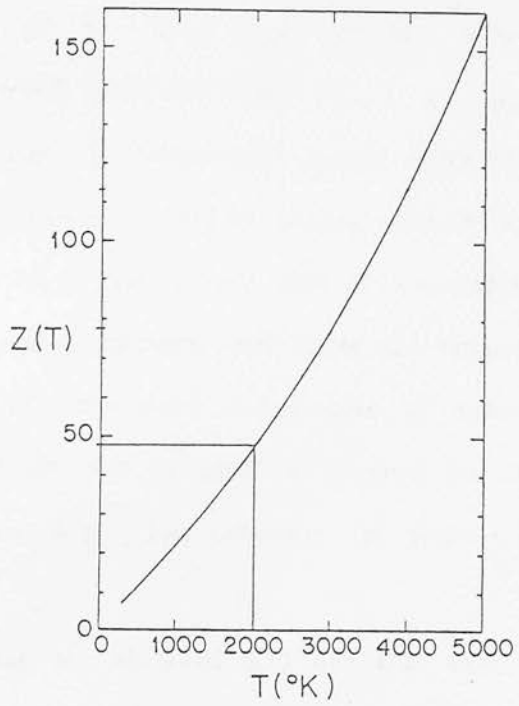

FIGURE 4.2.10a : The Partition Function Z(T) for H_2

The partition function for H_2 molecules, Z(T), is plotted as a function of temperature according to the harmonic-oscillator rigid rotator approximation (Herzberg 1945).

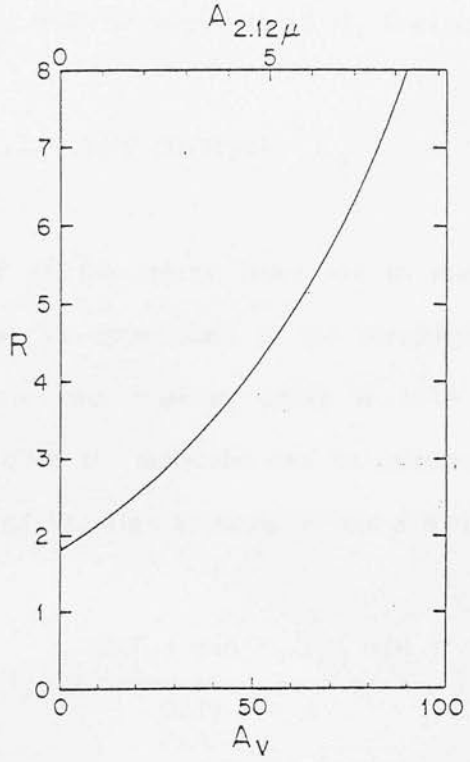

FIGURE 4.2.10b : The Ratio of the v=1-0 Q Branch to S(1) Line Intensity Versus Extinction for $T_{ex} = 2000$ K.

The ratio of the v=1-0 Q line blend to the S(1) line intensity $R \equiv \Sigma Q(J)/S(1)$ J=1,4, is plotted as a function of A_V and $A_{2.12\mu}$ at T = 2000 K. The van de Hulst 15 extinction curve is used (Johnson 1968).

In a similar manner, the intensity in the v=1-0 S(1) line relative to the total intensity in all H_2 lines, I_{tot}, can be calculated from a summation of eqn.(4.2.1), which gives the ratio, $I_{v=1-0\ s(1)}/I_{tot} \approx 1/10$, for T = 2000 K. Summation over a temperature range 4000-500 K, characteristic of the conditions expected in rapidly cooling post-shock gas, results in the slightly lower value 1/15. Due to our lack of knowledge regarding the form of the post-shock cooling function, and hence the temperature dependence of the H_2 column density, the more conservative of these two estimates (i.e. $I_{v=1-0\ s(1)}/I_{tot} \approx 1/10$) will be used to calculate the total H_2 luminosity from the dereddened v=1-0 S(1) line luminosity (cf. Scoville et al. 1982).

Integrating the observed S(1) line flux over the entire area mapped and adopting a distance of 3 kpc results in S(1) line luminosities at the east and west lobes of 4 and 5 L_0, respectively. Further assuming that $A_{2.12\mu m}$ = 3.3(±1) mag over the entire surface area of H_2 line emission, a total dereddened S(1) line luminosity of ~ 180 L_0 is calculated, which at T = 2000 K corresponds to a total luminosity in all H_2 lines of

$$L(H_2)_{tot} \approx 1800\ (D/3kpc)^2\ \ L_0$$

Furthermore, if all the energy levels are in thermal equilibrium at this same temperature then an upper limit to the dereddened column density of hot H_2 molecules at the two brightest peaks is 10^{19} cm^{-2}. Finally, the mass of vibrationally excited H_2 molecules can be calculated from eqns.(4.2.1) & (4.2.2), knowing the total line flux at earth, F, for a source at distance, D, as follows

$$M(H_2,T_X) = \frac{Z(T_X)\ \exp(T_U/T_X)\ m(H_2)}{G(J)\ h\ \nu\ A}\ F\ (4\ \pi\ D^2) \qquad (4.2.6)$$

where, $m(H_2)$ is the mass of the H_2 molecule, T_u is the temperature of the upper level, and the other parameters are as defined previously. For the v=1-0 S(1) line and assuming, T_X = 2000 K, this equation can be expressed in more familiar astrophysical terms

$$M(H_2) = 1.5\times10^{-3} \left[L_{v=1-0\ S(1)}/L_0\right]\ M_0 \qquad (4.2.7)$$

Thus, for a total dereddened v=1-0 S(1) line luminosity of $L_{v=1-0\ S(1)}$ = 180 $(D/3kpc)^2\ L_0$, the corresponding mass in hot H_2 molecules is

$$M(H_2)_{hot} = 0.27\ (D/3kpc)^2\ \ M_0$$

Although the most often quoted distance to the DR21 region is 3 kpc, it is possible that this value is mistaken. If the DR21 region, and by implication the entire Cygnus X complex, is located at a distance of only 1.5 kpc, then the predicted luminosity and mass of vibrationally excited H_2 emission are 500 L_0 and 0.07 M_0, respectively. These values are still considerably in excess of any other currently known galactic H_2 emission-line source; i.e. the total dereddened luminosity of H_2 line emission estimated for the Orion shock-excited outflow source is only 200 L_0 (Beckwith et al. 1983). It is therefore contended that DR21 is probably the most luminous galactic H_2 emission-line source yet discovered.

Finally, the mass transfer rate through the shocks that give rise to the luminous H_2 line emission can be estimated simply by dividing the total mass in hot H_2, as derived above, by the average lifetime of H_2 in the vibrational state. The time spent by a H_2 molecule in the hot (T_S > 1000 K) post-shock zone can be calculated as follows

$$t_{hot} \approx [N(H_2)_{hot}/n(H_2)_{post\text{-}shock}]/V_{shock} \qquad (4.2.7)$$

Inserting the previously determined values, $N(H_2)_{hot} \approx 10^{19}$ cm^{-2}, $n(H_2)_{post\text{-}shock} \approx 10^5$ cm^{-3} and $V_{shock} \approx 30$ kms^{-1} results in a shocked layer of thickness $\sim 10^{14}$ cm and a lifetime for vibrationally excited H_2, $t_{hot} \approx 1$ yr. The mass transfer rate through the shocks is then

$$\dot{M}_{shock} = M(H_2)_{hot}/t_{hot} \approx 0.3\ (D/3kpc)^2\ \ M_0\ yr^{-1}$$

This is a phenomenal mass transfer rate and implies that, providing the outflow retains its present vigour, a large part of the DR21 molecular cloud will be processed through shocks in the span of only 10^5-10^6 yr. This may significantly alter the chemical composition of the ambient cloud gas (viz. Sec.[5.5]).

4.2.(h) THE H_2 LINE EMISSION ASSOCIATED WITH W75S(IRS1)

A map of the H_2 v=1-0 S(1) line intensity distribution in the W75S region is presented in Fig.[4.2.11] and its spatial relationship to the DR21 H_2 source is illustrated in Fig.[5.1.1]. The line emission is resolved into a double-lobed structure consisting of two main peaks separated by a projected distance of $\sim$ 1 (D/3kpc) pc, and connected by a diffuse halo of weaker line emission. A peak S(1) line flux of 2.1×10^{-20} Wcm^{-2} is observed in a 20 arcsec beam coincident with the young-stellar object W75(IRS1). Assuming an excitation temperature of 2000 K, and following the analysis described above, then the peak column density of hot H_2 is $N(H_2)_{hot} \sim 10^{17}$ cm^{-2}, the total luminosity in all H_2 lines is $L(H_2) \sim 5$ (D/3kpc) L_0, and the mass of hot H_2 molecules is $M(H_2)_{hot} \sim$

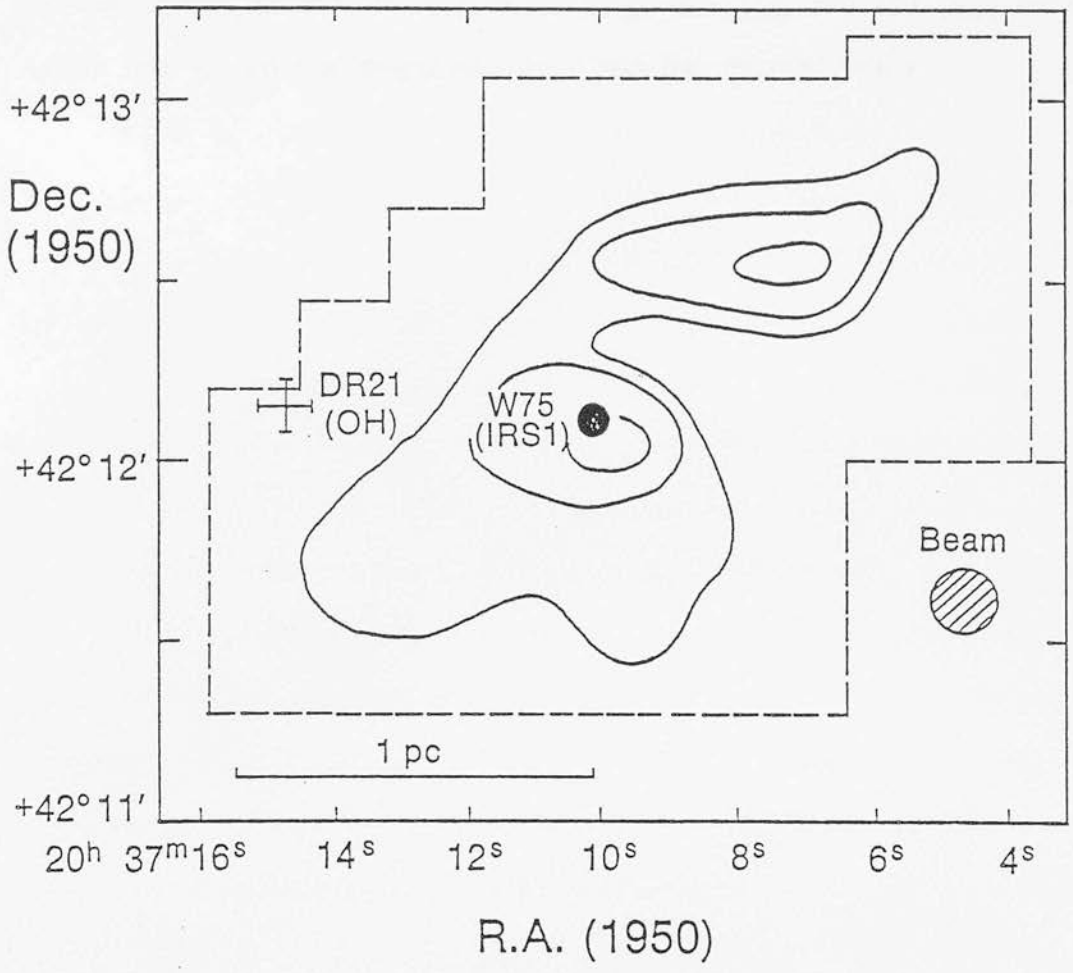

FIGURE 4.2.11 : Intensity contour plot of the W75 H2 source in the v=1-0 S(1) line using data obtained on an 18 arcsec grid with an 18 arcsec beam. The first intensity contour level and the subsequent contour level spacings are 7(-13) Wcm-2ster-1. The dashed line indicates the region mapped, the hatched circle shows the beam size, and a linear scale, corresponding to a distance of 3 kpc, is provided. The positions of W75(IRS1) and DR21(OH) are as indicated.

7.5×10^{-4} (D/3kpc) M_0. Since W75(IRS1) is apparently embedded in the same dense ridge of gas and dust that adjoins the DR21 complex, significant extinction may be present at 2 μm. Indeed, if W75S is typified by an extinction similar to that derived for DR21 then $L(H_2)$, $N(H_2)_{hot}$, and $M(H_2)_{hot}$ are each more than an order of magnitude larger than the observed values.

4.3.(a) INTRODUCTION TO THE CO OBSERVATIONS

For the purpose of studying the physical conditions in molecular clouds the most useful spectral lines are those of ^{12}CO and ^{13}CO. The relatively high abundance of this molecule ($[^{12}CO]/[H_2] = X(CO) = 10^{-4}$) coupled with the long spontaneous lifetime for the J=1-0 transition ($t = 1/A_{10} = 1/6\times10^{-8} \approx 0.5$ yr) combine to produce high intensity and widely observable emission for physical conditions typical to most molecular cloud environments. For this reason CO observations have become the major technique for studying the astrophysics of interstellar clouds, acting as a tracer of H_2 column density, temperature and kinematics in the clouds. Moreover, as the conditions requisite for excitation of the CO molecule are relatively well understood, and the CO molecule itself can be approximated by a simple rigid linear rotator, relationships expressing the physical properties of the emitting gas in terms of the observable parameters are relatively straightforward to derive and apply.

In this section, it is shown how the CO observations can be employed as an extremely effective probe of the physical and dynamical state of the gas internal to the DR21 molecular outflows. In combination with the infrared H_2 data these relatively high-angular and high-spectral resolution millimeter-wave CO observations present an opportunity to undertake a detailed comparative study of a molecular outflow to an extent hitherto unavailable.

4.3.(b)

THE OBSERVING METHOD EMPLOYED FOR THE CO OBSERVATIONS

Observations of the millimeter-wavelength J=1-0 transitions of ^{12}CO, ^{13}CO, $C^{18}O$ and the H53α radio recombination line of hydrogen were obtained during the period 1-4 May 1985, using the 45-m telescope of the Nobeyama Radio Observatory in Japan. The front end consisted of a cooled shottky-diode receiver mounted at the Cassegrain focus with a measured system noise temperature, T_{sys}(115 GHz) = 600-800 K, followed by an IF system and a set of sixteen 2048-channel acousto-optical spectrometers; the velocity resolution at 115 GHz was 0.1 kms^{-1}. The pointing accuracy of the telescope was measured to be < 10 arcsec in both azimuth and elevation from repetitive observations of SiO masers. The data were taken in a position-switching mode and the temperature calibration was established using an ambient temperature rotating chopper in front of the receiver. The intensity scale is in the antenna temperature, T_a^*, corrected for atmospheric and ohmic losses. Since the beam-to-source coupling efficiency is effectively unity for the observations presented here, the corrected radiation temperature, T_r, is derived from T_a^* simply by dividing by the measured beam efficiency, η_B (see Kutner & Ulich 1981).

Repeated measurements of Jupiter were used to determine the half-power beam width, θ, and the forward beam efficiency at 115 Ghz, which was calculated using the relationship

$$\eta_B = \frac{T_a^*}{T_b[\,1-\exp[-\ell n2(D/\theta)^2]\,]} \qquad (4.3.1)$$

where, T_a^* is the measured antenna temperature, T_b is the brightness

temperature of Jupiter at frequency ν (here, it is assumed that T_b(115 Ghz) = 183 K; Ulich, Cogdell & Davis 1973; Ulich et al. 1980) and D is the diameter of Jupiter's disc at the time of observation. The half-power beam width was obtained by deconvolution of the measured beam width, knowing the exact angular diameter of Jupiter at the epoch of observation and assuming a circular disc of uniform brightness. The derived half-power beam width and beam efficiency at ν = 115 Ghz are, θ(HPBW) = 15(±1) arcsec, and, η_B = 0.36, respectively; a comparison with similar measurements made at other important frequencies is given in Table[4.3.1]. The observations are internally consistent to ±5% and the absolute calibration uncertainty is ±30%.

4.3.(c) THE CO J=1-0 LINE PROFILES

Using the Nobeyama Radio Observatory 45-m millimeter-wave telescope, the spatial and velocity distribution of ^{12}CO J=1-0 (hereafter, CO) emission has been mapped at the highest-angular resolution currently available with a single dish (15 arcsec) over an area on the sky, 6 arcmin (E-W) by 4 arcmin (N-S), centred on the DR21 molecular cloud core. The map origin was strategically chosen to lie exactly midway between the peaks of H_2 line emission in the east and west lobes of the DR21 outflow source. The coordinates of the CO map origin are

	RA(1950)	DEC(1950)
CO MAP (0,0) POSITION :	$20^h\ 37^m\ 14.8^s$	$+42^o\ 08'\ 56"$

A high signal-to-noise CO J=1-0 profile measured at the above map position, where the line profile was found to be both brightest and broadest, is

TABLE 4.3.1 :

MEASURED BEAM WIDTHS AND EFFICIENCIES OF THE NOBEYAMA 45-M TELESCOPE

FREQ GHz	T_b(JUPITER) K	θ arcsec	η_B %
115	183	15	36
98	181	20	44
49	163	36	51

OBSERVED MILLIMETER LINES

MOLECULE	TRANSITION	FREQ (GHz)
12CO	J=1-0	115.271204
13CO	J=1-0	110.20137
C18O	J=1-0	109.782182
C32S	J=1-0	48.990964
C34S	J=1-0	48.206956
C32S	J=2-1	97.980968
HI	n=54-53	42.951687
HI	n=52-51	48.153664

shown in Fig.[4.3.1]. The high-velocity wings are clearly evident and extend to beyond +/- 30 kms^{-1} from the DR21 rest velocity, taken to be at V_{lsr} = -2.5 kms^{-1}. The profile appears rather symmetric with smooth sides, a flat top, and a weak self-reversal at V_{lsr} = -3 kms^{-1}. Contrary to previous low-angular resolution studies (Fischer et al. 1985; Richardson et al. 1986), it is contended here that self-absorption in the CO J=1-0 line by lower-excitation foreground gas is probably important, at least over the central few kms^{-1} around the line core.

Representative CO and ^{13}CO J=1-0 spectra taken at several positions along the H_2 emission-line lobes are shown in Fig.[4.3.2] and the complete set of CO profiles measured along the major outflow axis (NE-SW) are shown in Fig.[4.3.3]. The CO profiles associated with the western (negative-RA) and eastern (positive-RA) offsets in Fig.[4.3.2] are located at the peaks of the high-velocity blue and red integrated CO emission (to be described in the next section), respectively. Although the CO profiles are, on the whole, rather symmetric, there is convincing evidence for the presence of asymmetries in the wings of several of these profiles, the sense of which agree with the velocity shifts found from the H_2 line profiles at roughly the same positions in the outflow lobes (i.e. the west lobe is blue-shifted, whilst the east lobe is primarily red-shifted).

The high-velocity wings that are so prominent in the CO spectra, are extremely weak in ^{13}CO and totally absent in $C^{18}O$ emission, which, requiring high volume densities for excitation ($n(H_2) > 10^4$ cm^{-3}) shows a steep decline in brightness with small angular displacement from the DR21 cloud core. The sharp emission feature centred at V_{lsr} = 8 kms^{-1} originates from foreground emission associated with the W75N molecular cloud which is located ~ 18

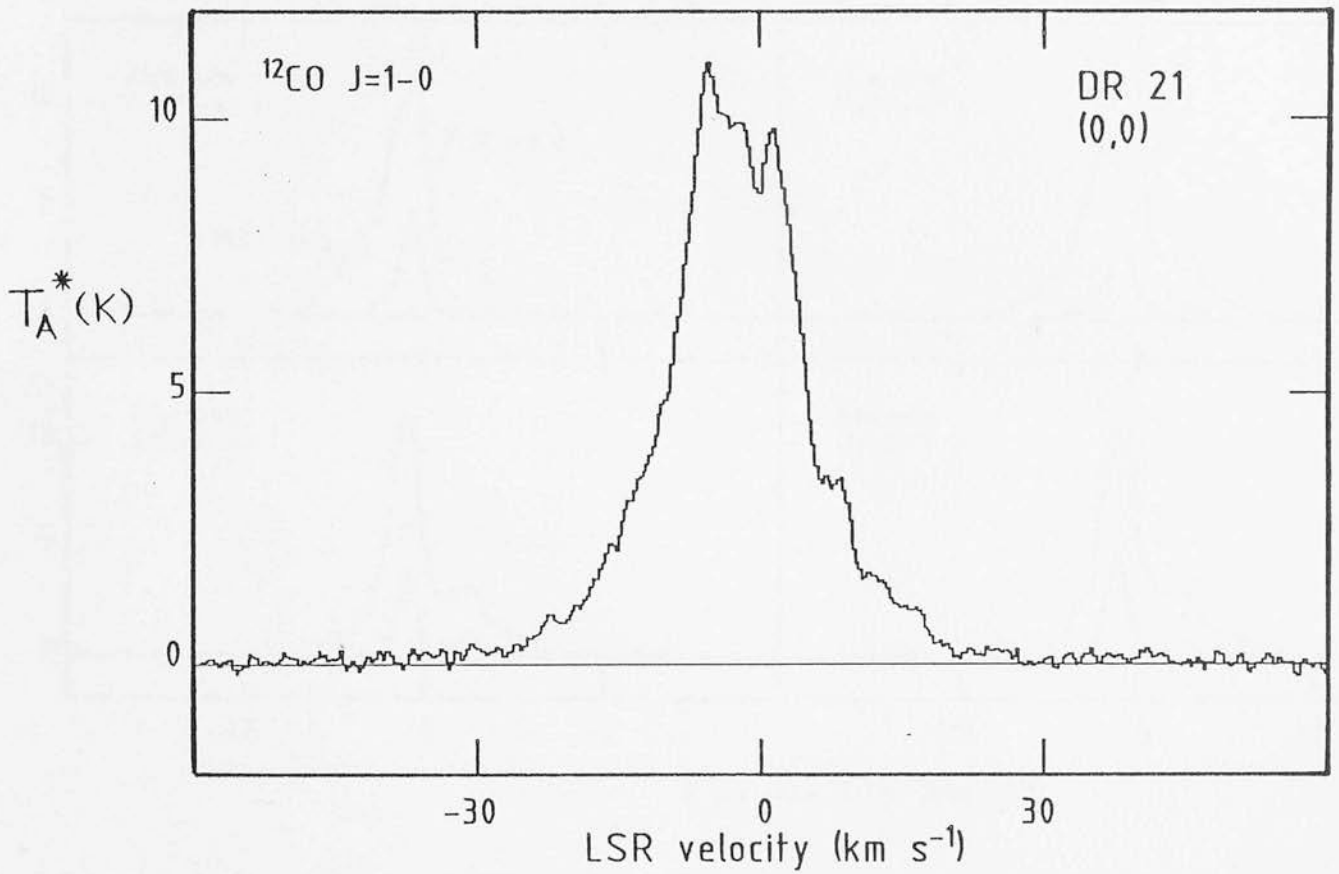

FIGURE 4.3.1 : 12CO J=1-0 profile measured at the proposed location of the central outflow source in DR21; i.e. map offset (0,0). The beam size is 15 arcsec and the velocity resolution is 0.3 kms-1.

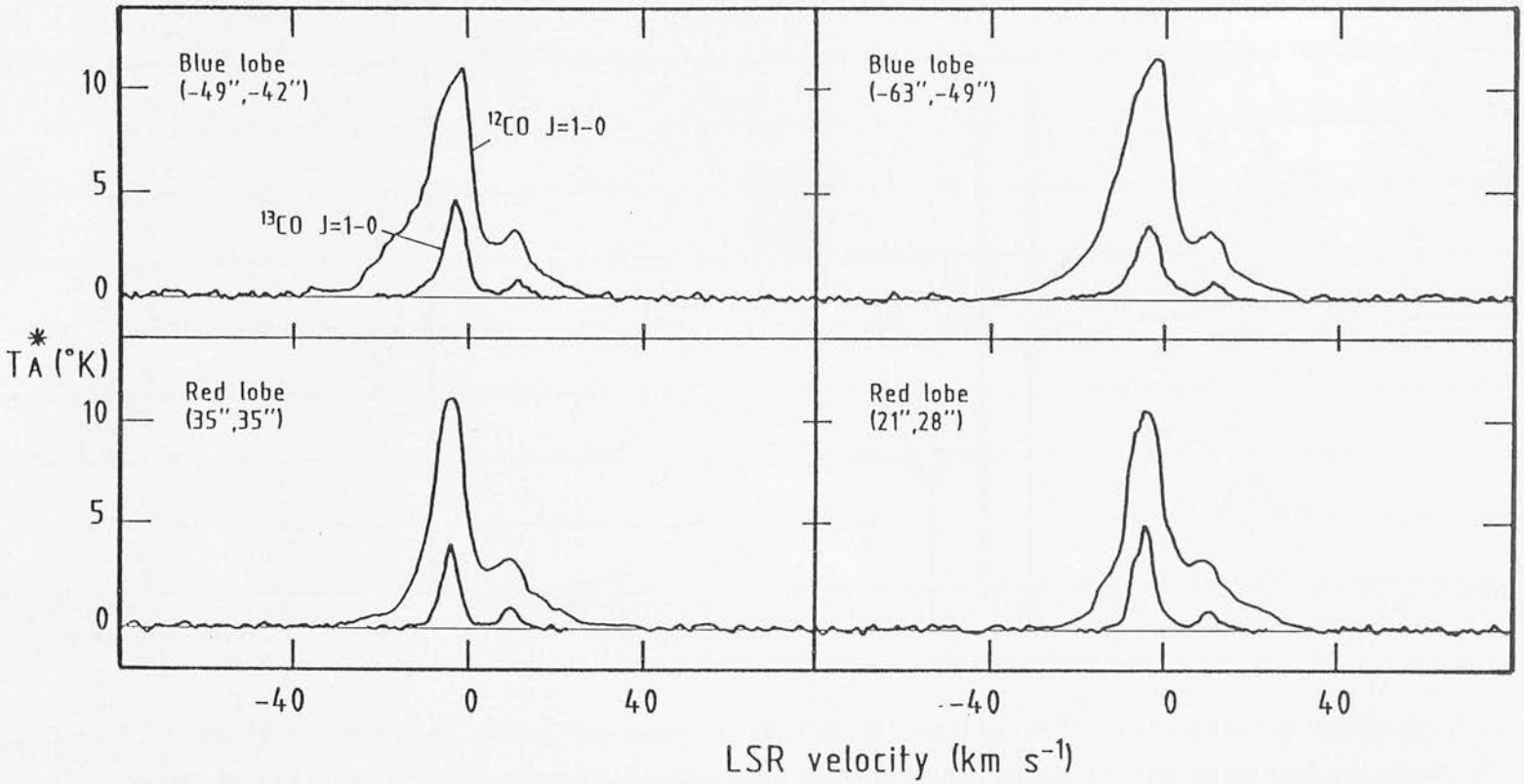

FIGURE 4.3.2 : 12CO and 13CO J=1-0 profiles measured at two locations around the blue and red high-velocity outflow lobes. Contamination by the W75N cloud gives rise to the emission component at +8 kms-1.

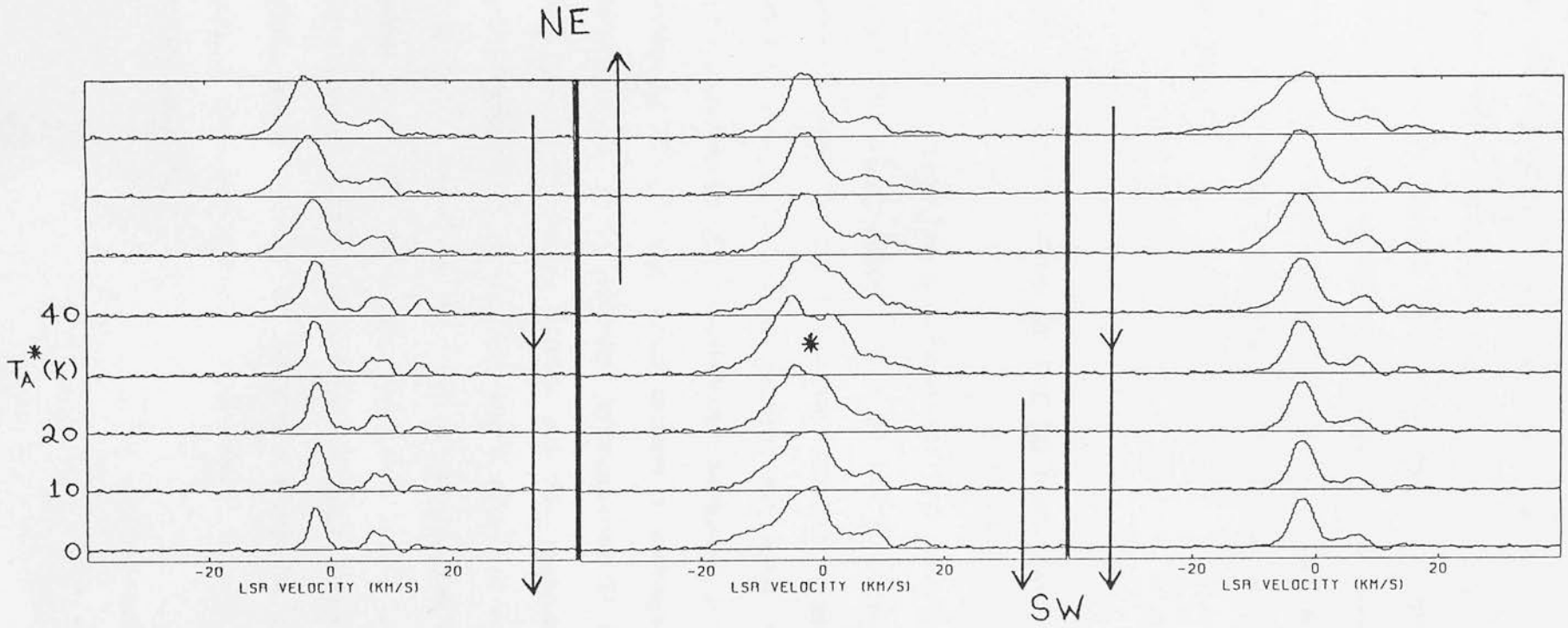

FIGURE 4.3.3 : 12CO profiles measured along the major axis (NE-SW) of the DR21 high-velocity outflow. The asterisk indicates the profile which corresponds to the map offset (0,0) which is the proposed position of the central outflow source. The angular separation between consecutive measurements is 15 arcsec.

arcmin to the north of DR21 and extends over the entire area mapped. Fortunately, this extraneous emission componenent is rather narrow in velocity width and uniform in brightness and consequently does not perturb the intrinsic emission outwith the velocity range 6-12 kms^{-1}; data within this range could not be used. In contrast to the red-shifted CO emission, the blue-shifted emission suffers no visible contamination over the entire area mapped. The excellent signal-to-noise presented by these spectra is representative of the entire data set which is composed of over 300 separate spectra, spaced on a 15 arcsec grid.

4.3.(d) THE APPEARANCE OF THE CO J=1-0 MAPS

A contour map of the total integrated ^{12}CO J=1-0 line antenna temperature, spanning the velocity range, -30 to 30 kms^{-1}, is shown in Fig.[4.3.4]. The complex structure displayed in this map immediately suggests that the DR21 CO cloud does not take on a simple geometry but, rather, shows extreme evidence for edge brightening and a preferential elongation, both N-S and E-W. An interpretation of this map, which presents a convolution of many different velocity structures, is best attempted by segmenting the integrated emission into individual 2 kms^{-1} velocity intervals and then comparing the results. In this manner, Figs.[4.3.5a] & [4.3.5b] represent a mosaic of velocity-channel maps in the high-velocity blue and red wings of the CO profile; for the red-shifted velocities, data within the velocity range, 6-10 kms^{-1}, are not displayed due to line-of-sight contamination by emission associated with the neighbouring W75N molecular cloud. Although the spatial distribution of CO line emission with velocity is extremely structured, some notable features appear in these maps which are listed below:

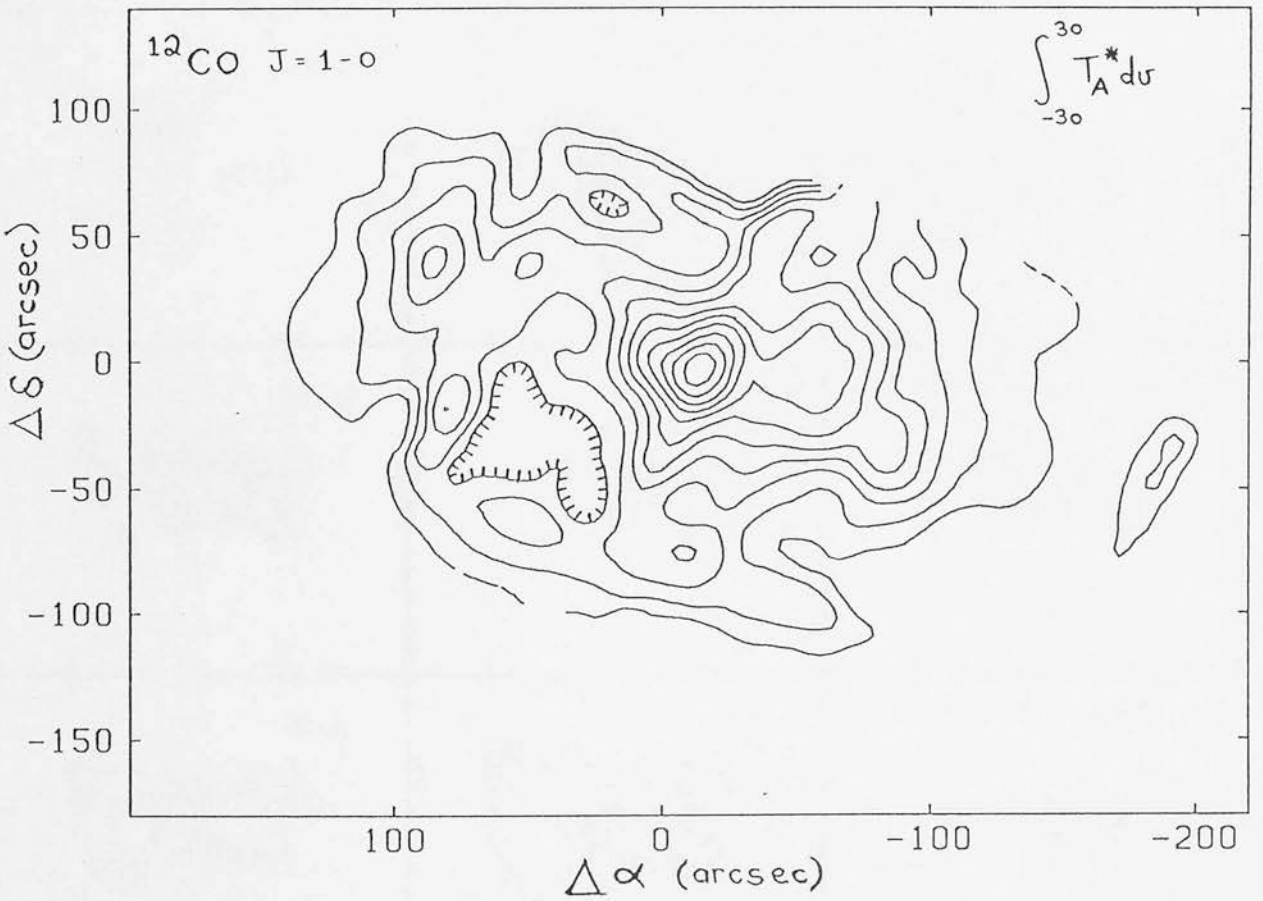

FIGURE 4.3.4 : Contours of integrated 12CO J=1-0 line antenna temperature over the velocity range (-35 to 35 kms-1) toward the DR21 region. The beam size is 15 arcsec, the lowest intensity contour is 80 K-km/s, and the contour spacing is 12 K-km/s.

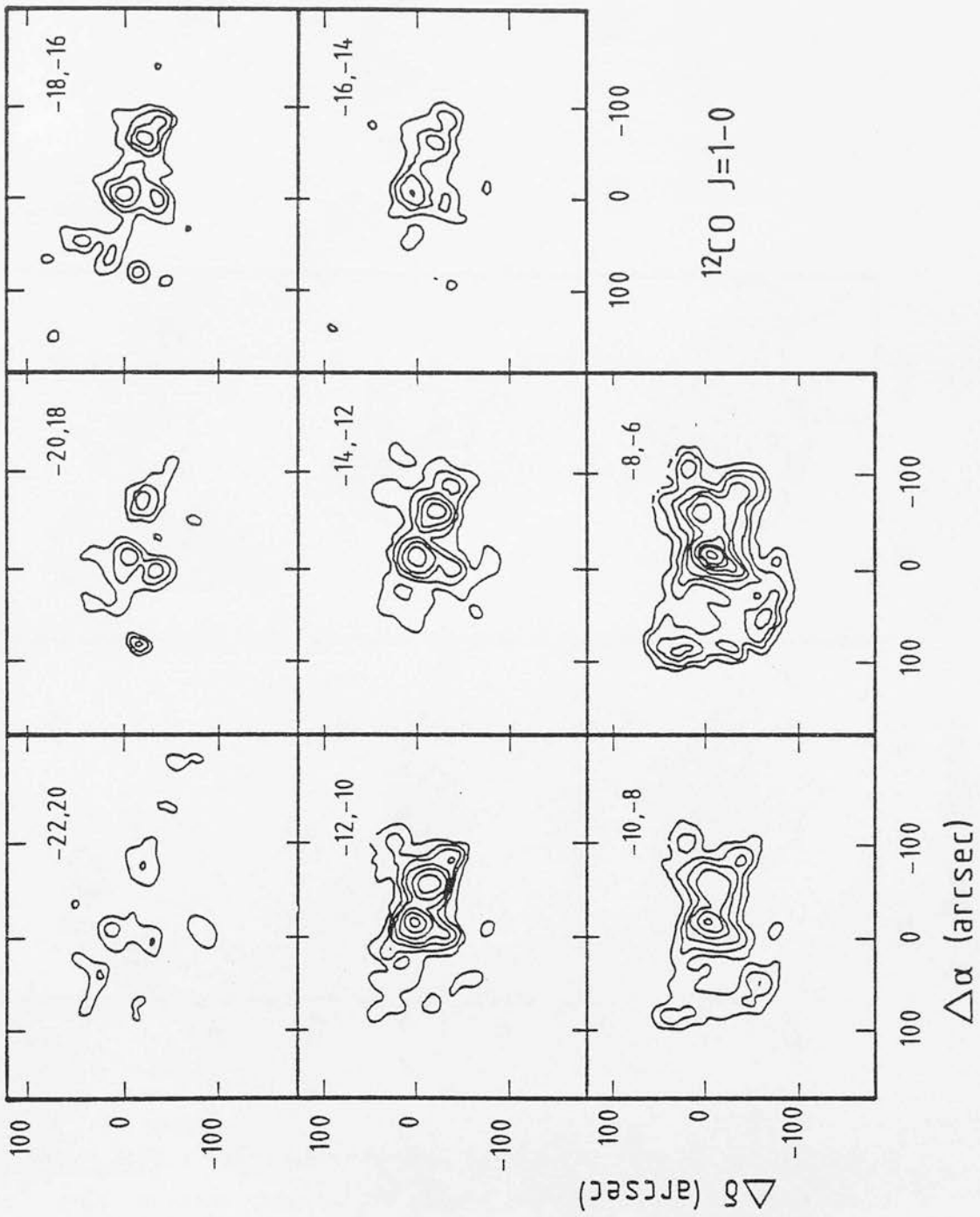

FIGURE 4.3.5a : Blue-shifted velocity channel maps of integrated 12CO J=1-0 antenna temperature toward the DR21 outflow. The maps are integrated over 2km/s intervals. The lowest intensity contour and subsequent contour spacing correspond to 1 K-km/s.

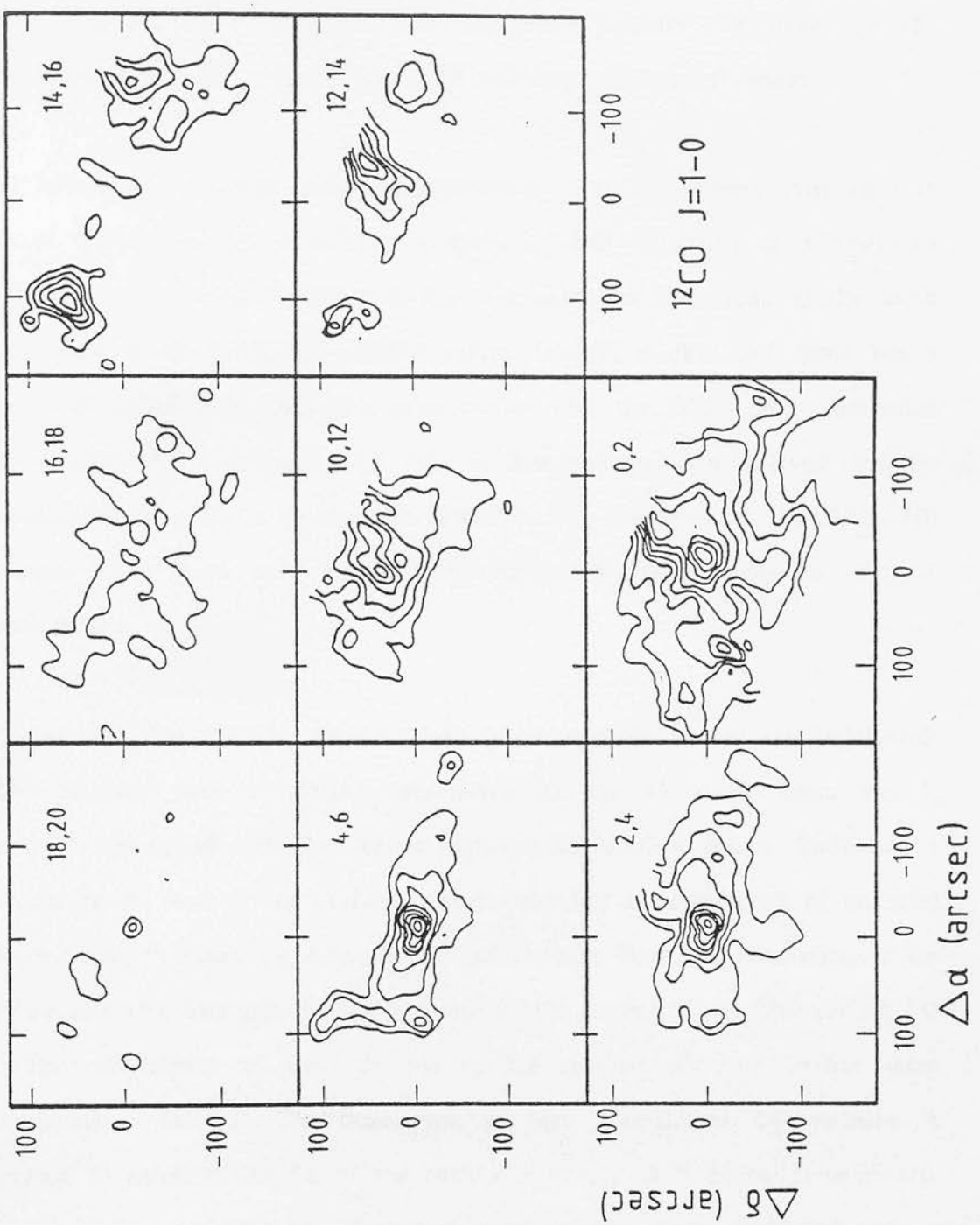

FIGURE 4.3.5b : Red-shifted velocity-channel maps of integrated 12CO J=1-0 antenna temperature toward the DR21 outflow. The maps are integrated over 2 km/s internals. The lowest intensity contour is 2 K-km/s and the contour spacing is 1 K-km/s for the highest-velocity maps and 3 K-km/s for the lower-velocity maps.

(1) In general, the bulk of the emission at low-velocity shifts from the line core (V_{lsr} = -2.5 kms^{-1}), is both significantly brighter and more centrally concentrated than the emission associated with the high-velocity wings.

(2) In the lower-velocity channels, particularily over the velocity intervals (-10 to -6 kms^{-1}) and (0 to 4 kms^{-1}), there is clear indication of a shell-like emission feature lying 80 arcsec to the east and extending round to the north and south of the DR21 CO outflow centre. Internal to the shell, there lies a cavity of depleted CO emission, juxtaposition with the DR21 radio continuum source. As will be discussed more fully in later sections, it is believed that this shell/cavity structure is dynamically related to the expansion of the DR21 HII region, which need not necessarily belong to the DR21 molecular outflow phenomenon.

(3) At high blue-shifted velocities, three bright emission clumps are highlighted. The brightest peak is spatially unresolved by the 15 arcsec beam and is probably associated with the central high-velocity outflow source. Positioned 1 arcmin to the west of the outflow centre, there lies a second peak of extended emission which forms the blue-shifted outflow lobe. Both the orientation of the major axis (NE-SW) and the linear extent (> 100 arcsec) of the blue-shifted CO outflow are similar to those defined by the shocked H_2 emission-line maps presented in Sec.[4.2]. The third peak of high blue-shifted CO emission is located 30 arcsec to the SE of the outflow centre, in a direction perpendicular to the major outflow axis. This third peak is most likely associated with a second high-velocity flow which is dynamically independent of the main NE-SW outflow.

(4) At high red-shifted velocities, the emission morphology is again composed of three major condensations. However, the overall emission distribution is significantly more confused than at blue-shifted velocities. Indeed, the continuity between adjacent velocity-channel maps is almost nonexistent, thus indicating that the red-shifted emission is not only spatially but is also kinematically clumped. As is indicated by the high signal-to-noise CO profile measured at the central map position (Fig.[4.3.3]), the central outflow source forms a bright and compact peak of emission that is clearly visible over the velocity range (0 to 10 kms^{-1}). In the adjacent velocity intervals (10 to 14 kms^{-1}), the central peak weakens and a second peak located approximately 1 arcmin to the NW of the map origin appears. This peak is located within an extended ridge of emission which runs along a SE-NW axis, originating at the map centre and extending northwards to beyond the northern boundary of the map. The third peak of high red-shifted emission is isolated to the velocity range (12 to 16 kms^{-1}) and appears as a well-defined clump located approximately 100 arcsec to the NE of the outflow centre, diametrically opposite to the high-velocity blue lobe. Some faint, extended red-shifted emission is also present to the SW and is probably kinematically associated with the blue-shifted outflow gas at this position.

The velocity-channel maps are most effective when used as a tool for investigating the detailed structure of the velocity field at high-spectral resolution. A disadvantage inherent to this method, however, is that, due to the narrow spectral coverage, the signal-to-noise ratio within each velocity-channel map is not of sufficient quality to properly display low surface-brightness emission features. In order to study the spatial distribution of the fainter emission components of the DR21 outflow system and also to help smooth out some of the other sources of noise that are inherent to the present data set, it was therefore necessary to increase the velocity bin size and replot the

velocity-channel maps using only five velocity intervals across the line profile. Relative to the DR21 systemic velocity (V_{lsr} = -2.5 kms^{-1}), these velocity intervals are defined as follows :

LOW	: V_{lsr} =	-5 to 0 kms^{-1}
INTERMEDIATE-BLUE	: =	-5 to -12 kms^{-1}
INTERMEDIATE-RED	: =	0 to 6 kms^{-1}
HIGH-BLUE	: =	-12 to -30 kms^{-1}
HIGH-RED	: =	10 to 30 kms^{-1}

The red-shifted velocity interval (6 to 10 kms^{-1}) was not used due to contamination by emission at V_{lsr} = 8 kms^{-1} from the nearby W75N molecular cloud. Also, the LOW-velocity interval is dominated by emission from the quiescent DR21 molecular cloud and no information can be derived regarding the outflow gas from this component. In Fig.[4.3.6], contour maps of the four remaining INTERMEDIATE and HIGH-velocity components are presented. These maps show the same general morphological and spectral features as were derived from the higher-spectral resolution images, only the signal-to-noise is considerably improved and is now of sufficient quality to permit intercomparison of the CO emission in the red and blue-shifted velocity intervals. Accordingly, Fig.[4.3.7] shows a superposition of the HIGH-RED and HIGH-BLUE CO emission components.

As a result of the high-angular resolution employed in making these CO observations, the relative spatial distribution of HIGH-RED and HIGH-BLUE CO emission is significantly more structured and complex than is normally observed using smaller-diameter millimeter telescopes. Nonetheless, the comparison in Fig.[4.3.7] reveals several extremely interesting features. First, I

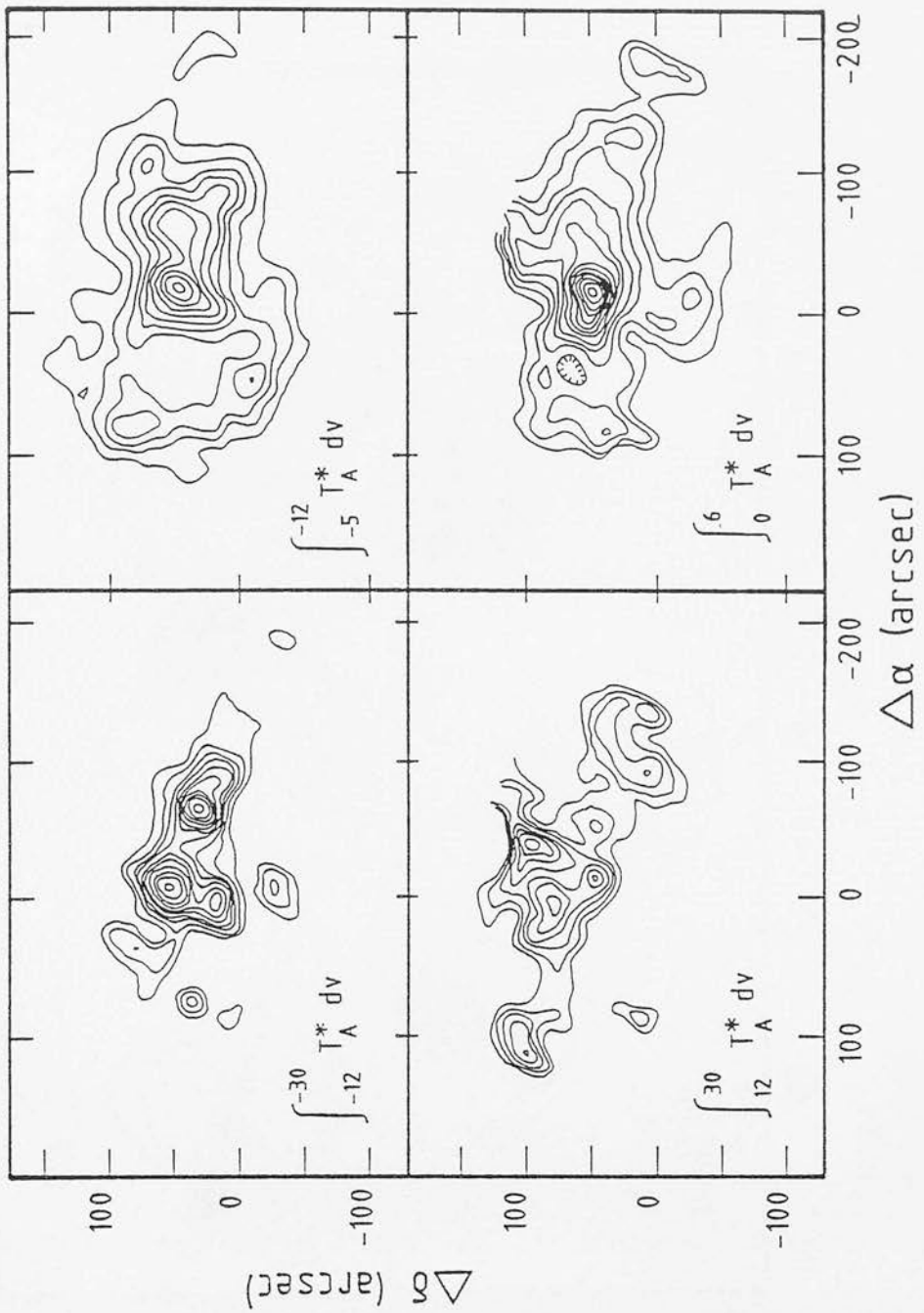

FIGURE 4.3.6 : Contour maps of the integrated intensity of the high-velocity and intermediate-velocity redshifted and blueshifted CO J=1-0 emission in DR21. For the high-velocity maps, the lowest contour is 5 K-km/s, and the contours are spaced by 1.5 K-km/s. For the intermediate-velocity maps, the lowest contour is 15 K-km/s and the contour spacing is 4 K-km/s. The beam size is 15 arcsec.

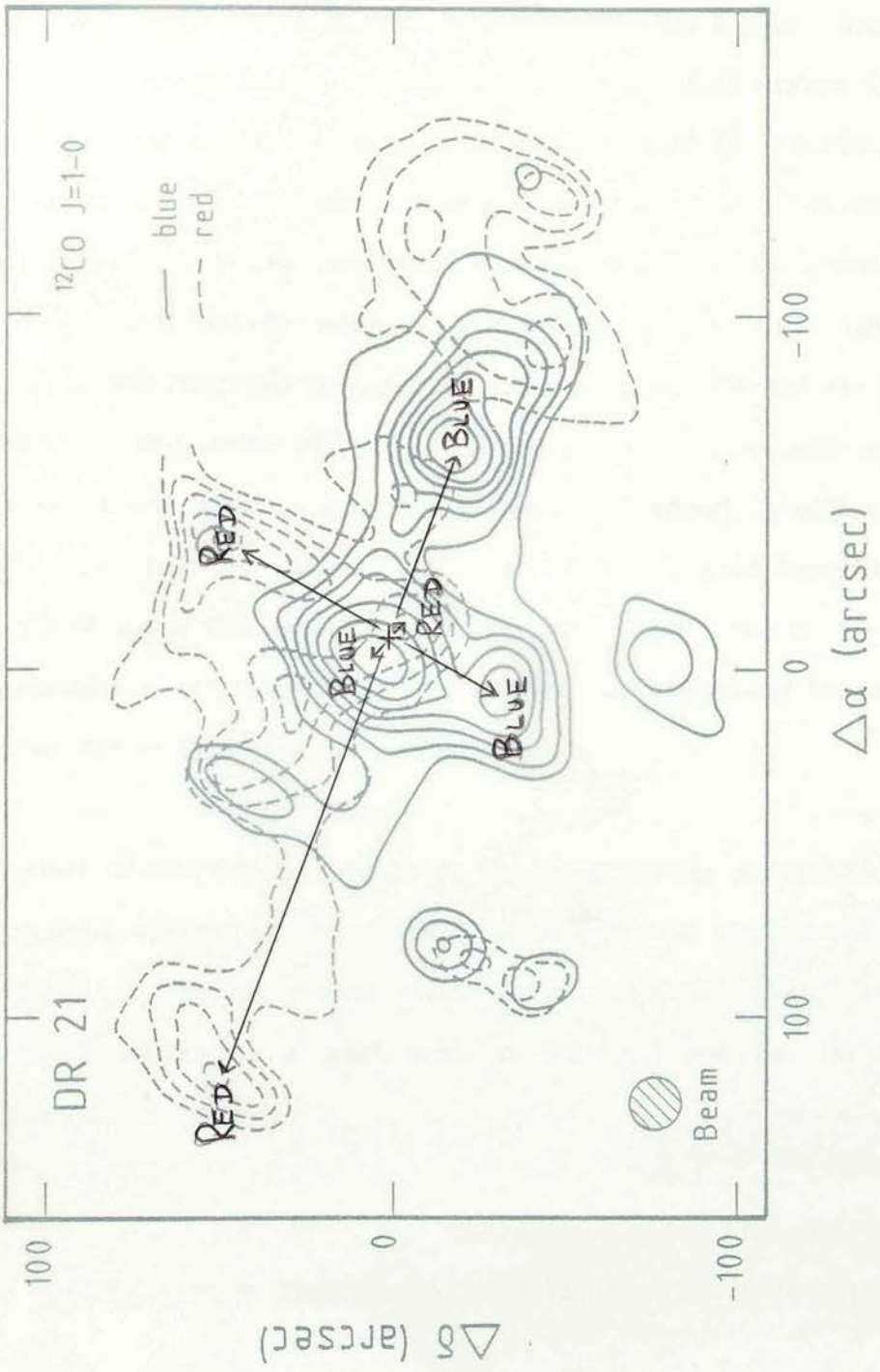

FIGURE 4.3.7 : A superposition of the high-velocity blue and red-shifted integrated intensity contours as shown in Fig.[4.3.6]. The transparent overlay shows the orientation of the three bipolar flows alluded to in the text.

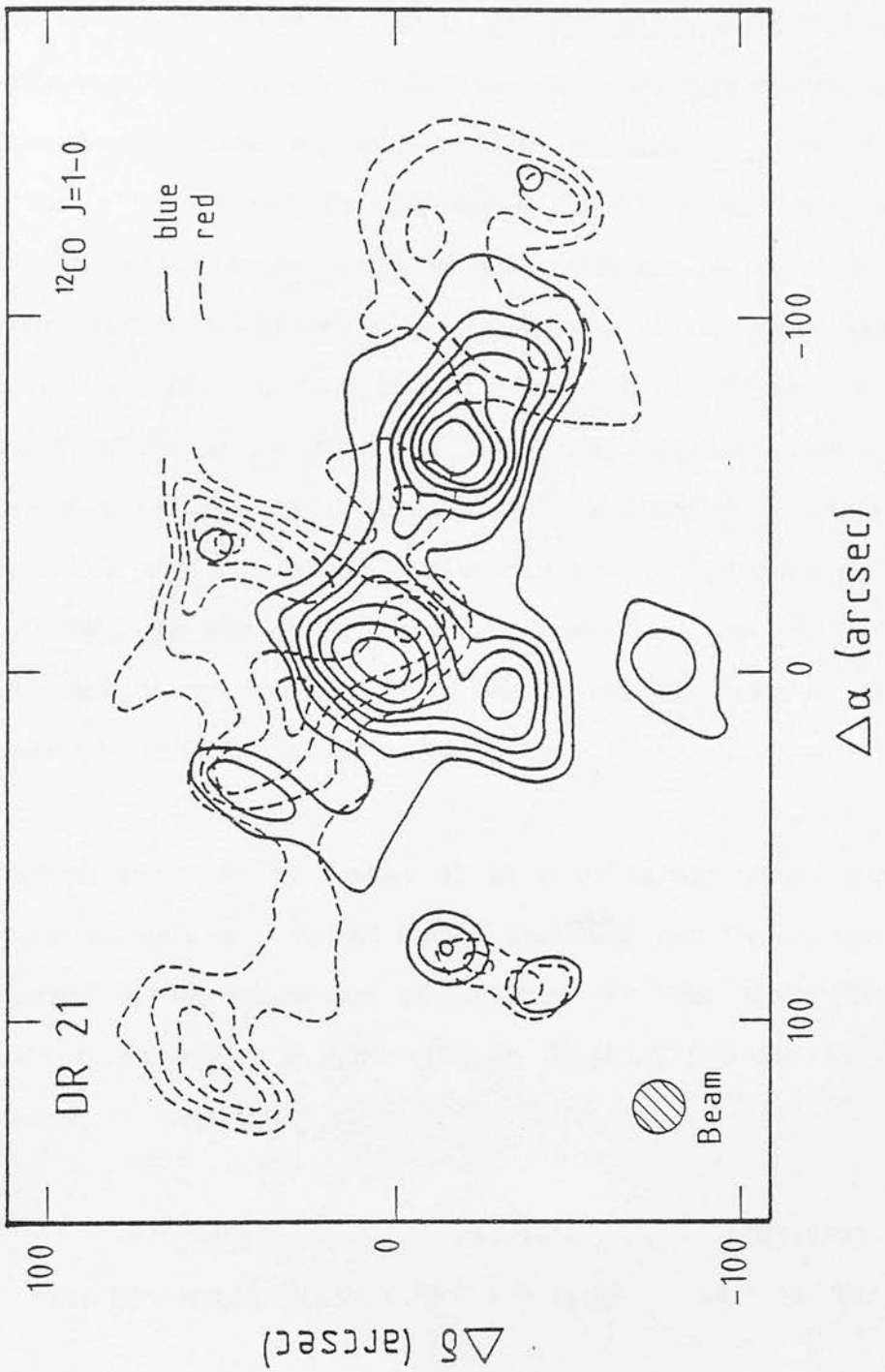

FIGURE 4.3.7 : A superposition of the high-velocity blue and red-shifted integrated intensity contours as shown in Fig.[4.3.6]. The transparent overlay shows the orientation of the three bipolar flows alluded to in the text.

bring to notice the presence of three spatially distinct bipolar flows that apparently emanate from a common origin which may be identified with the central driving source of the DR21 outflows; the relative orientations of these three bipolar flows are clearly indicated by arrows in Fig.[4.3.7]. The first bipolar flow is the largest in scale (> 200 arcsec), has a major axis running NE-SW, is composed of the brightest blue and red-shifted outflow lobes, and exhibits the best spatial correlation with the vibrational H_2 emission; the red lobe lies to the NE and the blue lobe to the SW of the proposed outflow centre. The second bipolar flow, is of intermediate size (~ 100 arcsec) and has an axis oriented NW-SE which is perpendicular to the major axis of the primary bipolar flow; this time, the red lobe lies to the NW and the blue lobe to the SE of the outflow centre. The third bipolar flow is the most compact (~ 20 arcsec) and, considering the pointing errors (~ 7 arcsec), is only a tentative identification. The major axis of this compact flow is aligned almost parallel to the NE-SW major axis of the largest-scale bipolar flow, however, the sense of the bipolarity is apparently transposed, with the red lobe located to the SW and the blue lobe to the NE of the outflow centre.

A best estimate for the position of the central driving source which powers the observed outflows is derived through association with the common point of intersection of the major axes characterizing the three bipolar flows. This position is marked by a small cross in Fig.[4.3.7] and has the following coordinates:

	RA(1950)	DEC(1950)
DR21 CO OUTFLOW CENTRE :	$20^h\ 37^m\ 14.0^s$	$+42^\circ\ 08'\ 58''$

The above proposed position of the central CO outflow source lies within

one beam spacing of the map origin (offset: 0,0), which, in itself, is a remarkable occurrence considering that the CO map origin was chosen with sole reference to the infrared H_2 observations. The accuracy with which the position of the outflow centre was predicted almost certainly testifies to the existence of a common dynamical origin for both the high-velocity CO and shock-excited H_2 emission, that is, both the millimeter-wave and infrared emission components are presumably excited by the same outflow phenomenon.

The shell-like clump of HIGH-RED CO emission located at the outer edge of the south-western, blue-shifted outflow lobe is difficult to explain in the context of a freely-propagating linear outflow model. With outwards displacement from the outflow centre, along the SW direction, the flow first appears red-shifted, then becomes blue-shifted, and finally turns red-shifted once again. Obviously, the detailed kinematics of the outflow gas is more complex than just linear flow along this lobe. Indeed, the outflow appears to wiggle back and forth in radial velocity, somewhat reminiscent of the proposed behaviour of some extragalactic radio jets (see Sec.[6.6]), only on a much smaller scale. These peculiar kinematic trends, which are also mimiced in H_2 v=1-0 S(1) line emission (see Fig.[4.2.6] & Table[4.2.2]), are probably best represented by the HIGH-BLUE/HIGH-RED and INTERMEDIATE-BLUE/INTERMEDIATE-RED mass-ratio versus position plots shown in Fig.[4.3.10a] & [4.3.10b].

To aid in the interpretation of the kinematic details within the outflow lobes, a position-velocity (PV) plot of the CO emission at all observed positions along the major (NE-SW) outflow axis is presented in Fig.[4.3.8]. The central high-velocity outflow source is clearly evident in this diagram, as are the red and blue outflow lobes. Especially prominent is the clumpy nature of the

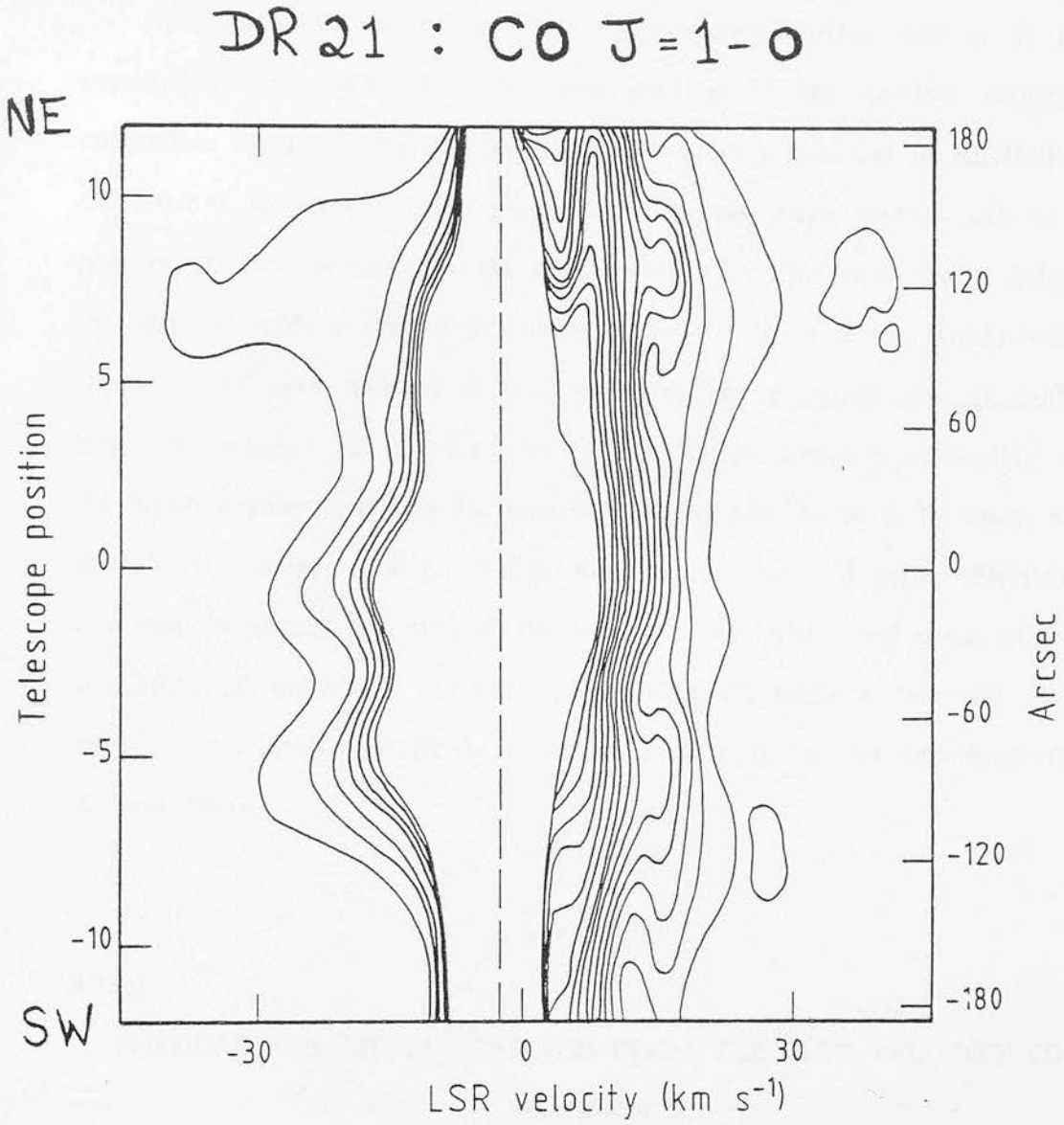

FIGURE 4.3.8 : Velocity-position diagram for 12CO emission along the major axis of the high-velocity flow (NE-SW) in DR21. The outflow centre is located at telescope position '0' and the high-velocity blue (west) lobe is at position '-5'. The angular resolution is 15 arcsec and the velocity resolution has been smoothed to 0.5 km/s.

high-velocity red-shifted emission components, which are located at the outer extremities of both outflow lobes.

An estimate of the width of the high-velocity outflow lobe is of great importance for gaining a better understanding of the outflow collimation mechanism. To aid in this respect, Fig.[4.3.9] shows a cross-cut in HIGH-BLUE CO antenna temperature taken perpendicular to the major outflow axis at the position of peak emission in the blue (west) lobe. This plot clearly indicates that the CO outflow lobe is extremely narrow (~ 20 arcsec in width) with a strong central peak and should thus be termed a jet rather than an outflow lobe. This estimate for the diameter of the CO jet compares favourably with the higher-angular resolution H_2 observations presented in Sec.[4.2], which show that the H_2 emission-line jet at this same position has a diameter (FWHM) of less than 20 arcsec. The ratio of the lengths of the major and minor axes for the DR21 CO outflow is therefore greater than 10. DR21 is thus one of the most highly-collimated of all the molecular outflow sources yet discovered (Bally & Lada 1981).

4.3.(e)

PHYSICAL PARAMETERS DERIVED FROM THE HIGH-VELOCITY CO EMISSION

In order to investigate the physics underlying the enigmatic DR21 outflow phenomenon, it is first necessary to gain estimates of the mass, energy, and momentum of the gas in the flow. Estimates of these quantities in turn depend on estimates of the optical depths, excitation temperatures and filling factors of

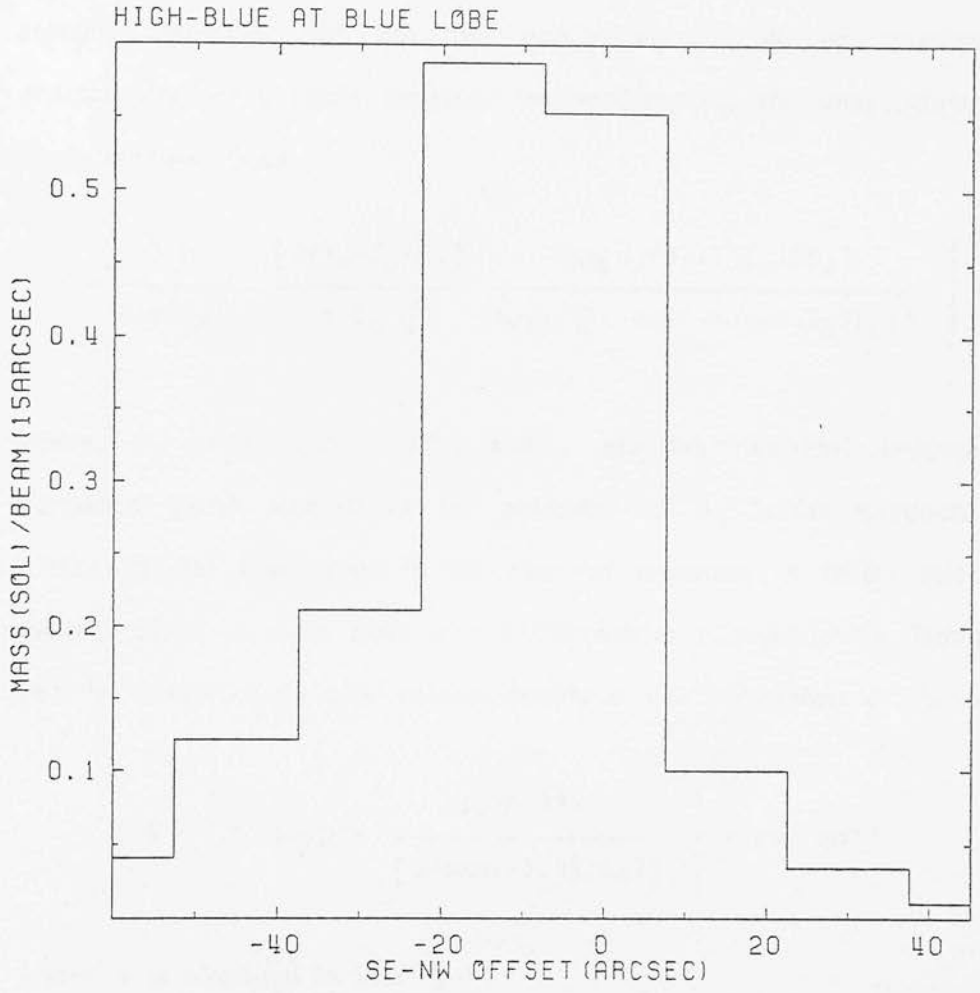

FIGURE 4.3.9 : The spatial distribution of mass in high-velocity blueshifted gas along a cut taken perpendicular to the major outflow axis at the peak of CO emission in the high-velocity blueshifted lobe. This plot effectively shows the width of the outflow lobe at this position (see Fig.[4.3.7]). The angular resolution is 15 arcsec.

the emitting gas, quantities which result in determination of the gas column density as a function of velocity.

The total column density of high-velocity molecular gas can be calculated from the integral of the optical depth over the line profile. For a linear, rigid, rotating molecule that has the populations of all its rotational levels characterized by a single excitation temperature, T_X, the total column density, N, is obtained from

$$N = \frac{3\ h}{8\ \pi^3\ \mu^2} \quad \frac{[\,2(T_X+T_O/6)\,]}{[\ T_O\ ]} \quad \frac{\exp[\,J_\ell(J_\ell+1)T_O/2T_X\,]}{(J_\ell+1)[\,1-\exp[-(J_\ell+1)T_O/T_X]\,]} \int \tau_\nu\ d\nu \qquad (4.3.2)$$

where, T_O ($= h\nu_{10}/k \approx 5.53$) and μ are the rotational temperature and permanent dipole moment of the molecule, and J_ℓ is the rotational quantum number of the lower state in the observed transition. A recent calculation of the CO dipole moment gives μ = 0.1098 debyes (Chackerian & Tipping 1983). For the CO J=1-0 the total column density in CO is therefore of the form

$$N = 2.39\times10^{14} \quad \frac{(T_X+0.93)}{[\,1-\exp(-5.53/T_X)\,]} \int \tau\ dv \quad cm^{-2} \qquad (4.3.3)$$

where, v is measured in kms^{-1}.

The opacity in CO emission can be deduced from observations of the antenna temperature in the main, $T_a^*(CO)$, and isotope, $T_a^*(^{13}CO)$, lines. If both lines are optically thin and if the excitation temperature of the two species is the same, then the ratio of the line intensities would be the same as the ratio of their respective abundances. During the past few years a considerable number of observations have been published, from which it appears that for most

outflow sources, the high-velocity CO emission is usually somewhat optically thick whilst the ^{13}CO emission is optically thin (Plambeck et al. 1983, Snell et al. 1984 and Margulis & Lada 1985). Under such conditions, the CO optical depth, τ_{12}, can be obtained from the observed antenna temperatures as follows

$$R = \frac{T_a^*(^{12}CO)}{T_a^*(^{13}CO)} = \frac{1-\exp(-\tau_{12})}{1-\exp(-\tau_{13})} = \frac{1-\exp(-\tau_{12})}{1-\exp(-\tau_{12}/89)} \qquad (4.3.4)$$

where it is assumed that $[^{13}CO/CO] = \tau_{13}/\tau_{12} = 1/89$.

Considering the generally accepted conclusion that the high-velocity CO emission is optically thick, and therefore presumably also thermalized, it is somewhat alarming that the observed antenna temperatures in the far-wings of the CO line are almost always less than 1/10 of that observed in the line core. This implies that either the J = 0,1 levels are not thermalized or the lines are emitted in clumpy gas that does not uniformly fill the beam. Indeed, there exists strong observational evidence which corroborates the notion that the high-velocity gas in molecular outflows is spatially clumped. Richardson et al. (1986) have undertaken a multi-line analysis of the DR21 outflow at low spatial resolution. They conclude that a single-phase radiative transfer model is inadequate and suggest that a 2-component model (i.e. Norman & Silk 1980), consisting of dense (10^6 cm^{-3}) clumps immersed in a less dense (10^3 cm^{-3}) interclump gas of higher temperature, may present a superior fit to their data. Similar conclusions have been drawn from HCN and HCO^+ isotope and multi-transition analyses of the Orion and NGC2071 high-velocity outflows (White, Avery & Richardson 1984; Wootten et al. 1984).

In view of the overwhelming evidence in favour of high density molecular condensations within a variety of different high-velocity outflow sources, it will

be assumed, henceforth, that the CO lines are thermalized and that the analysis is best carried out in terms of the area beam-filling factor, f (cf. Fischer et al. 1985), where, by definition

$$f = \frac{T_a^*(CO)/\eta_B}{[5.53/[\exp(5.53/T_X)-1]-0.93]} \quad \frac{1}{[1-\exp(-\tau)]} \qquad (4.3.5)$$

Introduction of the filling factor into eqn.(4.3.4) results in the reduction of the mean source column density by a factor f. In the limit $T_X \gg 2.75$, the cosmic background term can be neglected, and the mean column density of CO gas averaged over the beam can be expressed simply as follows

$$\bar{N}(CO) = 4.30\times10^{13} \quad \frac{(T_X+0.93)}{\exp(-5.53/T_X)} \int \frac{T_a^*}{\eta_B} \quad \frac{\tau \, dv}{[1-\exp(-\tau)]} \qquad (4.3.6)$$

For the specific case of optically thin emission, $\tau/[1-\exp(-\tau)] \approx 1$. From the beam averaged column density, the total mass of gas in the beam is then

$$M_{gas} = \bar{N}(CO) \, [H_2/CO] \, \mu_g \, m(H_2) \, \pi \, \theta^2/4 \, D^2 \qquad (4.3.7)$$

where, $\mu_g = 1.36$, is the mean atomic weight of the gas, θ, is the angular diameter of a uniform disc source (FWHP) and $[H_2/CO] = 10^4$. Further, taking a mean optical depth, $\bar{\tau}$, for each velocity interval in the line profile, eqn.(4.3.7) then becomes

$$M_{gas} = 1.65\times10^{-7} \frac{T_x}{\exp(-5.53/T_x)} \frac{\tilde{\tau}}{[1-\exp(-\tilde{\tau})]} \left[\frac{\theta}{\text{arcsec}}\right]^2 \times \left[\frac{D}{\text{kpc}}\right]^2 \int \frac{T_a^*}{\eta_B} dv \quad M_0 \qquad (4.3.8)$$

The mass, momentum and energy in the flow is then calculated using the following relationships

$$\text{MOMENTUM} = P = M(\Delta v,\bar{\tau}).\text{mod}[\tilde{v}] \qquad (4.3.9a)$$

$$\text{ENERGY} = E = 1/2\ M(\Delta v,\bar{\tau}).\tilde{v}^2 \qquad (4.3.9b)$$

where, $M(\Delta v,\bar{\tau})$ is the total mass of gas, as defined by eqn.(4.3.8), within a specific velocity inteval, $\Delta v = v_1$ to v_2, with a corresponding mean optical depth in that velocity range of, $\bar{\tau}$, and a representative mean velocity of $\tilde{v} = (v_1+v_2)/2$. It is preferable to take mean values of M, v and τ over relatively wide velocity bins rather than to calculate respective values at each velocity-resolution element over the profile, as the later approach can add significant noise to the end results which is effectively smoothed out in the averaging process inherent to the first method. It is also worth noting that in the Rayleigh-Jeans limit, where $kT_X \gg h\nu$, the column density, mass, momentum and energy are directly proportional to T_X, so the results can be readily rescaled to a different T_X, if necessary.

For the purpose of analysing the kinematics and energetics of the outflow gas, the observed line profiles are segmented into five distinct velocity intervals,

evenly spaced relative to the LSR velocity of peak CO line emission. The velocity limits chosen to define the LOW, INTERMEDIATE and HIGH velocity intervals are as defined previously (Sec.[4.3.d]). In Table[4.3.2], characteristic values for the mean optical depth, as calculated using eqn.(4.3.4), are given for each velocity interval. Due to the masking of the high-velocity emission at low projected velocities by the quiescent emission of the ambient molecular cloud, accurate antenna temperatures for the LOW-velocity component are impossible to derive directly. An attempted to define the antenna temperature characteristic to the LOW-velocity component has, however, been made by assuming a constant antenna temperature equal to the average of the antenna temperatures derived for the innermost velocity channels of the INTERMEDIATE-RED and INTERMEDIATE-BLUE components. A lower limit to the optical depth at low velocity displacements from the line core was similarily estimated by assuming it to be identical to the average of the optical depths in the adjacent INTERMEDIATE-velocity components.

A parameter important for calculating the line-of-sight column density, as expressed by eqn.(4.3.6), is the excitation temperature, T_X, of the gas under study. Since the excitation temperature uniquely determines the level populations of a molecule, knowledge of the relative intensities of at least two transitions are essential for unambiguous determination of this quantity (see the LVG analysis of the CS molecule, as discussed in Sec.[4.4.e]). Unfortunately, for the present study, line intensity measurements were made for the CO J=1-0 transition only, therefore an accurate determination of T_X is not possible. As a second best alternative, however, the finding that the CO line emission in DR21 is optically thick, and hence thermalized, can be used to define an appropriate value for T_X equal to the peak brightness temperature observed in the core component of the central CO line profile, that is $T_X \sim 40$ K. Observations of

TABLE 4.3.2 :

CO OPTICAL DEPTHS AND BEAM-AVERAGED COLUMN DENSITIES

R(12/13) $(=\int T_a^*(CO)dv / \int T_a^*(^{13}CO)dv)$

POSITION	VELOCITY RANGE HIGH	INTERMEDIATE	LOW
OUTFLOW CENTRE	25	10	1.6
BLUE LOBE	30	13	3.0

Derived average optical depth :

$\bar{\tau}$ (high) = 3

$\bar{\tau}$ (intermediate) = 8

$\bar{\tau}$ (low) = 8

$\bar{\tau}$ (quiescent) > 50

N(H2) cm-2

POSITION	VELOCITY RANGE HIGH	INTERMEDATE	LOW	TOTAL
OUTFLOW CENTRE	1.7(21)-5.3(21)	6.3(21)-4.5(22)	2.4(21)-1.9(22)	1.0(22)-6.9(22)
BLUE LOBE	1.6(21)-4.8(21)	3.9(21)-3.0(22)	2.1(21)-1.7(22)	7.6(21)-5.2(22)

Calculated for : Tx(CO) = 40 K
[CO]/[H2] = 1(-4)

the CO J=2-1 transition in the DR21 flow are planned within the next few months and should help considerably to uniquely determine the true value of T_x over the entire extent of the DR21 cloud core.

Having briefly outlined the method used to calculate the column densities of the high-velocity gas participating in the DR21 outflow, it is now possible to derive values for the beam-averaged column density of H_2 gas in the HIGH-, INTERMEDIATE-, and LOW-velocity components of the CO profile; this has been done for localized regions around the outflow centre and the position of peak high-velocity emission in the blue (west) lobe, the results of which are presented in Table[4.3.2]. The lower limit assumes optically thin emission and the upper limit encorporates the velocity dependent optical depth, also given in Table[4.3.2]. On average, the total column density in high-velocity gas lies between 5×10^{21} and 5×10^{22} cm^{-2} at these peak positions and is expected to be up to an order of magnitude lower in the extended outflow emission. The ratio of column density, and hence the mass of gas, in the HIGH-velocity components relative to the total line column density is between 10% and 20%, for optically thin and thick conditions, respectively; the corresponding ratio for the LOW-velocity component is around 40% to 50%.

Defining the average antenna temperaure as, $\overline{T}_a^* = \int T_a^* dv / \int dv$, it is found that typically, $\overline{T}_a^*(HIGH)/\overline{T}_a^*(LOW) < 0.1$, and $\overline{T}_a^*(INTER)/\overline{T}_a^*(LOW) = 0.5\text{-}0.8$. As the CO line is optically thick, even in the HIGH-velocity wings, the observed variation in antenna temperature over the CO profile is effectively generated by a corresponding variation in the beam-filling factor, which must decrease with increasing velocity offset from the line core. This trend, in turn, necessitates that the high-velocity gas be significantly more clumped than the low-velocity gas. The important issue concerning clumping of the outflow gas is

discussed more throughly in Sec.[5.4].

Using the above defined relationship between integrated antenna temperature and beam-averaged column density, the spatial distribution of outflow mass in the HIGH- and INTERMEDIATE-velocity components has been calculated along both a NE-SW and SE-NW axis, bisecting the outflow centre. These mass distributions are shown in Figs.[4.3.10a] & [4.3.10b], along with the respective BLUE/RED mass-ratios, for both velocity components. The mass-ratio plots give one of the best representations of the bipolar character of the DR21 molecular flows. For the NE-SW mass slice, which runs along the major DR21 outflow axis, the blue-shifted (to the SW) and the red-shifted (to the NE) outflow lobes are clearly represented, as is the sudden redwards shift in the mass distribution at the south-western extremity of the blue lobe. The mass-ratio plots for the INTERMEDIATE-velocity components show a similar trend to those exhibited by the HIGH-velocity components, excepting the presence of the narrow, blue-shifted shell component located ~ 80 arcsec to the NE of the outflow centre. As was stated in Sec.[4.3.d], it is believed that this prominent shell feature does not belong to the outflow phenomenon but, rather, is dynamically associated with the expanding DR21 HII region. The distribution of mass along the SE-NW axis, also shows radical differences between the red and blue-shifted veocity components. Both the HIGH-BLUE/HIGH-RED and INTERMEDIATE-BLUE/INTERMEDIATE-RED mass-ratio plots, exhibit a clear bipolar distribution with blue-shifted emission located to the SE and red-shifted emission to the NW of the outflow origin. The sense of these velocity shifts agree with those inferred from the velocity-channel maps presented in Sec.[4.3.c].

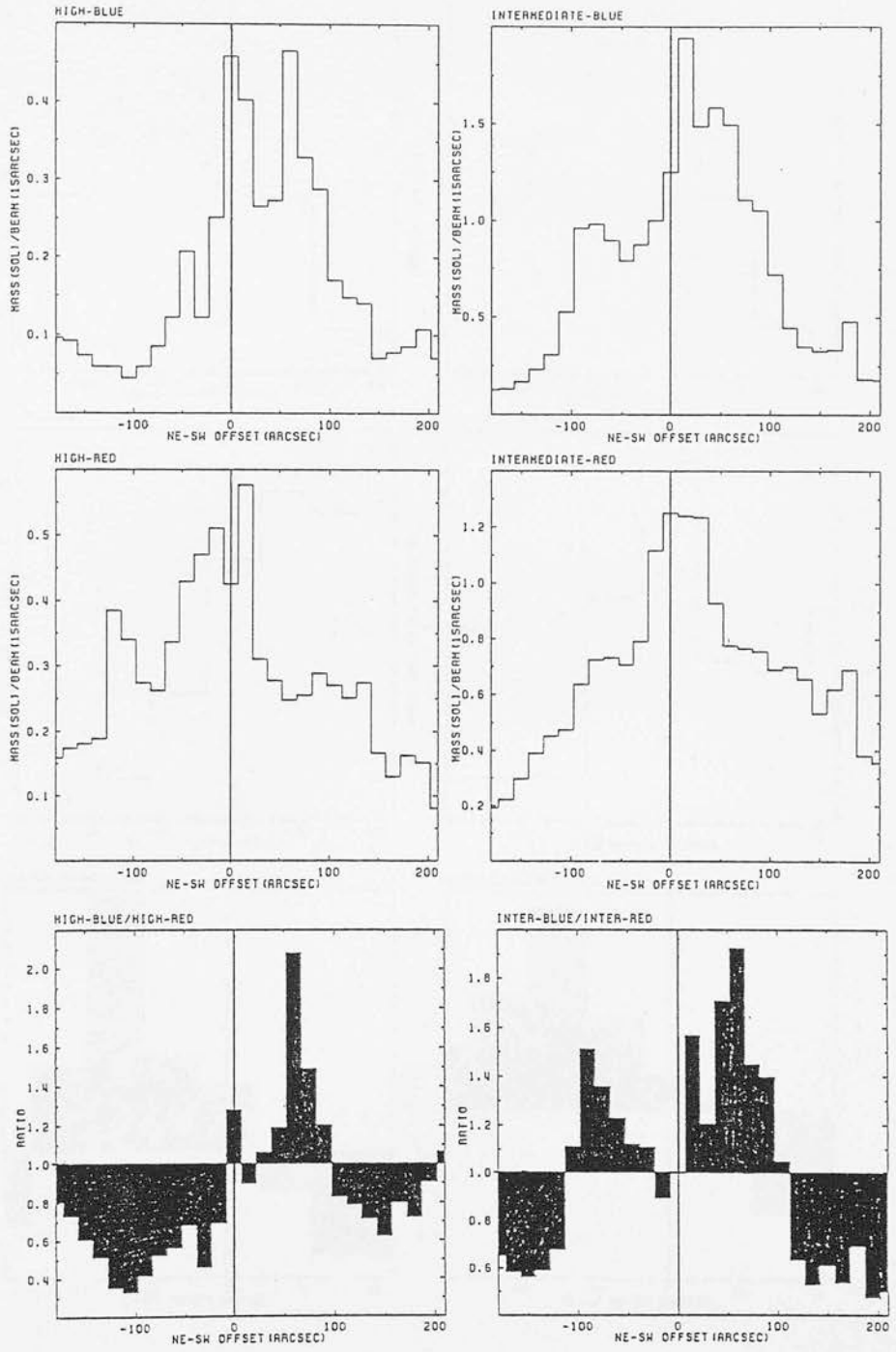

FIGURE 4.3.10a : The spatial distribution of mass, as derived from CO column density, along the major axis of the DR21 high-velocity outflow. The mass in the high and intermediate, blue and red velocity components is calculated as well as the ratio of mass at blue and red velocities (lowest plot). The outflow centre is at offset '0' (solid line). The bipolar nature of the outflow is especially clear in the ratio plots.

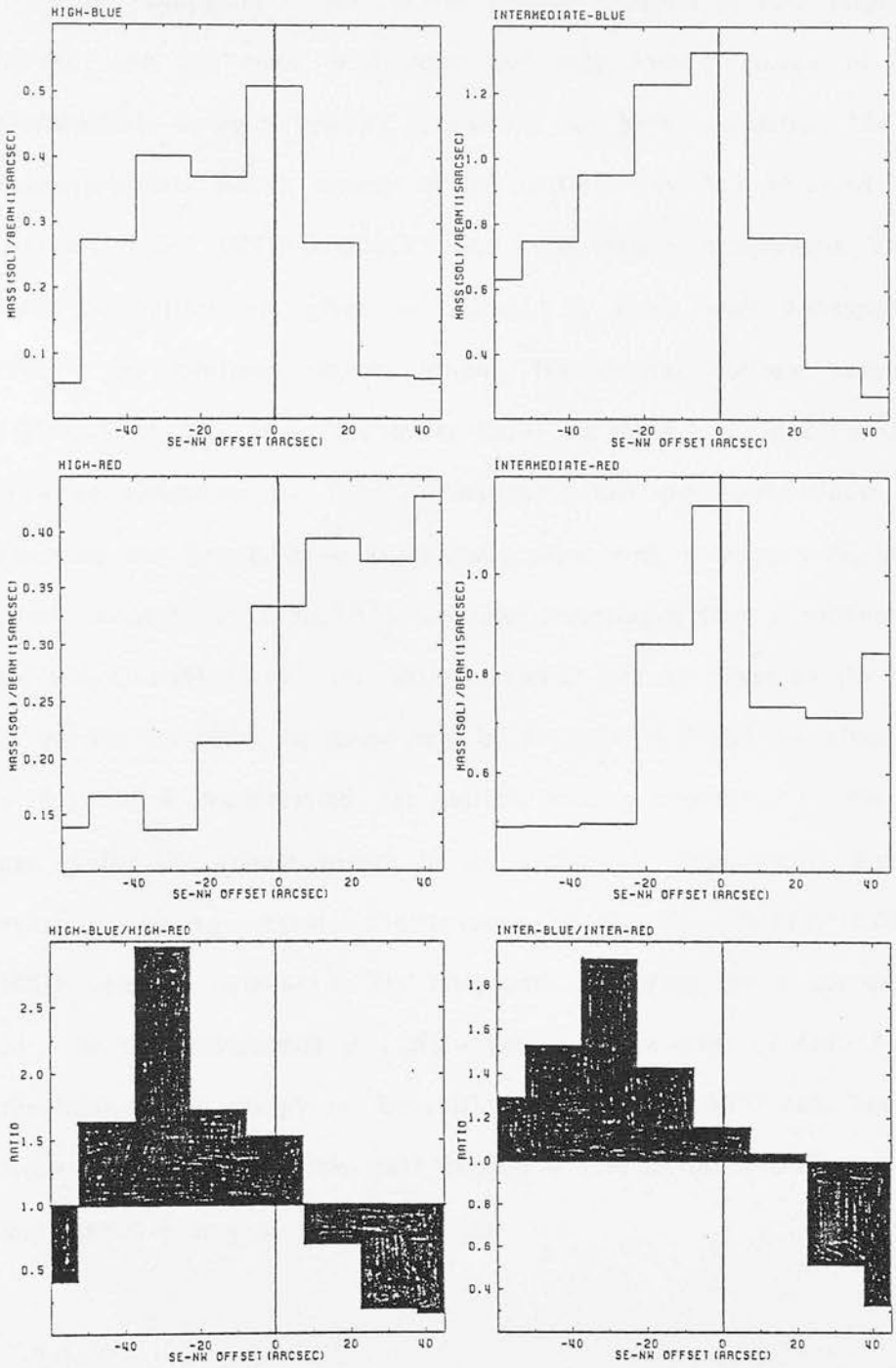

FIGURE 4.3.10b : Same as for Fig.[4.3.10a], only, this time, the mass distribution is calculated along an axis perpendicular to the major outflow axis and parallel to the outflow axis of the second, smaller scale, bipolar outflow (see Fig.[4.3.7]). As for the major outflow, the SE-NW oriented outflow studied here shows clear bipolarity with respect to the central outflow source, located at offset '0'. In conjunction with Fig.[4.3.10a], this figure proves the existence of at least two spatially independent bipolar outflows within the DR21 region that apparently emmanate from a common driving source.

From summation of the derived column densities at each position observed in the map the mass, momentum and bulk kinetic energy of outflow gas characteristic to each velocity component has been calculated. The total mass, momentum and kinetic energy in the outflow was then obtained by summing over the HIGH, INTERMEDIATE and LOW velocity components. The results of these calculations are given in Table[4.3.3], along with corresponding values specific to localized regions around the central outflow source and the high-velocity blue lobe. The lower limits correspond to optically thin emission with no correction for flow orientation, whilst the upper limits are derived assuming the line emission is optically thick with a velocity-dependent optical depth, as given in Table[4.3.2], and also assuming a flow orientation relative to the line-of-sight of 60^0; this latter correction has no effect on the derived mass of gas but increases the momentum by a factor of 2 and the kinetic energy by a factor of 4. As expected, the outflow mass is dominated by the low-velocity gas, whilst the kinetic energy in the outflow is more evenly distributed with velocity, having equal contributions from the INTERMEDIATE- and HIGH-velocity components. The total mass in outflow gas is approximately 2000 M_0, the total momentum in outflow gas is on the order of 4×10^{42} $gcms^{-1}$, and the total kinetic energy in the outflow is roughly 3×10^{48} erg. The central and western high-velocity peaks each contain ~ 10% of the overall mass, momentum and kinetic energy of the outflow gas.

TABLE 4.3.3 :

OUTFLOW PARAMETERS DERIVED FROM CO OBSERVATIONS

VELOCITY COMPONENT	MASS Mhvf (Mo)	MOMENTUM Phvf (gcms-1)	ENERGY Ehvf (erg)
BLUE LOBE			
high	1.7 - 5.5	7.2(39) - 4.5(40)	7.3(45) - 9.3(46)
inter	4.3 - 34	5.1(39) - 8.1(40)	1.6(45) - 4.9(46)
total	8.3 - 58	1.2(40) - 1.3(41)	8.7(45) - 1.5(47)
CENTRE			
high	1.3 - 4.1	5.3(39) - 3.3(40)	5.3(45) - 7.1(46)
inter	7.1 - 57	8.5(39) - 1.3(41)	2.5(45) - 8.1(46)
total	11 - 85	1.6(40) - 1.7(41)	8.1(45) - 1.5(47)
TOTAL			
high	32 - 100	1.3(41) - 8.0(41)	1.3(47) - 1.6(48)
inter	141 - 1127	1.7(41) - 2.7(42)	5.1(46) - 1.6(48)
total	272 - 2023	3.3(41) - 4.0(42)	1.9(47) - 3.3(48)

Calculated for : Tx(CO) = 40 K
[CO]/[H2] = 1(-4)

4.3.(f)

THE PHYSICAL PROPERTIES OF THE QUIESCENT GAS AS DERIVED FROM THE $C^{18}O$ OBSERVATIONS

Cold H_2, although being the dominant material component of molecular clouds in the Galaxy, is exceedingly difficult to observe (viz. Sec.[3.1]). Unfortunately, the strong vibrational H_2 line emission, as investigated in this work, is biased towards active regions of localized shock-excitation, hence, the physical parameters derived from the infrared H_2 lines are anomalous with respect to the ambient molecular cloud medium and cannot be used as a measure of the total H_2 column density. On the other hand, as shown in the preceeding sections, CO, the next most abundant molecular constituent of interstellar clouds, is readily detected in a wide range of environments by means of its millimeter-wave spectrum. Moreover, detailed studies have shown that a quantitative relationship exists between CO and H_2 column densities in a variety of Galactic structures (Liszt 1973; Dickman 1975; Dickman 1978; Elmegreen & Elmegreen 1979; Plambeck & Williams 1979).

As the emission of ^{12}CO is generally strongly saturated at typical molecular cloud densities (i.e. $n(H_2) > 10^3$ cm^{-3}), a determination of the column density of the quiescent gas component must rely on measurements of the ^{13}CO and $C^{18}O$ isotopes which, due to their lower abundances, are less prone to saturation. The constant of proportionality relating the abundance of CO to that of H_2 is poorly known and contributes a major source of error to this method. Dickman (1979), Langer et al. (1980), Wilson, Langer & Goldsmith (1981) and Ferking, Langer & Wilson (1982) have specifically addressed the problem of determining quantitatively the abundance of CO under different interstellar conditions from observations of the ^{13}CO and $C^{18}O$ isotopes. The hydrogen

column densities employed in these studies were derived from visual extinctions obtained using star counts.

Several problems are inherent in the determination of CO column densities from ^{13}CO measurements. The ^{13}CO emission may be saturated at moderate depth into a cloud (Wannier 1980 and Langer et al. 1980) and the relative abundance of ^{13}CO to ^{12}CO and $C^{18}O$ may be enhanced by chemical fractionation (Langer 1977, Langer et al. 1980 and Langer et al. 1984) and isotope selective photodestruction (Bally & Langer 1982). In contrast, the $C^{18}O$ isotopic species is not subject to such processes and thus provides the least ambiguous probe of the line-of-sight H_2 column density. In this section, observations of the $C^{18}O$ transition are therefore used to derive the best available estimate of the mean volume density, mass and line-of-sight optical extinction characteristic of the DR21 molecular cloud core.

The LTE column density of $C^{18}O$ is obtained under the following two important assumptions : (i) the molecules along the line-of-sight possess a uniform excitation temperature, which is common to all rotational levels of the CO molecule; and (ii) the J=1-0 excitation temperature of all the isotopic species are equal (and implicitly given by the kinetic temperature, T_k). As was shown in Sec.[4.3.e], the CO emission is usually optically thick under typical molecular cloud conditions. Consequently, a common excitation temperature, T_x, can be derived from the peak CO radiation tempertaure as follows

$$T_r^{12} = T_o^{12} \left[f_{12}(T_x) - f_{12}(T_b) \right] \qquad (4.3.10)$$

where, $T_o^{12} = (h\nu_{12})/k \approx 5.53$, $T_b = 2.7$ K and

$$f_{12}(T) = [\exp(T_O^{12}/T)-1]^{-1}$$

The ~~common~~ CO excitation temperature is therefore given by

$$T_X = 5.53\ [\ell n[1+5.53/(T_r^{12}+0.82)]]^{-1} \qquad (4.3.11)$$

Further noting that the $C^{18}O$ emission is optically thin (to be confirmed later), then the peak $C^{18}O$ radiation temperature is related to T_X and the line centre optical depth, τ_O^{18}, via

$$T_r^{18} = T_O^{18}\ [f_{18}(T_X)-f_{18}(2.7)]\ [1-\exp(-\tau_O^{18})] \qquad (4.3.12)$$

and thus, using $T_O^{18} = 5.27$, τ_O^{18} may be determined

$$\tau_O^{18} = -\ell n\{1-T_r^{18}/5.27[[\exp(5.27/T_X)-1]^{-1}-0.166]^{-1}\} \qquad (4.3.13)$$

Similarily, for ^{13}CO, $T_O^{13} = 5.29$, and τ_O^{13} is given by

$$\tau_O^{13} = -\ell n\{1-T_r^{13}/5.29[[\exp(5.29/T_X)-1]^{-1}-0.164]^{-1}\} \qquad (4.3.14)$$

Since, τ_O, is related to the column density, N, by

$$\int \tau_\nu\ d\nu \approx \tau_O\ \Delta V\ \nu/c$$

$$= \frac{8\ \pi^3\ \mu^2\ \nu}{3\ h\ c}\ \frac{N}{Z}\ [1-\exp(-T_O/T_X)] \qquad (4.3.15)$$

where, ΔV is the line full-width at half-intensity in velocity units, μ is the permanent dipole moment of the molecule (= 0.1098 debye), and Z is the

partition function, one obtains

$$N = \frac{3\ h\ \Delta V}{8\ \pi^3\ \mu^2}\ \frac{\tau_O\ Z}{[\,1-\exp(T_O/T_X)\,]} \qquad (4.3.16)$$

As was discussed previously in Sec.[4.2.(g)], the rotational partition function can be estimated using the rigid linear-rotator approximation, with $T_X(J) = T_X$, giving

$$Z = 2(T_X/T_O) \qquad (4.3.17)$$

Substitution of this approximation into eqn.(4.3.16), results in the following LTE expressions for the iosotopic column densities

$$N_{18} = 2.39\times10^{14}\ \Delta V_{18}\ \tau_O^{18}\ T_X\ [\,1-\exp(-5.27/T_X)\,]^{-1}\ \ cm^{-2} \qquad (4.3.18)$$

and

$$N_{13} = 2.39\times10^{14}\ \Delta V_{13}\ \tau_O^{13}\ T_X\ [\,1-\exp(-5.29/T_X)\,]^{-1}\ \ cm^{-2} \qquad (4.3.19)$$

Nine $C^{18}O$ spectra have been measured over a 30 arcsec radius centred on the DR21 cloud core, which is also the nominal location of the high-velocity CO outflow source. The mean radiation temperature and full-width at half-maximum of these spectra are, $T_I^{18} = 4.0$ K and $\Delta V_{18} = 3\ kms^{-1}$, respectively. Furthermore, from the peak CO radiation temperatures, measured from spectra taken at the same positions, a characteristic excitation temperature, $T_X = 40$ K, is assumed. For these observed line parameters, a line centre

optical depth, $\tau_0^{18} = 0.13$, and $C^{18}O$ column density, $N_{18} = 3.1\times10^{16}$ cm^{-2}, are derived. To transform the isotope column density to a more informative H_2 column density, knowledge of the $C^{18}O$ relative abundance is required. From the numerous studies cited previously, the relative abundancies, $[^{12}CO]/[H_2] = 10^{-4}$, $[^{12}C]/[^{13}C] = 89$ and $[^{16}O]/[^{18}O] = 490$ are adopted. The total H_2 column density is then given by

$$N(H_2) = 5\times10^6 \, N_{18} \approx 1.5\times10^{23} \quad cm^{-2}$$

The mean H_2 number density over the central 1 arcmin (= 1 pc) is then

$$n(H_2) = 5\times10^4/L \quad (cm^{-3}/pc)$$

where, L is the line-of-sight distance through the cloud core in pc. This mean number density agrees favourably with other independent estimates derived from the 1-mm continuum emission from associated dust grains (= 5×10^4 cm^{-3}, Werner et al. 1975) and from the collisional excitation of the high-dipole-moment HCN molecule (> 10^4 cm^{-3}, Morris et al. 1974). Having determined the H_2 column density, the mass of the DR21 cloud core mass is then calculated from

$$M_{core} = 5\times10^6 \, N_{18} \, \mu_g \, m(H_2) \, \pi \, (r_c)^2 \qquad (4.3.20)$$

where, $m(H_2)$ is the mass of the H_2 molecule, μ_g is the mean atomic weight of the gas ($\mu_g = 1.36$) and r_c is the core radius. Expressed in astrophysical units, M_{core} is given by

$$M_{core} = 8000 \, (r_c/1pc)^2 \, M_0$$

Thus, taking a core radius of 0.5-1.0 pc (≅ 30-60 arcsec), a best estimate for the mass of the DR21 cloud core is, M_{core} = 2000-8000 M_0.

To investigate the dyanamical equilibrium of the DR21 cloud core (ie. whether stable or unstable to gravitational collapse) a comparison of the core mass as derived from the $C^{18}O$ observations with the virial mass may prove useful. The kinetic energy (including thermal and turbulent motions) and the gravitational potential energy are respectively, $(M_{core})\Delta V^2/2$ (where, ΔV is the FWHM of the $C^{18}O$ profile) and $-2G(M_{core})^2/r_c$. Equating the kinetic and gravitational energies results in the condition

$$M_{vir} \approx (\Delta V^2 . r_c)/G$$

$$= 230 \ [\Delta V/kms^{-1}]^2 \ (r_c/pc) \ M_0 \qquad (4.3.21)$$

Taking the observed FWHM, ΔV = 3 kms^{-1}, and again assuming a core radius, r_c = 0.5-1.0 pc, a virial core mass, M_{vir} = 1100-2100 M_0, is derived. Therefore, within the observational and associated errors, $M_{core} > M_{vir}$, and it appears that the dense cloud core is most probably gravitationally bound. Of course, a proper analysis should also take into account the presence of internal magnetic pressure, which, if suitably large, can act as an additional resistive component against gravity, thus increasing M_{vir}.

Finally, the $C^{18}O$ observations can also be used to estimate the line-of-sight visual extinction through the DR21 cloud core, using the empirically determined quantitative relationship (i.e. Dickman 1978)

$$N(H_2) \approx 10^{21} \ (A_V/mag) \ \ cm^{-2} \qquad (4.3.22)$$

Inserting the derived column density, $N(H_2) = 1.5\times10^{23}$ cm^{-2}, results in a value for the visual extinciton through the cloud core of, $A_V \approx 150$ mag. This large extinction helps explain why the central 1 arcmin of the DR21 cloud core is totally opaque in the visual and near-infrared, even out to 20 μm, and is a stong emitter in the millimeter continuum.

4.3.(g) H53α HYDROGEN RECOMBINATION LINE EMISSION

Spectra of the H53α recombination line of hydrogen (42.951687 GHz) were measured with a 36 arcsec beam at 15 arcsec spacing over a 1 arcmin radius centred on the high-velocity outflow centre. A mosaic of these spectra is illustrated in Fig.[4.3.11]. The centroid of the recombination line emission, presumably also the centre of the DR21 compact HII region, is offset from the CO high-velocity outflow origin by ~ 15 arcsec to the east; as the H53α and CO lines were measured simultaneously, this offest cannot result from pointing errors. The deconvolved radius of the ionized region is ~ 30 arcsec, in good accord with the 6 and 2 cm radio continuum distributions (Dickel et al. 1985). The H53α line has an emission centroid at $V_{lsr} = -2.5(\pm2.0)$ kms^{-1}, a total velocity extent, $\Delta V_t(FWZI) > 60$ kms^{-1}, and a full-width at half-maximum, $\Delta V(FWHM) = 42$ kms^{-1}. These line widths are considerably broader than expected for normal HII region expansion, in which case, if the lines were thermally broadened at $T_e \approx 10^4$ K, then $\Delta V_{th}(FWHM) \approx 0.215(T_e/m_p)^{1/2} = 21.5$ kms^{-1}, for a gaussian profile. It thus appears that some additional source of line broadening, other than pure thermal motion, is necessitated by these observations.

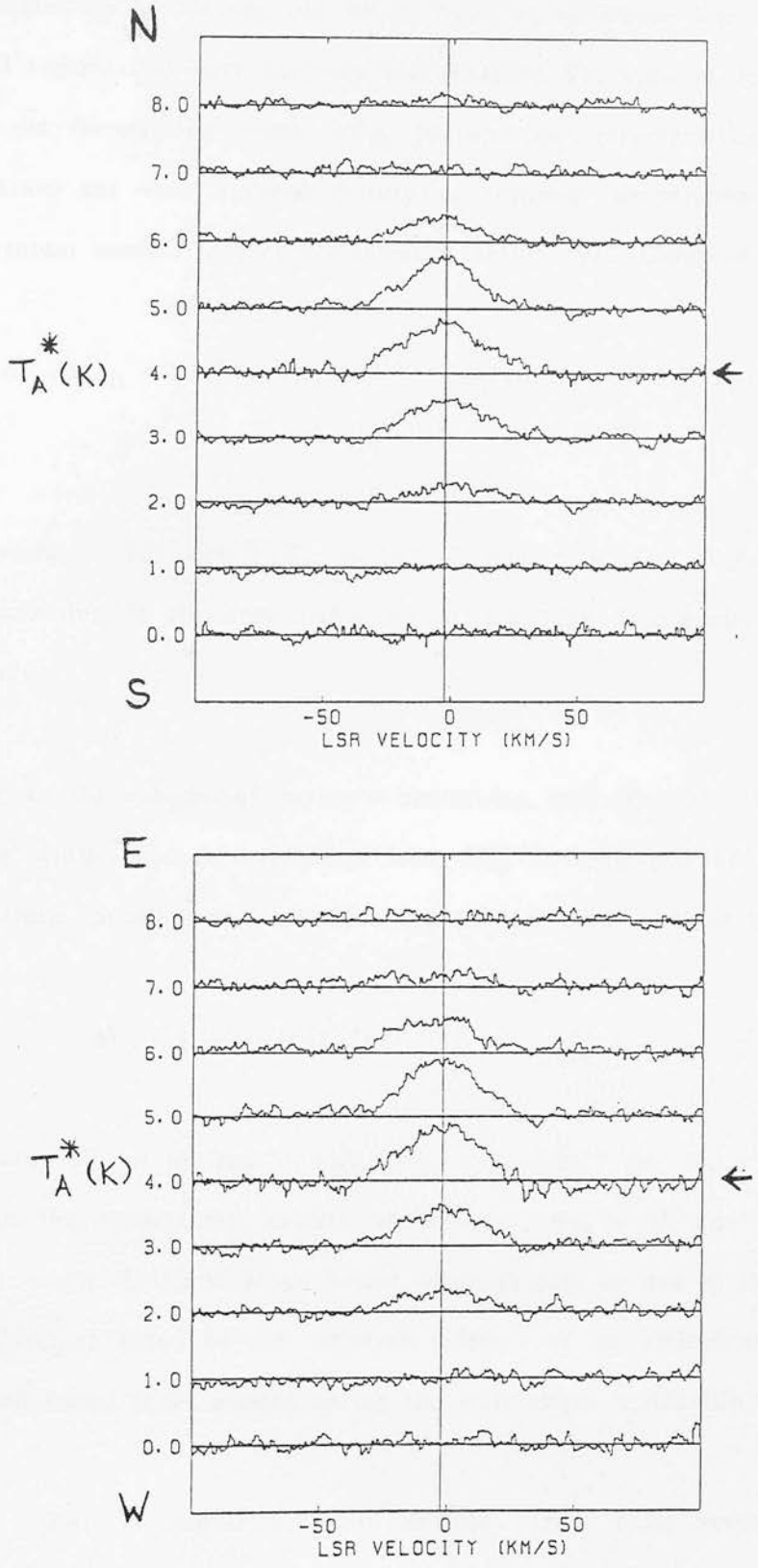

FIGURE 4.3.11 : H53α recombination-line profiles measured along a N-S and E-W axis centred on the DR21 high-velocity CO outflow source (arrow). The relatively strong and broad recombination emission comes from the DR21 HII region. The spacing between measurements is 15 arcsec and the beam-size is 36 arcsec.

Pressure broadening may affect radio recombination line profiles for compact HII regions that have high electron densities. The ratio of total line width, ΔV_t, to the thermal line width, ΔV_{th}, for hydrogen recombination lines arising from ionized gas with electron density n_e, electron temperature T_e, and principle quantum number n is (Brocklehurst & Seaton 1972; Garay et al. 1985)

$$\Delta V_t/\Delta V_{th} = \{1+[0.17(n/100)^{7.4}(n_e/10^4 cm^{-3})(10^4 K/T_e)^{0.1}]^2\}^{1/2} \quad (4.3.23)$$

For $n_e < 10^5$ cm^{-3}, $T_e \approx 10^4$ K and n = 53, $\Delta V_t/\Delta V_{th} \approx 1$. Pressure broadening is therefore negligible at the high frequencies concerned in this study.

In the absence of pressure broadening and non-LTE effects, the observed line width of a recombination line, ΔV_o, is comprised of thermal, ΔV_{th}, and intrinsic turbulent or macrosopic motions, ΔV_i, and is given by

$$\Delta V_o = [(\Delta V_{th})^2+(\Delta V_i)^2]^{1/2} \quad (4.3.24)$$

Using, ΔV_o = 42 kms^{-1} and ΔV_{th} = 20 kms^{-1} (ie. T_e = 8000 - 10000 K), then the macroscopic motions account for, $\Delta V_i \approx 35$ kms^{-1}, of the observed line width. This additional motion could in part be due to the expansion of the HII region aided by the outwards pressure of an ionized stellar wind, that is often found to be present during the early stages in the life of an O star.

Electron temperatures are obtained from radio recombination lines by measuring the ratio of the line and continuum optical depths. At frequencies

greater than a few hundred Mhz and at densities typical to those measured in compact HII regions, both the line and continuum will be optically thin, and the above ratio is obtained directly from the line and thermal continuum antenna temperatures, T_ℓ and T_c, respectively. The electron temperature can then be expressed as (Brown, Lockman & Knapp 1978)

$$T_e^* \approx [6.76\times10^3 \ \nu^{1.1} \ (\int T_\ell dv/T_c)^{-1}]^{0.89} \qquad (4.3.25)$$

where, ν, is the rest frequency of the line in GHz, T_e^* is the "LTE electron temperature" and the integrated line intensity is expressed in K-kms^{-1}. This equation is derived by assuming that the upper states of the hydrogen atoms are in LTE with the free electrons in the nebula. The deviations of the level population from LTE can be calculated (Brocklehurst 1972) and, for the range of electron densities and temperatures expected to prevail within the DR21 compact HII region (i.e. $8000 < T_e < 10000$ K and $10^3 < n_e < 10^5$ cm^{-3}), differ from the LTE values by only a few percent. In HII regions of high emission-measure, non-LTE effects can result in significant stimulated emission which causes an increased line intensity and hence a considerable underestimate of the electron temperature. The value of T_e^* derived using eqn.(4.3.25) must therefore be regarded as a probable lower limit to the intrinsic T_e.

From the observed spectra, a line-to-continuum ratio of 0.40 is obtained, which at the line frequency of H53α (= 42.951687 GHz), gives as a tentative estimate, $T_e^* \approx 8090$ K. This value is comparable to that derived for other compact HII regions (Garay et al. 1985).

If, as is suggested by the anomalously broad radio recombination lines, a compact, ionized stellar wind is associated with the driving source of the

high-velocity molecular flows observed in vibrational H_2 and rotational CO line emission, then it is improbable that observations of the infrared Brackett lines will provide further information as the large line-of-sight extinction to the cloud core will totally extinguish the line photons at wavelengths below 5 μm. Further development in this field, therefore, depends solely on the aquisition of high-angular resolution continuum and recombination-line data at millimeter and radio wavelengths.

4.4 OBSERVATIONS OF ROTATIONAL CS LINE EMISSION

4.4.(a) INTRODUCTION TO THE CS OBSERVATIONS

Emission from interstellar CS is well suited as a probe of the density of molecular cloud cores because several transitions are easily accessible to observations and the physical nature of this molecule make it easy to excite at densities ($n > 10^4$ cm^{-3}) characteristic of a wide variety of molecular cloud environments. Though the first few rotational levels of CS are excited at low temperatures, the large dipole moment (20 times larger than CO) makes CS more sensitive than CO to density variations. In light of this specific advantage, and with the intent of investigating the physical and kinematic structure of the dense gas in and around the DR21 outflow region, extensive mapping of the $C^{32}S$ J=1-0, $C^{34}S$ J=1-0 and $C^{32}S$ J=2-1 millimeter-wave line emission over an area on the sky encompassing both the DR21 cloud and its northern companion, W75S, has been undertaken.

Previous observations (Bally 1982; Thronson & Lada 1984; Kawabe et al. 1984; Kaifu et al. 1986, and other papers in IAU Symposium No.115), have clearly proven the effectiveness of the CS molecule as a tracer of both the dense components of high-velocity molecular outflows and the circum/interstellar discs thought to be responsible for their collimation. The existence of a massive, rotating, magnetically threaded neutral disc is a common prediction that often comprises the fundamental framework underlying theoretical interpretations of the molecular outflow phenomenon. This is because the efficient conversion of disc angular momentum to directed outflow along the disc rotation axis is the only mechanism yet conceived which can adequately account for the phenomenal

momentum transfer rates derived from observations of high-velocity CO emission from a large and rapidly growing sample of molecular outflows. With this knowledge in hand, the CS observations presented here are used to investigate the importance of the role played by the dense gas associated with the DR21 cloud core for shaping the high-velocity outflows and for stimulating the super-luminous shocked H_2 line emission. The CS observations also aid in our understanding of the physical structure of the high-velocity outflow gas and even suggest plausible clues as to its origin and eventual fate.

4.4.(b)

THE OBSERVING METHOD EMPLOYED FOR THE CS OBSERVATIONS

The observations were made on April 20-23 1986 using the 45-m radio telescope of the Nobeyama Radio Observatory. At 49 Ghz, the measured FWHM beamwidth of the telescope is 36 arcsec and the main beam efficiency, η_B, is 0.53. The corresponding values at 98 Ghz are 20 arcsec and 0.44, respectively.

The spectral lines of $C^{32}S$(J=1-0, 48.99100 Ghz), $C^{34}S$(J=1-0, 48.20695 Ghz) and $C^{32}S$(J=2-1, 97.98107 Ghz) were observed simultaneously with the aid of a beam splitter and two independent receivers. An acousto-optical radiospectrometer (AOS) system, consisting of eight 2,048-channel high-resolution and eight 2,048-channel low-resolution arrays, was used as the backend. The frequency resolution of the high(low) AOS is 37(75) Khz, which corresponds to a velocity resolution of 0.23(0.5) kms^{-1} and 0.11(0.23) kms^{-1} at 49 and 98 Ghz, respectively.

The system noise temperatures experienced during these observations were typically 700-1000 K at 98 Ghz and 500-700 K at 49 Ghz.

4.4.(c) THE SPATIAL DISTRIBUTION OF CS LINE EMISSION

The spatial distribution of the peak antenna temperature and integrated intensity in the CS J=1-0 and J=2-1 transitions are shown in Figs.[4.4.1] & [4.4.2], respectively. The dense ($n(H_2) > 10^4$ cm^{-3}) molecular gas sampled by the CS emission is distributed along a narrow ridge extending north-south for more than 6 arcmin ($\cong$ 6 pc, at 3 kpc) with an average width (FWHM) of less than 1 arcmin ($\cong$ 1 pc). The ridge is clumpy and exhibits three prominent centres of enhanced CS antenna temperature. The southernmost condensation is associated with the DR21 molecular cloud, the map origin being located at the best estimated position for the source of the high-velocity CO outflow (viz. Sec.[4.3.c]). The central condensation is spatially coincident with the W75S(OH) maser source, there being no obvious CS emission associated with the W75S(IRS1) young-stellar object, which is the stronger 20 μm continuum and H_2 emission-line source of the two. The W75S(OH) cloud is considerably brighter in integrated CS emission than the main DR21 cloud core. The most northerly condensation is by far the weakest of the three clouds in CS emission and is spatially associated with an H_2O maser discovered by Canto et al. (1976) and Genzel & Downes (1977). The W75S(OH) and DR21 molecular clouds are displaced by a projected angular separation of 3 arcmin ($\cong$ 3 pc) and the W75S(H_2O) maser source lies a further 1 arcmin ($\cong$ 1 pc) to the north of W75S(OH).

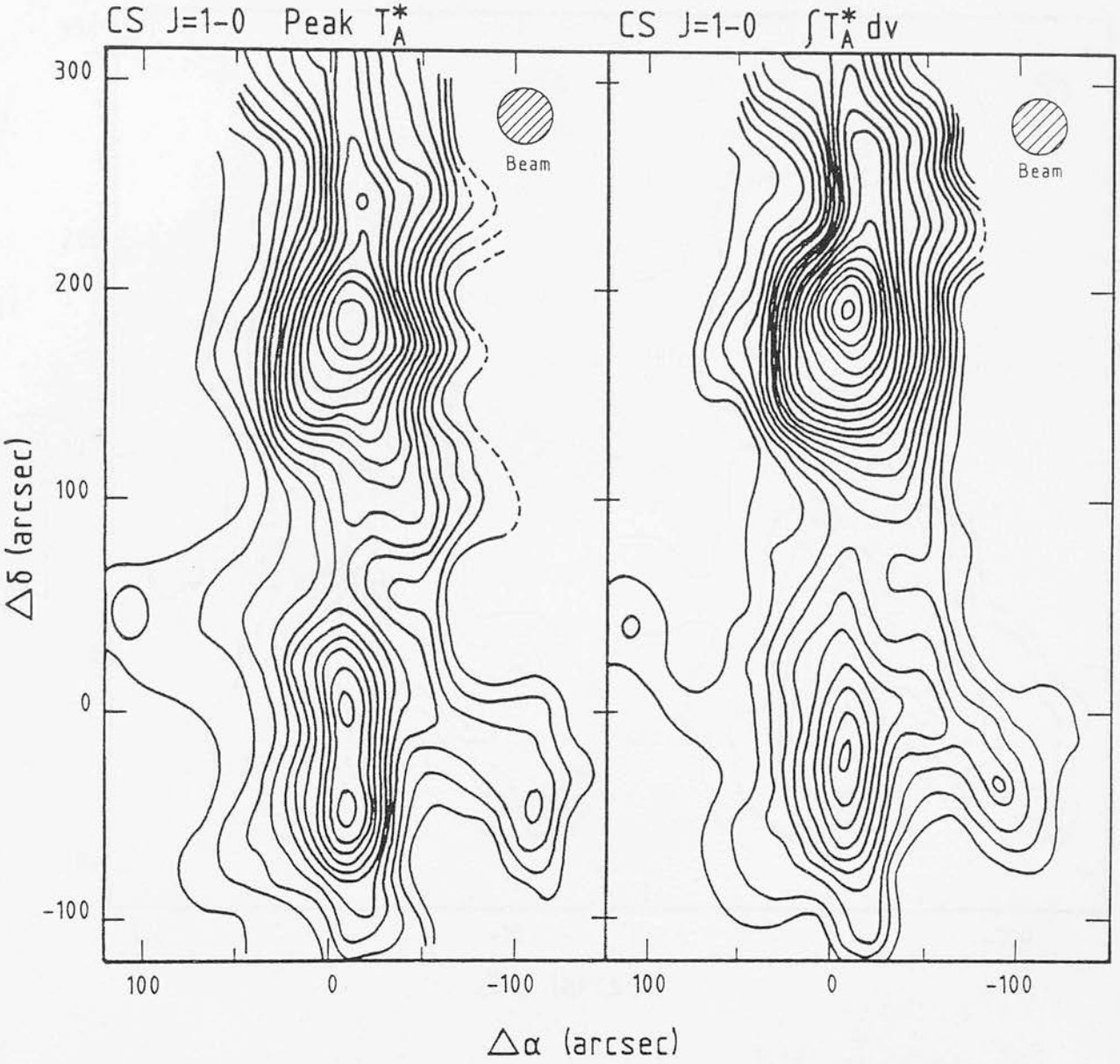

FIGURE 4.4.1 : (a) Contours of peak antenna temperature in the CS J=1-0 line over the DR21/W75S region. The beam size is 36 arcsec and the map origin is located at the position of the high-velocity CO outflow source in DR21. The lowest contour corresponds to 1K and the contour spacing is 0.5K. (b) Contours of integrated line intensity for the same region. The lowest contour corresponds to 5K-km/s and the contour spacing is 2K-km/s.

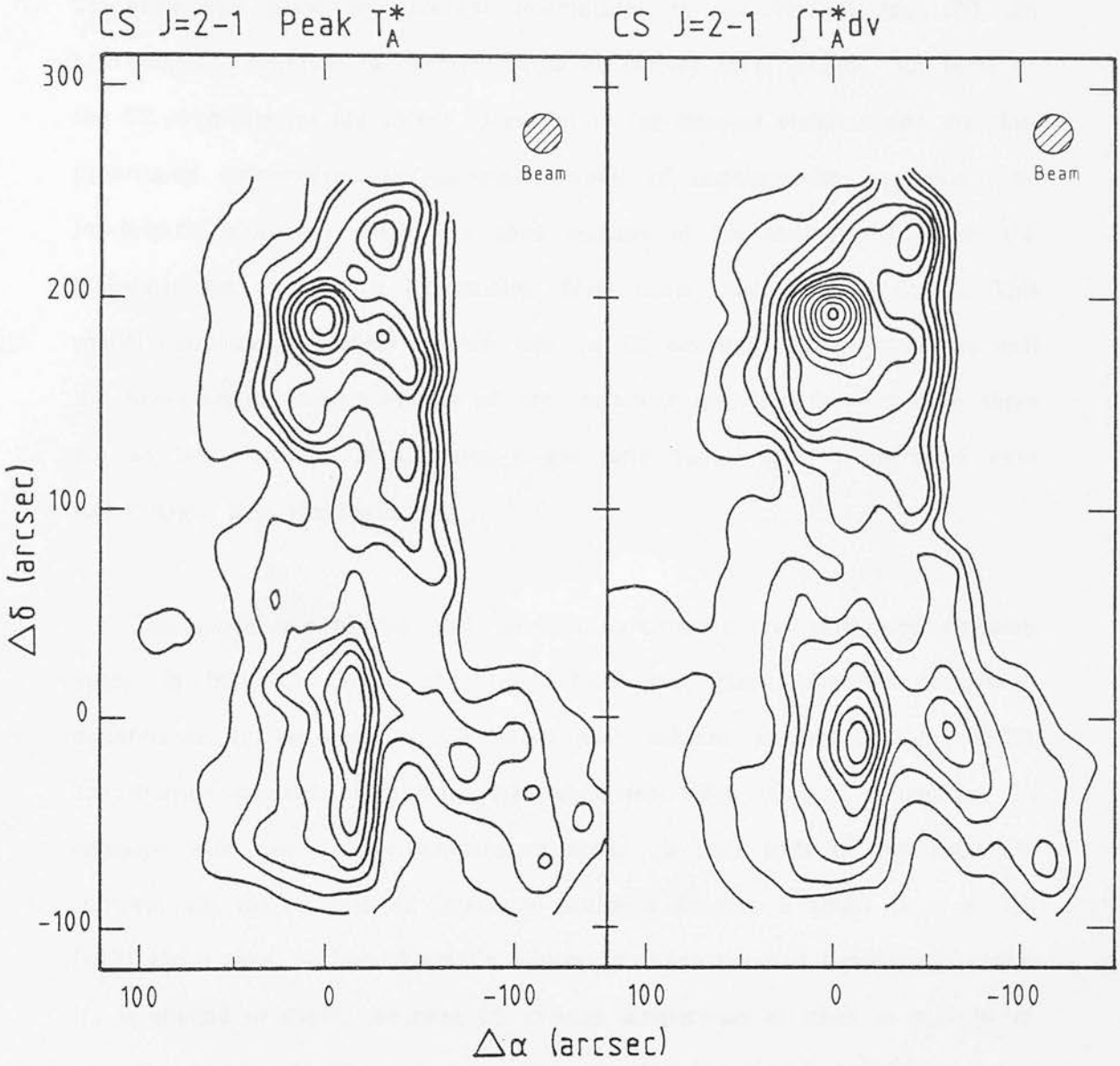

FIGURE 4.4.2 : (a) Contours of peak antenna temperature in the CS J=2-1 line over the DR21/W75S region. The J=2-1 transition was mapped simultaneously with the J=1-0 line, as shown in Fig.[4.4.1]. The beam size is 20 arcsec and the map origin is located at the position of the high-velocity CO outflow source in DR21. The lowest contour corresponds to 1 K and the contour spacing is 0.5 K. (b) Contours of integrated line intensity for the same region. The lowest contour corresponds to 3 K-km/s and the contour spacing is 2 K-km/s.

The spatial distribution of CS emission closely resembles the morphology of the 1-mm continuum (Werner et al. 1975) and HCN J=1-0 line emission (Morris et al. 1974), as illustrated in Fig.[5.1.1]. These relatively high-angular resolution CS maps also show an excellent resemblance to the 50 μm and 100 μm high-angular resolution far-infrared maps of Harvey et al. (1986). All three of the CS condensations are clearly identified in far-infrared emission and are thus presumably independent, self-luminous centres of ongoing star formation. The far-infrared emission, which is a good measure of the column density of the molecular gas, is well fit by emission from warm dust at T_d = 50 K. This spatial correlation therefore suggests that the CS emission similarily reflects well the line-of-sight column density of the molecular gas, that is, providing there are no large changes in the dust-to-gas ratio and/or dust temperature over scales larger than the beam size.

The appearance of the peak antenna temperature and integrated emission maps, in both CS J=1-0 and J=2-1 transitions, show important structural differencies. In the map of CS J=1-0 peak antenna temperature, the DR21 condensation consists of a thin, N-S elongated ridge of high brightness CS emission with two distinct temperature peaks, at both ends of the ridge. In contrast, the distribution of integrated emission exhibits a single peak at the DR21 cloud core, positioned exactly midway between the two temperature peaks. If, as alluded to above, the peak CS antenna temperature is taken as a probe of the gas column density and the integrated emission as an indicator of the overall profile width, then it appears that we may be viewing an almost edge-on disc of dense molecular gas with a high-velocity outflow located at its centre. Limb-brightening at the edges of the disc then gives rise to the double peaked structure observed in CS antenna temperature. Additionally, a steep radial density/temperature gradient in the disc plane may also help to generate

an apparent double-peak morphology due to self-absorption of the core emission by a lower-excitation foreground gas component. In CS J=2-1 emission, the peak antenna temperature map also shows a narrow ridge of elevated line temperature associated with the DR21 cloud core that is more structured and less centrally peaked than the distribution of integrated line emission. The CS J=1-0, and possibly also the J=2-1 observations, thus provide compelling evidence for the existence of a large and comparatively thin disc of neutral gas, oriented edge-on to the line of sight, and centred close to, but slightly offset to the south of, the proposed location of the DR21 high-velocity CO outflow source.

Another striking feature of these maps is the slender finger of bright CS emission emanating from the nothern part of the DR21 molecular disc and extending over 100 arcsec to the south-west. A corresponding north-eastern lobe is also present, and also extends to over 100 arcsec from the DR21 outflow centre, but is significantly less prominent than the south-eastern lobe. That these extended fingers of CS emission are real high-density extensions to the DR21 cloud core is confirmed by noting that a similar south-western filament is also observed in HCN J=1-0 emission (Morris et al. 1974), and that this molecule requires the presence of very dense gas ($n(H_2) > 10^5$ cm^{-3}) for collisional excitation. It is most likely that these peculiar filaments of dense gas are dynamically associated, in some broad sense, with the extended and extremely energetic bipolar outflow activity in the DR21 region, as outlined previously in shocked H_2 and high-velocity CO emission.

4.4.(d) THE VELOCITY DISTRIBUTION OF CS LINE EMISSION

In Figs.[4.4.3] & [4.4.4], a series of velocity-channel maps show the distribution of CS J=1-0 and J=2-1 line emission associated with the DR21 and W75S molecular clouds as a function of V_{lsr}, each adjacent map being spaced by 1 kms^{-1} intervals. In the J=1-0 transition, the W75S(OH) condensation dominates the CS emission at all velocities in the line profile and exhibits a peak in integrated emission over the velocity range, $-5 < V_{lsr} < -3$ kms^{-1}. The systemic velocity of the W75S(OH) cloud is therefore blue-shifted by 2 kms^{-1} relative to the DR21 cloud which exhibits a maximum in integrated CS line emission over the velocity range $-3 < V_{lsr} < -1$ kms^{-1}.

The bluewards shift in the peak velocity of the CS J=1-0 emission with increasing northwards displacement from the DR21 cloud core is perhaps better displayed by the position-velocity (PV) diagrams presented in Fig.[4.4.5]. Also revealed through these PV diagrams, is the presence of faint high-velocity wings associated with the DR21 molecular outflow (these are especially prominent in the J=2-1 emission) and also the presence of broad lines, with negligible wings, associated with the W75S(OH) source. The double peaked structure to the W75S cloud, in J=2-1 emission, results primarily from self-absorption of the background emission by lower-excitation foreground gas at $V_{lsr} = -2.5$ kms^{-1}. This foreground gas may be associated with the DR21 cloud, as it possesses a similar systemic velocity. The presence of self-absorption also explains why the peak line temperature of the CS J=2-1 transition associated with the W75S molecular cloud is significantly depressed relative to the J=1-0 (as will be shown later, the J=2-1 transition is always more optically thick than the J=1-0) and may also account for some of the complex structure seen in CS J=2-1 emission toward W75S at velocities close to the velocity of peak line reversal.

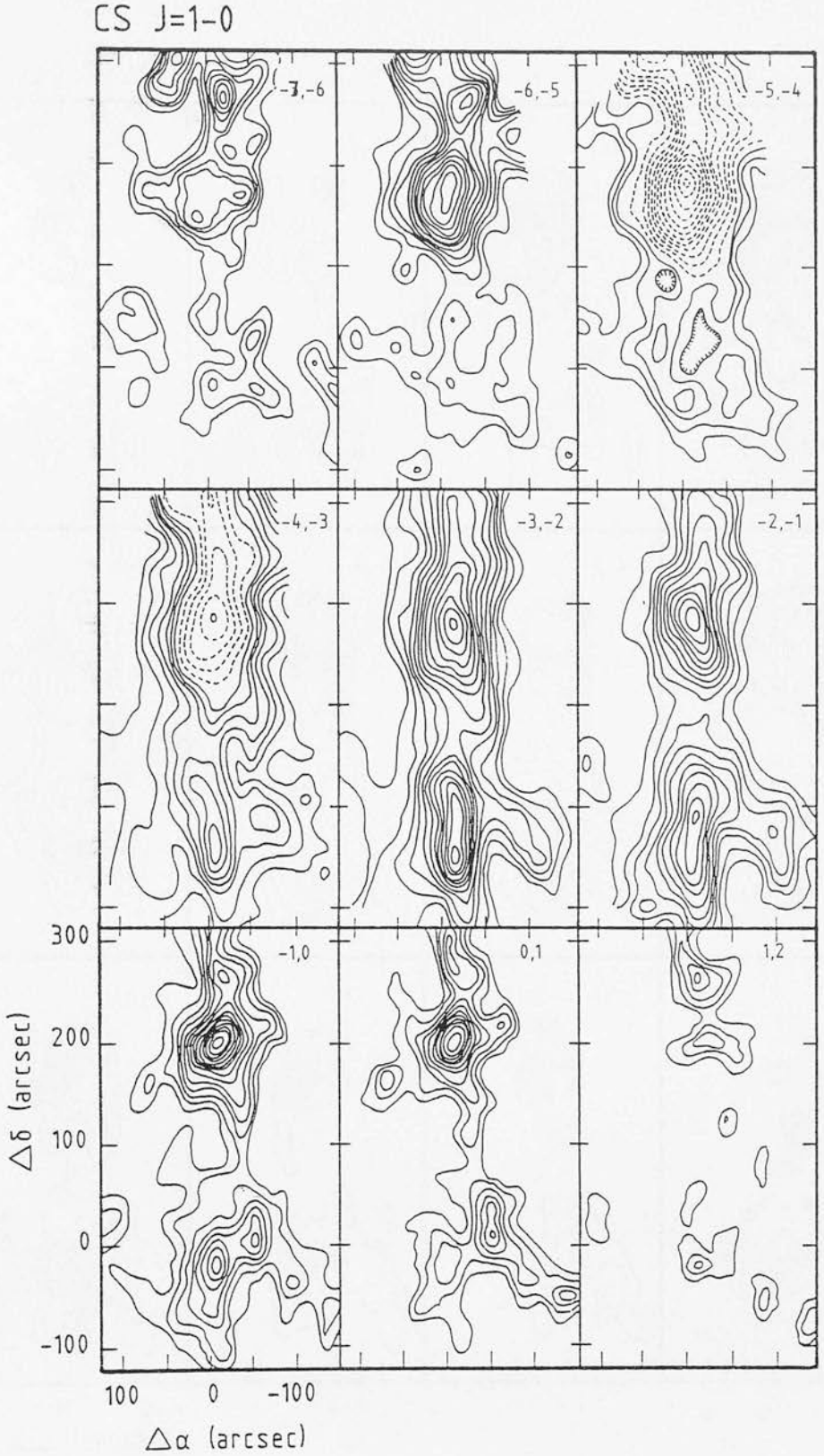

FIGURE 4.4.3 : A mosaic of velocity-channel maps in the CS J=1-0 line over the DR21/W75S region. The map origin is located at the position of the high-velocity CO outflow source in DR21. The beam size is 35 arcsec and the integration intervals are every 1 km/s, from -7 to +2 km/s. The dashed contours indicate that only every second contour is plotted.

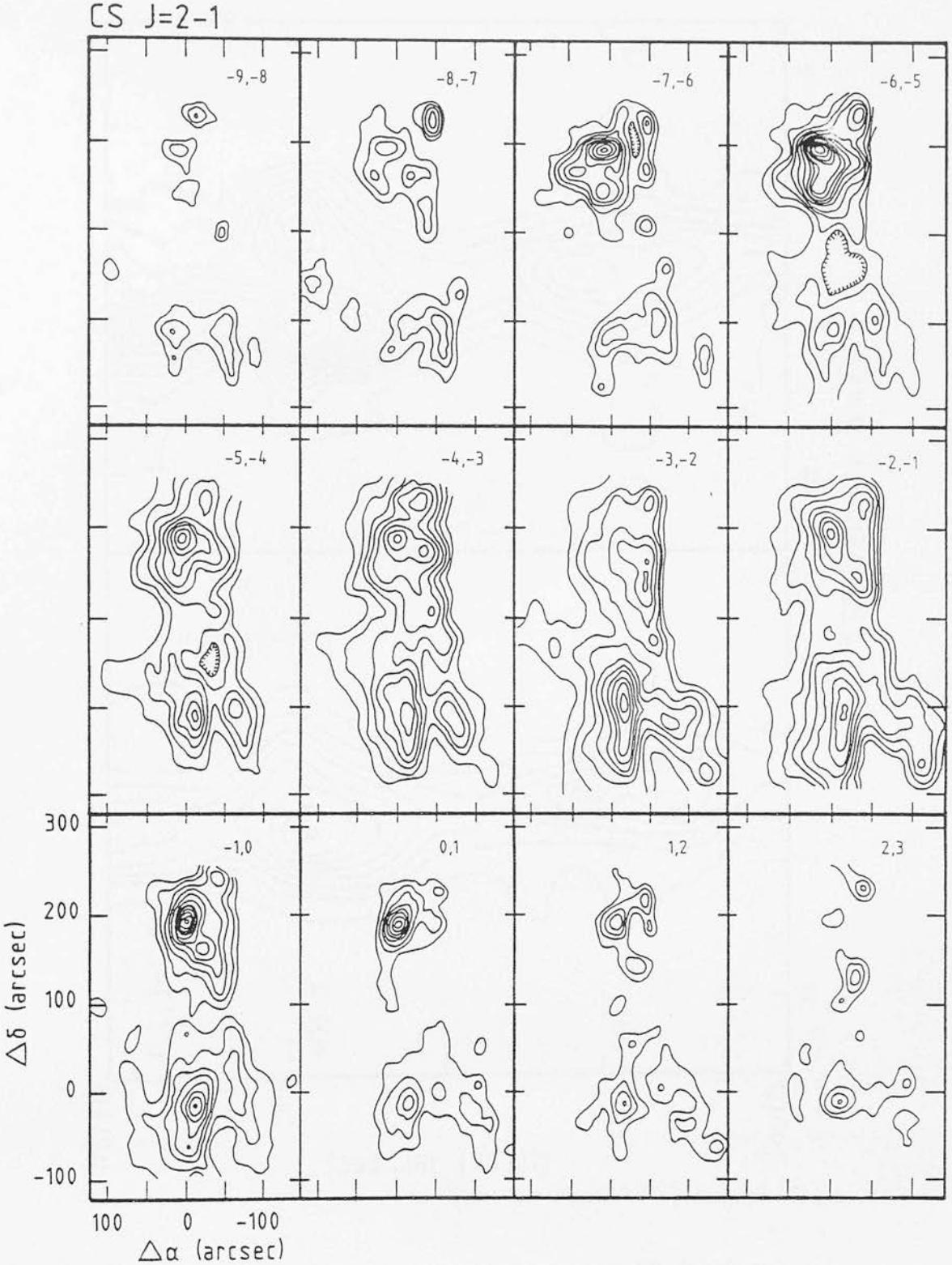

FIGURE 4.4.4 : A mosaic of velocity-channel maps in the CS J=2-1 line over the DR21/W75S region. The map origin is located at the position of the high-velocity CO outflow source in DR21. The beam size is 20 arcsec and the integration interval is 1 km/s, from -9 to +3 km/s.

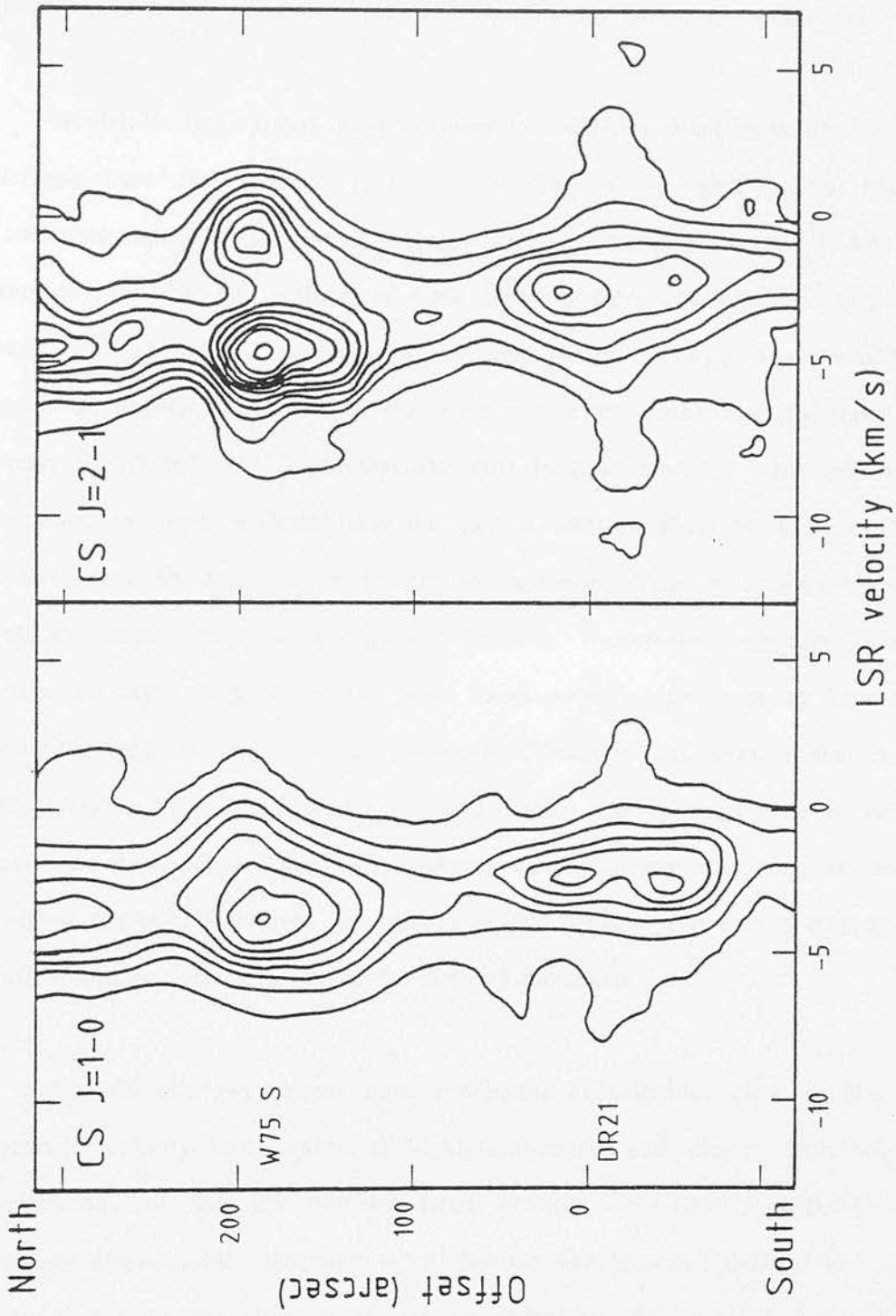

FIGURE 4.4.5 : Position-velocity plots in the CS J=1-0 and 2-1 lines along a north-south cut through both the DR21 and W75S cloud cores. The lowest contour for both plots is 0.5 K. The contour spacing for the J=1-0 and 2-1 plots are 1.0 and 0.6 K, respectively.

The CS line emission originating from the molecular ridge that connects the DR21 and W75S molecular complexes is characterized by narrow lines, thus indicating that the molecular ridge is a dynamically quiescent component.

The DR21 disc appears most prominent in CS J=1-0 emission and is clearly defined over the velocity range, $-4 < V_{lsr} < -1$ kms^{-1}. An extremely interesting aspect of the J=1-0 velocity-channel maps shown in Fig.[4.4.3] is the apparent shift in the position of peak emission from south of the disc centre, at $V_{lsr} = -3$ kms^{-1}, to north of the disc centre, at $V_{lsr} = -1$ kms^{-1}. The projected angular separation of the north and south peaks is approximately 100 arcsec ($\cong$ 1.5 pc). This south-to-north shift in peak emission with velocity may be taken as direct evidence that the disc is rotating about an axis through its centre with an approximate velocity of rotation, $V_{rot} \approx 1$ kms^{-1}. As the velocity displacement from $V_{lsr} = -2.5$ kms^{-1} increases, the disc gradually looses its rigid N-S composure and warps over to the east at blue-shifted velocities and to the west at red-shifted velcities. At even higher velocity displacements the disc merges smoothly with the primarily E-W oriented, high-velocity outflow lobes. The velocity-channel maps thus suggest that the outflow gas originates from the surface of the rotating disc and is then focussed further out to form two oppositely directed molecular jets.

The CS outflows appear most prominent at velocities close to the DR21 systemic velocity and exhibit a highly-collimated and clumpy structure. The morphology of the CS outflow lobes changes dramatically with increasing velocity displacement, becoming more clumped and less-well defined at velocities associated with the line wings. At all velocities, however, the extended CS emission from the outflow lobes is anomalously bright and exhibits a high contrast relative to the surrounding ambient cloud emission. An analysis of the

various physical processes that may be responsible for generating enhanced CS emission within the outflow is deferred till later (Sec.[5.5]).

PV plots along an E-W direction, parallel to the outflow axis, and bisecting the central high-velocity CO outflow source, are presented in Fig.[4.4.6]. In these plots the central outflow source and western ouflow lobe are clearly revealed, the first characterised by both blue- and red-wing emission, the second by blue-wing emission only. The strong blue-shifted emission associated with the western outflow lobe bears a strong resemblance to the CO and H_2 line profiles observed at this position, thus providing further confirmation for a physical association of the high-velocity CS emission with the outflow gas. Another interesting kinematic feature unveiled by the E-W PV diagrams is the sudden shift in line centre velocity at the western outflow lobe. This velocity jump is particularily evident in J=1-0 emission and may represent the inner boundary of a slowly expanding shell of dense gas swept up by the outflow. Such sharp velocity shifts are a common characteristic of ionization and shock fronts where the post-shock gas is compressed to form a thin shell of dense material moving at a slightly different velocity than the ambient cloud (Omodaka, Hayashi & Hasegawa 1984 & 1985).

4.4.(e) THE COLUMN DENSITY AND MASS OF HIGH-VELOCITY CS GAS

Using the $C^{32}S$ J=1-0, $C^{34}S$ J=1-0 and $C^{32}S$ J=2-1 data presented above, it is possible to derive an estimate for the mass of the dense component to the DR21 outflow via two relatively independent methods. One path available, is to use the main $C^{32}S$ J=1-0 and isotope $C^{34}S$ J=1-0 transitions to calculate the line optical depth and thence the total H_2 column density and mass, assuming

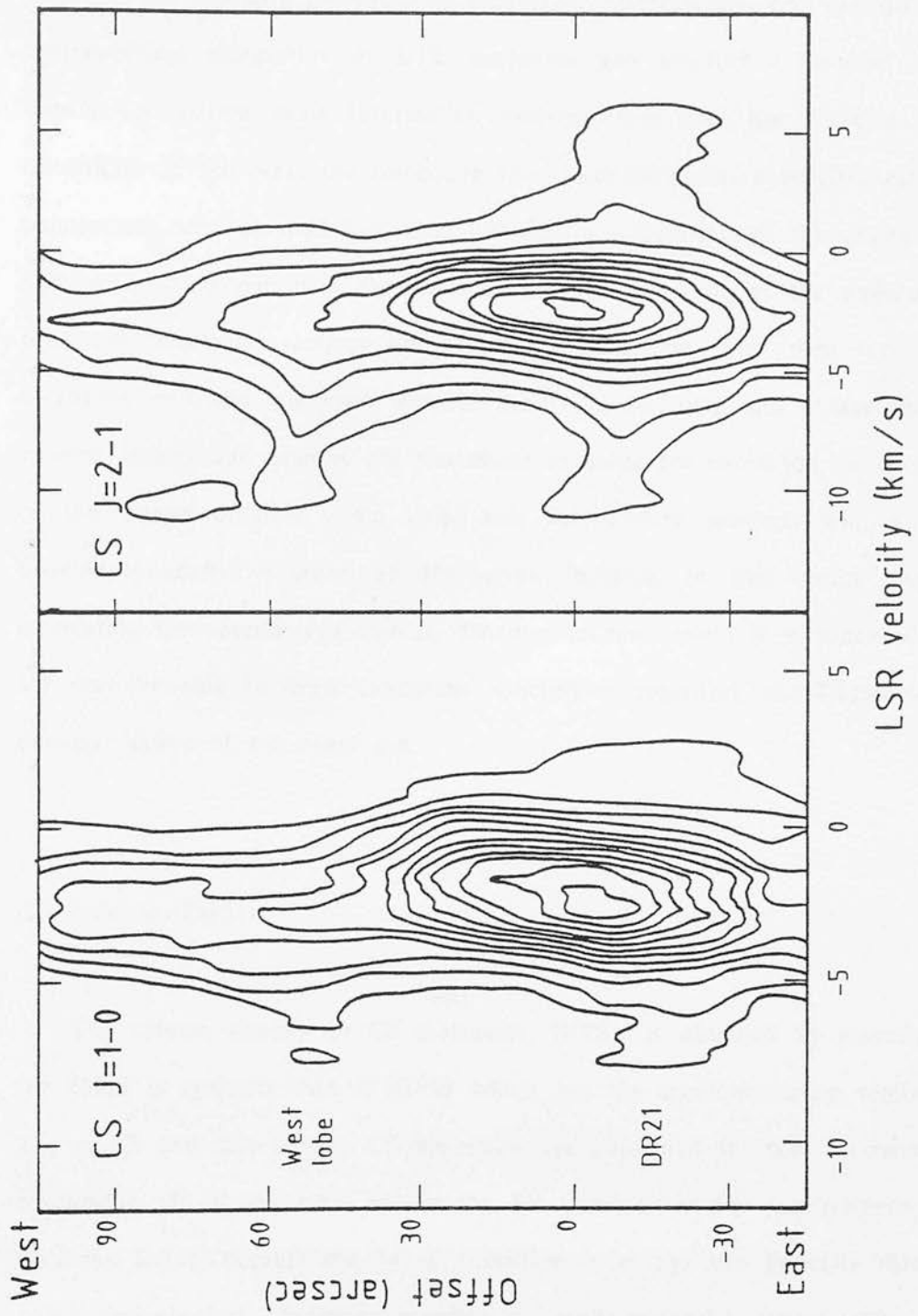

FIGURE 4.4.6 : Position-velocity plots in the CS J=1-0 and 2-1 lines along a east-west cut through the DR21 cloud core and bisecting the high-velocity, blue-shifted outflow lobe to the west. The lowest contour and the subsequent contour spacing is 0.5 K.

simple LTE conditions, an empirical H_2 to CS abundance ratio and a plausible geometry for the emitting gas. This method is identical to that employed for analysing the CO data presented in Sec.[4.3.e]. Alternatively, one can discard the oversimplified assumption of LTE excitation and conduct a detailed radiative transfer calculation using information derived from both the J=1-0 and J=2-1 transitions. In this way, the respective level populations, at a specific gas kinetic temperature, can be modelled, thus allowing a calculation of the optical depths and radiation temperatures characteristic to each transition of the molecule. The predicted radiation temperatures of each transition can then be directly compared with the observed spectra, therby constraining the characteristic gas volume density and relative CS abundance requisite for excitation. A comparison of the masses obtained from these two independent methods will, moreover, provide a useful estimate of the error involved in the results. Also, by calculating the volume and column densities independently, it is conceivable that we may be able to draw important conclusions regarding the fragmentary, or clumpy, nature of the dense gas.

(i) LTE METHOD

The column density in CS molecules, N(CS), is obtained by assuming that the cloud is optically thin in $C^{34}S$ which has the same excitation temperature, T_X, as CS and that all the CS molecules are populated in local thermodynamic equilibrium. It is preferable to use the J=1-0 transition for this purpose, rather than the J=2-1, because the J=1-0 transition is always less optically thick than J=2-1 for physical conditions common to most molecular clouds. Also, as no direct measurement of the $C^{34}S$ J=2-1 line was made, it is difficult to specify with absolute certainty the optical depth in this line, especially at low-velocity

displacements from the line core where the J=1-0 optical depth is measured to be substantial. The following analysis entails essentially the same steps as were outlined for the derivation of the high-velocity CO column density in Sec.[4.3.e].

In order to investigate possible variations in the physical properties of the gas emitting at different velocities in the observed line profile, the profile is segmented into three spectrally distinct portions, defined as follows:

LINE CORE : -4 to -1 kms-1

RED WING : -1 to +2 kms-1

BLUE WING : -7 to -4 kms-1

These velocity limits were chosen primarily to maximize the kinematic information inherent to the CS velocity-channel maps presented in Figs.[4.4.3] & [4.4.4]. In the following analysis, each of the above three velocity intervals are considered to be independent dynamical components.

The column density can be expressed in terms of the optical depth at line centre, τ_o, the profile velocity width at half-maximum, ΔV, and the partition function, Z, as follows (c.f. Sec.[4.3.f])

$$N = \frac{3\ h\ \Delta V}{8\ \pi^3\ \mu^2}\ \frac{\tau_o\ Z}{[\,1-\exp(-T_o/T_x)\,]} \qquad (4.4.1)$$

where, $Z = 2(T_x/T_o)$ and, for the CS J=1-0 transition, $T_o = h\nu_{10}/k = 2.35$. For the electric dipole moment of CS, the value, $\mu = 1.97$ debye, is taken as given by Mockler & Bird (1955). Eqn.(4.4.1) now becomes

$$N(CS) = 1.8\times10^{12} \frac{\Delta V\ T_X\ \tau_O}{[1-\exp(-2.35/T_X)]}\ cm^{-2} \qquad (4.4.2)$$

where, ΔV is expressed in kms^{-1}. Multiplying by the beam filling factor, f, as defined previously in eqn.(4.3.5), results in the following expression for the beam averaged column density

$$\bar{N}(CS) = 7.5\times10^{11} \frac{(T_X+0.4)}{\exp(-2.35/T_X)} \int \frac{T_a^*}{\eta_B} \frac{\tau_{10}}{[1-\exp(-\tau_{10})]}\ dv\ \ cm^{-2} \qquad (4.4.3)$$

Note that if the line is optically thin then the optical depth correction factor, $\tau_{10}/[1-\exp(-\tau_{10})] = 1$, otherwise, τ_{10} is obtained from the expression given previously in eqn.(4.3.4), taking in this case an abundance ratio of $[C^{32}S/C^{34}S] = 22.6$. As the optical depth correction factor can lead to a significant increase in the value of N(CS) if $\tau_{10} > 1$, it is vital that a good estimate of τ_{10} for each of the chosen velocity intervals be obtained. It was precisely for this puropose that simultaneous mapping in the $C^{32}S$ and $C^{34}S$ J=1-0 transitions was undertaken.

Due to the inherent faintness of the $C^{34}S$ isotope emission, in conjunction with the relatively short integration times employed for this study, it was possible to positively detect the isotope line from only a small portion of the area mapped, confined to a 1 arcmin diameter region centred on the DR21 outflow source (map offset 0,0). The position of strongest $C^{34}S$ J=1-0 emission is located 20 arcsec to the north of the outflow centre, at map offset (0,20), where a peak antenna-temperature ratio $T_a^*(C^{34}S)/T_a^*(C^{32}S) = 1/6$ is observed. Using eqn.(4.3.4), this ratio in turn implies a peak optical depth in the CS

J=1-0 transition of τ_{10} = 4 to 5. However, the average antenna temperature ratio, taken over the central 1 arcmin diameter region, $T_a^*(C^{34}S)/T_a^*(C^{32}S)$ = 1/10, is considereably less than observed at the (0,20) position and implies an average CS J=1-0 optical depth in the line core of τ_{10} = 2 to 3. Towards the extended CS emission associated with the DR21 shocked-outflow lobes, an upper limit, $T_a^*(C^{34}S)/T_a^*(C^{32}S) < 1/20$, is measured which is consistent with the terrestrial abundance ratio and clearly indicates that the extended CS J=1-0 emission is optically thin, even in the relatively strong line core. At the positions where the $C^{34}S$ isotope was detected, the line is narrow and does not appear to possess the wings that are so clearly evident in the $C^{32}S$ emission profiles. To assume that the high-velocity CS J=1-0 emission is optically thin over the entire area mapped is, therefore, regarded to be a relatively good approximation in this case.

Using the expression for N(CS) given in eqn.(4.4.3), it is then a straightforward process to calculate the total mass of gas for each velocity component in the line profile. The total mass of gas within one beam area is given by

$$M_{gas} = 4\times10^{-16} \; \bar{N}(CS) \left[\frac{X(CS)}{10^{-9}}\right]^{-1} \left[\frac{\theta}{\text{arcsec}}\right]^{2} \left[\frac{D}{\text{kpc}}\right]^{2} M_{\odot} \qquad (4.4.4)$$

where, θ is the FWHM beam size, in arcsec, D is the distance to the source, in kpc, and the mass of gas (hydrogen + helium), M_{gas}, is expressed in solar masses. To proceed with this line of analysis, it is necessary to specify values for the excitation temperature, T_X, and the CS abundance, $X(C^{32}S)$, relative to hydrogen. Noting the physical constraint that $T_X(CS) < T_X(CO)$, where $T_X(CO)$ = 40 K (viz. Sec.[4.3.e]), it will be assumed, for the moment, that $T_X(CS)$ = 20 K. It is worth noting, however, that as N(CS) and M_{gas} both scale linearly

with T_X, then any future alterations to this assumed value are easily encoprorated into the results. The uncertainty in the chosen value for T_X is expected to be of order ±10 K.

The abundance of CS and its variation in different molecular cloud environments is, like most other abundance determinations, poorly understood at present. The abundances quoted in the literature can differ by up to four orders of magnitude, from 10^{-8} to 10^{-12}, however, in a study of over 40 dark clouds Linke & Goldsmith (1980) find that values of X(CS) tend to lie mostly within the range 10^{-8} to 10^{-10}. In accordance with the Link & Goldsmith findings, a value, X(CS) = 10^{-9}, is assumed here to characterize the CS gas in the DR21 molecular cloud. These values for T_X and X(CS) are in good accord with those derived using the LVG model analysis, to be described in the second part of this section.

The kinematic features discussed in Sec.[4.4.d] can be associated with specific physical structures in the DR21 outflow system. In particular, it is suggested that (i) the optically-thick, low-velocity CS emission in the central parts of the DR21 cloud is associated with a massive neutral disc, (ii) the extended, optically-thin, low-velocity emission is associated with the compressed ambient gas swept up by the DR21 outflow and, (iii) the extended high-velocity red and blue emission arises from the outflow gas itself. These velocity components are titled the *disc*, *low-velocity outflow* and *high-velocity outflow*, respectively. The peak CS column density and total mass of gas characteristic to each velocity component, as derived from the LTE anlysis, are tabulated in Table[4.4.1]. The total mass of gas in the disc, low-velocity outflow, and high-velocity outflow are calculated to be on the order of 5.5×10^4, 10^4 and 1.5×10^4 M_0, respectively. It must be stressed, however, that these estimates may be in error by up to one

TABLE 4.4.1 :

CS J=1-0 'LTE' ANALYSIS

COMPONENT	τ_{1-0}	N(CS) cm-2 [1.]	M(H2) Mo [2.]
DISC	2	1.5(15)	5.5(4)
HIGH-VEL OUTFLOW	<< 1	3.3(14)	1.5(4)
LOW-VEL OUTFLOW	<< 1	2.5(14)	1.0(4)
W75 S	> 2	> 3.0(15)	> 1.5(5)

1 : Tx(CS) = 20 K
2 : [CS]/[H2] = 1(-9)

order of magnitude, primarily due to uncertainty in the CS abundance.

Although a direct measurement of the CS J=1-0 optical depth toward the W75S cloud is not available, on the bases of the DR21 analysis it is reasonable to anticipate that, $\tau_{10} > 2$. For this limit, a best estimate for the mass of the W75S cloud, $M_{gas} > 1.5 \times 10^5 M_0$, is derived, which is at least twice as large as the mass derived for the DR21 cloud core. This conclusion is clearly apparent in the velocity-channel maps in which the W75S source dominates the CS emission at most velocities in the profile.

The most striking aspect of these derived masses is that the mass of the DR21 molecular disc and high-velocity outflow are roughly comparable within the anticipated errors. The mass of the high-velocity outflow, as derived from the CS observations, is one order of magnitude higher than the mass derived from a similar analysis using the CO molecule ($\sim$ 2000 M_0, Sec.[4.3.e]). This discrepancy most probably reflects the fact that the CS emission is a better probe of the denser, slower-moving outflow gas whilst the CO emission arises primarily from the less-dense, faster-moving gas. The CS transition may thus be viewed as being a good tracer of the total outflow mass whilst CO is a better tracer of the bulk kinetic energy in the outflow. As will be discussed later, the significant difference in the mass estimates derived using the CS and CO emission brings to light a very important point, namely, that the density distribution of the gas may not be homogeneous. For example, if the outflow gas is composed mainly of dense ($n(H_2) > 10^5$ cm^{-3}) clumps then the CS emission facilitates a probe of the mass internal to these clumps, whilst the CO, due to its small dipole moment, is heavily biased as a probe of the mass in the more diffuse inter-clump medium.

If the characteristic outflow velocity in the dense gas is, $V_{hvf}(CS) = 5$ kms^{-1} (a generous estimate that is intended to partially account for the projection of the outflow axis relative to the line-of-sight), then, the outflow momentum is

$$P_{hvf}(CS) = 1.0 \times 10^{43} \quad g\ cm\ s^{-1}$$

and the bulk kinetic energy in the dense outflow gas is

$$E_{hvf}(CS) = 3.8 \times 10^{48} \quad erg$$

Furthermore, if the characteristic outflow age is 5×10^4 yr (viz. Table[5.5.1]), then this value for the kinetic energy corresponds to a mechanical luminosity in dense outflow gas , $L_m(CS) = 660\ L_0$, which is comparable to that calculated from the analogous analysis of the high-velocity CO emission (i.e. $L_m(CO) = 540\ L_0$).

(ii) LVG METHOD

As the CS molecule is primarily collisionally excited for typical conditions prevailent within dense molecular cloud cores, it is a relatively straightforward proceedure to calculate, under specific dynamical and physical conditions, the relative populations in each rotational energy level. The calculated distribution of level populations can then be used to predict the emergent intensities of various transitions which one would observe from a gas of excitation temperature as defined by the model. If more than one transition of a molecule is observed, then, it is possible to derive physical properties for the gas from a direct

comparison of the observed relative line intensities with those predicted by the model. The most commonly used radiative transfer code is one which employs the Sobolev Escape Probability Method as its basic framework and is usually termed the "Large Velocity Gradient" (LVG) model (Goldreich & Kwan 1974; Link & Goldsmith 1980; Snell, Langer & Ferking 1982).

Fundamental to the LVG approximation is the assumption that the doppler shifts between molecules located at different positions in the cloud are of sufficient magnitude that only local radiative transfer effects need be considered. Thus, different parts of the observed line profile are produced by essentially decoupled regions of the cloud. The association of a particular portion of the profile with a certain physical region of the moving source then depends primarily on the details of the assumed velocity field.

A simple LVG model was constructed to compute the excitation, and hence the predicted emission spectrum, as a function of CS relative abundance per velocity gradient, X(CS)/(dv/dr), gas kinetic temperature, T_k, and volume density, $n(H_2)$. The collisional excitation rate coefficients calculated by Green & Chapman (1978) for collisions with H_2 and a CS dipole moment of 1.97 debye (Mockler & Bird, 1955) were used and the level populations were solved numerically using the lowest 10 CS energy levels and assuming a velocity gradient, $V \propto r$. The results drived from this model are similar to those of Martin & Barrett (1978) and Link & Goldsmith (1980). Comparison of the LVG results with those of more complex microturbulent models (Snell 1980, White 1977) indicate that the excitation conditions are not very sensitive to the details of the radiative transfer. It is therefore conceivable that these simple LVG calculations may differ by no more than a factor of 3, or so, from the real values, even if the region is in turbulent rather than systematic motion.

As the exact value of the kinetic temperature is unknown, the LVG model was solved for the limiting kinetic temperatures, T_k = 10 and 40 K. The results are presented in Figs.[4.4.7a] & [4.4.7b], respectively, in the form of graphs that illustrate the dependence of $n(H_2)$ and $X(CS)/(dv/dr)$ on the value of $T_r(CS,J=2-1) \equiv T_{21}$, and the ratio $T_r(CS,J=2-1)/T_r(CS,J=1-0) \equiv R_{2/1}$. The upper limit of 40 K is derived from the peak radiation temperature observed in thermalized CO emission, which may represent the best available estimate of T_k. The velocity gradient, dv/dr, remains a free parameter in this model, a rough estimate of which may be derived from dividing the observed line width, $\Delta V_t(FWZI)$ = 20 kms^{-1}, by the physical dimensions of the emission region, r = 2 pc, resulting in the value, dv/dr = 10 $kms^{-1}pc^{-1}$. For the low-velocity emission in the line core a value, dv/dr = 1 $kms^{-1}pc^{-1}$, may be more appropriate.

A few general conclusions, regarding the excitation of CS, can be drawn from the model predictions, namely;

(a) Under conditions of low optical depth in the J=2-1 line (ie. $\tau_{21} < 1$), $R_{2/1}$ is a sensitive indicator of $n(H_2)$.

(b) For a given value of $X(CS)/(dv/dr)$ and $n(H_2)$, $R_{2/1}$ is a weak function of T_k, as long as $T_k > 10$ K.

(c) For weak lines with high optical depth, T_{21} and $R_{2/1}$ do not uniquely determine $n(H_2)$ and X(CS).

(d) In general, $R_{2/1}$ increases with increasing $n(H_2)$ and/or T_k and, decreases with increasing X(CS) and/or line optical depth.

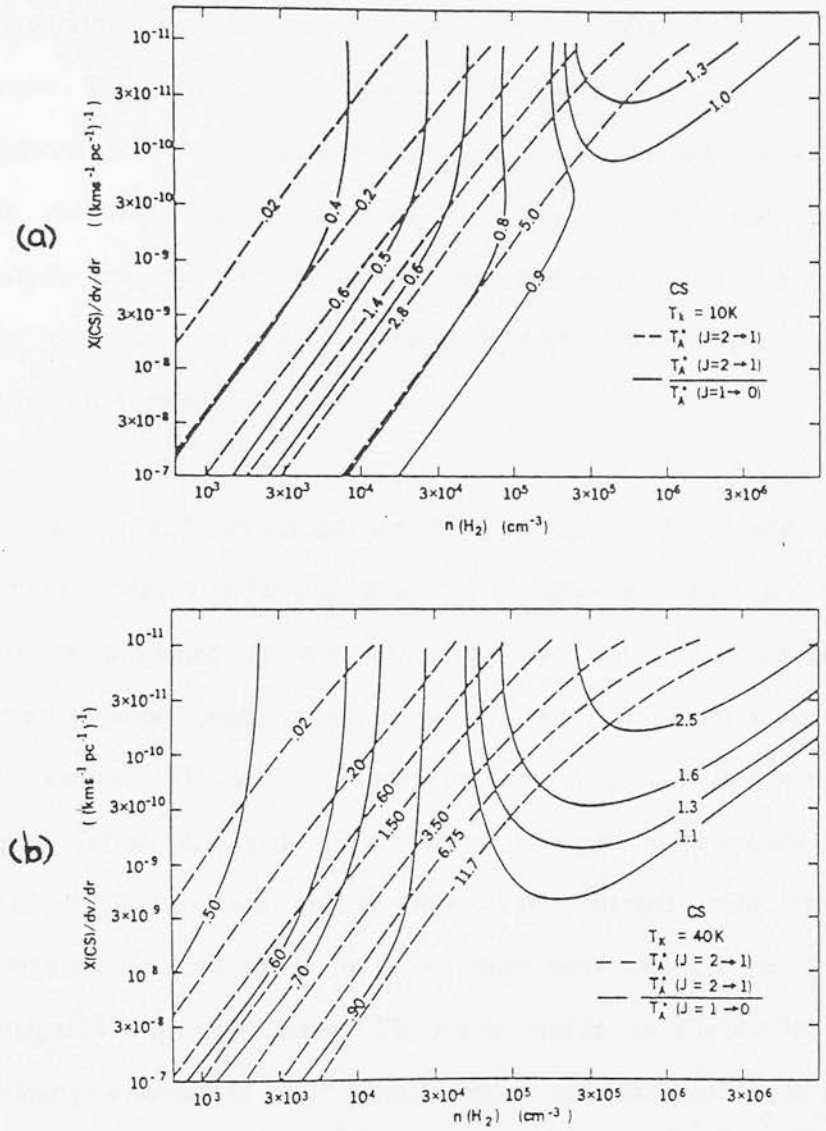

FIGURE 4.3.7 : Results of 10 level LVG radiative transfer model employing the rate coefficients of Green & Chapman (1978) (from Link & Goldsmith 1980). The LVG calculations described in this thesis are based on an identical transfer model; our results are therefore also determined by the above plots. The contours are of constant antenna temperature for the J=2-1 transition and of constant ratio of antenna temperatures. Plots are shown for the two limiting cases investigated in the text, namely, for gas at kinetic temperatures, Tk=10 K and 40 K.

The CS J=2-1 line emission will be preferentially enhanced, relative to the J=1-0 transition, in regions of the cloud where the volume density and temperature are highest and where the abundance and line optical depth are lowest. These physical requirements are most likely to be met within the dense, high-velocity, shock-heated outflow regions. It was thus the known sensitivity of the radiation temperature ratio, $R_{2/1}$, to different physical conditions that initially inspired the idea that simultaneous mapping of the CS J=2-1 & J=1-0 line emission over the DR21 high-velocity outflows would reap exciting and informative results.

Before a direct comparison between the CS J=1-0 and J=2-1 observations can be made, it is first necessary to convolve both emissions to the same beam size as projected on the sky. Fig.[4.4.8] shows a composite of nine high signal-to-noise spectra taken in the CS J=2-1 transition towards the location of the central CO outflow source; the central profile is positioned at the map origin (offset 0,0) and the others are arranged on a square grid of 20 arcsec spacing. These nine spectra have been merged with appropriate gaussian weighting to generate a 36 arcsec beam-convolved CS J=2-1 profile, which is compared with the central CS J=1-0 profile in Fig.[4.4.9]. In Fig.[4.4.10], a velocity-smoothed (1 kms^{-1} bins) version of these profiles is shown, along with the velocity dependence of the CS J=2-1/J=1-0 line-intensity ratio.

The CS J=2-1 profile exhibits prominent high-velocity wings which extend further and are considerably stronger than the corresponding high-velocity emission in the J=1-0 profile. Clearly, the CS J=2-1 transition is sampling a dense component of the high-velocity outflow. The variation of the intensity ratio with increasing displacement from the line core is particularily interesting;

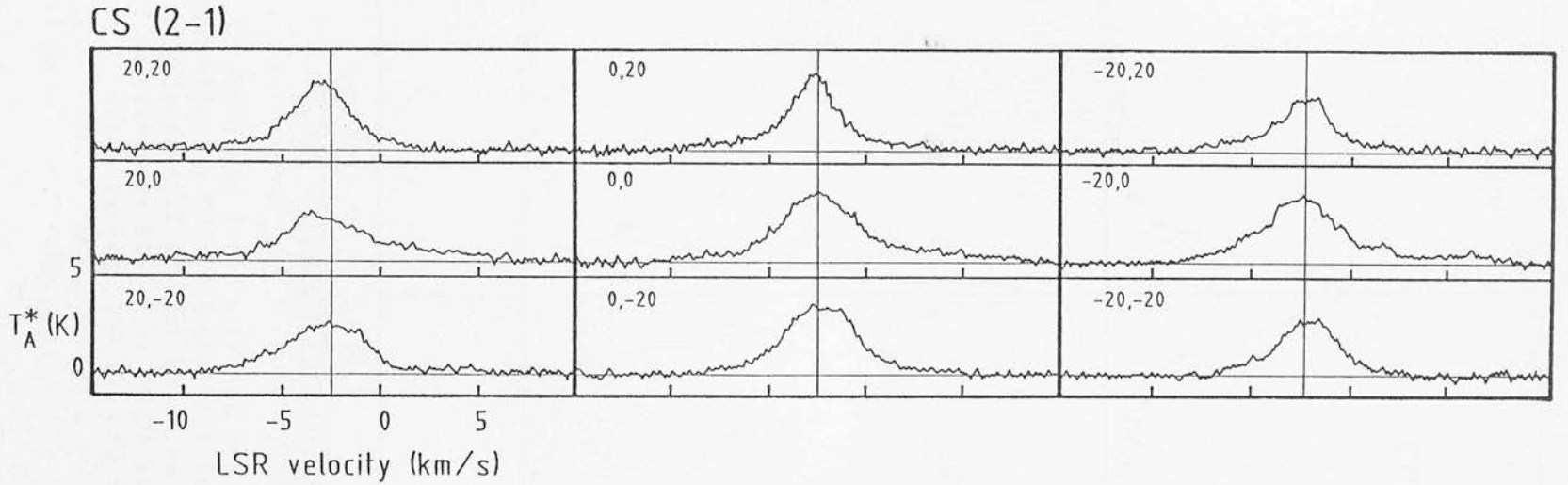

FIGURE 4.4.8 : A set of nine CS J=2-1 profiles measured on a square grid with 20 arcesc spacing centred on the position of the central high-velocity CO outflow source in DR21, which is also the position of peak integrated CS line emission. The beam size is 20 arcsec. The vertical line is positioned at -2.5 km/s and indicates the systemic velocity of the DR21 cloud.

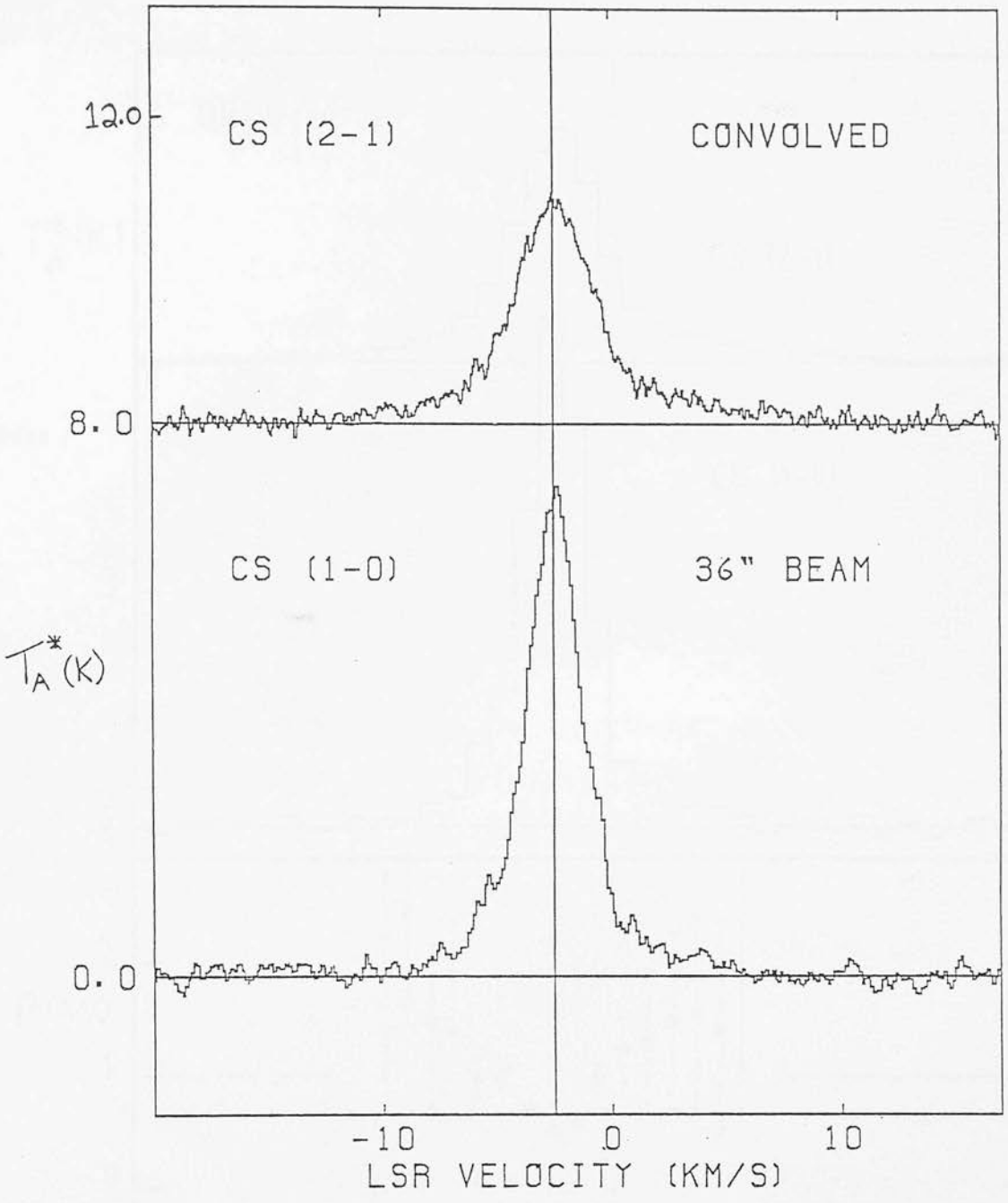

FIGURE 4.4.9 : CS J=2-1 and J=1-0 profiles measured at the location of the central high-velocity CO outflow source in DR21, which is also the position of peak integrated CS line emission. The 2-1 profile has been convolved to an effective beam size of 36 arcsec, using the nine individual spectra as shown in Fig.[4.4.8], and assuming a gaussian spread function. The velocity resolution is 0.1 km/s and 0.3 km/s for the 2-1 and 1-0 lines, respectively.

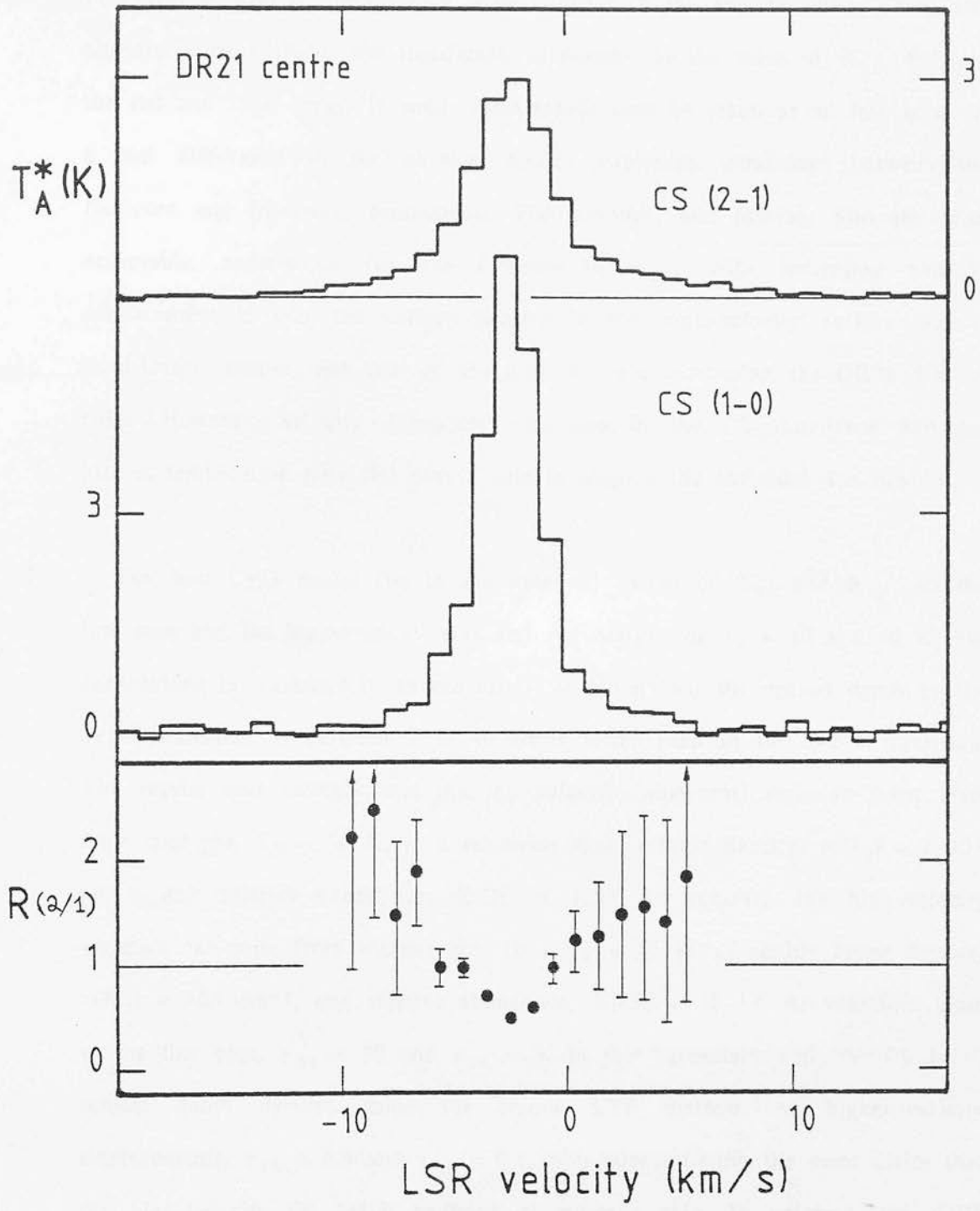

FIGURE 4.4.10 : A comparison of the CS J=2-1 and CS J=1-0 line profiles measured at the location of the high-velocity CO outflow source. Both profiles have been smoothed to a velocity resolution of 1 km/s. The lower plot shows the ratio of 2-1/1-0 integrated emission over the line profile in 1 km/s bins. The 2-1 profile is a gaussian convolution of nine individual spectra to give an effective beam size of 36 arcsec, comparable to the beam size at the CS J=1-0 frequency.

the value of $R_{2/1}$ increases monotonically from a lowest value of ~ 0.6 at velocities close to the DR21 systemic velocity (V_{lsr} = -2.5 kms^{-1}) to a value in excess of 2.0 in the far-blue wing and 1.5 in the far-red wing. There also appears to be a slight, but significant, asymmetry in the value of $R_{2/1}$ between the red and blue wings. In total, these trends may be taken as an indication of a real difference in the physical and/or excitation conditions between the line-core and line-wing components. The simplest, and possibly also the most acceptable, explanation for the increase in $R_{2/1}$ with increasing velocity displacement is that the volume density in the high-velocity outflow gas is significantly higher than that of the quiescent gas composing the DR21 disc or ridge. However, velocity dependent variations in the CS abundance and gas kinetic temperature may also play a role in shaping the individal line profiles.

The best LVG model fits to the observed values of T_{21} and $R_{2/1}$ in the line core and the high-velocity blue and red wings, for T_K = 10 and 40 K, are summarized in Table[4.4.2]. In general, it is found that the optical depth in the J=1-0 transition is between 3 to 10 times lower than in the J=2-1 transition. The results also indicate that the low-velocity (quiescent) emission must arise from cool gas, T_K = 10 K, at a relatively high volume density, $n(H_2) = 6\times10^5$ cm^{-3}, and relative abundance, $X(CS) = 10^{-9}$. In contrast, the high-velocity emission can arise from warmer gas, $10 < T_K < 40$ K, of slighly lower density, $n(H_2) = 10^5$ cm^{-3}, and relative abundance, $X(CS) = 10^{-10}$. At velocities close to the line core, $\tau_{21} > 30$ and $\tau_{10} \approx 8$, in fair agreement with the CS J=1-0 optical depth derived using the simple LTE method. At higher-velocity displacements, $\tau_{21} \approx 0.2$ and $\tau_{10} < 0.1$, thus substantiating the prior claim that the high-velocity CS J=1-0 emission is optically thin. In general, the LVG model returns a value for the excitation temperature of order, T_X = 10 K.

TABLE 4.4.2 :

RESULTS FROM 'LVG' ANALYSIS OF DR21 CENTRAL CS PROFILE

COMPONENT kms-1	T(2-1) K	R(2/1)	n(H2) cm-3 10K : 40K	X(CS) [1.] 10K : 40K	τ (2-1) 10K : 40K	τ (1-0) 10K : 40K
LINE CORE -3 to -2	6.8	0.7	6(5): *	1(-9): *	26 : *	8 : *
RED WING 2 to 6	1.1	1.5	3(5):8(4)	8(-11):2(-10)	0.3 : 0.2	<0.1 : <0.1
BLUE WING -6 to -10	1.2	2.0	1(6):1(5)	2(-11):1(-10)	0.2 : 0.1	<0.1 : <0.1

Tx = 8-10 K for all three velocity components.

1 : assume (dv/dr) = 1 kms-1pc-1 for LINE CORE
and = 10 kms-1pc-1 for WINGS

* : no fit was obtained for these input parameters.

So far, the LVG model has been used in only one dimension (velocity). However, as simultaneous maps in both the CS J=1-0 and J=2-1 transitions are available, it is possible to extend the analysis to three dimensions and thereby explore the variations in the physical conditions with both spatial and velocity displacement over the region mapped. This approach should lead to a considerable advance in our understanding of how the dense molecular gas is distributed and the role it plays in sustaining and collimating the high-velocity molecular outflows.

Figs.[4.4.11a,b,c] show contour maps of the CS J=2-1 and J=1-0 antenna temperatures and their ratio, $R_{2/1} \equiv [T_a^*(2\text{-}1)/T_a^*(1\text{-}0)][\eta_B(1\text{-}0)/\eta_B(2\text{-}1)]$, for the three velocity intervals; blue wing (-7 to -4 kms^{-1}), line core (-4 to -1 kms^{-1}) and red wing (-1 to 2 kms^{-1}). The CS J=2-1 antenna temperature maps are gaussian smoothed to an effective beam size of 36 arcsec, similar to the beam size measured at the frequency of the J=1-0 transition, and the map origin is the same as before (ie. centred on the best estimated position of the central CO outflow source). The morphology presented by each of the three velocity-channel maps is distinctly different. In particular, the $R_{2/1}$ ratio maps bring added contrast to several physical features that are poorly represented in the raw antenna temperature maps. The ratio maps are especially useful, because, as explained previously, if $\tau_{21} < 1$, the value of $R_{2/1}$ can be taken as a direct indicator of the volume density. Hence, in the simplest case, the ratio maps may give an immediate visual impression of the three-dimensional density structure over the region mapped, the higher the value of $R_{2/1}$ the higher being the density.

There are two important physical features highlighted in the $R_{2/1}$ ratio maps that are worthy of mention. The first feature is the high-velocity outflow

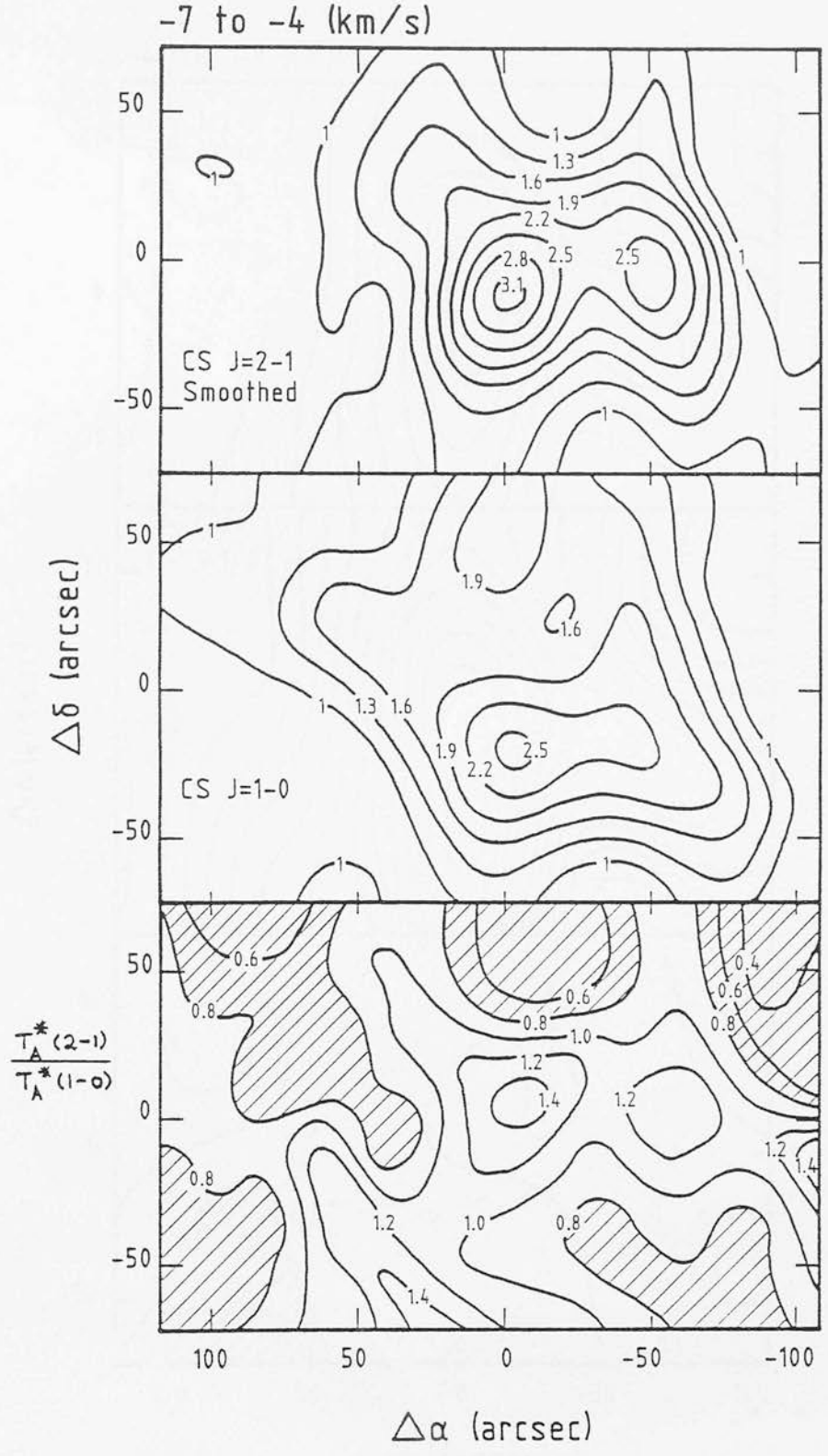

FIGURE 4.4.11a : Intensity contour maps in the CS J=1-0 and J=2-1 transitions for the velocity range, -7 to -4 km/s towards central high-velocity outflow region of the DR21 molecular cloud. The J=2-1 map has been gaussian smoothed to an effective resolution comparable to that of the J=1-0 map. The contours are numbered and are in units of K-km/s. The lower plot show the spatial distribution of the antenna temperature ratio, (2-1)/(1-0).

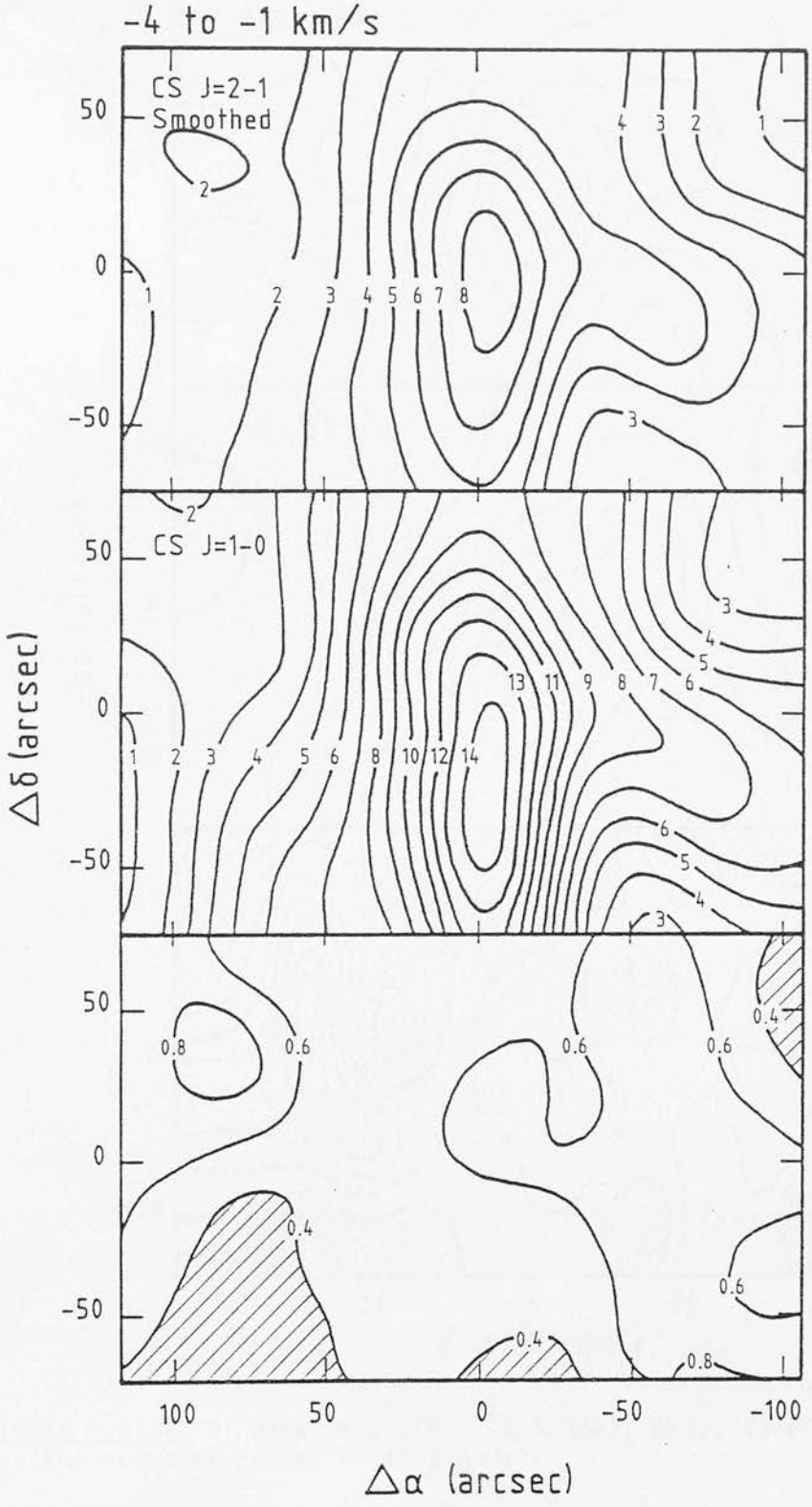

FIGURE 4.4.11b : same as for Fig.[4.4.11a], only, this time, for the velocity range, -4 to -1 km/s.

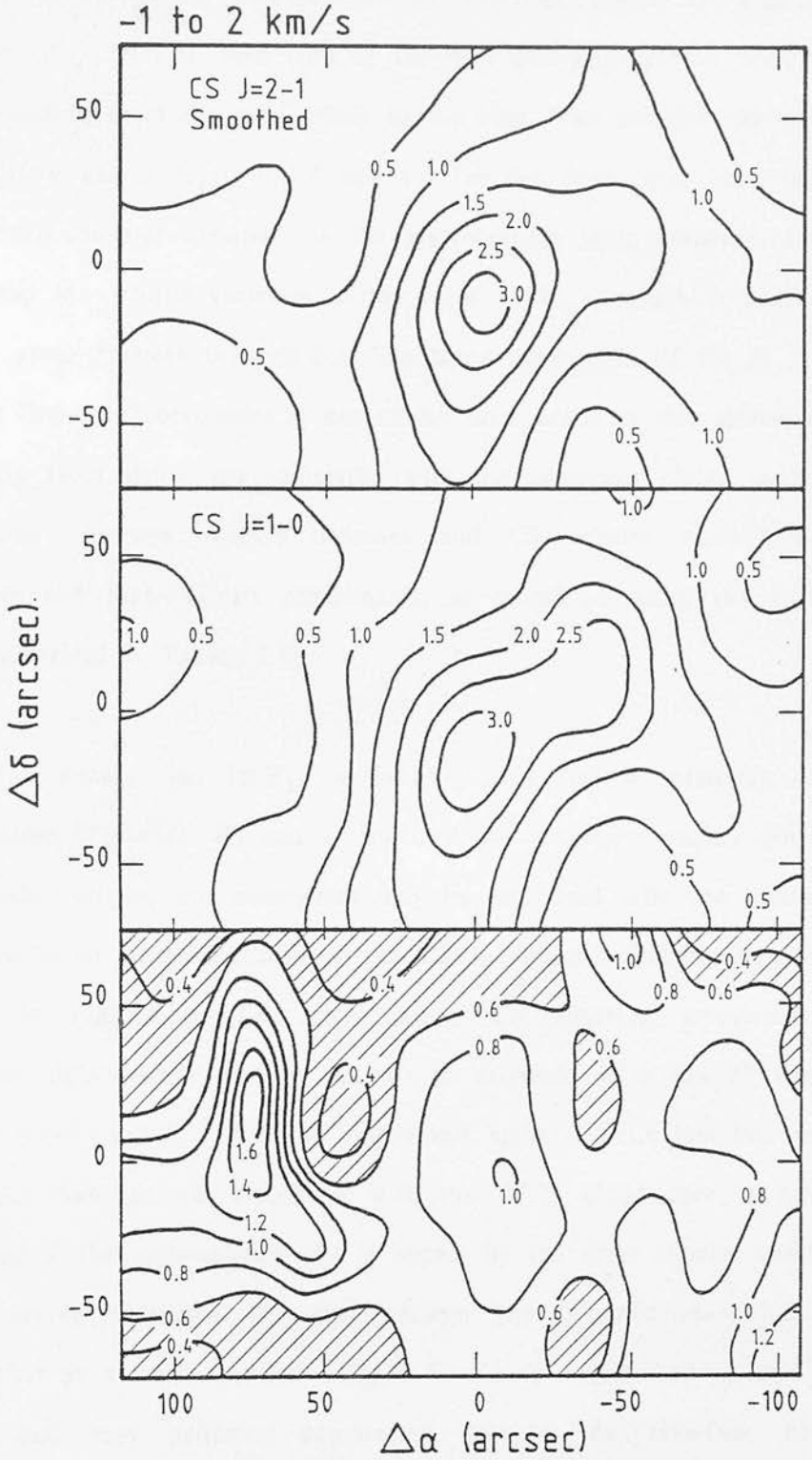

FIGURE 4.4.11c : same as for Fig.[4.4.11a], only, this time, for the velocity range, -1 to 2 km/s.

itself which is clearly outlined as an extended region of enhanced J=2-1 emission ($R_{2/1}$ > 1.0), seen both in the red- and blue-shifted velocity intervals and extending from the map origin to the west. The average value of $R_{2/1}$ in the outflow gas is $R_{2/1} \approx 1.4$ and 1.0 for the blue- and red-wing emission, respectively. In stark contrast to the high-velocity wing emission, the line-core ratio map shows little variation in the value of $R_{2/1}$ which is constrained to a narrow range between 0.6 and 0.8. The bland appearance of the $R_{2/1}$ ratio map for the line-core component is not totally unexpected as this emission originates primarily from dense gas associated with the quiescent cloud, which is itself featureless. Average volume densities and CS relative abundances for the line-core and high-velocity components, as calculated using the LVG method, are summarized in Table[4.4.3].

The densest gas ($n(H_2) = 6\times10^5$ cm^{-3}) has a relatively low kinetic temperature (T_k = 10 K) and is confined to a compact region centred on the CO outflow origin; this component may be associated with the dense molecular disc that is so clearly outlined in the CS J=1-0 peak antenna temperature map shown in Fig.[4.4.1a]. The high-velocity CS emission associated with the extended high-velocity outflow appears to originate in a gas of slightly lower density ($8\times10^4 < n(H_2) < 3\times10^5$ cm^{-3}) and higher kinetic temperature ($10 < T_k < 50$ K) than the gas associated with the DR21 cloud core; a result that is predicted if the high-velocity gas is heated by the same shocks which give rise to the strong vibrational H_2 line emission. The extended low-velocity emission is well fit by a warm gas ($10 < T_k < 50$ K) of density ($10^4 < n(H_2) < 6\times10^4$ cm^{-3}) and may delineate compressed gas at the interface between the high-velocity outflow and the ambient cloud. In agreement with the LVG analysis of the high signal-to-noise central CS profile, it is found that, on average, (i) the abundance of CS is slightly depleted in the high-velocity gas,

TABLE 4.4.3 :

RESULTS FROM 'LVG' ANALYSIS OF DR21 CS MAP

COMPONENT kms-1	T(2-1) K	R(2/1)	n(H2) cm-3 10K : 40K	X(CS) [1.] 10K : 40K	τ (2-1) [2.] 10K : 40K
DISC -4 to -1	6.0	0.7	6(5) : *	1(-9) : *	25 : *
HIGH-VEL OUTFLOW (RED) -1 to 2	1.5	1.0	1(5) : 4(4)	3(-10) : 8(-10)	0.9 : 0.6
HIGH-VEL OUTFLOW (BLUE) -7 to -4	1.7	1.4	3(5) : 8(4)	1(-10) : 4(-10)	0.5 : 0.4
LOW-VEL OUTFLOW -4 to -1	3.5	0.8	6(4) : 1(4)	5(-10) : 3(-9)	5 : 6
SHELL -7 to 2	0.6	1.9	6(5) : 1(5)	2(-11) : 6(-11)	0.2 : 0.1

Tx = 8-10 K for all velocity components

1 : assume (dV/dr) = 1 kms-1pc-1 for DISC and LOW-VELOCITY OUTFLOW
and = 10 kms-1pc-1 for HIGH-VELOCITY OUTFLOW and SHELL

2 : in general, $\tau(1\text{-}0) \sim \tau(2\text{-}1)/10$

* : no fit was obtained for these input parameters

X(CS) $\approx 6\times10^{-10}$, relative to the low-velocity quiescent cloud where, X(CS) > 10^{-9}, and, (ii) the optical depth in the line wings is everywhere lower than the optical depth in the line core.

The second physical feature revealed by the $R_{2/1}$ ratio maps is a thin shell-like condensation located approximately 80 arcsec to the east, at high-red velocities, and to the south-east, at high-blue velocities, of the outflow origin. The shell is of extremely high contrast, has a peak value, $R_{2/1} \approx 1.8$, and is separated from the outflow centre by an inner cavity of relatively low $R_{2/1}$. Although this shell-like component possesses a large value of $R_{2/1}$, the CS J=2-1 antenna temperature is quite low, $T_{21} \approx 0.6$, implying a correspondingly high volume density, $n(H_2) > 10^5$ cm^{-3}, and significantly low abundance, X(CS) $< 2\times10^{-11}$. One could speculate that this dense, well-defined shell may represent gas swept up at the boundary of the expanding DR21 HII region which is located within the cavity bounded by the DR21 cloud core (disc) and the shell itself. The location and overall morphology of the compact HII region relative to the other emission components belonging to the DR21 region is illustrated in Fig.[5.1.2]. From this figure, it is evident that the high-density CS shell does in fact lie on the eastern boundary of the slighly E-W elongated HII region. Evidence that further confirms the association of the CS shell with the expanding HII region derives from the CO velocity-channel maps presented in Sec.[4.3.d]. The INTERMEDIATE-velocity CO maps clearly show a similar shell/cavity structure located to the east of the outflow centre and spatially coincident with the CS shell. It is therefore conceivable that the shell feature observed in both CS and CO emission is an artifact of the dynamical interaction between the expanding HII region and the DR21 molecular cloud. At present, there are no observations available which unambiguously define the exact location of the compact HII region along the line-of-sight. It may be intimately

associated with the DR21 molecular cloud core and may thus play an important role in generating and sustaining some of the complex kinematics associated with this region. Alternatively, the HII region may lie on the back surface of the cloud and thus represent a chance line-of-sight projection. A discussion of the relative likelihood of these two possible geometries is prosponed till later (Sec.[5.1]).

To conclude this section, the quantitative results derived from the LVG model analysis are now used to make a rough calculation of the masses involved in the different dynamical components.

For the DR21 disc, the CS J=1-0 peak antenna temperature map presented in Fig.[4.4.1a] is used to estimate a diameter and thickness for the disc of, 2.0 and 0.5 pc, respectively. For an average density, $n(H_2) = 5\times10^5$ cm^{-3}, a solid disc of these dimensions has a total mass of order 5×10^4 M_0. This estimate compares favourably with the disc mass as derived previously using the crude LTE analysis (i.e. 5.5×10^4 M_0).

For the DR21 high-velocity outflow, the geometry is modelled by a solid cylinder, 1 pc in diameter and 3 pc in length, which is filled with neutral gas of average density, $n(H_2) = 10^5$ cm^{-3}. For these conditions, an outflow of the specified geometry and size would have a overall mass of 1.6×10^4 M_0. Again, this crude estimate shows good agreement with the LTE analysis (i.e. 1.5×10^4 M_0).

Chapter 5

DISCUSSION OF THE PHYSICAL STATE OF DR21 BASED ON ANALYSIS OF THESE OBSERVATIONS

5.1 MORPHOLOGICAL ASPECTS OF DR21 IN LIGHT OF THESE AND OTHER OBSERVATIONS

The morphological relationship of the shocked H_2 to other emission components of the DR21 molecular cloud complex is shown in Fig.[5.1.1]. The contours of HCN J=1-0 integrated intensity are from Morris et al. (1974) and the map of 1-mm continuum emission is from Werner et al. (1975). The bulk of the H_2 line emission at DR21 occurs on either side of, and at distances of 1-3 pc (equivalent to 1-3 arcmin, for D = 3 kpc) from, the DR21 cloud core. No H_2 line emission is visible within the central region, of radius ~ 1 pc, where extremely high densities ($n(H_2) = 10^5$-10^6 cm^{-3}) are known to exist (Henkel, Walmsley & Wilson 1980; Matsakis et al. 1977; Dickel et al. 1983; Dickel, Ho & Wright 1985; also, see Sec.[4.4] of this thesis). From observations of the relative intensities of the infrared Brackett alpha and gamma HI recombination emission emanating from the visually obscured DR21 HII region, Righini-Cohen, Simon & Young (1979) derive a visual extinction of $A_V > 100$ mag along the line-of-sight towards this region. This reddening estimate compares favourably with the totally independent estimate, as derived from the observations of the optically thin $C^{18}O$ J=1-0 line emission presented in Sec.[4.3.f]. It thus is highly plausible that the absence of observable 2.12 μm H_2 line emission along this direction is due to excessive extinction by dust grains concentrated within the dense cloud core.

A spatial correspondence between the extended HCN and the west lobe of H_2 line emission, which is clearly evident in Fig.[5.1.1], suggests that the shock-excited H_2 there is associated with a filament of dense molecular gas. If the distribution of HCN emission traces locally dense molecular gas ($n(H_2) > 10^5$ cm^{-3}), then the spatial correlation with H_2 line emission is not unexpected as the intensity of the S(1) line in a shock excitation model scales linearly with the pre-shock ambient gas density. Two simple illustrative examples of suitable geometries are (i) that the HCN emission defines a dense bar or ridge of compressed molecular gas upon which supersonic gas motions impinge; a dynamical interaction between the the neighbouring DR21 and W75N molecular clouds may tailor such a density structure and simultaneously sustain the requisite supersonic gas motions and, (ii) that the HCN emission coincident with the west lobe of H_2 line emission may arise from a dense, somewhat elongated, shell of compressed molecular gas swept up by an energetic outflow originating from within the DR21 cloud core. Indeed, the low resolution HCN map shows notable morphological similarity to the high-angular resolution CS maps presented in Sec.[4.4], which it is contended delineate the spatial distribution of compressed ambient gas at the boundary of an extremely collimated molecular outflow.

Absorption in molecular lines along the line-of-sight to the centre and eastern portions of the DR21 cloud core has previously been observed in NH_3 by Matsakis et al. (1981), in H_2CO by Forster et al. (1981), Dickel et al. (1983), and HCN by Dickel et al. (1985). Thus, foreground absorption of molecular line emission may play a large part in explaining the apparent absence of HCN emission coincident with the eastern lobe of H_2 line emission. However, as the spatial asymmetry observed in HCN emission is also reflected

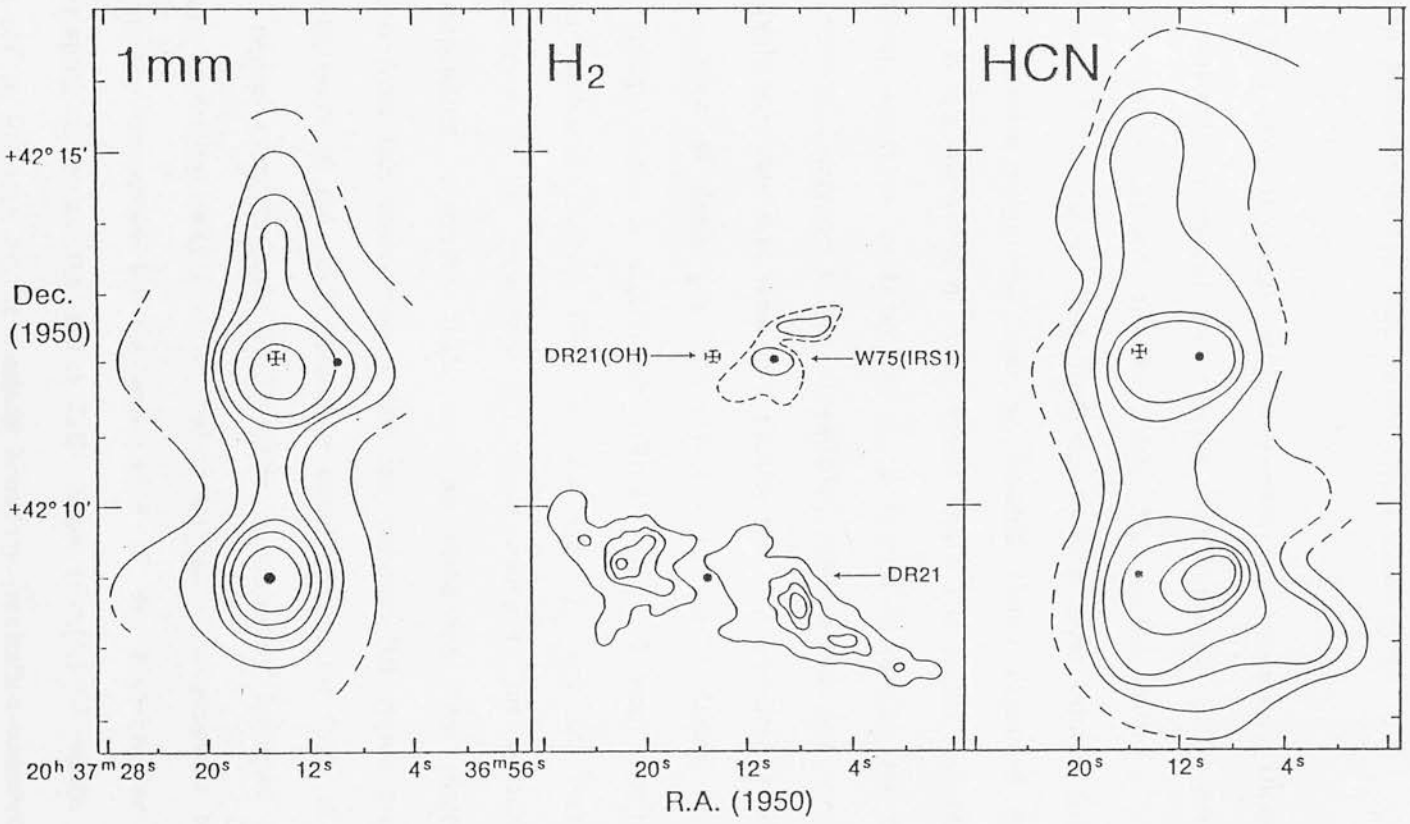

FIGURE 5.1.1 : A composite of three figures showing the relative spatial distribution of (a) HCN line intensity (Morris et al. 1974), (b) H2 line intensity (this work), and (c) 1-mm continuum flux (Werner et al. 1975).

in CS emission (see, Figs.[4.4.1] & [4.4.2]), which was found to suffer little if any self-absorption, it is still conceivable that there exists a real density gradient across the face of this region, with most of the dense gas being located primarily to the west of the DR21 cloud core.

Using the Hat-Creek millimeter-wave interferometer, Dickel et al. (1985) have mapped the spatial and velocity distribution of HCN emission over a 1 arcmin region centred on the DR21 HII region with a synthesized beam diameter of 15 arcsec. They find that, within their limited field of view, the HCN emission originates from an isolated clump displaced approximately 20 arcsec to the southwest of the compact DR21 HII region. As the peak of HCN emission, measured by Dickel et al., is located at roughly the same position as the peak of integrated CS J=2-1 emission presented in this work (Fig.[4.4.2]), it is highly probable that these two density sensitive emissions arise from the same condensation of dense gas with $n(H_2) > 10^5$ cm^{-3}. Dickel et al. suggest that this clump, which is slightly blueshifted (V_{lsr} = -5 kms^{-1}) with respect to the DR21 systemic velocity (V_{lsr} = -2.5 kms^{-1}), may be foreground material compressed by the expanding HII region owing to the apparent absence of a corresponding redshifted HCN emission component. An important conclusion drawn from this observation is that the compact HII region may be located on the backside of the DR21 molecular cloud, taking the form of a young blister HII region (Tenorio-Tagle 1979) which is ionization bounded to the west and freely-expanding away from us and to the east. The proposed blister mophology is further supported by the appearance of the high-angular resolution radio continuum maps of the DR21 HII region (Fig.[5.1.2]) which show a sudden cut-off in emission at the western boundary (ionization-bounded), with a much more gradual decrease in emission to the east (density-bounded).

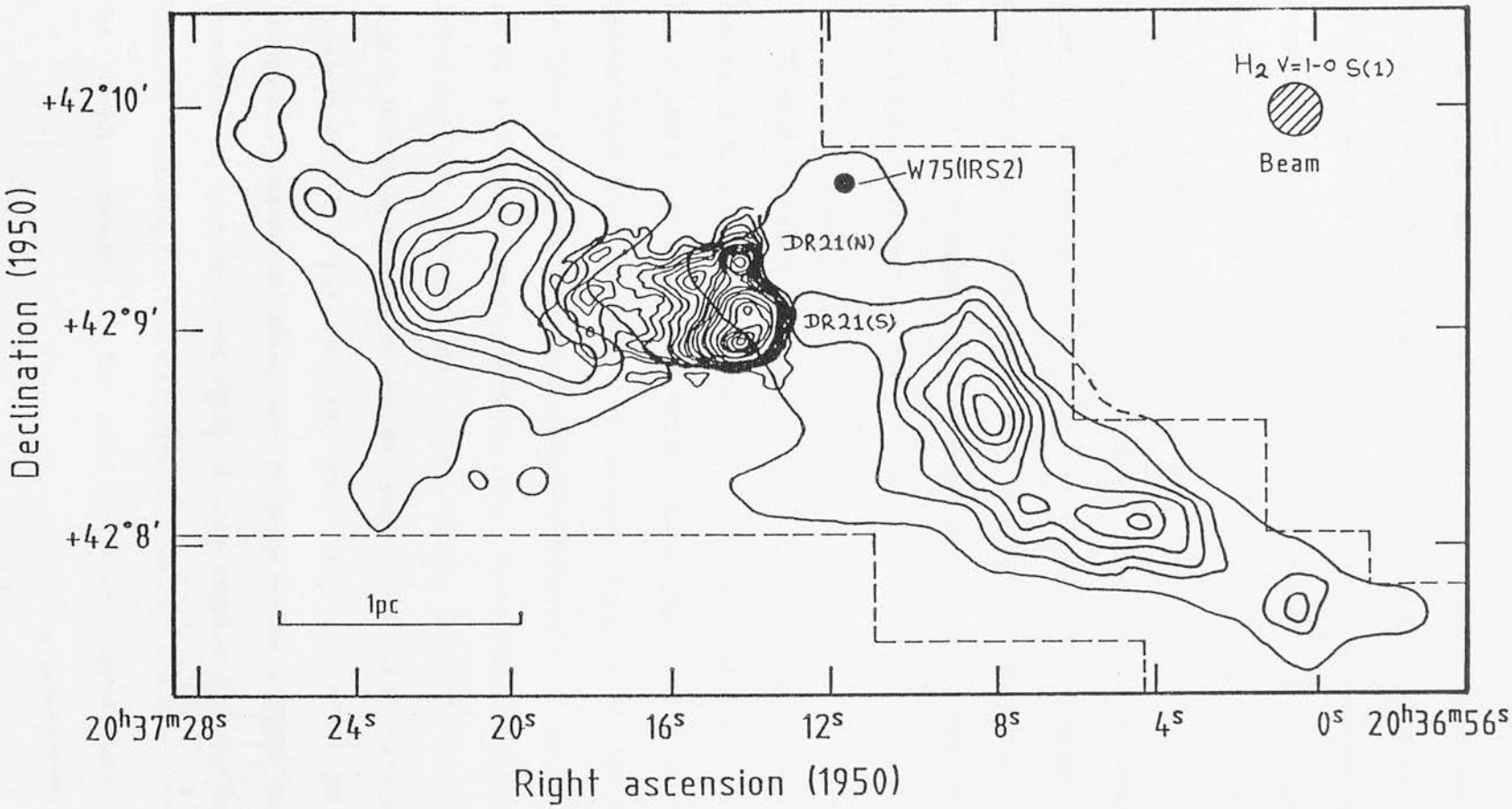

FIGURE 5.1.2 : An overlay of the contours of 2cm radio continuum (as measured by the VLA) on the contours of shock-excited H2 v=1-0 S(1) line emission as presented in this work. The radio continuum is thermal emission that arises from free-free processes within the compact DR21 HII region. A higher-angular resolution radio map is shown in Fig.[5.1.3].

At 1-mm wavelengths the DR21 region shows two emission peaks of comparable brightness at the positions of DR21 and W75S and a lower surface brightness extended component which joins the peaks and also extends several arcmin to the north of W75S. The 1-mm continuum emission, which is primarily due to thermal emission from cold dust grains directly associated with the molecular gas within the cloud cores, shows no evidence of any spatial correlation with the distribution of H_2 line emission. In particular, the western elongation so clearly evident in HCN, CS, CO and H_2 line emission is completely absent in the 1-mm continuum map, which intuitively suggests that this component is more probably a hollow wind-swept shell rather than a solid extension to the molecular-cloud core itself. The absence of secondary continuum peaks, further suggests that the extended, shock-excited H_2 emission is powered by a single central source, rather than a string of self-luminous sources spread out over the outflow lobes.

Thermal continuum observations, from 2.2 - 300 μm, recently published by Harvey et al. (1986), clearly show that the DR21 HII region is the brightest far-infrared source in the DR21/W75S complex. One of the most striking results derived from there observations is the much greater E-W than N-S extent of the DR21 source together with the elevated temperature to the east and possibly to the west of the main luminosity peak. Conversely, the optical depth map shows a region of higher dust column density elongated N-S. These authors suggest that these asymmeries may be related to the DR21 outflow phenomenon, in which case the higher dust temperatures may represent an area of enhanced deposition of mechanical energy due to dissipation at a shock front; the spatial correlation of warm dust and strong H_2 line emission certainly favours shuch a scenario. Moreover, the N-S elongation of enhanced dust column density exhibits the correct orientation if this ridge of dense material were to act as a

collimator for the predominantly E-W oriented molecular flows and, indeed, most probably originates from the same edge-on disc that is so clearly revealed by the maps of CS line emission presented in Sec.[4.4]. The 20 μm and 2 μm continuum emission show a broad resemblance to the 5 Ghz radio continuum map of Harris (1973), a result that is commonly found in regions where the near-infrared emission arises primarily from hot dust grains mixed with the ionzed gas of an HII region. There exist, however, significant small-scale dissimilarities between the infrared and radio continuum maps which indicate the presence of gradients in extinction between the individual continuum sources in the DR21 complex, as previously suggested by the interferometric H_2CO observations of Dickel et al. (1983) and the distribution of Brackett alpha hydrogen recombination line emission, mapped by Righini-Cohen, Simon & Young (1979). In particular, Harvey et al. find a peak 20 μm optical depth which lies close to Harris's radio source C (Fig.[5.1.3]).

One of the main goals of this work is to investigate the origin of the complex dynamical behaviour that gives rise to many of the observable peculiarities of the DR21 star-formation region. Of prime importance to the success of this task is an accurate measurement of the position of strongest high-velocity CO emission and its relation to the spatial distribution of the many other emission components within this complex region. Accordingly, Fig.[5.1.3] shows the best estimate for the position for the spatially unresloved source of the high-velocity CO emission, as presented in Sec.[4.3], superposed on the contours of 2 cm radio continuum emission, as presented by Dickel et al. (1986). Also shown are the positions of the 20 μm continuum peaks (Harvey et al. 1986) and the DR21 H_2O maser source discovered by Canto et al. (1975). Within the pointing errors of the millimeter-wave observations, the position at which the broadest CO profile occurs is coincident with both the strongest radio

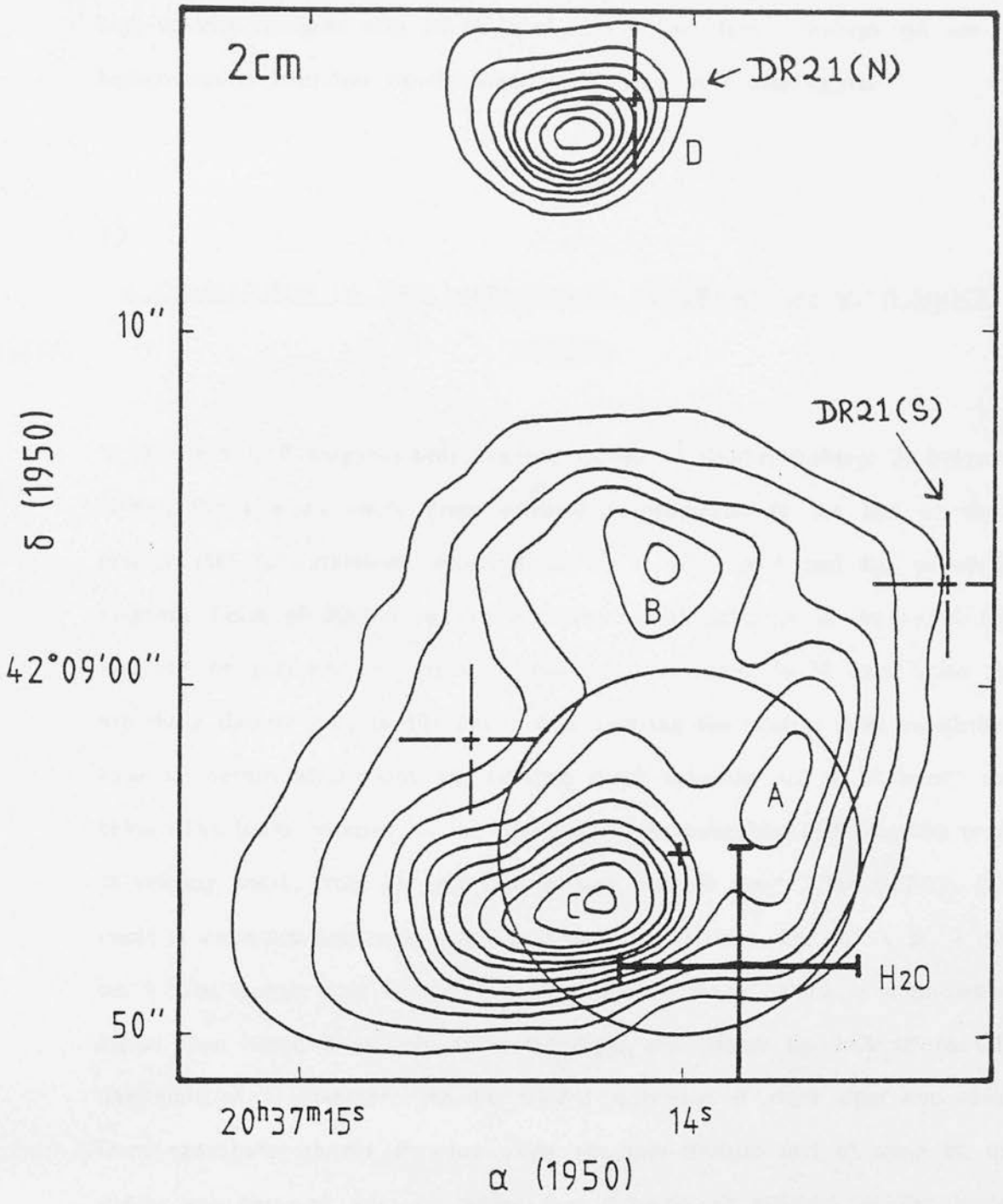

FIGURE 5.1.3 : The circle shows our best estimate for the location of the central high-velocity CO outflow source (i.e. position where the broadest CO lines are observed). The contours are of 2cm radio continuum emission and are taken from Dickel et al (1986) and the large crosses are the positions of the 20 μm infrared continuum peaks as observed by (Harvey et al 1986). The DR21 H_2O maser source lies within our error circle as also do the radio components A and C (Harris 1976).

continuum peak, termed component C by Harris (1973), and the H_2O maser source, but is not associated with any of the 20 μm continuum peaks. Tighter constraints on the exact location of the central engine that drives the high-velocity outflows may be obtained in the near future through the use of higher-angular resolution interferometric millimeter-wave observations.

5.2

A COMPARISON OF THE INFRARED H_2 OBSERVATIONS WITH SHOCK MODELS

The non-LTE magneto-hydrodynamic models of Draine, Roberge & Dalgarno (1983), for a plane shock front oriented perpendicular to the line of sight, predict that for pre-shock densities of $n_0 = 10^4$ cm^{-3} and for pre-shock magnetic fields of 50-100 μg the dereddened peak intensity in the v=1-0 S(1) line can be produced by shock velocities in the range 30-50 kms^{-1}. As the pre-shock density rises to 10^6 cm^{-3}, thus bringing the relative level populations close to thermal equilibrium, the required shock velocities fall to 20 kms^{-1} and below. The limits imposed by the dereddened line intensities and observed range in velocity width, from 25 kms^{-1} to greater than 50 kms^{-1} (Table[4.2.2]), thus imply a corresponding large range in pre-shock densities, i.e. $10^4 < n_0 < 10^6$ cm^{-3}. The upper limit to this predicted density range, which is considerably higher than expected at radii from the cloud core where the bulk of the H_2 line emission is observed, can be relaxed somewhat if more than one shock front contributes to the emission along the line-of-sight and if some of the shocks are observed edge-on rather than face-on as assumed in the model calculations. If such a broad distribution in density does exist within the shocked gas, then it is most readily accomodated if the outflow is inherently

clumpy on scales smaller than the beam size (≅ 0.2 pc for D = 3 kpc), as is discussed further in Sec.[5.4].

As alluded to above, the magneto-hydrodynamic shock models are also extremely sensitive to the local magnetic flux density, which under conditions of flux freezing, varies with the local gas density. In this respect, the absence of quantitative measurements of magnetic field parameters within optically obscured molecular clouds pose a fundamental uncertainty in the link between observation and theory.

The velocity widths of the H_2 line profiles must be viewed with caution when estimating the intrinsic flow velocities, because the large extent and degree of collimation of the DR21 H_2 emission-line source suggests that the direction of propogation of the outflow which stimulates the shocked H_2 emission may be rotated through a large angle with respect to the line of sight. Indeed, outflow velocities in the shocked molecular gas of > 150 kms^{-1} are predicted if the angle is large and the flow is well collimated. However, the apparent absence of a significant ionized gas component coincident with the shocked material in the H_2 lobes (note that in Fig.[4.2.5] faint Brackett gamma is observed at the east peak of H_2 line emission but is probably associated with the diffuse component of the DR21 HII region rather than shock ionization) precludes the existence of shock velocities much greater than 100 kms^{-1}, as under such conditions post-shock temperatures are typically, $T_S > 10^5$ K, and ionization of material, both upstream and downstream of the the shock front, is inevitable. If the gas now seen in H_2 emission was entirely ionized at some earlier stage in its passage through the shock front (this being an upper limit to the intensity of recombination line emission), then the ratio of Brackett gamma to S(1) intensities can be readily calculated from simple timescale arguments and

is on the order of 1/10. The observed upper limit to this ratio at the peaks of emission in the H_2 lobes is only 1/20 (2 sigma) and suggests that shock ionization in the DR21 H_2 jets is of minor importance.

It is improbable that the H_2 emission can derive solely from high-velocity (V_S > 50 kms^{-1}) dissociative J-type shocks (viz. Sec.[3.2]) as much of the total emission from the shock is radiated in the optical and ultraviolet as the post-shock gas cools from 10^5-5×10^3 K and the H_2 cooling is suppressed because reformation is not complete at T > 1000 K (typically $X(H_2) \approx 0.01$ at T = 2000 K). Also, at high densities, i.e. $n(H_2) > 10^7$ cm^{-3}, radiative cooling via H_2O line emission becomes important and can drain a significant fraction of the thermal energy from the post-shock gas. The most sophisticated J-type shock models available at present predict an intensity for the S(1) line that is roughly 1/10 of that produced by a non-dissociative C-type shock, for the same pre-shock density and shock velocity (McKee, Chernoff & Hollenbach 1984).

Although it is difficult to produce the observed strong emission in the S(1) line core by simple J-type shocks, it is still possible that fast shocks may contribute to the emission in the weaker high-velocity wings of the observed H_2 line profiles. Furthermore, as it is thought that the newly formed H_2 molecules in the cooling regions behind a dissociative shock lie in highly-excited vibrational levels (i.e. v=5; Duley & Williams 1986), the subsequent cascade down through lower vibrational levels may give rise to an emission spectrum which closely resembles that of ultraviolet fluorescence. A consequence of the J-type shock model is therefore that the H_2 excitation may differ substantially between the line core (thermal) and and the high-velocity wings (non-thermal). A comparative study of v=1-0 and v=2-1 profiles thus may provide a sensitive test for the existence of dissociative shocks, which, if present, should be

identified by an increase in the v=2-1/v=1-0 intensity ratio with increasing velocity displacement from the line core. This test, however, is of a suggestive nature only as the details of the excitation process following H_2 reformation in the cooling flows of fast shocks are poorly understood at present.

In my opinion, a more likely solution to the high-velocity H_2 emission problem, first suggested to account for the high velocity H_2 observed in Orion (Chevalier 1980; Nadeau, Geballe & Neugebauer 1982), is that the high-velocity emission arises from shocked cloudlets of dense molecular material moving outwards with velocities comparable to the flow velocity. The intense low-velocity emission would then originate in ambient molecular material that has been shocked and swept up to form a dense, slowly moving shell bordering the expansion region, while the fainter high-velocity emission comes from non-dissociative shocks propagating within the fast moving clumps. The clumps can either be pre-existing condensations that have been ram-pressure accelerated by the flow, or, alternatively, may result from entrainment of material due to the growth of fluid-dynamical instabilities at the flow/cloud boundary. The existence of a clumpy medium is further suggested by the low beam filling factors observed in the high-velocity portions of the CO and CS millimeter-line profiles, presented in Secs.[4.3] & [4.4], and discussed further in Sec.[5.4].

CONSOLIDATION OF THE HIGH-VELOCITY CO, CS AND SHOCK-EXCITED H_2 OBSERVATIONS

5.3.(a) A COMPARISON OF THE MORPHOLOGICAL STRUCTURE

As both the millimeter-wave CO J=1-0 and CS J=2-1 and the infrared H_2 spectroscopic mapping were conducted using instrumental beams of comparable size (15-20 arcsec), a direct comparison of the morphologies presented by these different measurements is straightforward.

Overlays of the HIGH-RED and HIGH-BLUE CO J=1-0 integrated intensity contours (Fig.[4.3.7]) on the DR21 H_2 v=1-0 S(1) emission-line map are shown in Figs.[5.3.1] & [5.3.2], respectively. The most significant result derived from this comparison is that although the CO and H_2 emission are obviously related in their overall distribution, both exhibiting bipolar, jet-like structures of clumpy emission oriented along a common NE-SW major axis, a more detailed analysis reveals a striking anticorrelation in the spatial distribution of the respective emission peaks. Such a spatial anticorrelation is not totally unexpected as the physical conditions requisite for the excitation of these two emissions are radically different; the rotational CO emission arises primarily from a relatively cool (T_k < 100 K) and diffuse medium ($n(H_2) < 10^3$ cm^{-3}), whilst, collisional excitation of the vibrational levels of the H_2 molecule can take place only in a dense and hot gas ($n(H_2) > 10^5$ cm^{-3}, T_k = 2000 K). The close association between the CO and H_2 emissions therefore indicates the presence of an extremely broad spectrum of physical conditions within the molecular gas composing the DR21 outflow lobes.

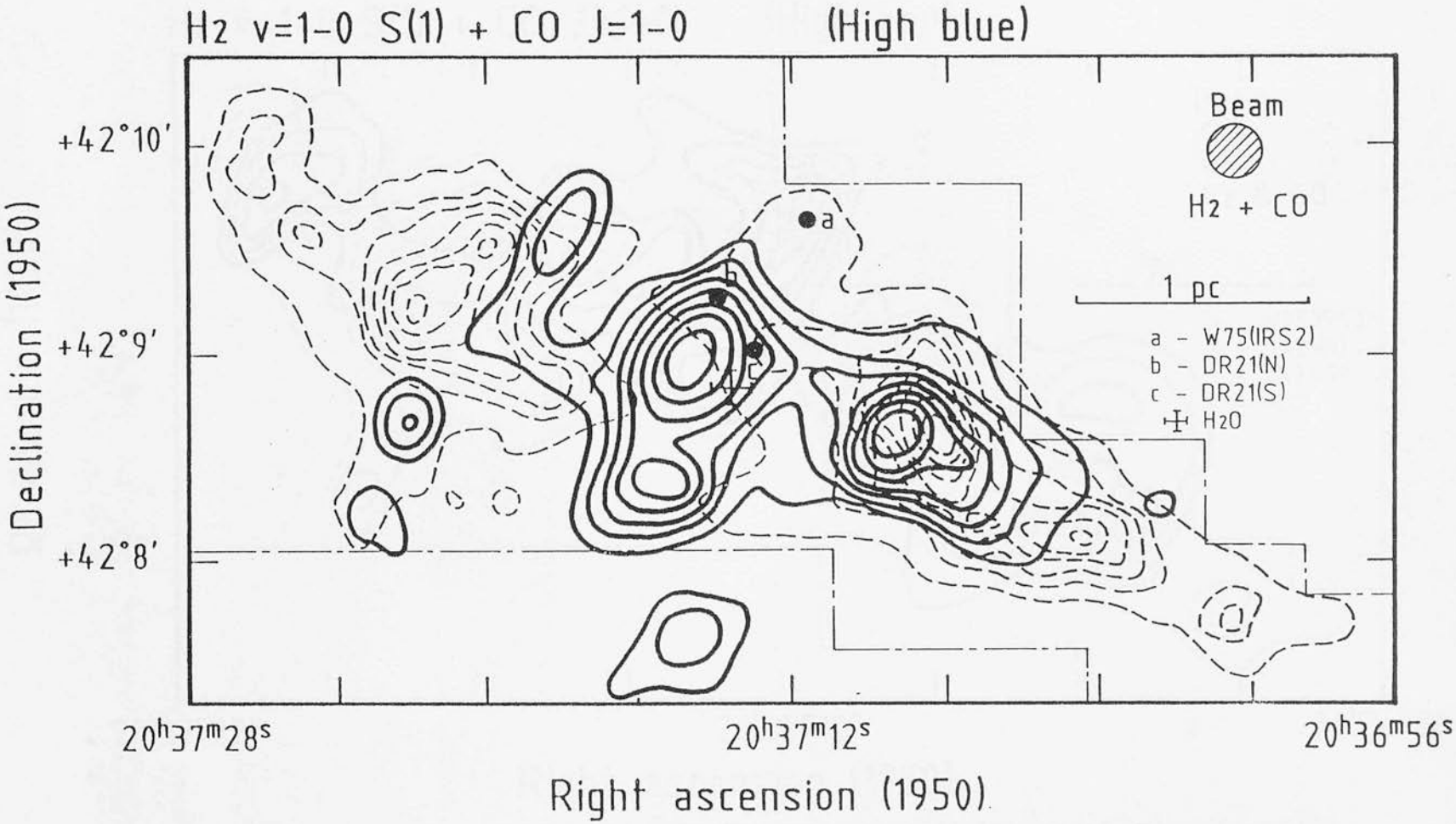

FIGURE 5.3.2 : An overlay of the contours of high-velocity blue-shifted CO integrated intensity on the contours of H2 v=1-0 S(1) line emission in the DR21 outflow. The infrared and millimeter beams are of comparable size (18 and 15 arcsec,respectively).

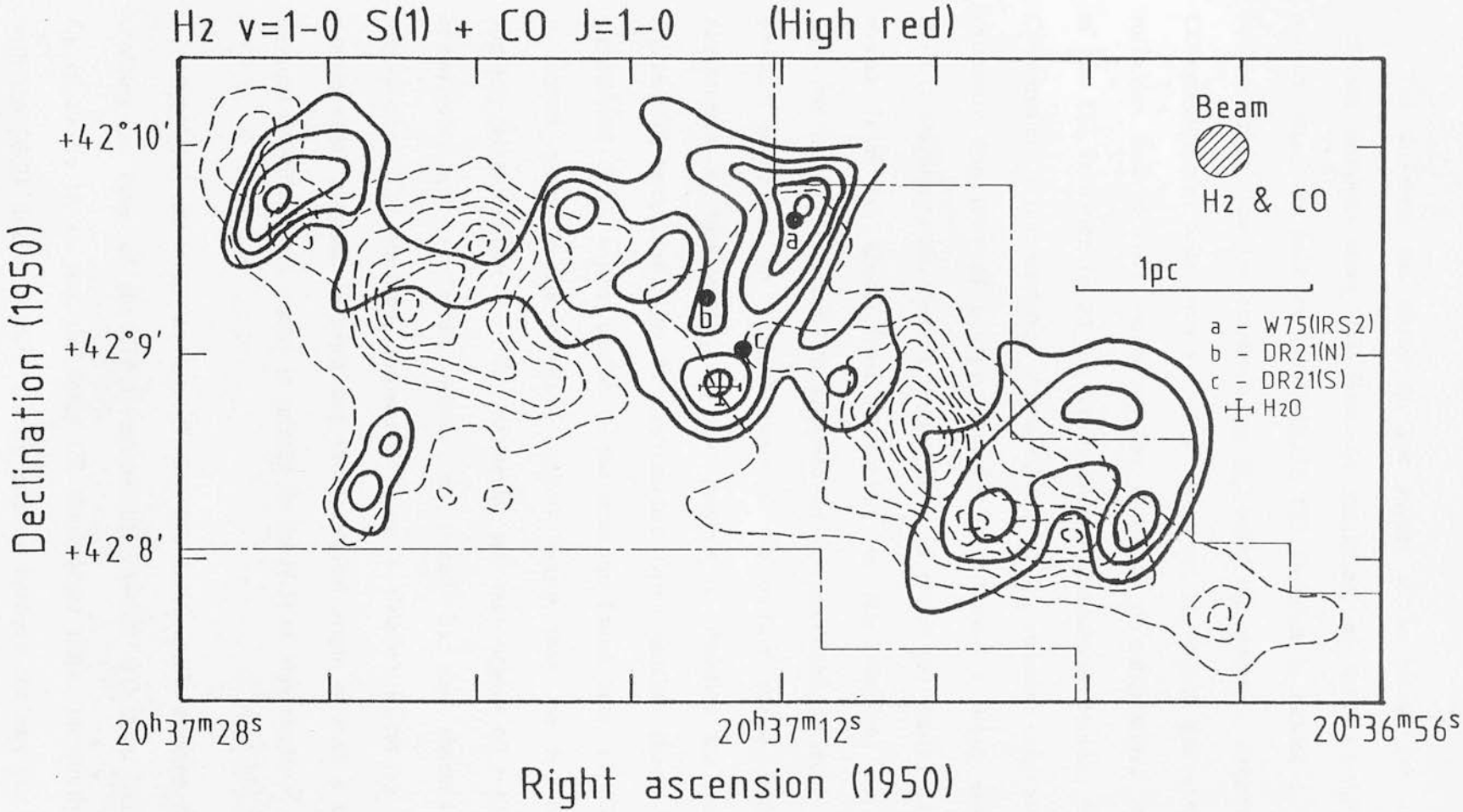

FIGURE 5.3.1 : An overlay of the contours of high-velocity red-shifted CO integrated intensity on the contours of H2 v=1-0 S(1) line emission in the DR21 outflow. The infrared and millimeter beams are of comparable size (18 and 15 arcsec, respectively).

The different gas phases do not appear to be mixed but originate at different locations along the flow. In particular, at the blue-shifted (west) outflow lobe, the peak of HIGH-BLUE CO emission is located closer to the outflow origin than the corresponding H_2 peak; this geometry suggests that the CO emission may arise from a shell of swept-up, post-shock gas which has had sufficient time to cool, via strong line radiation, to temperatures characteristic of the CO excitation (< 50 K). The spatial anticorrelation between the H_2 and CO emission is thus explained if the vibrational H_2 emission originates from an extremely thin layer of hot gas immediately following a strong shock, whilst, the CO emission arises from a thicker layer of cooler gas located further down stream from the shock front. According to this scenario, the peaks of high-velocity CO emission are expected to be positioned adjacent to the H_2 emission peaks and on the side closer to the outflow source. Such a spatial displacement of high-velocity CO and shocked H_2 emission has recently been reported in association with the well-studied Orion outflow source (Hasegawa, unpublished data), where, similar to the situation found here, the CO emission is located closer to the proposed outflow source than the H_2 emission. It appears, therefore, that the DR21 molecular jets may consist of a succession of compression and rarefaction waves, as traced by the shocked H_2 and high-velocity CO emission, respectively. For a detailed discussion of various models which may aid in explaining the dynamical origin of such a sequence of physical conditions, the reader is refered to Sec.[6.5] of this thesis.

Fig.[5.3.3] show an overlay of the CS J=1-0 peak antenna temperature contours on those of the DR21 infrared H_2 v=1-0 S(1) line emission. This figure clearly shows that the dense CS temperature ridge, previously identified with the DR21 disc, is located exactly midway between the east and west lobes

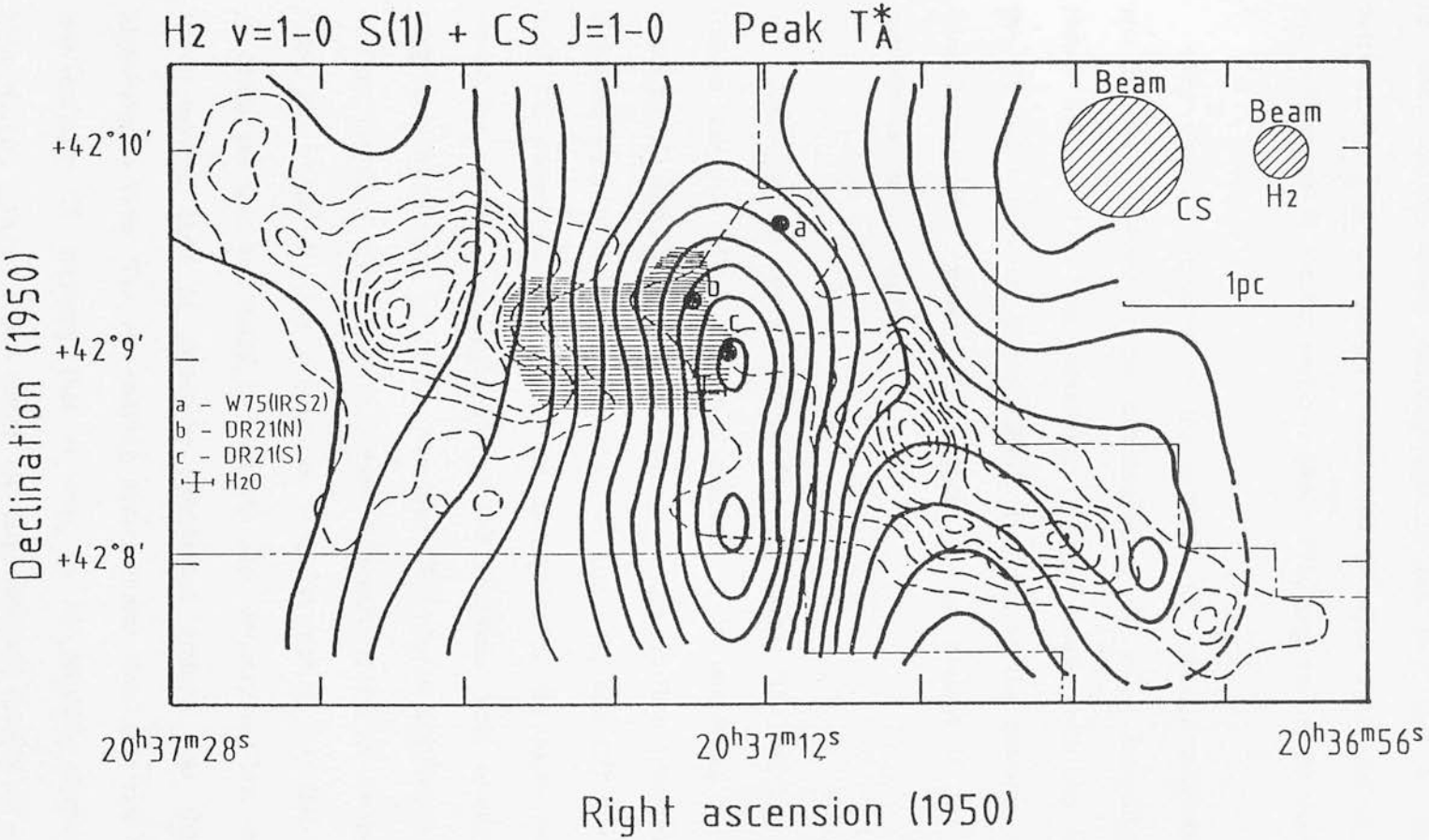

FIGURE 5.3.3 : An overlay of the contours of CS J=1-0 peak antenna temperture (full lines) on the infrared H2 emission line map (broken lines). The beam sizes for the CS and H2 observations are 36 and 18 arcsec, respectively. The positions of the DR21 infrared sources and H2O maser are indicated. The hatched region shows the extent of the DR21 radio continuum emission associated with the DR21 HII region.

of shock-excited H_2 emission. Furthermore, the disc is apparently oriented with its plane aligned almost perpendicular to the E-W axis of the main DR21 outflow; this is a well known characteristic of discs which aid in the propulsion and collimation of bipolar outflows (~~Bally~~ Lada 1986 and references therein).

The spatial relationship of the extended CS emission with the shocked H_2 jets is best displayed by the distribution of CS J=2-1 integrated emission, as shown in Fig.[5.3.4]. This correlation probably results from the observation that the CS J=2-1 emission is particularily sensitive to the presence of broad lines with high-velocity wings, which ought to be present if the dense gas is participating in the outflow.

Although the overall distribution of diffuse CS J=2-1 emission closely follows the run of shocked H_2 emission, it is interesting to note that the positions of peak integrated CS emission in the outflow lobes are significantly displaced with respect to the positions of peak H_2 and CO line emission. The main CS peaks appear to lie at the boundaries of the high-velocity flows, as traced by the H_2 and high-velocity CO emission. This comparison therefore suggests a scenario in which the extended CS emission associated with the DR21 outflow lobes originates from two quite different dynamical components (see the discussion of the H_2 line profiles in Sec.[5.2]), namely; (i) fast-moving clumps of dense gas that are mixed in with the high-velocity outflow itself, and (ii) a slower-moving shell of swept-up compressed ambient gas that borders the high-velocity flow. The fast-moving dense clumps thus give rise to the diffuse, low-intensity CS emission that is seen to be spatially correlated with the high-velocity outflow lobes whilst the large column density of compressed gas associated with the wind-swept shell gives rise to the intense CS emission peaks. It is even possible that impaction of the high-velocity outflow gas with the

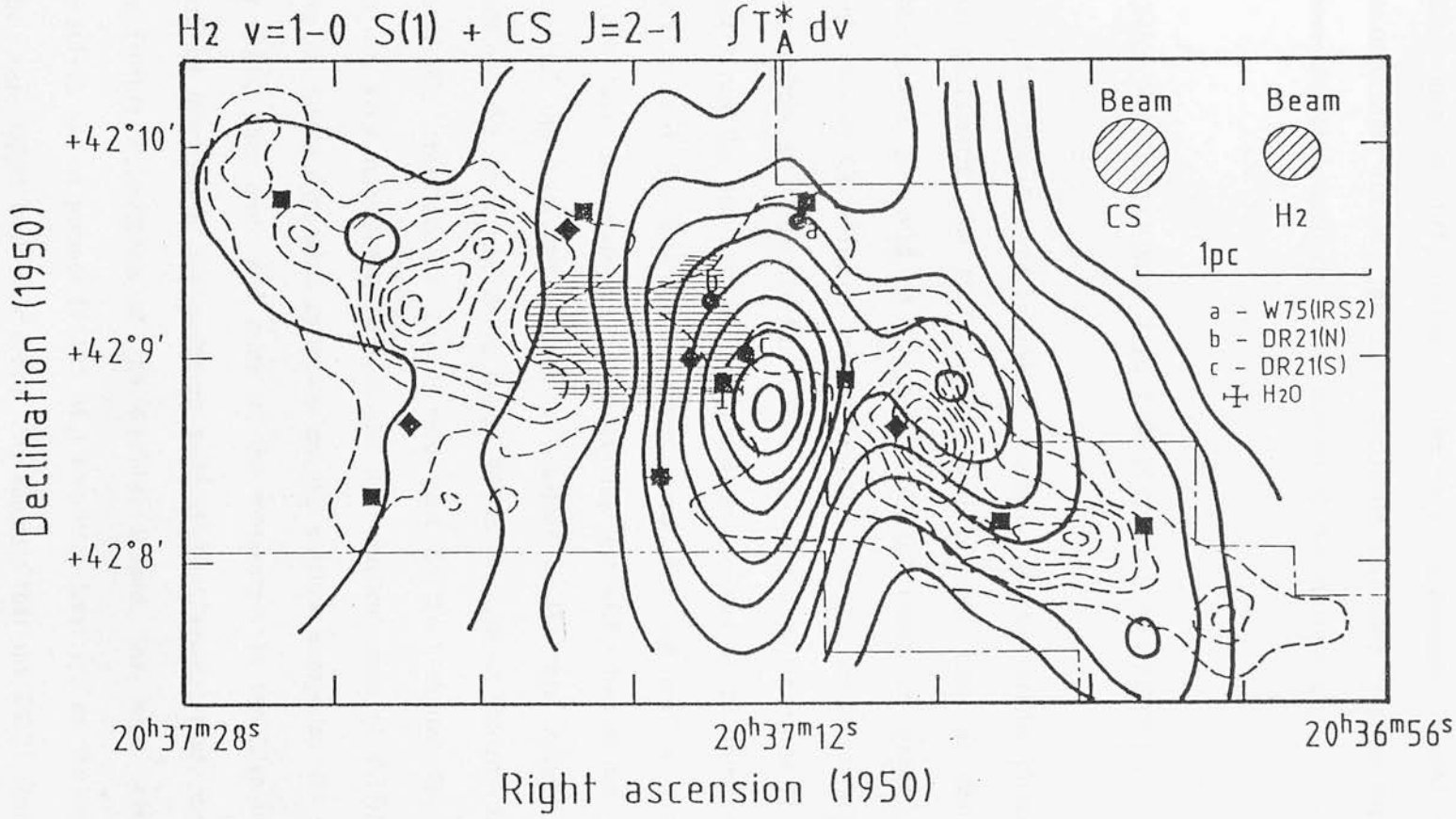

FIGURE 5.3.4 : An overlay of the contours of CS J=2-1 integrated emission (full lines) on the infrared H2 emission line map (broken lines). The beam sizes for the CS and H2 observations are 20 and 18 arcsec, respectively. The positions of the DR21 infrared sources and H20 maser are indicated as are the positions of the high-velocity blueshifted (filled diamonds) and redshifted (filled squares) CO peaks. The hatched region shows the extent of the radio continuum emission associated with the DR21 compact HII region.

denser CS clumps may cause glancing reflections, which change the direction of propagation of the flow, thereby explaining a dynamical origin for several of the kinks and wiggles which characterize the H_2 jets. Indeed, the CS clumps, which may be pre-existing entities, are consistently located ahead of the positions were the H_2 jets show maximum deflection, just as expected if these dense clumps impeed the radial motion of the outflow gas.

5.3.(b) A COMPARISON THE THE PHYSICAL PROPERTIES

Table [5.2.1] gives an overall summary of the various physical parameters that characterize the DR21 outflow and proposed disc, as derived using the observations presented in Chapter 4 of this thesis. In general, the H_2 and high-velocity CO emission provide the best available probes of the energetics of the outflow gas while the CS emission provides a better probe of the denser gas that forms the disc and the compressed gas located at the interface between the outflow and the ambient molecular cloud. For the outflow component, it is found that the swept-up, slower-moving gas (CS observations) contributes to most of the mass and to roughly one-half of the total kinetic energy of the outflow, the other half being stored within the highest-velocity outflow material itself (CO observations). The derived mass of shock-excited H_2 gas constitutes only a very small ~~percentage~~ fraction of the total outflow mass (< 0.1%) and therefore has no direct dynamical influence on the outflow energetics. As time evolves it is expect that more and more of the momentum in the high-velocity outflow will be imparted to the swept-up ambient cloud matter, thus, inevitably leading to further deceleration of the outflow. Indeed, the large mass observed in swept-up gas at present (> 10^4 M_0) entails at least 1/5 of the derived mass for the entire DR21 molecular cloud; this suggests that the DR21 flow is already of

TABLE 5.2.1 :

A COMPARISON OF THE PHYSICAL PARAMETERS DERIVED FROM THE INFRARED AND MILLIMETER-WAVE OBSERVATIONS.

	PARAMETER	1. CO	2. CS	
	$N(H_2)_{disc}$	2.0(23)	1.0(24)	cm^{-2}
	$N(H_2)_{hvf}$	5.0(22)	3.0(23)	cm^{-2}
	$M(H_2)_{disc}$	1.0(4)	5.5(4)	M_0
	$M(H_2)_{hvf}$	2.0(3)	1.5(4)	M_0
	$\dot{M}(H_2)_{hvf}$	0.04	0.2	$M_0\ yr^{-1}$
	P_{hvf}	4.0(42)	1.0(43)	$g\ cm\ s^{-1}$
	E_{hvf}	3.3(48)	3.8(48)	erg
3.	$\dot{P}_{hvf}$	2.5(30)	6.3(30)	$g\ cm\ s^{-2}$
	L_{hvf}	540	660	L_0
	$M(H_2)_{hot}$	0.3		M_0
4.	$\dot{M}(H_2)_{hot}$	0.3		$M_0\ yr^{-1}$
	$L(H_2)$	1800		L_0
	$L*$	2(5)		L_0
	$L*/c$	2.6(28)		$g\ cm\ s^{-2}$

1. : $X(CO) = 10^{-4}$ and $T_x(CO) = 40$ K

2. : $X(CS) = 10^{-9}$ and $T_x(CS) = 20$ K

3. : dynamical timescale, $t_d(CO) = 2pc/35kms^{-1} = 5\times10^4$ yr
$t_d(H_2) = 3pc/60kms^{-1} = 5\times10^4$ yr

4. : lifetime of hot $H_2 = t_{hot} \approx 1$ yr.

considerable age.

Although the bulk of the mass composing the outflow gas is most probably derived from the entrainment and sweeping up of ambient cloud material, an as yet undefined portion of the high-velocity CO emission will, however, arise directly from the molecular gas forming the high-velocity wind itself. With sufficient angular and spectral resolution it should therefore be possible to isolate the swept-up ambient gas from the molecular wind which provides the momentum to drive the shocks. As will be discussed in Sec.[6.4.c], this distinction is extremely important if one hopes to gain a better understanding of the physical nature of the central mass-loss mechanism

One of the main goals of this work is to test whether the high-velocity CO emission in the DR21 molecular outflows is truly a tracer of the post-shock gas behind the hot shocks that give rise to the anomalously luminous H_2 line emission. As pointed out by Beckwith (1980) and later discussed by Fischer et al. (1985), if the shock-excited H_2 line radiation accounts for most of the post-shock cooling in an isothermal shock then the rate at which energy is radiated in these lines is expected to be about equal to the rate at which bulk kinetic energy is deposited into the post-shock gas. Thus, assuming constant outflow velocities over the flow lifetime, one would expect that, $E_{hvf}/t_d = L_m = L(H_2)$, where t_d is the outflow lifetime, $L(H_2)$ is the total luminosity in all H_2 cooling lines, and L_m is the flow mechanical luminosity as given in Table[5.2.1]. For the case of the DR21 outflow, it is found that the total dereddened H_2 luminosity in the shock-excited jets is a factor of 2 to 3 greater than the mechanical luminosity in the flow as estimated from the high-velocity CO emission. This contradiction may result from three causes, namely, (i) the dereddened H_2 luminosities may be too high due to an

overestimate of the 2.12 μm extinction, (ii) the CO emission may not probe the entire mass of post-shock gas and (iii) the crude estimate of the flow lifetime may be too large. Although it is difficult to differentiate between these various options it is probably simplest to contend that a solution to this problem lies in an overestimate of the flow lifetime. If, as is highly likely, the flow has decelerated with age, then the mean outflow velocity would be larger than observed at present; this would then reduce the flow lifetime, resulting in a corresponding increase in the mechanical luminosity. A factor of 2 to 3 reduction in the outflow age (i.e. $t_d \approx 10^4$ yr) is required in order to balance the isothermal shock conditions.

Finally, it is interesting to compare the total luminosity radiated in shock-excited H_2 line emission with the bolometric luminosity of the DR21 star-forming region, as the ratio of these two quantites can be used to parameterize the relative importance of shock heating/cooling to the overall energy budget. For the DR21 outflow source, a luminosity ratio, $L(H_2)/L* \approx 0.01$, is calculated, which is comparable to that derived previously for the analogous outflow sources associated with the NGC 2071 (Bally & Lane 1985) and Orion (Beckwith 1983) star-forming regions. Although the efficiency of generation of strong H_2 line emission depends critically on the particular stage of evolution of the outflow system under study (see, Sec.[6.4.c]) and also on the physical composition of the cloud environment in which it is embedded, empirically, it appears that for an outflow system in its most active stage, a good guess as to the upper limit of the luminosity in shocked H_2 line emission is ~ 1% of the bolometric luminosity of the central source.

5.4

THE IMPORTANCE OF CLUMPS IN THE HIGH-VELOCITY OUTFLOW GAS

5.4.(a) A THEORETICAL PERSPECTIVE

Considerable evidence has accumulated from our infrared and millimeter-wave observations that the dense molecular gas participating in the DR21 ouflow may be inhomogeneous in density and possess complex velocity structure. In particular, the small beam filling factors, $f < 0.1$, characteristic of the emission in the high-velocity portions of the CO and CS profiles as well as the extremely broad wings characteristic to several of the shock-excited H_2 line profiles are best explained if the emission originates from an ensemble of rapidly moving, dense clumps with dimensions considerably smaller than the beam diameter. Several authors have attempted to investgate the effects of clumping upon observed line profiles, the most notable being the works of Norman & Silk (1980), Martin et al. (1985) and Richardson et al. (1986). In this section, several aspects of these models, in conjunction with the empirical constraints derived from the observations presented in Chapter 4, will be employed in order to determine the range of physical conditions that exist within the clumpy medium that consitutes the DR21 outflows.

In the following analysis, it is assumed that the basic characteristics of the observed profiles are reproduced by a model cloud consisting of optically thick fragments whose intrinsic velocity widths are much less than the observed profile width, which is produced by relative motion of the fragments. Any number of clumps are allowed to enter the beam, however, no two clumps are permitted to have the same V_{lsr}, thus radiative transfer effects are nonexistent.

For each clump in the beam, the column density of H_2 gas, $N(H_2) = n_c.r_c$, through the centre of the clump is related to the observed CS and ^{13}CO column densities, in LTE, by

$$n_c.r_c = 7.3\times10^{22} \left[\frac{T_x}{40\ K}\right]^2 \left[\frac{X(13)}{10^{-6}}\right]^{-1} \left[\frac{\Delta V(13)}{1\ kms^{-1}}\right] \tau_{13}\ \ cm^{-2} \qquad (5.4.1)$$

and

$$n_c.r_c = 1.8\times10^{23} \left[\frac{T_x}{20\ K}\right]^2 \left[\frac{X(CS)}{6\times10^{-10}}\right]^{-1} \left[\frac{\Delta V(CS)}{1\ kms^{-1}}\right] \tau_{CS}\ \ cm^{-2} \qquad (5.4.2)$$

where, τ_{13}, and, τ_{CS}, are evaluated for the ^{13}CO J=1-0 and $C^{32}S$ J=2-1 transitions, respectively. As the CS emission is more sensitive to high volume densities than ^{13}CO, let us first outline the analysis using this molecule.

Having used the observed line optical depth to derive the combined column density factor $n_c.r_c$, a second independent equation relating n_c and r_c is then required to determine each separately. If the clumps are self-contained, relatively long-lived entities, then their existence must result from constructive interplay between the physical conditions characteristic to both the clump and interclump medium (ICM). Accordingly, values for n_c and r_c are solved for three different physical circumstances, namely, that the clumps are (i) in virial equilibrium, (ii) in free-fall collapse, and (iii) ram-pressure confined by interaction with the outflow gas

(i) Clumps in virial equilibrium ;

The velocity which determines the dynamical evolution of the clump is the velocity of H_2 molecules, $\Delta V_c(H_2)$, which for purely thermal motions is roughly a factor of three larger than the radiatively important velocity, $\Delta V_c(CS)$ or $\Delta V_c(CO)$; at normal molecular cloud temperatures, $\Delta V_c(H_2) \approx 1$ kms^{-1}. For a virialised, isothermal clump, with $\mu = 1.36$, the following relationship results

$$\Delta V_c(H_2) = 1.9 \left[n_c / 10^4 cm^{-3} \right]^{0.5} \left[r_c / 1pc \right] \quad kms^{-1} \qquad (5.4.3)$$

Combining eqns.(5.4.2) & (5.4.3) then gives the characteristic density and size of a typical clump

$$n_c = 10^6 \left[\frac{T_x}{20\ K} \right]^4 \left[\frac{X(CS)}{6\times10^{-10}} \right]^{-2} \left[\frac{\Delta V_c(CS)}{\Delta V_c(H_2)} \right]^2 \tau_{cs}^2 \quad cm^{-3} \qquad (5.4.4)$$

and

$$r_c = 0.05 \left[\frac{T_x}{20\ K} \right]^{-2} \left[\frac{X(CS)}{6\times10^{-10}} \right] \left[\frac{\Delta V_c(H_2)}{1\ kms^{-1}} \right] \left[\frac{\Delta V_c(H_2)}{\Delta V_c(CS)} \right] \tau_{cs}^{-1} \quad pc \qquad (5.4.5)$$

and the mass of each clump is

$$M_c = 19 \left[\frac{T_x}{20\ K} \right]^{-2} \left[\frac{X(CS)}{6\times10^{-10}} \right] \left[\frac{\Delta V_c(H_2)}{1\ kms^{-1}} \right]^3 \left[\frac{\Delta V_c(H_2)}{\Delta V_c(CS)} \right] \tau_{cs}^{-1} \quad M_0 \qquad (5.4.6)$$

Taking, $\tau_{CS} < 1$, as an upper limit to the optical depth in the high-velocity wings of the CS J=2-1 transition, and assuming a partially turbulent clump medium with $\Delta V_c(H_2)/\Delta V_c(CO) = 2$ and $T_X = 20$ K, then the

typical clump properties are, $n_c < 2\times10^5$ cm^{-3}, $r_c > 0.1$ pc and $M_c > 40$ M_0. The corresponding clump parameters, as derived from an analogous analysis of the ^{13}CO emission, where it is assumed that $\tau_{13} < 1$ and $T_x(CO) = 30$ K, are $n_c < 2\times10^4$ cm^{-3}, $r_c > 0.4$ pc and $M_c > 160$ M_0. A direct comparison of the CS and ^{13}CO predictions therefore lends strong evidence that favours the existence of a gravitationally bound two-phase medium, in which the densest and probably also the coolest gas is confined to small clumps (radiating in CS emission) that are mixed in with a warmer and more diffuse ICM (seen primarily in CO emission).

(ii) Clumps in gravitational free-fall ;

The Jeans mass for a gas of density, n_c, and temperature, T_c, can be expressed as follows

$$M_j = 10 \left[\frac{T_c}{25\ K}\right]^{3/2} \left[\frac{n_c}{10^4 cm^{-3}}\right]^{-1/2} M_0 \qquad (5.4.7)$$

Thus, for a typical clump density, $n_c = 10^5$ cm^{-3}, and temperature range, T_c = 10-50 K, the corresponding Jeans mass falls in the range, M_j = 1-10 M_0. Refering back to the virial analysis described in the preceeding section, where it was found that $M_c > 40$ M_0, it appears that if the clumps are primarily held together by their own gravitational potential then collapse of the most massive clumps is conceivable, if not inevitable. It is then a simple matter to show that if the clumps are in free-fall collapse, rather than virial support, the clump properties can be derived from the virial analysis, simply by rescaling in the following manner

$$n_c(\text{free-fall}) \longrightarrow 2.n_c(\text{virial})$$

$$r_c(\text{free-fall}) \longrightarrow r_c(\text{virial})/2$$

$$M_c(\text{free-fall}) \longrightarrow M_c(\text{virial})/4$$

The physical properties expected to characterize the free-falling clumps are then, $n_c < 4\times10^5$ cm^{-3}, $r_c > 0.05$ pc and $M_c > 10\ M_0$, for $\tau_{cs} < 1$.

(iii) Clumps in ram-pressure confinment ;

As the millimeter-wave observations show little evidence for substantial variations in the gas temperature, i.e. T_k = 10-40 K, but suggest quite large variations in volume density, i.e. $n(H_2) = 10^3$-10^6 cm^{-3}, any model which assumes a two-phase medium composed of high-density clumps immersed in a more diffuse ICM cannot preserve its initial identity under purely thermal conditions owing to pressure imbalance between the two gas phases. It is therefore tempting to follow the conclusions of Norman & Silk (1980) and investigate a model in which the dense clumps are ram-pressure confined by dynamical interaction with the high-velocity outflow gas, which presumably constitutes the ICM. If the clumps are ram-pressure confined then the following condition holds

$$n_c = n(\text{ICM}) \left[\delta V_c / \Delta V_c(H_2) \right]^2 \qquad (5.4.8)$$

where, n(ICM) is the density in the ICM medium, $\Delta V_c(H_2)$ is the internal

sound speed in the clump, and, δV_c is the clump velocity relative to the outflow velocity, or, when expressed in more familiar astrophysical terms

$$n_c = 10^5 \left[\frac{n(ICM)}{10^3 cm^{-3}}\right] \left[\frac{\delta V_c}{10\ kms^{-1}}\right]^2 \left[\frac{1\ kms^{-1}}{\Delta V_c(H_2)}\right]^2 \quad cm^{-3} \qquad (5.4.9)$$

The clump radius can be derived by substitution of eqn.(5.4.9) into eqn.(5.4.2), giving

$$r_c = 0.15 \left[\frac{T_x}{20\ K}\right]^2 \left[\frac{X(CS)}{6\times10^{-10}}\right]^{-1} \left[\frac{n(ICM)}{10^3 cm^{-3}}\right]^{-1} \left[\frac{\delta V_c}{10\ kms^{-1}}\right]^{-2} \tau_{cs} \quad pc \qquad (5.4.10)$$

Again, using as an upper limit, $\tau_{cs} < 1$, the characteristic clump properties, $n_c = 10^5\ cm^{-3}$ and $r_c < 0.15$ pc, are obtained, which agree favourably with those derived previously. However, an advantage inherent to the ram-pressure mechanism that does not apply under conditions of gravitational confinment is that in the former case, the acceleration of clumps of different mass and size leads naturally to a correlated dispersion in clump velocity.

As a consequence of ram-pressure acceleration, a cloudlet of size r_c, if acted upon over a path length, d, aquires a velocity

$$V_c = \epsilon\ \Delta V_c(H_2)\ [d/r_c]^{1/2} \qquad (5.4.11)$$

where, ϵ, is a geometrical factor of order unity; alternatively

$$V_c \approx 3 \left[\frac{d}{1\ pc}\right]^{1/2} \left[\frac{r_c}{0.1\ pc}\right]^{-1/2} \left[\frac{\Delta V_c(H_2)}{1\ kms^{-1}}\right] \quad kms^{-1} \qquad (5.4.12)$$

Thus, to accelerate the clumps to velocities of order, $3 < v_c < 10$ kms^{-1} (half-width at zero-intensity of CS profiles), over a distance of 1 pc, requires corresponding clump radii in the range, $0.1 < r_c < 0.01$ pc. Moreover, as a result of the inverse relation between clump velocity and clump radius, the largest and most massive clumps are expected to be the slowest moving whilst the smallest clumps are the fastest moving. This predicted velocity dispersion, in which the smallest clumps give rise to the emission which forms the faint high-velocity wings of the observed profiles, may then explain why the beam filling factors apparently decrease with increasing velocity offset from the line core.

As for the origin of the clump mass function, several interrelated processes may be responsible, namely, (i) dynamical interaction between the outflow gas and pre-existing density inhomogeneities within the parent molecular cloud, (ii) entrainment of material into the flow resulting from fluid-dynamical instabilities at the outflow/cloud boundary, (iii) the fragmentation or break-up of larger clumps to form smaller clumps, and (iv) if collision times scales are sufficiently short, the coalescence of small clumps to form progressively larger clumps. If, as was shown previously, the largest clumps have masses exceeding the Jeans limit (i.e $M_c > 10\ M_0$), then it is further conceivable that impaction of pre-existing density condensations in the ambient cloud by the high-velocity outflow may lead to accelerated high-mass star formation over time scales comaparable to the outflow lifetime, i.e. 10^4-10^5 yr.

Important to understanding the origin of the clumps is an estimate of the typical clump lifetime which, for steady-state equilibrium conditions, may give useful information on the rate at which new clumps are generated. For the slowest moving clumps the primary destruction process is probably the continuous leakage of mass caused by the frictional drag between the clump and the ICM. However, for the faster moving clumps, probably the most effective and certainly the most rapid destruction mechanism involves the evaporation of material from the clump surface through shock heating. The lifetime of a clump is then determined by the time taken for a shock to traverse the clump, which is

$$t_{destroy} = (r_c/V_{shock})$$

$$= 10^5 \left[\frac{r_c}{0.1\ pc}\right] \left[\frac{\delta V_c}{10\ kms^{-1}}\right]^{-1} \left[\frac{n_c}{10^5 cm^{-3}}\right]^{1/2} \left[\frac{\dot{n}(ICM)}{10^3 cm^{-3}}\right]^{-1/2} yr \qquad (5.4.13)$$

The clump lifetime in the high-velocity flow is thus on the order of 10^3-10^5 yr, being shortest for the smallest and slowest moving clumps. To proceed with this line of thought, the preceeding argument suggests that once a clump is entrained into or swept up by the ouflow, if it is sufficiently massive, it will retain its identity for a major fraction of the flow lifetime. Although the largest clumps are relatively unaffected by shock evaporation, this is presumably not the case for the smaller clumps, which are destroyed in only a fraction of the flow lifetime. The continuous replenishment of the smaller clumps is then a prerequisite for their existence in the high-velocity outflow.

Further limits on the size scale and number of clumps filling the beam can be derived from an analysis of the smoothness of the emission in the high-velocity portions of the CO and CS profiles. The quantity of interest here is the fluctuation in antenna temperature, $\delta T_a^*/T_a^*$, between adjacent spectral elements of the profile. In essence, the smoothness of the profile wings depends on the number of clumps occupying each spectral-resolution element, which can be calculated from an estimation of the beam filling factor, f, as defined by eqn.(4.3.5).

Taking as an upper limit to the average antenna temperature of the HIGH-velocity components of the CO and CS line profiles at the central outflow position, $T_a^*(\text{wing}) \approx 1.0$ K, the values, $f \approx 0.1$ and 0.3, are obtained for excitation temperatures of $T_X = 40$ and 10 K, respectively. If the low values of f are interpreted as arising from nonuniform emission within the beam, presumably in the form of many isolated, optically thick clumps of size less than the beam diameter, then f may be expressed in terms of the number of clumps in the beam, N, the velocity dispersion within each clump, ΔV_c, the observed total profile width, ΔV_t, the characteristic size of each clump, r_c, and the beam diameter employed to make the observations, R, as follows

$$f(\text{wing}) = N \frac{\Delta V_c}{\Delta V_t} \left[\frac{r_c}{R}\right]^2 \approx 0.1$$

Thus, f can be viewed as the combined velocity and area dilution factor which, if, as argued in Sec.[4.3.f], the CO emission is thermalized, must decrease monotonically from unity at the line core to roughly one tenth of that value in

the far line wings. As show above, the observed order of magnitude drop in f cannot solely be explained by a velocity dependence in the excitation temperature but must result primarily from spatial and spectral fragmentation of the emission within the beam.

Refering back to the clump models described in the preceeding section, ΔV_c = 0.3 kms^{-1} and r_c = 0.1-0.05 pc are taken as characteristic properties of the clumps. Then, from the observed profile full-widths at zero intensity, $\Delta V_t(CS)$ = 20 kms^{-1} and $\Delta V_t(CO)$ = 60 kms^{-1}, and the projected beam diameter, R = 0.3 pc (for an assumed distance of 3 kpc), it is found that the total number of emitting clumps in the beam is, N(CS) = 60-240 and N(CO) = 130-500, respectively. Knowing the total number of clumps filling the beam, the number of clumps within each velocity-resolution element, $\Delta V_{res} \approx 0.5$ kms^{-1}, is then simply $N(\Delta V_{res}/\Delta V_t)$ and the typical fluctuation in intensity between adjacent resolution elements is $[\,(\Delta V_t/\Delta V_{res})/N\,]^{1/2}$. For the CS J=2-1 and CO J=1-0 lines, this analysis predicts fluctuations in the profile wings of order, $\delta T_a^*/T_a^*$ = 0.8-0.4 and 0.9-0.5, respectively.

These predicted ranges in intensity fluctuation can now be compared with the observed spectra. The tightest constraint regarding the smoothness of the intensity distribution in the line wings is observed from the high signal-to-noise CO J=1-0 spectrum taken at the outflow centre, as shown in Fig.[4.3.1]. Clearly, the random intensity fluctuation between adjacent velocity channels is no greater than 30% at any velocity in the wings were the line intensity is measured with confidence. Hence, considering the above predicted limits on, $\delta T_a^*/T_a^*$, one is forced to conclude that if the high-velocity portions of the CO profile originate from the superposition of emission from many randomly moving clumps, then the number of clumps required to fill the beam must be extremely large (i.e. N

> 500) and the characteristic size of each clump must be correspondingly very small (i.e. r_c < 0.05 pc) in order to preserve the inherent smoothness of the line wings. The clump models discussed previously can accomodate such small clump sizes only in the limit of very small line centre optical depths (i.e. τ < 0.5). This result is somewhat disconcerting as it contradicts the high optical depths (τ_{10} > 1) derived from comparison of the main and isotopes CO lines.

The foregoing analysis, although inconclusive, is useful in that it brings to notice the possibility that the combined assumption of optically thick emission in a highly clumpy medium, as has been assumed in the past by most workers in this field, may not provide a unique explanation for the apparent low beam-filling factors commonly derived for the high-velocity wings of optically thick line profiles. Rather, more elaborate radiative transfer codes, that take into account the presence of turbulence and the coupling of line photons between nearby clumps, may be justified. Such models can then be used to investigate the detailed physics underlying the observed lack of structure in the high-velocity wings of optically thick CO line profiles at both high-angular and high-spectral resolution.

More informative constraints on the velocity width and size distribution of the clumps in the DR21 and other outflow sources must await observations at higher spectral and spatial resolution in several transitions of a molecule. It is possible that observations of higher transitions in the submillimeter region, which are more sensitive to high densities and temperatures than the transitions observed here, may reap the best astrophysical returns.

5.5 THE CS ABUNDANCE IN THE HIGH-VELOCITY OUTFLOW GAS

Probably, one of the best available methods for calculating the CS abundance in the high-velocity gas is to compare the column density in the high-velocity wings of the optically thin CS J=1-0 emission with the column density over the same velocity range as derived from the optically thin ^{13}CO emission. Assuming local thermodynamic equilibrium and a single excitation temperature common to all energy levels of both the CS and CO molecules, the following expression is obtained for the ratio of the abundancies in the high-velocity emission

$$\frac{X(CS)}{X(^{13}CO)} = \frac{f(CS)}{f(CO)} \frac{N(CS)}{N(^{13}CO)} \qquad (5.5.1)$$

where, f, is the area filling factor. At the position of brightest high-velocity emission in the blue-shifted outflow lobe, the observed column densities result in the following abundance ratio

$$\frac{X(CS)}{X(^{13}CO)} = \frac{f(CS)}{f(CO)} \frac{3\times10^{14}}{2.5\times10^{16}} = 1.2\times10^{-2} \frac{f(CS)}{f(CO)}$$

There are two perspectives from which one can view this ratio. First, it could be naively assumed that all lines are emitted from the same volume of gas, ie. $f(CS)/f(CO) \approx 1$, so that $X(CS)/X(^{13}CO) \approx 1.2\times10^{-2}$ is taken to represent the actual abundance ratio in the outflow gas. This approach has a particularily interesting outcome as the best empirical estimate for this ratio in other dense clouds is, $X(CS)/X(^{13}CO) = 5\times10^{-5}$, (Thronson & Lada, 1984; Takano, 1986). Thus, if the CS and CO emissions are coexistive, then the results presented here imply that the high-velocity CS emission from the DR21 outflow lobes is overabundant relative to ^{13}CO by at least two orders of

magnitude. Kuiper, Zuckermann & Rodriguez-Kuiper (1981) and Thronson & Lada (1984) have already claimed evidence for an overabundance of CS, of similar magnitude, in the high-velocity gas associated with the Orion molecular outflow.

The enhancement of the CS abundance in molecular outflows was first predicted by Igleias & Silk (1978), and later by Hartquist, Oppenheimer & Dalgarno (1980) and Mitchell (1984), who present detailed model calculations of shock chemistry which indicate that although the CO molecule is hardly affected by the passage of a strong shock front, the sulphur-bearing molecules are overabundant by at least two orders of magnitude in the post-shock gas. It is exciting to conjecture that the large enhancement of CS in the DR21 outflow, obtained assuming $f(CS)/f(^{13}CO) \approx 1$, is caused by the same shocks which give rise to the anomalously bright vibrational H_2 line emission. If the large enhancement in CS is indeed real and if it does owe its origin to chemical processing in fast shocks, then the extremely extended and structured nature of the CS emission over the DR21 outflow, which is unlike any other molecular cloud source yet observed, may result directly from interaction between the dense gas comprising the quiescent cloud core and the energetic molecular outflows which permiate the DR21 star-forming region.

The prediction of a large overabundance of CS molecules in the DR21 and several other molecular outflow sources depends solely on the assumption that the CO and CS emissions arise from the same volume of gas (ie. equal filling factors). However, there is as yet no direct observational evidence in support of this claim. Indeed, from the low antenna temperatures observed in the high-velocity wings of the thermalized CO emission, it has already been suggested that small scale clumping within the outflow gas is most probably a

realistic occurrence. It is therefore conceivable that the large observed ratio of $N(CS)/N(^{13}CO)$ results primarily from a correspondingly low value of $f(CS)/f(^{13}CO)$, that is to say, the CS gas may be significantly more clumpy than the CO gas. Such a situation is intuitively acceptible, since the critical density of CO is approximately one order of magnitude lower than that of CS, so that the CO emission could arise from a less dense interclump medium whilst CS emission may arise primarily from higher-density clumps immersed within this medium. Assuming a CS relative abundance, $X(CS) = 6\times10^{-10}$, as derived from the LVG analysis, and taking the canonical terrestrial abundance for ^{13}CO, $X(^{13}CO) = 10^{-6}$, then, from the observed column densities the ratio of the beam filling factors is

$$\frac{f(CS)}{f(^{13}CO)} = \frac{X(CS)}{X(^{13}CO)} \frac{N(^{13}CO)}{N(CS)} \approx 0.08$$

It is therefore concluded that if the CO emission uniformly fills the beam, then, in order to account for the anomalously high CS column densities, the high-velocity CS gas must be clumpy and fill less than 10% of the beam area.

Although it is difficult to chose between the two available options, namely, (i) enhanced X(CS), and (ii) small f(CS), with the limited spatial resolution used for the current observations, it is noteworthy that the general theme emerging from most of the discussions presented in this chapter is that the high-velocity gas that constitutes the DR21 hypersonic outflows is most probably inhomogeneous in its density structure. Such conditions severely complicate analysis of the observations especially if the size of the clumps is smaller than the spatial resolution employed. It therefore follows that, further progress in this important area of molecular cloud structure is dependent on the application of

higher-angular resolution interferometer techniques, as isolation of individaual clumps may then be possible.

6.1 INTRODUCTION TO THE MODELS

A fundamental constraint governing the type of dynamical model chosen to explain the energetic activity associated with the DR21 outflows is that it must account for the *large luminosity* seen in the shocked H_2 line emission (~ 1800 L_0). Furthermore, the model must also predict an origin for the *high-velocity flows* (> 50 kms-1) and their *peculiar jet-like morphology*. There are five dynamical mechanisms for the large-scale excitation of vibrational H_2 which may individually or collectively explain the observed phenomenology, namely, (i) a cloud-cloud collision, (ii) an expanding HII region, (iii) a supernova explosion, (iv) a young high-mass stellar wind and, (v) an energetic protostellar outflow, the relative merits of which are discussed below.

6.2 THE CLOUD-CLOUD COLLISION MODEL

Previous millimeter-wave observations of CO, HCN and H_2CO (Dickel et al. 1978; Morris et al. 1974; Wilson et al. 1982), which show good agreement with the high-angular resolution CO and CS observations presented in Chapter 4, indicate the existence of two separate clouds seen in projection over the DR21/W75 region, one associated with the DR21/W75S star-forming complex and the other with the W75N molecular cloud. Both clouds are of similar mass ~ 5×10^4 M_0, have mean diameters ~ 25 pc, and core densities ~ 10^5 cm^{-3}. Although the line-of-sight velocity difference between the two clouds is ~ 12 kms^{-1}, the common spatial extent of both velocity components suggests that the

two clouds may be undergoing physical interaction. In particular, low-angular resolution observations of CO emission toward the DR21 cloud show a large-scale gradient in the radial velocity of the W75N component which may result from differential retardation in a cloud-cloud collision; the interaction appears to be most pronounced along a line-of-sight intercepting the DR21 cloud core (Dickel et al. 1978). Unfortunately, the CO observations presented herein are of too high angular resolution and insufficient field-of-view to perceive any large-scale kinematic structure similar to that observed by Dickel et al.

Assuming a deprojected intercloud motion, $V_{rel} \approx 15$ kms^{-1}, and that all of the presently observed bulk kinetic energy of both clouds can be efficiently channelled into radiative shock heating, a shock luminosity, L_S, of $4\times10^4 > L_S > 400\ L_0$, over a duration of $10^4 < d/V_{rel} < 10^6$ yr, where d is the cloud diameter, is potentially available from such a cloud-cloud collision. The estimated total luminosity in H_2 lines from DR21 ($\sim 1800\ L_0$) lies close to the middle, and well below the upper limit of this range.

The main advantage of invoking this mechanism to account for the H_2 line emission is that it is energetically favourable, being able to supply the required high luminosities in shock-excited emission at a steady rate over a long period of time. In this scenario the shocked H_2 delineates the interface between the two clouds which most probably takes the form of a thin wrinkled layer (or, series of layers) oriented perpendicular to the direction of cloud-cloud motion. In the case of DR21, a N-S relative motion of the clouds would explain the E-W orientation and sheet-like appearance of the H_2 line emission. The shock front will extend across the entire diameter of the cloud with an intensity distribution ($I_S \propto n_0.V_S^3$) which peaks at the cloud core and decreases

monotonically toward the edges. The break in H_2 line emission at the centre can be explained by a corresponding increase in the 2 μm extinction (Righini-Cohen et al. 1979).

Cloud-cloud collisions can result in gravitationally unstable regions in a gas cloud if the free-fall time of the compressed gas is less than the collision time-scale. This condition is most likely to occur for relatively slow collisions between cold, dense molecular clouds. Thus, an ongoing cloud-cloud collision, of duration > 10^5 yr, will not only explain the high H_2 luminosities but may also trigger massive star formation within or close to the DR21 cloud core; it is the photoionizing radiation from these newly-formed stars that gives rise to the luminous HII region as revealed in radio continuum emission. The neighbouring molecular cloud cores W75S and W75N do not lie along the proposed interaction zone and, most probably, are separate self-induced star formation centres, physically isolated from the dynamical influence of the cloud-cloud interaction.

This simple model might also account for the high-velocity flows and planar morphology of the H_2, and possibly the CO, line emission in DR21. As the two clouds collide a thin layer of highly compressed molecular gas will form at their interface. The build up of a radial pressure gradient within the interface layer will then force the shocked material to flow outwards at supersonic velocities from the centre towards regions of lower pressure, which will preferentially be along an E-W plane, perpendicular to the relative cloud-cloud motion. It is this high-velocity planar outflow that may give rise to the broad wings and highly-collimated emission observed in the H_2 and CO lines.

For the above suggested geometry, in which the appearance of the H_2 lobes reflect our edge-on perspective of a supersonically expanding layer of

compressed and shocked gas, the broadest H_2 and CO line profiles are expected to be localized to the very centre of the DR21 cloud core and will become monotonically narrower with increasing outwards displacement. On the whole, the profiles should remain rather symmetric with position over the high-velocity outflow region. Both of these predictions are notable characteristics of the observations presented in Chapter 4. Furthermore, if the density profile of shocked molecular gas is sharply peaked in the N-S direction at the mid-section of the compressed layer then the large degree of collimation and internal sinuosity of the H_2 emission-line source would be as expected for an almost edge-on layer that is broken at the centre by heavy internal or foreground extinction. The slender filament of bright CS emission extending over several parsecs to the west of the DR21 cloud core, may represent yet another manifestation of the cloud-cloud collision model. Indeed, the exceedingly high mass associated with this feature ($> 10^4$ M_0) makes it hard to argue otherwise.

Unfortunately the simple cloud-cloud collision scenario, as portrayed above, is plagued by two major drawbacks. First, although non-magnetic shock models predict abundant production of H_2 line emission in low-velocity shocks, the more recent MHD shock models of Draine, Roberge & Dalgarno (1983), being the most elaborate published to date, predict v=1-0 S(1) line intensities more than an order of magnitude lower than the peak observed intensities for $V_S <$ 20 kms^{-1}. This apparent discrepancy may be somewhat relaxed if, as argued above, the shocked layer is viewed edge-on rather than face-on as assumed in the model calculations because then the line-of-sight column density of hot H_2 molecules can be increased in proportion to the diameter/thickness ratio of the shocked layer. As suggested by Draine et al., a definitive test for the existence of low-velocity shocks in dense molecular clouds, and hence the feasibility of the cloud-cloud collision model, could involve a search for strong, collisionally

excited [OI] 63 μm and 146 μm line emission (e.g. Genzel et al. 1985). A high ratio of rotational to vibrational H_2 line emission would also be expected.

The second problem faced by this model, again arising from a direct comparison of the observations with theory, involves the acceleration of a small portion of the compressed cloud material to velocities in excess of ~ Mach 50. Recent three-dimensional numerical simulations of low-density interstellar cloud collisions, presented by Lattanzio et al. (1985), confirm the predicted formation of a thin layer of compressed outflowing material located along the interaction zone, but cannot generate the large velocities characteristic to parts of the DR21 outflow. Ejection velocities in the shocked cloud material, as predicted by these models, are significantly less than Mach 20; a simple analytical check further confirms the numerical predictions.

We leave the cloud-cloud collision scenario, therefore, with the concluding remark that although such a model has many attractive benefits, it is most unlikely that a cloud-cloud collision can explain the dynamical origin of the highest-velocity gas flows which play an important role in the making of the enigmatic phenomena which characterize the DR21 star-forming region. Other physical mechanisms that are capable of accelerating the dense outflow gas to hypersonic velocities must therefore be investegated.

6.3 THE EXPANDING HII REGION MODEL

Deep within the core of the DR21 molecular cloud complex lies an extremely luminous compact HII region. Fig.[5.1.2] displays an overlay of the 2 cm radio continuum (Roelsfema, private communication) on the contours of

infrared H_2 line-emission. It is immediately apparent from the small size of the HII region relative to that of the shocked gas region that the H_2 line emission in the outer parts of the lobes cannot be caused by expansion of the HII region alone. However, it remains to determine to what extent the H_2 line emission bordering on the HII region could be stimulated by the expansion.

The mechanical energy flux available from the isotropic expansion of an HII region can be expressed in the following manner

$$L(HII) = E_{exp}/t_{exp} \approx (n_e+n_p)\ k\ T_e\ 4\ \pi\ (r_{exp})^2\ V_{exp} \qquad (6.3.1)$$

where, n_e and n_p are the electron and proton particle densities, T_e is the temperature of the ionized gas, r_{exp} is the radius of the HII region, V_{exp} is the velocity of expansion and t_{exp} is the expansion time. For the DR21 compact HII region, $T_e \approx 10^4$ K, $r_{exp} \approx 0.3$ pc and $n_e \approx 2.5\times10^3$ cm^{-3} (Harris 1973). If the HII region expands supersonically at $V_{exp} = 40$ kms^{-1}, as indicated by the broad radio recombination line profiles discussed in Sec.[4.3.(g)], then $t_{exp} < 10^4$ yr and $L(HII) \approx 115\ L_0$. This predicted luminosity is more than one order of magnitude lower than that inferred from the H_2 line observations along the line-of-sight to the DR21 HII region and, therefore, cannot account for the bulk of the observed shock phenomenology. The HII region expansion, however, may account for some of the diffuse H_2 line emission immediate to the ionization front, especially in the eastern lobe where the lower H_2 intensity contours follow closely the outer boundary of the HII region. It is therefore conceivable that a dense shell of swept-up ambient molecular gas may be associated with the expanding HII region shock front. Indeed, the existence of such a dense shell has already been inferred from the CO velocity-channel maps (Sec.[4.3.d]) and the CS J=2-1/J=1-0 line-intensity

ratio plots (Sec.[4.4.e]).

In accordance with the discussion in Sec.[4.1], it is conceivable that the HII region is a "blister" located close to the back surface of the DR21 molecular cloud and may not be physically associated with the DR21 molecular outflow. The main reason why the star(s) that ionize the compact HII region cannot simultaneously drive the observed outflows, at this present epoch, derives from recombination time scale considerations. In essence, it is most probable that the "classical" picture of the birth of an HII region may be incorrect because it ignores the role of pre-main-sequence mass loss in the formation of cavities around the star and in controlling the escape of Lyman continuum radiation (Spitzer 1978; Bally & Scoville 1982; Simon et al. 1983). For a star having a Lymann continuum flux, N_{lyc}, a mass loss rate, $\dot{M}_w$, at a velocity, V_w, the Lyman continuum radiation is effectively trapped within a few stellar radii for mass-loss rates given by (Wright & Barlow 1975)

$$\dot{M}_w > \dot{M}_{crit} = m(H)\ V_w \left[4\ \pi\ N_{lyc}\ (R_i/\alpha)\right]^{1/2} \qquad (6.3.2)$$

where, R_i, is the radius at the origin of the flow and, α, is the Case B recombination coefficient ($\alpha = 2.60\times10^{-13}$). When expressed in more familiar astrophysical units, the foregoing expression becomes

$$\dot{M}_{crit} = 10^{-7} \left[\frac{V_w}{100\ kms^{-1}}\right] \left[\frac{N_{lyc}}{10^{46}s^{-1}}\right]^{1/2} \left[\frac{R_i}{10^{12}cm}\right]^{1/2} M_0 yr^{-1} \qquad (6.3.3)$$

For $N_{lyc} = 10^{48}$ photons s^{-1}, $R_i = 10^{14}$ cm and $V_w = 100$ kms^{-1}, $\dot{M}_{crit} = 10^{-5}\ M_0\ yr^{-1}$. Similarily, if the mass loss originates from a disc surrounding a star at a distance R_d from the star, the Lyman $\frac{n}{\lambda}$ continum is confined to a

region a few times R_d in radius if $\dot{M}_w > \dot{M}_{crit}$. The DR21 molecular outflow most probably has a mass-loss rate $\dot{M}_w > 10^{-3}$ M_0 yr^{-1}, at an outflow velocity $V_w < 100$ kms^{-1}. Hence, according to the above argument, it is almost certain that the mass-loss rate of the DR21 high-velocity flow is sufficient to inhibit the formation of an extended ionized envelope. It is therefore concluded that the object that powers the molecular outflow cannot simultaneously ionize the DR21 HII region.

The photon trapping problem can, however, be circumvented if the momentum in the outflow gas does not dissipate too rapidly, in which case, the shocks may survive for a relatively long time following the demise of the outflow stage. In such a picture, it may be possible that the shocks we presently observe outline a decaying outflow which has been created, sometime in the past, by the star(s) that are now observed as the exciting agents of the thermal radio continuum emission. This two-stage evolutionary model, in which pre-main-sequence (PMS) outflow preceeds the approach of the star onto the ZAMS, is consistent with the dynamical age of the CO outflow ($\sim 5\times10^4$ yr) which, in turn, is comparable to the PMS evolution time of a massive star ($\sim 10^5$ yr for $M > 10$ M_0), i.e. the time the star takes to evolve from the formation of an hydrostatic, optically thick core to the main sequence (Appenzeller 1982; Larson 1973; Iben 1965).

Although a two-stage evolutionary model is highly attractive it does have one major shortcoming, in that, the CO observations presented in Sec.[4.3] suggest that the central object is still undergoing excessive mass-loss at the present epoch and thus cannot be the ionizing agent for the DR21 HII region. It may still be possible, however, that the small scale outflow localized to the DR21 outflow source may represent a new mass-loss outburst phase, implying

that the outflow process may evolve through periodic and short-lived, but highly-energetic, bursts rather than a continuous flow taking place over the entire outflow lifetime. The escape of ionizing photons may then take place during an inactive phase of the mass-loss cycle. It is worth noting that the expansion lifetime of the DR21 HII region ($t_{exp} < 10^4$ yr), which can be taken to define an upper limit to the lifetime of the quiescent mass-loss phase, is, indeed, comparatively short in comparison to the total outflow lifetime ($\sim 5\times10^4$ yr).

To summarize the foregoing discussion, it is almost certain that the HII region expansion cannot generate sufficient driving pressure to account for the large luminosity observed in H_2 line-emission, nor can it explain the extremely extended and structured morphology of the shocked outflow gas. The location of the DR21 HII region along the line of sight is as yet undetermined. However, the existence of high mass-loss rates associated with the central driving object in conjunction with the appearance of the radio continuum maps suggest that the HII region may be a blister located on the back surface of the DR21 cloud and thus may be dynamically and radiatively isolated from the central outflow system.

6.4 THE SUPERNOVA EXPLOSION AND STELLAR WIND MODELS

6.4.(a) SETTING-UP OF THE INITIAL CONDITIONS

One of the fundamental questions that arise from the observations presented in this thesis is: "what is the source of the energy and momentum required to drive the high-velocity outflows and how do these physical quantities change

with time?" The evolution of a stellar wind within a dense molecular cloud depends primarily on whether the wind energy is released in a single burst (i.e. a supernova expolosion) or over an extended period (i.e. a continuous stellar wind) and also on the initial wind velocity (Beckwith, Natta & Salpeter 1983).

As a first-order approximation, simple self-similar solutions can be used to derive and compare the physical parameters predicted by different flow models. Several of the models to be investegated here, have previously been used by Beckwith et al. (1983) to investigate the energetics of the Orion outflow source. More recently, an extremely informative paper by Dyson (1984), describes how a "simple minded" observer can manipulate the similarity solutions to derive information on the wind parameters from the observed flow characteristics, such as shock velocity, shock radius and outflow mass. Dyson also investigates the more realistic case of a stellar wind within a molecular cloud characterized by a radial density gradient.

The assumptions implicit in the following interpretation of the flow characteristics, are (1) that the outflow is spherically symmetric, (2) that it is the hypersonically expanding shock front and associated shell of dense swept-up ambient material which gives rise to the observed H_2 and CO line emissions, respectively, and (3) that magnetic fields play a minor role in the dynamical evolution of the outflow.

For the case of the DR21 outflow, and for that matter, most other outflow sources discovered to date, the density distribution of the parent molecular cloud is most probably not spherically symmetric, however, it is contended that the overall energetics of the problem would not be greatly different from the spherically symmetric case. A similar point of view has been expressed recently

by Okuda & Ikeuchi (1986) and Kwok & Volk (1986), who used spherically symmetric, self-similar calculations in order to investigate the importance of radiation pressure for driving bipolar outflows in molecular clouds characterized by a radial density gradient. This particularly realistic situation is considered as of the models investigated below.

Solution of the similarity equations gives either the initial total energy E_0 for the case of an explosive event, or the wind mechanical luminosity L_W for the case of a constant luminosity stellar wind. The input parameters to these equations are the observable quantities, the shell (or shock) radius R_S, the shell (or shock) velocity V_S, the stellar wind velocity V_W, and the pre-shock molecular cloud density, n_0. Unfortunately, from H_2 emission-line observations alone, the pre-shock density is not directly obtainable and must be calculated using an intermediary shock model together with several naive assumptions. The method used to estimate the mean pre-shock number density from the observed total luminosity emitted in shock-excited H_2 lines, is essentially an energy conservation argument, and is outlined below.

The fundamental assumption is that the H_2 line emission arises from the hot post-shock gas created by the supersonic expansion of a stellar wind bubble into a dense molecular cloud medium. With reference to the shock models discussed in Sec.[5.2], it is anticipated that shock velocities in the range, $10 < V_S < 50$ kms^{-1}, and pre-shock number densities, $no > 10^5$ cm^{-3}, are prerequisites for the excitation of strong H_2 line emission. For these initial conditions, eqn.(2.2.1) predicts that the post-shock temperature will be in the range 10^3-10^5 K. Over this temperature range, the dominant coolant in a cloud is vibrationally excited H_2 (McKee & Hollenbach 1980). Therefore, it will be taken for granted that the bulk of the kinetic energy of the stellar wind responsible for driving the

high-velocity outflows is converted into radiation by H_2 molecules. To allow for some degree of flexibility, an efficiency factor, ϵ, is introduced, which specifies the fraction of the total mechanical luminosity which emerges in the infrared lines of the H_2 molecule.

To proceed, let us first calculate the total H_2 luminosity expected from a spherically symmetric shock impinging upon a medium of mean density, $\rho_0 = n_0 \mu_0 m(H)$, where $\mu_0 \approx 2.0$. The pressure required to push the shock is given by

$$P_S = \left[n_0 \mu_0 m(H) \right] V_S^2 \qquad (6.4.1)$$

As the shocked region is assumed to be a spherical shell of radius R_S on the sky, then the total force acting on the shell is simply, $(4 \pi R_S^2) P_S$. (It is worth noting, that these order of magnitude estimates are also appropriate for the case of a swarm of colliding cloudlets within the bubble forming the shock, since the working surface area would still be of the order of the square of the affected region). Having defined the integrated force acting on the shell, the total mechanical luminosity is then given by

$$L_m = 4 \pi R_S^2 \left[n_0 \mu_0 m(H) \right] V_S^3 \qquad (6.4.2)$$

Introducing the conversion efficiency factor, ϵ, described earlier, then the total H_2 line luminosity predicted is

$$L(H_2) = 4 \pi \epsilon R_S^2 \left[n_0 \mu_0 m(H) \right] V_S^3 \qquad (6.4.3)$$

To estimate the overall efficiency, it seems appropriate to return to the best studied and brightest H_2 source, the Orion molecular outflow, for which, much

detailed theoretical modelling has been made. The most comprehensive shock models are those presented by Chernoff et al. (1982) and Draine et al. (1982) who, by matching their numerical models with the observations of Beckwith et al. (1983), find that the Orion shocks are best fitted by the following physical parameters; $L(H_2) = 300\ L_0$, $R_S = 2\times10^{17}$ cm, $V_S = 36$ kms^{-1} and $n_0 = 2\times10^5$ cm^{-3}. Inserting these optimum values into eqn.(6.4.3), gives, $\epsilon = 0.1$, as a best estimate. Further assuming that the environments in the Orion and DR21 molecular outflows are broadly similar, then eqn.(6.4.3) becomes

$$L(H_2) = 600 \left[\frac{\epsilon}{0.1}\right] \left[\frac{R_S}{1.0\ pc}\right]^2 \left[\frac{n_0}{10^4 cm^{-3}}\right] \left[\frac{V_S}{20\ kms^{-1}}\right]^3 L_0 \qquad (6.4.4)$$

From the observations presented in Sec.[4.2] the total luminosity in H_2 line emission in the DR21 outflow region is 1800 L_0 at a shock radius of roughly $R_S = 1.5$ pc and with a shock velocity of order 25 kms^{-1} (FWHM of H_2 S(1) line profiles). Substitution of these observed values into eqn.(6.4.4) results in a value for the pre-shock density, $n_0 \approx 7\times10^3$ cm^{-3}. In order to simplify the analysis, a mean pre-shock density , $n_0 = 10^4$ cm^{-3}, a shock velocity, $V_S = 25$ kms^{-1}, a shock radius, $R_S = 1.5$ pc, and a total H_2 line luminosity, $L(H_2) = 1800\ L_0$, will be taken as characteristic values. It is acknowledged that variations in magnetic field strengths between different star-forming molecular clouds may exist and that these variations may somewhat influence the above naive assumptions, however, it is stressed that present interest is only in the macroscopic details of the outflow process and not in the detailed microscopic structure of the flows which may indeed be severely distorted by the effects of magnetic pressure and non-uniform ambient density.

For a stellar wind/explosion model, the evolution of the H_2 luminosity can be broadly disected into three distinct phases, namely;

Phase 1 : "dissociated phase", characterized by $V_S > 50$ kms^{-1}. Little or no H_2emission is produced over a duration, $t = t_{diss}$.

Phase 2 : "luminous phase", applicable for $10 < V_S < 50$ kms^{-1}. Strong H_2 emission over a period of time, $t = t_{lum}$.

Phase 3 : "non-luminous phase", applicable for $V_S < 10$ kms^{-1}. The velocity is too low in order to excite significant vibrational H_2 line emission.

Obviously, the relative duration of these phases depends strongly on the initial wind velocity and on the deceleration of the shock front, which can vary significantly from model to model. Physical circumstances which result in, $t_{lum} \gg t_{diss}$, are the most favourable to observation because the relative number of such sources per unit area on the sky will be greatest, therefore, they will presumably be the easiest to find.

6.4.(b) THE SUPERNOVA EXPLOSION MODEL

The interaction of supernovae with molecular clouds is a subject of growing interest. Supernova remnants are observed to collide with dense clouds (Wooten 1977; Scoville et al. 1977; Burton et al. 1986), and have been suspected of inducing localized star formation. Moreover, Beckwith et al. (1978) have even

gone so far as to suggest that a supernova may have played a role in creating the shocked H_2 emission and high-velocity ouflows associated with the Orion Molecular Cloud. Here, the opportunity is taken to revitalize this notion, and thereby consider the observable consequences of a supernova having exploded in the recent past within the DR21 molecular cloud core.

One must first, however, answer the obvious question : "will the cloud harbouring the supernova survive the initial explosion or will it disintegrate under the impact?" This question is most simply answered through a comparison of the initial explosion energy (~ 10^{51} erg) with the clouds gravitational binding energy. In the simplest case of a spherical, homogeneous cloud of mass M_c and number density n_c, the gravitational binding energy E_g will be

$$E_g = 4\times10^{40} \left[M_c\right]^{5/3} \left[nc\right]^{1/3} \quad \text{erg} \qquad (6.4.5)$$

For the DR21 cloud core, where, $M_c \approx 5\times10^4\ M_0$ and $n_c \approx 5\times10^4\ cm^{-3}$ (viz. Sec.[4.4] & Table[5.2.1]), this gives, $E_g \approx 10^{50}$ erg, which is an order of magnitude lower than the initial supernova explosion energy. However, much of the energy of a supernova in a dense cloud is probably lost by absorption on dust, and radiation in the infrared, so the available energy for disruption of the parent cloud is only a small portion of the initial explosion kinetic energy. Wheeler, Mazurek & Sivaramakrishnan (1980) have considered this problem and conclude that large clouds, with $M_c > 10^4\ M_0$, will absorb the initial dynamical effects of a supernova explosion with only small reprocussions. This criterion for cloud survival is easily satisfied for the specific case of the DR21 molecular cloud.

In a homogeneous medium, a supenova remnant (SNR) passes through four evolutionary stages: (1) "Ejecta dominated", or free expansion ($R_S \propto t$); The mass of the ejecta exceeds that swept up in the ambient medium so that most of the energy is in kinetic form. (2) "Sedov-Taylor", or adiabatic ($R_S \propto t^{2/5}$); The swept-up mass, M_S, exceeds the total ejected mass for $R_S > 1.9(M_S/M_0)^{1/3}$ $(n/10^4\ cm^{-3})^{-1/3}$ pc, and beyond this radius the evolution of the remnant approaches the Sedov-Taylor similarity solution (Sedov 1959). (3) "Radiative" ($R_S \propto t^{2/7}$); Energy losses due to radiation lead to the formation of a cold dense shell surrounding a hot interior. (4) "Merge with the interstellar medium"; When the shell velocity is comparable to the r.m.s. velocity in the ISM and the pressure is comparable to the ambient value, the SNR merges with the ISM.

Models describing the evolution of a Type II SN in a dense molecular cloud have been presented by (Shull 1980a and Wheeler, Mazurek & Sivaramakrishnan 1980). The initial free expansion and adiabatic (Sedov) phases are extremely short, and at high cloud densities may even be absent. The expansion quickly evolves to the radiative phase (100 yr at $n = 10^4\ cm^{-3}$), thus forming a cold, dense shell which moves outward just inside a shock front of radius R_S and velocity V_S. A similarity analysis of the mass, momentum and energy conservation equations results in the following self-similar solutions.

$$R_S(t) = 1.3\times10^{-11}\ (E_0/n_0)^{3/14}\ (t)^{2/7}\ \text{pc} \qquad (6.4.6a)$$

$$V_S(t) = 9.8\times10^{5}\ (1/A)\ [R_S(t)/t]\ \text{kms}^{-1} \qquad (6.4.6b)$$

$$M_S(t) = 3.5\times10^{-2}\ \{4/3\ \pi\ [R_S(t)]^3\}\ n_0\ M_0 \qquad (6.4.6c)$$

where, $A = 3.5$, and V_S, E_0, n_0 and t are in kms^{-1}, erg, cm^{-3} and sec,

respectively. The quantity, A, is a constant which varies from model to model, but is always of order unity (Shull 1980a). Fitting the adopted values of R_S, V_S and n_0 with this model requires an age, $t = 1.8\times10^4$ yr, an initial explosion energy, $E_0 = 9\times10^{49}$ erg, and a current shell mass, $M_S = 5000\ M_0$. These age and explosion energy estimates are certainly well within the expected range for a supernova having occurred within the DR21 molecular cloud in the recent past.

An estimate of the efficiency of energy conversion from the initial impulsive event to the swept-up shell can be derived from the following ratio

$$\delta(t) = \{1/2\ M_S(t)\ [V_S(t)]^2\}/E_0 \qquad (6.4.7)$$

The efficiency of energy conversion in this case is, $\delta(t = 1.8\times10^4\ \text{yr}) \approx 30\%$. Furthermore, the total lifetime of the H_2 emitting phase is, $t_{lum} = 5\times10^4$ yr, and, $t_{lum}/t_{diss} \approx 10$.

The momentum involved in supernovae can be estimated from models of these events. Type II SN probably eject a mass of at least 4 M_0 with a velocity of $\sim$ 4000 kms^{-1}, corresponding to an ejecta momentum of 3×10^{42} $gcms^{-1}$, whereas Type I SN probably involve less mass, but somewhat higher velocities. The model of Chevalier (1980) which gives a good fit to observed SN light curves, yields a momentum of 2.4×10^{42} $gcms^{-1}$, not too dissimilar to the Type II SN. It thus appears that a momentum conserving supernova explosion, which is almost certainly the case for conditions within dense molecular clouds, can transfer at least 2×10^{42} $gcms^{-1}$ to its immediate environs. This available source of momentum is comparable in magnitude to the derived momentum of the DR21 outflows; in this respect, a supernova explosion possessess a distinct

advantage over the stellar wind models investigated below, which are all momentum deficient.

The structure of an embbeded SNR is not well defined but is expected to consist of a hot X-ray-emitting interior, surrounded by a thin HII shell at ~ 10^4 K followed by a more extended zone of warm, partially ionized gas produced by the penetrating X-rays (the thickness of this X-ray precursor depends on the ambient cloud density, being extremely thin at the densities considered here). In this neutral shell, most of the x-rays are reprocessed into infrared by grains, which are heated together with the gas to temperatures ~ 300 K. Assuming a SNR luminosity evolution of the form, $L(SN) \propto t^{-7/8}$ (Shull 1982), then for the values of explosion energy and cloud density calculated above, Shull's model predicts a bolometric luminosity > 10^4 L_0 at a time 10^4 yr after the explosion event, in fair agreement with the observed bolometric luminosity of the DR21 region (~ 10^5 L_0). Clearly, the detection of hard X-rays which escape the cloud would be a key distinguishing feature of the SNR and would unequivocally prove the existence of a SNR within the DR21 cloud core.

6.4.(c) THE STELLAR WIND MODELS

The evolution of a wind driven shell can fall into either of two regimes; the momentum conserving case (Steigman 1975) or the energy conserving case (Castor et al. 1975). The factor that differentiates between the two cases is the ability of the hot shocked material inside the shell to sustain its temperature and thus exert pressure forces on the shell. The quantites that determine whether or not this will occur are L_W, the kinetic energy input rate of the

stellar wind, and L_r, the radiative losses of the hot material interior to the shell. For $L_w \gg L_r$, the losses are negligible, the interior pressure of the bubble is significant, and energy is conserved. If $L_w \ll L_r$, the hot shocked stellar wind gas cools rapidly, no pressure forces exist, and momentum conservation is the better approximation. As explained by Dyson (1984), the most sensitive parameter which determines the current state of the energy budget at the interface region, separating the stellar wind from the ambient cloud, is the stellar wind velocity, and hence, the effective temperature of the post-shock wind gas. Using an approximation to the cooling function, appropriate for the temperature regime $10^5 < T < 10^7$ K, Dyson derives the following equation, which specifies the critical velocity at which the transition from energy to momentum conservation occurs in a medium of specified pre-shock density n_0

$$V_{crit} = 500\ (n_0\ \mu_0\ \dot{M}_w)^{1/9}\ \ kms^{-1} \qquad (6.4.8)$$

where, M_w, is the characteristic stellar mass loss rate. Substituting, $n_0 = 10^4$ cm^{-3}, which is the mean density assumed to characterise the DR21 cloud core, gives $300 < V_{crit} < 500$ kms^{-1}, for the corresponding mass loss range $10^{-6} < \dot{M}_w < 10^{-4}$ M_0 yr^{-1}. It is important to note that the above equation applies only to the special case of a purely spherical stellar wind within a homogeneous, constant density molecular cloud.

(i) AN ENERGY-DRIVEN STELLAR WIND ($V_w \gg V_{crit}$)

During this phase the outflow system has a four zone structure, shown schematically in Fig.(6.4.1a), consisting of (a) an innermost, hypersonic stellar wind, characterised by a mass-loss rate M_w, and terminal velocity V_w; (b) next,

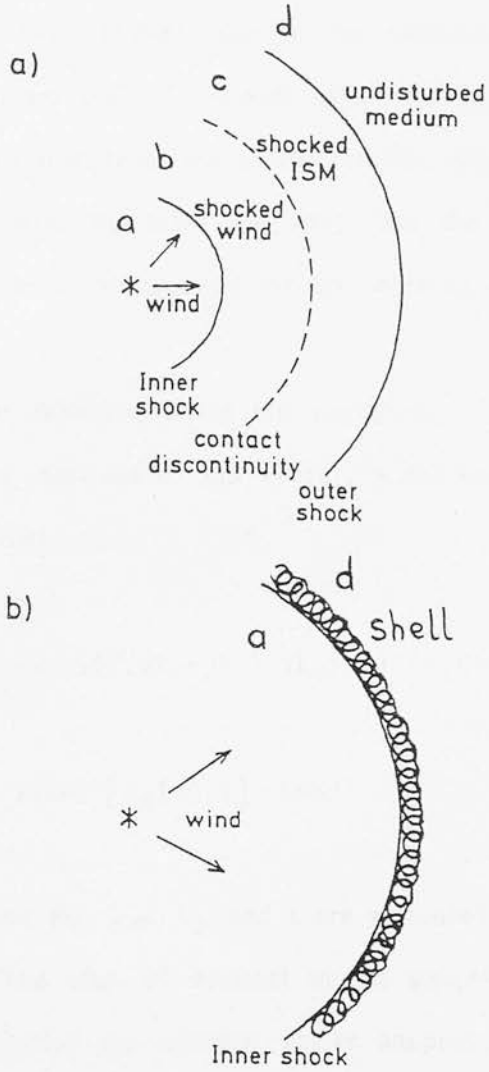

FIGURE 6.4.1 : (a) An energy-driven wind (Weaver et al 1977). The stellar wind is divided into four distinct regions: (a) the supersonic stellar wind, (b) the shocked stellar wind, (c) the shocked ambient medium, and (d) the preshock ambient medium. The two shocked gases (b) and (c) are divided by a contact discontinuity.

FIGURE 6.4.1 : (b) A momentum-driven wind (Steigman 1975). The relatively low-velocity stellar wind impinges directly onto the dense swept-up shell of ambient cloud matter which forms as a result of efficient cooling of the shocked gas.

a hot, almost isobaric region consisting of shocked stellar wind mixed with a small fraction of the swept-up cloud gas; (c) a thin, dense, cold shell at radius R_S expanding at a velocity V_S and containing most of the swept-up ambient cloud gas; (d) ambient molecular cloud gas of density n_0. Weaver, McCray & Castor (1977) and Shull (1980b) discuss the evolution of this type of model. Basically, the swept-up shell of ambient cloud material (region c) is assumed to be thin and is separated from the shocked stellar wind (region b) by a contact discontinuity (at radius R_S from the star), and the expanson of the shell is primarily due to thermal pressure of the hot interior, region (a).

Assuming that radiative losses are negligible, then, from the conservation equations for mass, momentum and energy, a similarity analysis results in the following relationships

$$R_S(t) = 5.4\times10^{-10}\ (125/154\ \pi)^{1/5}\ (L_w/n_0)^{1/5}\ t^{3/5}\ \text{pc} \qquad (6.4.9a)$$

$$V_S(t) = 9.8\times10^{5}\ (1/A)\ [R_S(t)/t]\ \text{kms}^{-1} \qquad (6.4.9b)$$

where, A = 5/3 and R_S, L_w, V_S, and t are measured in pc, ergs^{-1}, kms^{-1} and sec, respectively. The mass of material in the swept-up shell, M_S, is given by eqn.(6.4.7c). Substituting the relevant values adopted for the DR21 outflow, a wind mechanical luminosity of, $L_w = 1.1\times10^{38}$ ergs^{-1}, at a time, $t = 3.8\times10^{4}$ yr is obtained. The integrated energy impacted by the stellar wind over its entire lifetime is therefore, $E_w \approx 10^{50}$ erg; note that this is comparable in magnitude to the instantaneous energy released during a SN explosion (viz. Sec.[6.4.(b)]). The luminous H_2 line emitting phase lasts for a period, $t_{lum} = 3\times10^{5}$ yr, and the relative lifetimes of the luminous to dissociated phases is, $t_{lum}/t_{diss} = 30$, a factor of three longer than the explosion model. The efficiency of momentum,

σ, and energy, δ, transfer from the stellar wind to the outflow material, identified with the swept-up shell, are similarily expressed as follows

$$\sigma = (15/77)(V_w/V_S) \qquad \text{and} \qquad \delta = (15/77) \tag{6.4.10}$$

Thus, for the case of an energy-driven wind, δ = 19%. This is in rough agreement with the CO observations presented in Sec.[4.3], which indicate that the mechanical luminosity of the outflow gas is an order of magnitude lower than the above calculated luminosity of the stellar wind. Also, it is worth noting that σ can become very large if $V_w \gg V_S$.

(ii) A MOMENTUM-DRIVEN STELLAR WIND ($V_S \ll V_{crit}$)

If the stellar wind velocity is relatively low, there is no true adiabatic expansion phase, and the evolution is governed mainly by momentum conservation with the wind momentum impinging directly onto the shell of swept-up cloud matter. The shock structure expected in this model is shown schematically in Fig.(6.4.1b). Again, the wind luminosity and outflow age can be determined from a self-similarity solution of the conservation equations, thus giving

$$R_S(t) = 8.2\times10^{-11}\,[6/(2\pi)]^{1/4}\,[L_w/(V_w\,n_0)]^{1/4}\,t^{1/2} \tag{6.4.11a}$$

$$V_S(t) = 9.8\times10^{5}\,(1/A)\,[R_S(t)/t] \tag{6.4.11b}$$

where, A = 2 and M_S is again given by eqn.(6.4.8). Here, M_S, V_S, and R_S are in M_0, kms^{-1}, and pc, and are identified with the mass of swept-up material,

the outer shock velocity and radius, respectively.

As can be seen from eqn.(6.4.8), the upper limit for V_w that satisfies momentum conservation is, $V_w < 500$ kms^{-1}. The mechanical luminosity and age required to fit the observed radius and velocity of the DR21 outflow source are then 3.4×10^{38} L_0 and 3.2×10^4 yr, respectively; calculated for an assumed stellar wind terminal velocity of, $V_w = 300$ kms^{-1} (Simon et al. 1983; Persson et al. 1984; Garden & Geballe 1986). The total mechanical energy expended is 3.4×10^{50} erg, the luminous H_2 line emitting phase lasts for, $t_{lum} = 2\times10^5$ yr, and, $t_{lum}/t_{diss} = 25$. Furthermore, the efficiencies of momentum and energy transfer from the wind to the swept-up shell are, respectively

$$\sigma = 1 \qquad \text{and} \qquad \delta = (V_S/V_w) \tag{6.4.12}$$

Thus, in contrast to an energy-conserving wind, the transfer of energy in a momentum-conserving wind is most efficient when V_w and V_S are of comparable magnitude. Comparing the values of δ obtained from the energy and momentum models, gives the important result that an energy-driven wind is more efficient, by the factor $(15/77)(V_w/V_S)$, than a momentum-driven wind at imparting bulk kinetic energy (and momentum) to the surrounding ambient cloud medium; here, δ = 8% as compared to 20% obtained using the energy conserving model. Under circumstances where the wind velocities are large, an energy-driven wind therefore facilitates more efficient energy and momentum transfer to the surrounding ambient medium than does a momentum-driven wind.

(iii)

A STELLAR WIND IN A CLOUD WITH A RADIAL DENSITY GRADIENT

In an attempt to add some degree of reality to the aforementioned models, the evolution of a stellar wind embedded within a centrally condensed molecular cloud characterized by a variable density distribution will now be investigated. A radial power-law density distribution is assumed, i.e. $\rho = \rho_0 (r/r_0)^{\beta}$. The reason for this choice is twofold. First, postulating a simple radial power-law distribution preserves the ability to express the hydrodynamics in a self-similar form (Dyson 1984). The second, and most fundamental reason, is that during the epoch of cloud collapse, leading to star formation, the protostellar core accrets matter faster than the rest of the cloud, thus leading to a localized density gradient, centred on the accretion core. Self-similar solutions to the gravitational collapse of molecular clouds show that, $\beta = -3/2$, (free fall) in the inner core region and, $\beta = -2$, in the outer accretion envelope (Mouschovias 1976; Shu 1977). The evolution of a stellar wind within a medium characterized by a radial density gradient has been studied analytically by Konigl(1982), Dyson (1984) and Kwok & Volk (1986). These authors discuss the well known fact that if mass conservation applies in a steady mass-loss process, then the radial velocity structure of the wind is inherently related to the particular form of the radial density distribution of the surrounding ambient medium. For such a mass-conserving outflow, it is simple to prove that (i) if $\beta > -2$, then the stellar wind shell decelerates monotonically with time, (ii) if $\beta < -2$, then the shell undergoes rapid acceleration, leading to the onset of Rayleigh-Taylor instabilities and resulting in premature disruption of the shell, and (iii) if $\beta = -2$, then a constant velocity flow results.

The time evolution of R_S and V_S can again be solved using a simple self-similar analysis, with the results

$$R_S(t) = [C\ L_w/(\rho_0 r_0^{-\beta})]^{1/(5+\beta)}\ [t]^{3/(5+\beta)} \qquad (6.4.13a)$$

$$V_S(t) = 3/(5+\beta)\ [R_S(t)/t] \qquad (6.4.13b)$$

$$M_S = 4\pi/(3+\beta)\ (\rho_0 r_0^{-\beta})\ [R_S]^{(3+\beta)} \qquad (6.4.13c)$$

and

$$L_w = 1.7\times10^{-4}\ M_S\ V_S^3\ R_S^{-1}\ [(77+29\beta+2\beta^2)/18]\ L_0 \qquad (6.4.13d)$$

where,

$$C = [(3+\beta)(5+\beta)^3]/[6\pi(7+2\beta)(11+\beta)] \qquad (6.4.13e)$$

As a trial example, the specific case where, β = -3/2 (free-fall), will be considered. For this assumed radial density distribution, and taking, $n_0 = 10^4$ cm^{-3} at a radius r_0 = 1.5 pc, as necessitated by the H_2 observations, the stellar wind luminosity is found to be, $L_w = 1.1\times10^{38}\ L_0$, the outflow age is, $t = 5.5\times10^4$ yr, and the mass of swept-up ambient cloud material participating in the outflow is, $M_S = 10^4\ M_0$. The duration of the luminous H_2 emitting phase is now $t_{lum} = 5.5\times10^7$ yr, several orders of magnitude longer than any of the other models considered; this is, however, not a realistic timescale as the formation phase of a massive star lasts for only 10^5-10^6 yr. Although the inclusion of a radially decreasing ambient density distribution aids significantly

in sustaining the supersonic outflow velocities over an extended period of time, the additional mass that must be moved is roughly twice that involved in the constant density models. These two opposing effects tend to cancel each other out, thus resulting in a value of L_w similar to that required in the constant density situation.

The efficiency of energy transfer is now given by

$$\sigma = 3(5+\beta)/[\,(7+2\beta)(11+\beta)\,] \qquad (6.4.14)$$

which, for $\beta = -3/2$, gives, $\sigma = 28\%$; note that, $\sigma = 19\%$, for the constant density case. As for the $\beta = 0$ case, the shell momentum in an energy-conserving interaction can be many times the wind momentum (i.e. $\delta > 20$ for $\beta = -3/2$ and $V_w > 1000$ kms^{-1}; Kwok & Volk 1986).

6.4.(d) A COMPARISON OF THE WIND/EXPLOSION MODELS

The time evolution of V_s, R_s and $L(H_2)$ for each of the four models described above are shown graphically in Figs.[6.4.2a], [6.4.2b] and [6.4.2c], respectively. These graphs give a clear presentation of the influence imparted by the different flow structures on the observed parameters. The main points to note are as follows ;

(i) In the velocity vs. time plot, the SNR has the steepest deceleration, the energy-driven wind with ($\beta = -3/2$) has the slowest rate of decline, and stellar winds with ($\beta = 0$) fall in between these limiting cases. This trend results

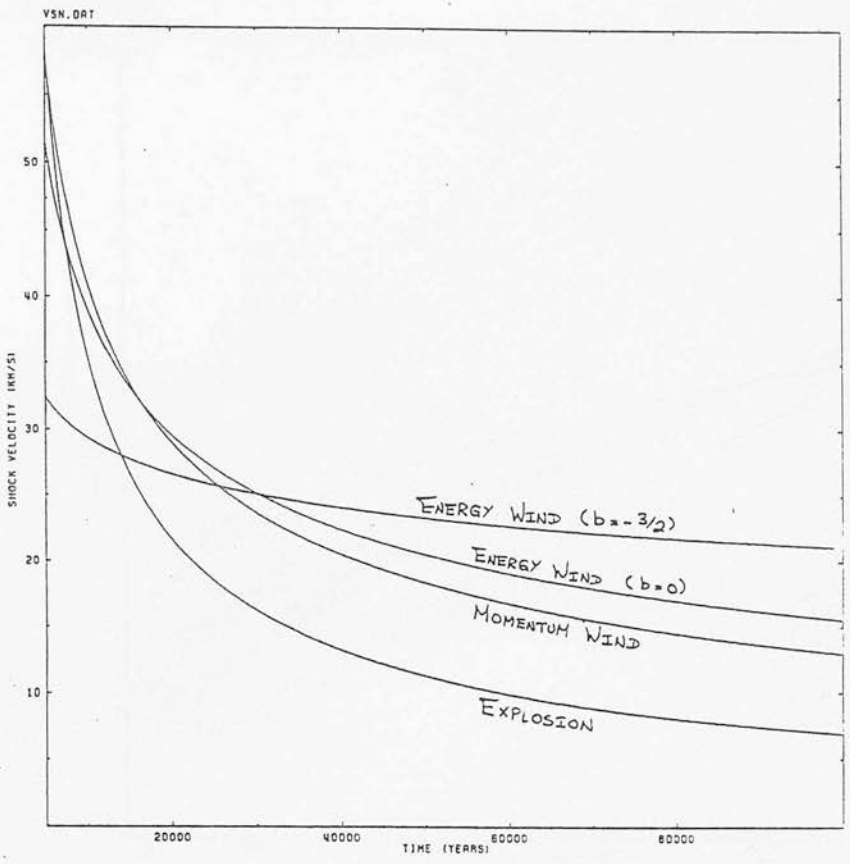

FIGURE 6.4.2a : A plot of velocity (km/s) against time (years) for the swept-up shell created by four different wind models. The models investigated are (i) an explosion, (ii) a momentum-conserving stellar wind, (iii) an energy-conserving stellar wind in a constant density medium (b=0), and (iv) an energy-conserving stellar wind in a medium with a radially decreasing density gradient (b=-3/2). The basic assumptions are that the ambient cloud density, n=1(4)cm-3, and shell-velocity, Vs=25kms-1, at a shell radius, Rs=1pc, as defined by the H2 observations of the DR21 shock-excited outflow.

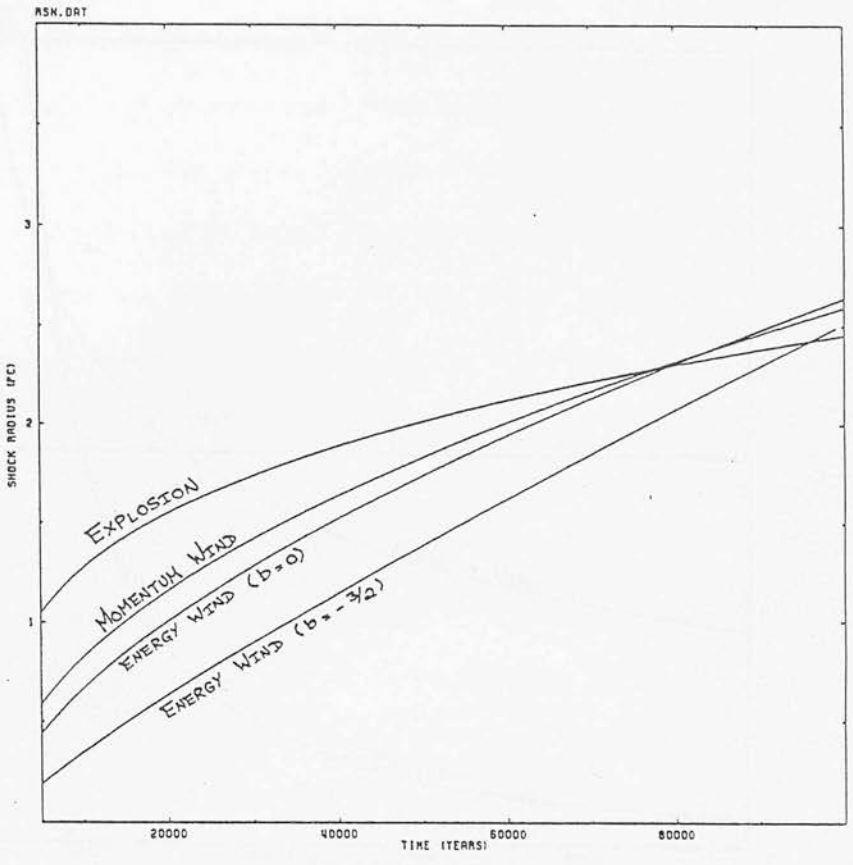

FIGURE 6.4.2b : A plot of shell radius (pc) against time (years) for the four wind models as described in Fig.[6.4.2a].

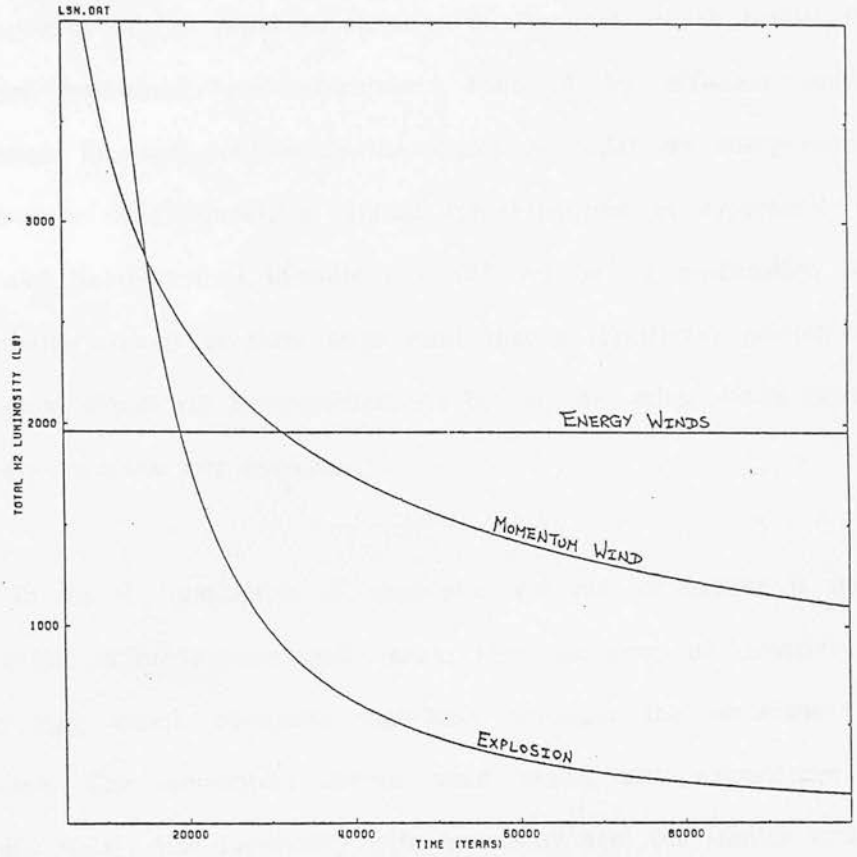

FIGURE 6.4.2c : A plot of shock luminosity (Lo) against time (years) for the four wind models as described in Fig.[6.4.2a].

primarily from a combination of the relative radiative cooling efficiencies and ambient density distributions which differ between the different models.

(ii) In the radius vs. time plot, the SNR ends up with the smallest radius; a consequence of the rapid deceleration of the shell which results in a lowering of the post-shock gas temperature followed by efficient cooling via line radiation. In stark contrast to the explosion model, an energy-conserving wind (with β = -3/2) undergoes almost free-expansion at supersonic velocities for most of its dynamical lifetime (> 10^6 yr); in all probability, the wind will eventually expand to such large radii that a significant portion of its parent molecular cloud will be disrupted. As before, the stellar winds (with β = 0) fall in between these two extremes.

(iii) In the H_2 luminosity vs. time plot, the rate of decline is steepest for the SN explosion model; this again results from the onset of radiative cooling at an early age, which continues vigorously throught the remainder of the SNR lifetime. The momentum driven wind model also experiences a monotonic decline in H_2 line luminosity with increasing age, for similar reasons, only less severe. By definition, the energy-conserving wind models (both β = 0 and -3/2) necessarily follow constant H_2 luminosity tracks; this results simply because both the wind luminosity and the efficiency of energy transfer to the shell are assumed to be time invariant.

6.4.(e) RADIATION PRESSURE AS A DRIVING AGENT

To gain further understanding of the physical nature of the driving mechanism that powers the energetic DR21 outflows and its relationship to similar outflow phenomena observed in other star-forming regions, it is instructive to compare the momentum transfer rate and mechanical luminosity of the stellar wind that supposedly drives the observed outflows with the radiative momentum flux and radiative luminosity of the central stellar object. To derive these quantities, one must first decide whether the wind is energy or momentum driven, as the results will differ depending on which model is chosen (Dyson 1984). Yet another alternative, which has been the most common approach so far taken by most observers, is to naively consider only the energetics and kinematics of the outflow material (as derived directly from observations of the high-velocity CO emission), thus bypassing an analysis of the wind itself; this approach will be pursued here only to facilitate a comparison of the DR21 outflow with the results for observations of other outflow sources.

To derive these quantities, the outflow dynamical lifetime ($t_d = R_{hvf}/V_{hvf} \approx 2pc/30kms^{-1} = 5\times10^4$ yr) is used to estimate the average force required to drive the flow ($\dot{P}_{hvf} = P_{hvf}/t_d$) and the mechanical luminosity of the flow ($L_{hvf} = E_{hvf}/t_d$), and the far-infrared luminosity is used to estimate the radiative luminosity ($L*$) and radiative momemtum flux ($L*/c$). Estimates of $\dot{P}_{hvf}$ and L_{hvf} for the DR21 outflow are derived using values for the flow kinetic energy and momentum as quoted in Table(5.2.1). For the energy-driven stellar wind model a wind velocity, $V_w = 2000$ kms^{-1} is assumed, and for the momentum-driven model a wind velocity of, $V_w = 300$ kms^{-1} is taken (see Sec.[6.4.c]). Using these parameters, the ratios of the wind/outflow mechanical luminosities to the stellar radiant luminosity are as follows;

$$L_w(\text{energy-driven})/L* = [(77/9)(E_{hvf}/t_d)]/L* = 0.02$$

$$L_w(\text{momentum-driven})/L* = [(P_{hvf}/t_d)V_w]/L* = 0.12\ (V_w/300\text{kms}^{-1})$$

$$L_{hvf}/L* = (E_{hvf}/t_d)/L* = 0.005$$

The corresponding ratioes of the wind/outflow momentum fluxes to the stellar radiant momentum flux are as follows;

$$\frac{\dot{P}_w(\text{energy-driven})}{(L*/c)} = \frac{(154/9)[(E_{hvf}/t_d)/V_w]}{(L*/c)} = 7.4\ (2000\ \text{kms}^{-1}/V_w)$$

$$\frac{\dot{P}_w(\text{momentum-driven})}{(L*/c)} = \frac{[2(P_{hvf}/t_d)]}{(L*/c)} = 200$$

$$\dot{P}_{hvf}/(L*/c) = (P_{hvf}/t_d)/(L*/c) = 100$$

Fig.[6.4.3], is similar to that discussed by Lada (1986), and displays a plot of the mechanical luminosities (L_{hvf}) for all the outflow sources observed to date against the total radiant luminosity ($L*$) of their associated central driving objects. Although the scatter is large, there appears to be a general correlation between mechanical and bolometric luminosities which extends over at least five orders of magnitude in luminosity. The location of DR21 in this plot is consistent with the general trend shown by the other outflow sources. Being one of the most luminous star-forming regions yet observed, it is therefore acceptible that DR21 should exhibit a considerably larger mechanical luminosity than any of the other outflow sources, that is, apart from the Orion outflow

source which is of comparable bolometric luminosity and hence is the closest point to DR21 in this plot. The prominent location of DR21 in this plot clearly illustrates that the mechanical luminosity associated with the DR21 star-forming region is unique with respect to the majority of other presently known outflow sources. Obviously, selection effects play an important role in determing the appearance of this diagram, as, owing to the nature of the star formation process, there are many more low-luminosity than high-luminosity star-forming regions available for study. Also plotted in this diagram is the relation, $L_{hvf} = L*$, which defines a boundary, below which the outflows can be driven solely by the radiant luminosity of the central object. As all the sources fall below this line, it seems feasible that the energy in the radiation field is sufficient to drive the flows, including the extremely-luminous DR21 outflow, however, unreasonably large energy-conversion efficiencies are required.

To investigate further the likelihood of a radiation-driven mechanism, it is informative to plot the distribution of P_{hvf} (the driving force) against $L*$, as shown in Fig.[6.4.4]. Again, DR21 unveils itself as being the most powerful and luminous outflow source, yet known. Moreover, as all the points lie above the line defined by, $\dot{P}_{hvf} = L*/c$, it appears that the available radiation pressure of the central radiative object is insufficient to drive the observed flows.

The above comparison of the energetics of the DR21 outflow with outflows in other star-forming regions reveals two very important facts. Firstly, the DR21 outflow appears to be unique with respect to its extreme mechanical luminosity and requisite momentum transfer rates, presumably because it has a larger radiative luminosity and thus probably also a more massive star-forming core than most other presently known outflow sources. Secondly, the distributions exhibited in the (L_{hvf} vs. $L*$) and ($\dot{P}_{hvf}$ vs. $L*/c$), plots indicate that DR21 is

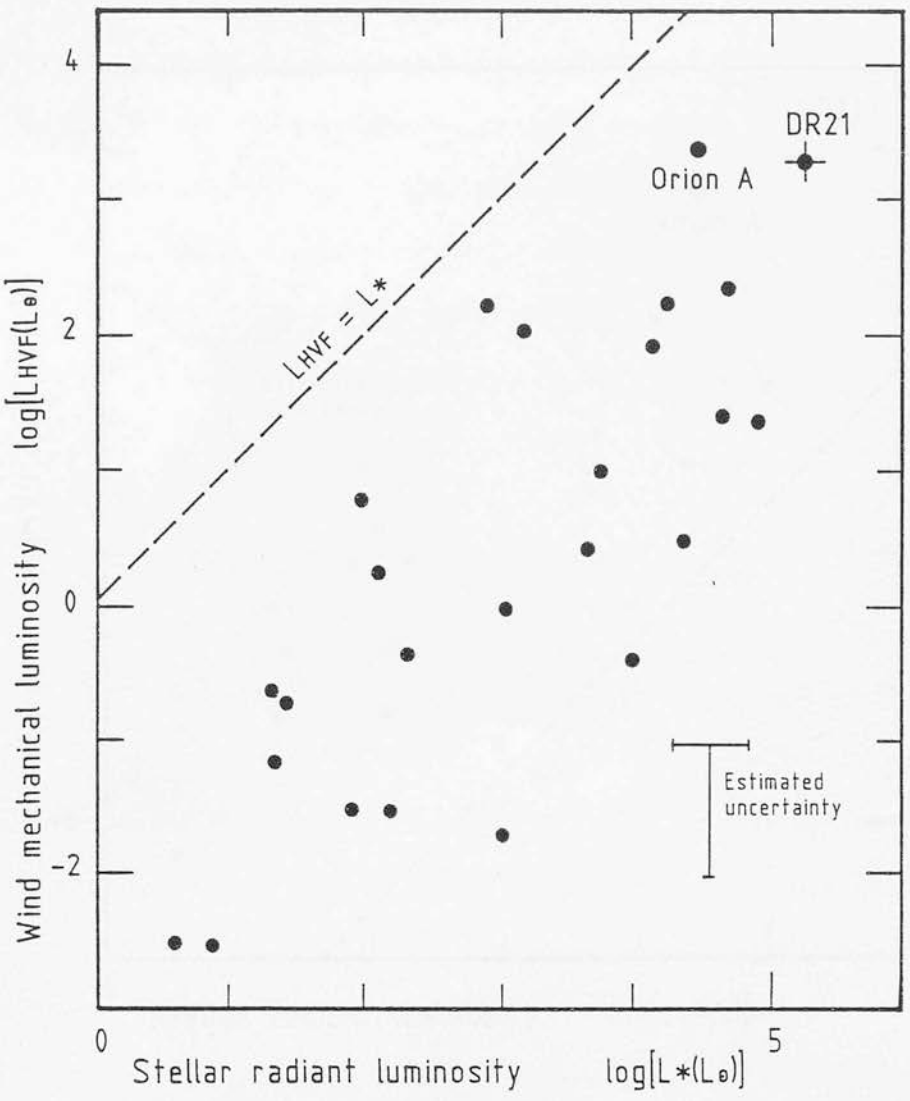

FIGURE 6.4.3: A plot of wind mechanical luminosity versus radiant luminosity of the central object for all outflow sources observed to date (adapted from Lada 1986). The positions of the DR21 and Orion outflow sources are indicated. Also shown is the line that corresponds to the limiting condition where the luminosity of the flow equals the radiant luminosity of the central driving object; as expected, all sources lie below this line.

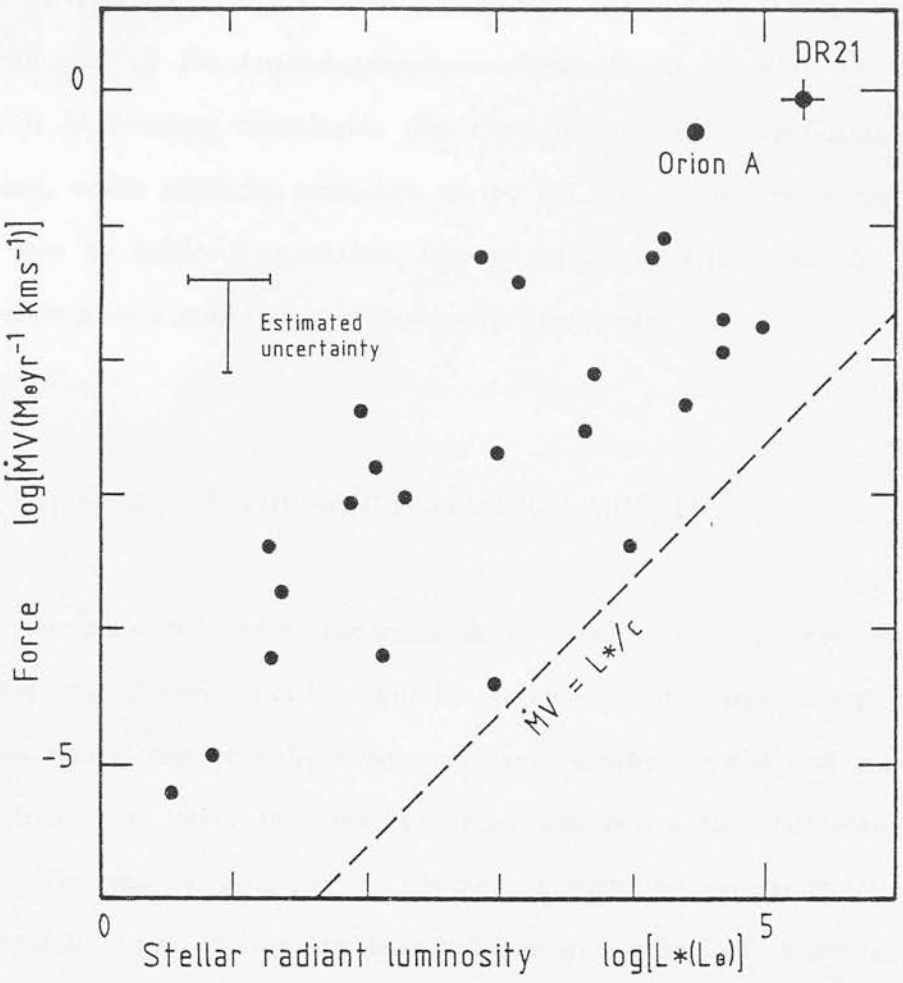

FIGURE 6.4.4 : A plot of the force required to drive the outflow versus the radiant luminosity of the central object for all outflow sources observed to date (adapted from Lada 1986). The positions of the DR21 and Orion outflow sources are indicated. Also shown is the line that corresponds to the condition that the force required to drive the observed flow equals the radiant force available from the central object (assumes single scattering). For all of the outflow sources, including DR21, the mechanical force required to drive the flow exceeds the available radiant force by several orders of magnitude, thus, radiation pressure alone is incapable of explaining the observed high-momentum fluxes that are ubiquitous to all outflows.

not anomalous relative to other outflow sources, but forms a high luminosity extension to the general trend. From this fact, it is suggested that the nature of the central driving mechanism (to be discussed further in Sec.[6.5.b]) which sustains the enigmatic outflow activity associated with the DR21 region may be similar to that of the lower-luminosity outflows found in other star-forming regions. It is therefore conceivable that a single, universally applicable driving mechanism, which scales in proportion to the radiative luminosity of the central object, may be sufficent to explain the ubiquitious occurrence of the outflow phenomenon over a wide range of bolometric luminosity.

6.4.(f) SUMMARY OF THE WIND/EXPLOSION MODELS

To summarize the above discussion, it is found that a supernova explosion origin for the observed outflow activity is energetically feasible and has the advantage that it can naturally supply the large kinetic energies and momentum fluxes required to drive the observed flows and power the shock-excited H_2 emission. The supernova model is, however, plagued by several problems, the most important being that an explosion will impart the bulk of its energy into a very compact region (< 1pc) and therefore cannot explain the extended outflow structure observed in the DR21 region, where high-velocity outward motions are observed over a radial distance from 1 - 3 pc. In this respect, the stellar wind models, which continuously inject fresh supplies of energy into the system, are more advantageous as they can excite shocked H_2 line emission over a larger radial extent and thus give a better fit to the observations. Stellar winds also have the additional advantage that their longer radiative lifetimes imply that they should be more frequently observed than explosive events. Moreover, the inclusion of a radially decreasing density distribution significantly aids in

prolonging the period of supersonic gas flow and associated shock-excited H_2 line emission. Consequently, this is expected to be the most common type of wind structure within the dense cores of star-forming molecular clouds.

As for the origin of the driving mechanism, it appears that the radiative luminosity of a typical high-mass, main-sequence star, of the same bolometric luminosity as the DR21 far-infrared source, fails to supply sufficient radiant pressure to drive the observed outflows, by one order of magnitude for energy-driven winds and by more than two orders of magnitude for momentum-driven winds. In the most favourable case of an energy-driven stellar wind, more than 10 multiple scatterings in the line photon are required to match the observations. This suggests that the luminous main-sequence O stars which give rise to the compact DR21 radio HII region may play a minor role, if any, in powering the high-velocity neutral gas flows. It is, therefore, conceivable that these flows may require the presence of a more exotic driving mechanism. A discussion of alternative mechanisms and their applicability to the momentum problem, is presented in the following sections.

6.5 ANISOTROPIC OUTFLOWS AND THEIR COLLIMATION

6.5.(a) WHY ANISOTROPIC OUTFLOWS ?

In the preceeding section an attempt was made to understand the origin and time evolution of the driving agent responsible for powering the observed outflows in the DR21 star-forming region. For simplicity, the analysis neccessarily assumed a spherically symmetric wind, however, the observations show clear evidence for an anisotropic outflow geometry. A large number of

models, encorporating a broad spectrum of different physical processes, have been proposed in the literature to explain the collimation of luminous extragalactic radio jets emanating from active galactic nuclei. It seems reasonable to expect that the focussing mechanism responsible for bipolar molecular outflows within galactic star-forming regions may be analogous, in a broad sense, to scaled down versions of the esoteric extragalactic jet phenomenon (Kundt 1984). Due to the possible importance of magnetic fields for directing ionized fluids along a prefered axis, many models have invoked magnetic effects as the fundamental focussing mechanism, however, the presence of a magnetic field is not an essential ingredient as other physical mechanisms, such as thermal pressure confinment in a non-magnetic medium, can also create highly-collimated jets (Konigl 1982; Sanders 1983).

In the following sections, different methods are discussed for the focussing of an initially spherically symmetric wind located at the centre of a flattened molecular cloud. The physical characteristics predicted by the various models are then compared with those of the DR21 hypersonic jets to determine which model best fits the available observations.

6.5.(b) THE JET MODELS

The evolution of stellar winds in inhomogeneous media has been studied theoretically by Canto (1980) and Konigl (1982). These authors show that originally spherical wind bubbles can evolve into ovoids if the cooling time of the shocked wind is sufficiently short, or, into De Laval nozzles if radiative cooling is inhibited and adiabatic conditions prevail. As descibed in Sec.[6.4.(c)], the condition for the formation of an adiabatic stellar wind within a dense

molecular cloud medium is, $V_w > 500$ kms^{-1}, else, the momentum conserving case will be more appropriate.

(i) ENERGY-DRIVEN JETS

If the (proto-)stellar outflows are indeed adiabatic then the exciting possibility arises that the physical conditions in these flows may bear some resemblance to the physical conditions thought to be characteristic of extragalactic jets. The evolution of an adiabatic wind bubble in an anisotropic density distribution has been studied analytically by Blandford & Rees (1974), Konigl (1982), and Sanders (1983), and numerically by Norman et al. (1981 & 1986), Hardee (1982), Wilson & Falle (1985) and Ferrari et al. (1986), to name but a few. It is important to note, however, that these studies strictly apply to extragalactic plasma jets, and require to be scaled down by tens of orders of magnitude in both power and linear extent in order to facilitate direct comparison with molecular outflows.

Hydrostatic confinment simply means that the gas pressure inside the jet is balanced by the pressure of a surrounding ambient medium (i.e. $P_j(z) = P_{ex}(z)$) so that the transverse shape of the jet r(z) is determined entirely by the pressure gradient in the external medium. The fundamental characteristics predicted by the pressure confined adiabatic model for jet formation within a flattened ambient density distribution can be roughly summarized as follows.

Assuming mass conservation along an adiabatic jet, then, for the power-law distributions

$$r = r_0(z/z_0)^{\epsilon} \qquad (6.5.1a)$$

$$\rho_j = \rho_{j0}(z/z_0)^{\eta} \qquad (6.5.1b)$$

$$V_j = V_{j0}(z/z_0)^{\delta} \qquad (6.5.1c)$$

where, r is the jet radius, ρ_j is the jet density, V_j is the jet velocity, z is the radial distance along the jet and, z_0 is the radial distance of the jet base (i.e. the location of the transonic point), the following important relationship results

$$\eta = -\delta - 2\epsilon \qquad (6.5.2)$$

For the special case of free-expansion, $\delta = 0$, $\epsilon = 1$, and $\eta = -2$.

A more interesting case is that of a jet confined by a power-law density profile in the ambient medium of a flattened cloud. Such a case was first discussed by Blandford & Rees (1974), who developed the Twin-Exhaust Model to explain the collimation of bipolar plasma jets in radio galaxies and quasars. More recently, Konigl (1982) has applied the Twin-Exhaust Model to bipolar molecular flows, where the energy source is a young star with a strong stellar wind, and the confining agent is a dense molecular cloud. This model has even been used to explain the highly collimated and clumpy structure of optical/radio jets associated with young T Tauri stars (Tapia et al. 1983; Mundt, Brugel & Burke 1986). Norman et al. (1986) note that because the basic physics underlying the Twin-Exhaust Model are effectively scale invariant, this simple model may be used to explain the formation of bipolar jets for a broad range of astrophysical environments.

As the hot adiabatic bubble of stellar wind gas is accelerated along the direction of elongation (i.e. parallel to the minor axis of the flattened cloud), the interaction layer becomes subject to the Rayleigh-Taylor instability which grows on a timescale $[r/(dV/dt)]^{1/2}$, and which could lead to the formation of De Laval nozzles. From the De Laval nozzle which forms the base of the jet, where the flow becomes supersonic, the velocity increases by only a factor of two to its asymptotic value, so is approximately constant (i.e. $\delta = 0$). If the external pressure also obeys a power-law of form, $P_{ext} \propto r^{\alpha}$, and the jet material has a ratio of specific heats γ (= 5/3 and 7/5 for atomic and molecular gas, respectively), then, $\epsilon = -\alpha/(2\gamma)$ (Blandford & Rees 1974; Sanders 1983). In this case, the degree of collimation in a pressure confined jet is increased relative to that of a free jet, providing, $\alpha > -2\gamma$.

Konigl (1983) and Sanders (1983) note that for, $\alpha < -2$, pressure confinment is impossible since the internal jet pressure cannot fall as fast as the pressure in the surrounding ambient medium. If, however, $\alpha > -2$, then a jet with initially greater internal than confining pressure (i.e. an under-expanded jet) could effectively "break free" and expand freely with $\epsilon = 1$, and with the internal jet pressure dropping as $P_j \propto r^{-2\gamma}$, or faster than the ambient medium, until the latter pressure catches up and the jet is once again reconfined. As the jet is compressed its internal pressure overshoots the ambient pressure and the cycle of events is repeated. Thus, the sudden expansion of an under-expanded jet on ejection from the De Laval nozzle may set up a train of compression/rarefaction waves that propagate along the length of the jet.

Detailed numerical simulations of the propagation characteristics of supersonic pressure-confined jets (see Norman, Smar & Winkler 1986, and references therein) clearly indicate that perturbations at the jet boundary, induced either

by sudden changes in the external pressure distribution or the non-linear growth of long-wavelength Kelvin-Helmholtz instabilites, can generate a succession of oblique (incident and reflected) shocks internal to the jet. Furthermore, Rayleigh-Taylor instability of the central cavity can make the flow intermittent (Blandford & Konigl 1979), and also can introduce large chunks of dense cloud gas into the flow, which may then be shocked (Choe & Henriksen 1986). These theoretical considerations therefore predict the occurrence of rich morphological structure along the entire length of the jets.

For low external pressures, and hence low Mach numbers, laboratory experiments indicate that these quasi-periodic internal shocks, or "Mach disks", show a tendency to be regularily spaced along the jet with a separation given by (Prandtl 1904)

$$L_j = W_j.M_j \qquad (6.5.3)$$

where, M_j, is the jet Mach number and, W_j, is the jet radius. Moreover, as the periodic shocks originate from an innward compression of the beam they tend to sustain the collimation of the jet out to considerable distances from the driving source. For higher external pressures and Mach numbers, however, Prandtl's empirical relationship breaks down and a saturation wavelength, $L_j \approx 2.W_j$, is obtained due to the formation of strong oblique shocks internal to the jet (e.g. Hartmann & Lazarus 1941). Thus, depending on the Mach number of the jet and also on the ratio of the external to internal pressures, an oscillation wavelength in the range, $W_j.M_j < L_j < 2W_j$, is predicted to characterize a supersonic, pressure confined jet.

The striking resemblance between these numerical predictions and the presence of regularily spaced shock-excited emission-line knots within the DR21 H_2 jets suggests that these hypersonic jets may indeed be collimated by some form of pressure confinment process. If so, then it should be possible to estimate the jet radius from eqn.(6.5.3), knowing the knot spacing and assuming a realistic value for the jet Mach number. Assuming that the jet is composed mainly of shocked neutral gas at a mean temperature, $T_j \approx 500$ K, then the internal sound speed of the jet material is, $C_j \approx 3$ kms^{-1}, and the Mach number is, $M_j = 10(V_j/30 \text{ kms}^{-1})$. Using these values, the following limits are obtained for the jet width

$$0.1\ (L_j/1.0\ \text{pc})/(V_j/30\ \text{kms}^{-1}) < W_j < 0.5\ (L_j/1.0\ \text{pc})\ \text{pc}$$

Thus, if the DR21 jets are pressure confined then the intrinsic jet radius may be quite small compared to the jet length (~ 3 pc). This prediction agrees with the highest angular resolution H_2 maps, in which the innermost jet structure appears extremely sinuous and is barely resolved with a 10 arcsec beam (~ 0.2 pc at the distance of DR21). In this picture, one may expect the formation of a De Laval nozzle at the outer boundary to the dense cloud core where the radial pressure gradient is steepest. Furthermore, the compression shocks are expected to be strongest in the inner regions of the flow, due to sudden reacceleration on emergence from the nozzle; damping by viscous forces causes the shocks to become weaker with increasing distance along the jet. These general features fit the observations rather well and give added strength to the confinment model.

So far, the argument presented in favour of the adiabatic pressure-confinment model has involved morphological evidence only. It is,

however, necessary to consider whether such a model can also account for the observed physical properties of the DR21 molecular jets before accepting its validity.

For the sake of simplicity, the adiabatic jet is modelled as a collimated, pressure-confined flow. The neutral material filling the jet has a particle density, n_j, and a velocity, V_j, in an axially symmetric, linear channel of radius, W_j. The jet material is assumed to derive from a stellar wind characterized by a spherical mass-loss rate $\dot{M}_w$, of which, a fraction, ζ, (= 0.5 for a bipolar geometry) is diverted into the jets. The mechanical luminosity of the jets can then be expressed as follows

$$L_m = 1/2\ \zeta\ \dot{M}_w\ (V_j)^2 \qquad (6.5.4)$$

For a pressure-confined jet, the jet diameter is given by balance between the internal jet pressure and the pressure of the ambient molecular cloud. The condition for pressure confinement can thus be written as

$$n_0 . T_0 = n_j . T_j \qquad (6.5.5)$$

where, n_0, n_j and T_0, T_j are the ambient cloud and jet, densities and temperatures, respectively. Additionally, for linear flow through a cylinder, the following relationship results

$$n_j = [\zeta\ \dot{M}_w]/[\pi\ \mu\ m(H)\ (r_j)^2\ V_j] \qquad (6.5.6)$$

Combining eqns.(6.5.4), (6.5.5) and (6.5.6) then gives

$$M_w = 1/\zeta \left[2 \pi \mu \, m(H) \right]^{2/3} \left[(n_0 T_0)/T_j \right]^{2/3} (r_j)^{4/3} L_m^{1/3} \qquad (6.5.7)$$

and

$$V_j = \{2/[\pi \mu \, m(H)]\}^{1/3} \left[(L_m T_j)/(n_0 T_0) \right]^{1/3} (r_j)^{-2/3} \qquad (6.5.8)$$

If most of the jet kinetic energy is converted into a radiative shock at the "head" of the jet, where the supersonic flow collides with ambient cloud material, then the cloud shock velocity, V_c, is related to the jet velocity as follows

$$V_c = \left[n_j/(2n_0) \right]^{1/2} V_j = \left[T_0/(2T_j) \right]^{1/2} V_j \qquad (6.5.9)$$

Finally, in order to link the model predictions with the observations, it is assumed that in the radiative shock at the jet terminus, a significant portion of the jet mechanical luminosity will be converted into shock-excited H_2 line emission, where the conversion efficiency, κ, is given by

$$L_m = \kappa \, L(H_2) \qquad (6.5.10)$$

If, $V_j > 100$ kms^{-1}, then a significant portion of the shock luminosity is radiated at optical and UV wavelengths, the remainder being radiated as H_2 line emission. Due to our poor understanding of the quantitative effects resulting from dissociation shocks, it is assumed here that the optical/UV and infrared emissions have similar weights, thus, $\kappa = 2$. Parameterizing eqns.(6.5.7) & (6.5.8) in astrophysical units gives

$$\dot{M}_w = 1.36 \times 10^{-5} \left[(n_0 T_0)/T_j \right]^{2/3} (r_j)^{4/3} L(H_2)^{1/3} \; M_\odot \; yr^{-1} \qquad (6.5.11)$$

and

$$V_j = 55\ [(L(H_2)T_j)/(n_0T_0)]^{1/3}\ (r_j)^{-2/3}\ \text{kms}^{-1} \qquad (6.5.12)$$

where, $L(H_2)$, r_j, n_0, and $T_{0,j}$ are expressed in L_0, pc, cm^{-3} and K, respectively.

For the DR21 jets, the following values are chosen; $n_0 = 10^4$ cm^{-3}, $T_0 = 30$ K, $T_j = 500$ K, $r_j = 0.2$ pc and $L(H_2) = 1800\ L_0$. The value of n_0 is taken as a representative mean over the central 6 pc of the DR21 cloud core, T_0 is derived from the peak CO antenna temperature on the assumption that the J=1-0 line is thermalized, r_j and $L(H_2)$ are obtained from the v=1-0 S(1) H_2 emission maps shown in Figs.[4.2.2] & [4.2.3], and T_j is derived assuming that the gas internal to the jet is significantly heated by the wind/cloud shocks. The uncertainty in the pre-shock density is probably a factor of five, whilst, for the jet temperature, the uncertainty is more like a factor of two to three. For the values chosen above, $\dot{M}_w = 10^{-3}\ M_0\ yr^{-1}$ and $V_j = 220$ kms^{-1}, are the best estimates with corresponding tolerances of, $5\times10^{-4} < M_w < 10^{-2}\ M_0\ yr^{-1}$ and $100 < V_j < 450$ kms^{-1}, respectively. Consequently, from eqn.(6.5.9) a best estimate for the cloud shock velocity, $V_c = 38$ kms^{-1}, is obatined with a tolerance of, $25 < V_c < 55$ kms^{-1}.

These predicted ranges in the mass-loss rate and cloud-shock velocity compare favourably with the CO and H_2 emission line observations of the DR21 jets, thereby giving further strength to the confinment model. It is interesting to note that this model predicts extremely high velocities within the jet flow; such high velocity gas may be detectable in 21 cm atomic hydrogen

line emission, or possibly in v=1-0 S(1) H_2 line profiles if high-sensitivity measurments are made of the line wings. Intuitively, one expects the jet flows to consist of a mixture of both atomic gas (dissociated H_2 from high-velocity shocks) and small high-density molecular clumps, entrained through the jet walls and accelerated to velocities comparable to the jet-stream velocity (see Sec.[5.2] & [5.6]). A final prediction of the adiabatic pressure-confinment model is that the mechanical luminosity of the wind, $L_m = 1/2\ \dot{M}_w(V_j)^2 \approx 10^{37}$ erg, is one order of magnitude less than required by the spherical energy-driven winds considered in Sec.[6.4.(c)]. As for the spherical winds, however, the momentum flux through the jets is still too large to be explained by single scattering of photons emanating from the central DR21 luminosity source.

(ii) MOMENTUM-DRIVEN JETS

The assumption of adiabaticity may not strictly apply for the physical conditions characteristic of dense molecular clouds where rapid flow deceleration and efficient cooling may take place. Indeed, velocity profile measurements of the infrared Brackett HI recombination lines, thought to arise from the ionized stellar winds of young or currently forming stars (Simon et al 1983; Persson et al 1985; Garden & Geballe 1986), supply strong evidence that the terminal velocities of most young stellar winds are less than 300 kms^{-1}; this is in agreement with the condition that, $V_w < 500\ kms^{-1}$, for the formation of a momentum-deriven wind (see Sec.[6.4]). If efficient cooling is important, then the shocked wind region degenerates to a very thin, cool, dense shell and the focussing mechanism of the adiabatic pressure-confinment model (i.e. the formation of a De Laval nozzle) ceases to work (Tenorio-Tagle & Rozyczka (1986)). Canto (1980) has proposed an extremely elegant model for stellar wind

collimation under conditions were efficient cooling takes effect. Again, a flattened cloud density distribution is introduced in order to perform the initial collimation of an originally spherical wind bubble. The important difference between Canto's model and the adiabatic model is that the wind velocity vectors glance the outer wind-swept shell at large angles thus inducing material flow along the walls of the ovoid which, in turn, helps to collimate the wind via momentum conservation. Rozyczka & Tenorio-Tagle (1985) have carried out detailed numerical 2-D hydrodynamical simulations based on the Canto collimation concept and follow the non-steady state evolution of a stellar wind within a dense anisotropic molecular cloud. Their findings agree with those of the much simpler Canto model, however, by encorporating evolution of the system they find that extremely collimated jets can form and propagate to large distances from the power source. Furthermore, at the sides of the elongated shell, strong shear motions develop on the border between the shell and the shocked wind region which result in turbulent motions and possibly the entrainment of clumps into the flow. Long-wavelength, Kelvin-Helmholtz instabilities are also prone to develop under a wide range of physical conditions and can lead to periodic oscillation of the jet boundaries, in a manner similar to the abiabatic model. They also find that for dense cloud conditions, adiabatic winds tend to produce a series of bubbles rather than highly collimated jets, indeed, they confidently state that "the presence of molecular jets may necessitate the requirment of cooling flows".

In conclusion, it appears that pressure confinment by the ambient cloud medium may play a significant part in creating the highly-collimated neutral jets observed in DR21, however, the effect of radiative cooling may slightly modify the time evolution and morphology of the overall outflow system. Both the abiabatic and cooling models predict periodic oscillations of the jet boundary

which are clearly present in the DR21 jets.

The exciting possibility therefore exists that the molecular jets associated with early stages of star formation may provide a unique opportunity to study cosmic jets in a much broader context. In contrast to extragalactic jets, for the comparatively nearby molecular jets, one can measure important physical quantities such as density, radial velocity and maybe even the proper motion of "hot spots". Because many important parameters pertaining to galactic jets are (or will be) directly observable, it is then conceivable that they may lead to a significantly better understanding of the physics governing the jet phenomenon than do extragalactic jets.

6.5.(c) THE ROTATING MAGNETIC DISC MODELS

The existence of massive, rotating discs of cold, dense, neutral interstellar material juxtaposition with the driving engines of high-velocity bipolar outflows is now accepted as firm observational fact. The general consensus is that these massive structures originate from the noisotropic collapse of a magnetic proto-cloud (Mestel 1985), as under these conditions rotation with an axis perpendicular to the large-scale magnetic field may damp faster than rotation with an axis parallel to the field. This preferential damping mechanism is believed to take place during the early stages of cloud contraction when the ionization fraction of the gas is sufficient to couple the cloud matter to the magnetic field, thus forcing the angular momentum vector to point in the same general direction as the magnetic field; at later stages in the collapse, when densities are higher and temperatures cooler, the ionization fraction drops and the field may no longer be frozen with the gas. Observational confirmation of

the preferential contraction scenario has been presented by Moneti et al. (1984) and Cohen, Rowland & Blair (1984), who, using polarization measurements of background stars as an indicator of magnetic field direction, find that for more than half of the bipolar outflows observed, the outflow and magnetic axes are aligned to within $\sim 20^{\circ}$.

The growing body of observational evidence pointing towards the ubiquity of interstellar discs in star-forming regions (e.g. Torrelles et al. 1983; Bieging 1984; Hasegawa et al. 1984; Kawabe et al. 1984; Takano et al. 1984) has stimulated precipitous interest in the development of a new generation of outflow models which include as a natural ingredient the magneto-hydrodynamic (MHD) interaction between a central rotor and an open-ended magnetic field. The first versions of this basic idea (Hartmann & MacGregor 1982; Draine 1983) considered the likelyhood of fast rotating stars as being the underlying rotors. The more recent models, instead, invoke the more natural viewpoint that the observed bipolar outflows are centrifugally driven, MHD winds emanating from the same interstellar discs in which the protostars themselves are embedded (Pudritz & Norman 1983; Uchida & Shabita 1985; Pudritz 1985; Pudritz & Norman 1986). The basic concept is that the acceleration of the bipolar flows results from the winding up of the magnetic field by the rotation of the underlying contracting disc. The acceleration of the disc gas is directed parallel to the open magnetic field lines and takes effect up to a critical point in the flow as defined by the Alfven radius, R_a, (where the magnetic and thermal pressures are equal). At radii, $r \gg R_a$, the field is unable to force the gas to co-rotate with the disc and the transverse velocity decreases as $1/r$. Magnetic acceleration therefore only occurs between the disc surface and the Alfven radius, and the outflow gas aquires terminal poloidal speeds of order ΩR_a, where, Ω, is the angular momentum of the underlying disc. The highest

velocities predicted by this model therefore increase with increasing disc rotation and magnetic field strength. Another advantage specific to this model is that MHD winds are extremely efficient in extracting angular momentum and rotational energy from the disc and therefore promote rapid accretion onto a central protostar with very low specific angular momentum transfer. The presence of MHD winds, therefore, naturally solve the age old problem of angular momentum growth during cloud collapse. Moreover, the high accretion rates can significantly heat and ionize the disc core and thus may explain the origin of the ultra-compact ionized winds commonly observed toward the infrared point sources found at the centre of the neutral discs (Persson et al. 1984; Simon et al. 1983; Garden & Geballe 1986).

A necessary constraint introduced by this model is that the central objects of all outflows must still belong to a pre-main-sequence phase. Several other predictions arise from the MHD models which, in the light of further observations, may provide a concrete test of the nature of the acceleration mechanism. First, and foremost, the mass ejection takes the form of a hollow cylindrical shell which rotates with the disc, of radius R_d, out to the magnetically defined alfven radius, $R_a \approx 10(R_d)$. Second, the outflow gas is accelerated up to the terminal velocity ($V_w \approx 50$ kms^{-1}), attained at the alfven radius, in a gradual and monotonic fashion. Third, the existence of a massive, rotating and slowly collapsing disc is an absolute necessity. Fourth, the existence of a compact ionized or X-ray emitting accretion core at the centre of every outflow source should also be observable. A major disadvantage of the purely magnetic models is that, unlike the pressure confinment models, they cannot create the highly-collimated supersonic flows reminiscent of the DR21 H_2 emission-line jets, as the importance of magnetic confinment deteriorates rapidly at distances comparable to, or larger than, the alfven radius.

Having briefly outlined the basic concepts underlying the current magnetic outflow models, a comparison between there predicted attributes and those characteristic of the DR21 jets can now be made. Using a somewhat ad hoc model Pudritz and Norman (1986) have predicted that for a massive molecular outflow, similar to that found in DR21; at radii $10^{17} < r < 10^{18}$ cm, the molecular flow originates from a cool neutral disc envelope, with a mass-loss rate, $M_w > 10^{-3}\ M_0\ yr^{-1}$, and a terminal velocity of, $V_w \approx 50\ kms^{-1}$, which is reached at the alfven radius, $R_a = 10^{18}$-10^{19} cm. The momentum transport rate in the wind is extremely high ($M_w V_w/[L*/c] > 100$) compared to non-magnetic models (viz. Sec.[6.4.f]) and results because the escape velocity from the disc surface is only a small fraction of that characteristc of a star. Indeed, a centrifugally propelled MHD wind emanating from the surface of rotating disc, is the only presently known mechanism, appart from a SN explosion, that can naturally supply sufficient momentum flux to drive the massive molecular outflows in luminous star forming regions such as DR21.

The slowly rotating, edge-on disc that is so clearly prominent in CS line emission (viz. Sec.[4.4]) has a radius on the order of 1 pc and is thus in good agreement with the hydromagnetic disc model predictions. However, the presence of a rotational component perpendicular to the outflow axis, as is also predicted by this model, is not evident in the high-angular resolution CO observations discussed in Sec.[4.3]. Due to the large distance to DR21 ($\cong$ 3 kpc), the spatial resolution at the source is only 10^{18} cm which may be insufficent to resolve fine rotational structure due to beam overlap. Further observations at higher-angular resolution than used in the present study in a variety of millimeter molecular line transitions are clearly warranted.

In conclusion, it appears that purely magnetic and purely non-magnetic models cannot by themselves account for the observed characteristics particular to the DR21 molecular outflows. A best fit solution requires specific attributes common to both types of models; the large momentum transport rates can only be explained by mass ejection from the surface of a rotating and magnetized interstellar disc, whilst, at larger distances from the central driving source, the formation of highly-collimated supersonic jets requires that either pressure or momentum confinment be the dominant process. Further understanding of this exciting and potentially rewarding area of astrophysical study will benefit greatly from advancements both in observing technique and theoretical interpretation.

6.6 SCHEMATIC MODELS OF THE DR21 OUTFLOW

Common to all areas of pioneering scientific research, there comes a stage in the presentation of new data, when, in order to make further headway, one is forced to relax ones conservative approach and explore the meaning of ones work in a more imaginative sense. Probably the most descriptive method available for portraying a visual idea to others is through the use of a simple schematic model which qualitatively expresses rather than quantitatively justifies the fundamental physics underlying the idea.

In line with this reasoning, the opportunity is now taken to present two purely schematic models which, it is suggested, may best consolidate the observations of the DR21 outflow. The first model involves an equilibrium situation where mass outflow is accompanied by balanced accretion, mediated by the gravitional attraction of a hypothetical magnetized and rotating protostellar disc. The second model is considerably more contrived and relies on the

presence of at least two physically independent molecular outflows emanating from the surroundings of a recently formed OB star cluster. It is stressed that, due to the inherent complexity of the DR21 star-forming region, these models are necessarily oversimplified and are, therefore, of a purely suggestive nature only.

6.6.(a) MODEL 1 : AN ACCRETION DRIVEN OUTFLOW

The reasoning behind this model stems from the surprising discovery of two apparently perpendicular bipolar high-velocity CO flows, both of which emanate from a common origin located somewhere internal to the DR21 cloud core/molecular disc (see Fig.[4.3.7]).

The largest and most prominent bipolar flow is aligned NE-SW and is definitely an outflow as it is spatially associated with luminous and extremely high-velocity shock-excited H_2 line emission. Also, the high-velocity CO and H_2 lobes are located too far out from the outflow centre to be gravitationally bound, as a mass of $> 5\times10^5$ M_0 would be required in the central regions; this mass is one order of magnitude larger than the core mass as derived from the CS observations.

Steady-state conditions strike a natural balance in many astrophysical contexts, especially if gravity is the dominant force involved. It is thus natural to expect that if the massive disc central to the DR21 outflow system is gravitationally bound, then the observed mass outflows may be accompanied by mass accretion, with both the outflow and accretion flow possessing comparable momentum transfer rates (Pudritz 1985). It is therefore suggested here that the

second smaller-scale bipolar flow, which is oriented perpendicular to the major outflow axis and almost parallel to the DR21 disc plane, may represent the accretion flow which feeds the outflow. A schematic illustration of the geometry envisaged by this model is shown in Fig.[6.6.1].

In essence, the proposed accretion, which is directed along the disc plane, provides a reservoir of latent potential energy which through some vague MHD process (Norman & Pudritz 1986) is converted into ordered kinetic energy, taking the form of a molecular outflow directed perpendicular to the disc plane (see Sec.[6.5.(b)]). The major advantage of this model, therefore, is that it can explain the origin of the two perpedicular CO flows. Moreover, if the disc is threaded by a compressed magnetic field, and if the ionization fraction is sufficient to couple the field to the disc, then the disc rotation can twist the field lines to such an extent that large non-perpendicular vectors are induced at the disc surface (Belcher & MacGregor 1976; Pudritz 1985). Mass inflow along the twisted magnetic field lines threading the outer parts of the rotating disc will then result in a systematic radial-velocity field, which to an observer looking edge-on to the disc, will appear as a bipolar flow with the same velocity sense as the disc rotation. These predictions agree with the observations (Fig.[4.3.7]); i.e. the NW-SE high-velocity CO bipolar flow is oriented almost parallel to the plane of the CS disc and shows the same velocity trend (blue-shifted to the south and red-shifted to the north of the outflow centre) as the disc rotation (Fig.[4.4.3]).

A fundamental test of the accretion/outflow model is that the observed velocities in the proposed CO accretion flow should agree with the free-fall velocity calculated from the known size and mass of the central disc. From the measured disc parameters

$M_{disc} = 5 \times 10^4 \ M_0$

$r_{disc} = 1$ pc

$h_{disc} = 0.5$ pc

$n_{disc} = 5 \times 10^5$ cm^{-3}

a free-fall velocity of ~ 20 kms^{-1} is derived; this is in excellent agreement with the observed velocity extent of the CO profiles in the NW-SE bipolar lobes. Furthermore, from a visual inspection of Fig.[4.3.7], it is apparent that the two bipolar flows are of comparable integrated brightness in HIGH-velocity CO emission, thus implying that the mass transfer rates in the two flows are also of comparable magnitude, just as predicted for the case of a balanced system.

A possible problem faced by the accretion/outflow model is that the observed rotational velocity of the disc is only 1 kms^{-1} whereas if the disc were to be rotationally supported against its own gravity a rotational velocity of order 15 kms^{-1} is necessitated. How, then, is it possible to explain the apparent sub-Keplerian velocity field of the disc? A solution to this paradox may once again derive from the presence of magnetic fields, which, if frozen to the gas, may magnetically brake the disc rotation by converting the angular momentum of the disc into radial momentum of the bipolar outflow. For such a magnetically coupled process, where both the increased ionization fraction in the disc and the luminosity of the central driving source derives solely from accretion heating, the disc rotation, V_r, can be expressed in terms of the ratio of the outflow mechanical energy flux, L_m, in the outflow gas to the luminosity of the central source, $L*$, as follows (Pudritz & Norman 1986)

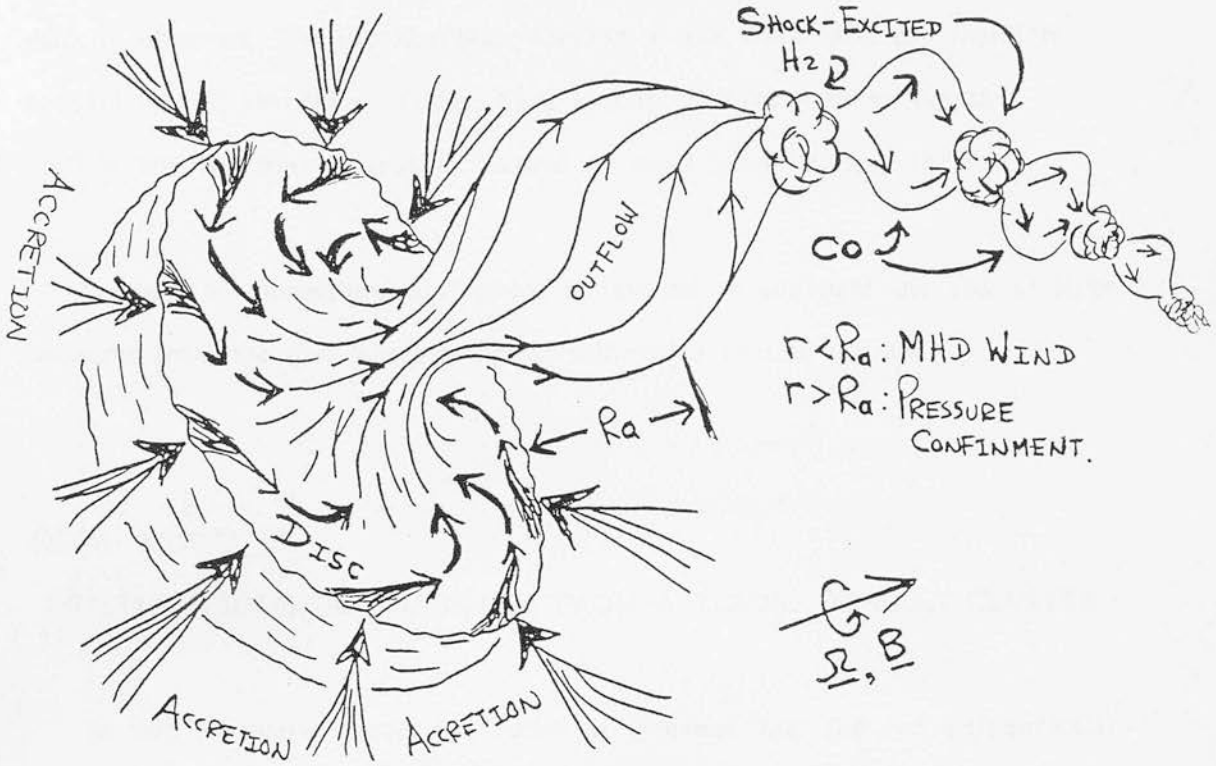

FIGURE 6.6.1 : A schematic model of a centrifugally driven MHD wind. The magnetic torque drives mass-loss along a direction parallel to the magnetic field B and the angular momentum Ω vectors and perpendicular to the disc plane. At large distances from the disc surface (i.e. $r \gg R_a$), the outflow is assumed to be recollimated by either momentum or pressure confinment within the surrounding molecular cloud medium. The confinment causes compression and rarefaction regions to develop along the jet, which give rise to the shocked H_2 and high-velocity CO emission, respectively.

$$V_r = 5.4 \left[\frac{M_d}{M_0}\right]^{1/2} \left[\frac{10^{12.5}\,cm}{R_d}\right]^{1/2} \left[\frac{L_m/L_*}{10^{-2}}\right]^{1/2} \quad kms^{-1} \qquad (6.6.1)$$

Inserting the observed values, Md = 5(4) Mo, Rd = 1 pc, Lm/L* = 5(-3), a disc rotation of, Vr = 0.9 kms-1, is derived, which is exactly the rotational velocity observed. The sub-Keplerian rotation of the DR21 disc can therefore be explained if the disc is braked by a hydromagnetically driven bipolar outflow and the mass balance is restored by rapid accretion onto the disc.

Pressure or momentum confinment is invoked to collimate the jets at large distances from the disc where magnetic collimation fails to operate.

6.6.(b) MODEL 2 :

MULTI-DIRECTIONAL OUTFLOWS FROM A YOUNG OB STAR CLUSTER

In this alternative model the notion is proposed that the two perpendicular bipolar outflows seen in the DR21 region originate from separate outflow centres, most probably from two or more massive stars in a currently forming or recently formed OB star cluster located deep within the DR21 molecular cloud core. For this scenario to work, two separate discs are required to drive the two bipolar flows. The largest disc (resolved by the CS observations) drives the main NE-SW bipolar flow and a considerably smaller disc (unresolved by our CS observations) is further required in order to drive the smaller-scale SE-NW bipolar flow. It may even be possible that the plane of the large disc has different orientations on different size scales, with the inner disc being warped though a large angle with respect to the outer disc. At present, the multi-flow hypothesis has no solid founding, appart from the observed existence

of two perpendicular bipolar flows, and as such is only mentioned here for the sake of completeness. Nonetheless, it is an entertaining idea which definitely requires further thought and observational investigation.

As present opinion leads us to believe that every star undergoes an energetic stage of rapid mass-loss during a large fraction of its formative years, then it would seem inevitable that during the formation of a young OB star cluster, several outflows may be active at the same instant in time. An important line of study would be to investigate theoretically how these coeval flows would interact and effect one another. In particular, a question of direct relevance to the present study which justifies theoretical attention, is; "would the flows from the individual high-mass (proto)stars of a young cluster forming within a massive disc merge and expand as one united super-flow or would they retain their own identities and give rise to multiple bipolar structures?"

The DR21 molecular cloud complex has been mapped in the v=1-0 S(1) transition of H_2, the J=1-0 transition of CO, the J=1-0 & 2-1 transitions of CS and the 53α recombination line of hydrogen. These observations reveal the existence of a highly-collimated, bipolar flow consisting of two large and massive lobes of shocked, hypersonically-expanding molecular gas. This hitherto unknown bipolar flow is singular to the presently studied sample of young-stellar outflow sources, in that it is the largest, most massive and most luminous of all the members. At the outflow origin there lies a massive, slowly rotating disc which presumably provides the energy and momentum flux to drive the extended, highly-energetic outflows. This disc may aid in the initial collimation of the outflow at distances close to the cloud core. From analysis of a variety of different observations, it is further suggested that the luminous DR21 compact HII region may not be physically associated with the central outflow system but, rather, may represent the line-of-sight projection of a blister HII region that is located on the back surface of the DR21 molecular cloud.

The DR21 outflow most probably owes its large size (> 5 pc) to its old age; a flow lifetime of ~ 5×10^4 yr is estimated, which is comparable to the time-scale for the contraction phase of a massive protostar. The momentum flux required to drive the observed dynamics and luminosity in high-velocity CO and shock-excited H_2 line emission cannot be supplied either by the expansion of the luminous DR21 HII region, or by the radiation pressure of the central object. A cloud-cloud collision, although energetically favourable, cannot accelerate the compressed gas to the hypersonic velocities (> Mach 50) observed

in this region. Consequently, a magneto-hydrodynamically collimated molecular wind driven by mass accretion onto the surface of a slowly rotating, massive disc is the only mechanism available at present, barring a recent supernova explosion, which can account for the exceedingly large momentum fluxes that are required to power the observed mass motions in the DR21 region. It is further found that the correlation between the outflow energy and the luminosity of the central driving source, that is a well-known characteristic of low-luminosity outflow sources, also applies for the more luminous star forming-regions in the galaxy. Such a correlation may result if the size of the disc which drives the outflows scales in proportion to the luminosity of the central object, which may arise if the luminosity derives from shock heating associated with accretion of material from the inner surface of the disc onto the central object.

Another important result derived from the high-angular resolution millimeter-wave observations is the identification of a second spatially distinct high-velocity CO bipolar flow, which is aligned along an axis oriented perpendicular to the axis of the main outflow. Both flows apparently possess a common geometric centre that is located within the DR21 cloud core. The smaller scale bipolar flow may be interpreted as collimated accretion of ambient cloud material onto the disc surface, the collapse of which, subsequently supplies the energy to drive the large scale outflows. Alternatively, there may exist more than one outflow source within the DR21 cloud core, possibly the result of coeval star formation during the making of a young OB star cluster. As a multi-directional outflow geometry cannot be explained by any of the outflow models proposed to date, these observations are important in that they should stimulate the development of new models which can accommodate such complexities.

The DR21 H_2 emission-line jets exhibit profiles with velocity widths (> 100 kms^{-1} from the cloud rest velocity) that greatly exceed the molecular dissociation limit ($V_{diss} \approx 50$ kms^{-1}). The highest-velocity emission may arise from cloudlets of dense molecular gas that move outwards at almost the flow velocity, whereas the intense emission that characterizes the line-core probably arises from shocked ambient gas that is swept up to form a dense, slowly-moving shell that borders the expansion region. Outflow velocities in the DR21 jets of order 100 kms^{-1}, as observed here, are similar to those that characterize the Orion outflow and indicate that the Orion outflow is not truly unique with respect to its ultra-high velocities. The bulk of the outflow gas, however, is probably expanding at considerably slower velocities, as the CO profiles exhibit wings which extend no further than +/- 50 kms^{-1} from the DR21 rest velocity. Indeed, the CS observations, which are an excellent probe of the location and velocity structure of the densest gas in the outflow system, are characterized by profiles that extend to only +/- 10 kms^{-1} from the rest velocity. Owing to the exceedingly large mass derived from integrating the CS line emission over the full extent of the outflow lobes (> 10^4 M_0), it is almost certain that this slower moving, but still highly-supersonic, dense gas is associated with the swept-up, compressed ambient medium rather than the driving wind itself. The high-velocity CS gas may be overabundant by two orders of magnitude, in good agreement with the predictions of numerical shock models.

The vibrationally-excited H_2 and rotational CO & CS emissions arise from spatially separate regions of the flow, each region characterized by different values of density, temperature and velocity. This implies the presence of a complex mixture of physical conditions within the molecular gas that forms the

DR21 outflow lobes. The low beam filling factors derived from the high-velocity wings of the CO and CS profiles further suggest that the outflow medium is composed of many small clumps that fill only ~ 10% of the total surface area. From analysis of the smoothness of the high-velocity portions of the observed line profiles it appears that if the outflow gas is clumped, then these clumps must be very small (<0.01 pc) in order to suppress large fluctuations in the emission between adjacent velocity channels. It is suggested that more detailed radiative transfer models in conjunction with higher spatial and spectral resolution observations are required in order to investigate further the velocity width and size scale of the clumps and to quantify the importance of turblence in the outflow gas.

The detailed internal structure of the molecular outflow jets, as delineated by the shock-excited H_2 line emission, indicates the presence of an exceedingly clumpy medium, with the brightest emission peaks periodically spaced along the jet axis in a remarkably regular fashion. This periodic clumping is highly reminiscent of laboratory measurements and theoretical models of pressure confined, fluid-dynamical jets that are commonly employed to explain the observed morphology of extragalactic plasma jets. It is therefore suggested that the large scale collimation mechanism operative in the DR21 molecular cloud may involve unstable pressure confinment after sudden ejection from a nozzle, formed at the outer boundary of the dense cloud core. If such physics do pertain, then the presence of substantial lateral motions within the jet may excite a train of oblique shocks, the interaction of which, result in the formation of a succession of compression and rarefaction waves that are periodically spaced along the jet axis. The shock-excited H_2 emission-line clumps may then be associated with the compression regions, where the oblique shocks converge, and the gaps in between with the rarefaction regions, where

the jet expands freely and cools rapidly. A detailed high-angular resolution study of the spatial distribution and shape of the shock-excited emission-line knots should be able to test this hypothesis.

The exciting possibilty exists that if the molecular outflows seen within our own galaxy are collimated via a scaled down version of the same physical mechanism that collimates the relativistic plasma jets of luminous radio galaxies, then a detailed kinematic study of energetic molecular jets may supply useful information that may help develop our limited understanding of how jets form in general. It may also be true that a more detailed study of the role played by gravitational accretion onto massive protostellar discs, the mechanism now believed to power the molecular flows in star-forming regions, may also lead to a better understanding of the physical nature of the driving engine at the heart of active galactic nuclei and other accretion dominated systems. Clearly, continued studies of molecular flows within galactic star-formation regions are of vital importance not only for improving our understanding of the star-formation process but also because of their direct application to many other interesting areas of astronomy.

APPENDIX 1 : IMPORTANT H_2 VIBRATION/ROTATION LINES.

TRAN	WAVELENGTH (um)	FREQ cm(-1)	G(J)	Eupper (K)	A sec(-1)
1-0 S(0)	2.2235	4497.41	5	6471	2.53(-7)
1-0 S(1)	2.1218	4712.91	21	6956	3.47(-7)
1-0 S(2)	2.0338	4917.01	9	7584	3.98(-7)
1-0 S(3)	1.9576	5108.40	33	8365	4.21(-7)
1-0 S(4)	1.8920	5285.52	13	9286	4.19(-7)
1-0 S(5)	1.8358	5447.25	45	10,341	3.96(-7)
1-0 S(6)	1.7880	5592.9	17	11,522	3.54(-7)
1-0 S(7)	1.7480	5720.8	57	12,817	2.98(-7)
1-0 S(8)	1.7147	5831.9	21	14,221	2.34(-7)
1-0 S(9)	1.6877	5925.1	69	15,722	1.68(-7)
1-0 S(10)	1.6665	6000.6	25	17,311	1.05(-7)
1-0 S(11)	1.6504	6059.0	81	18,979	0.53(-7)
1-0 Q(1)	2.4066	4155.25	9	6149	4.29(-7)
1-0 Q(2)	2.4134	4143.47	5	6471	3.03(-7)
1-0 Q(3)	2.4237	4125.87	21	6956	2.78(-7)
1-0 Q(4)	2.4375	4102.57	9	7584	2.65(-7)
1-0 Q(5)	2.4548	4073.72	33	8365	2.55(-7)
1-0 Q(6)	2.4756	4039.5	13	9286	2.45(-7)
1-0 Q(7)	2.5001	3999.9	45	10,341	2.34(-7)
1-0 O(2)	2.6269	3806.79	1	5987	8.54(-7)
1-0 O(3)	2.8025	3568.21	9	6149	4.23(-7)
1-0 O(4)	3.0039	3329.03	5	6471	2.90(-7)
1-0 O(5)	3.2350	3091.19	21	6956	2.09(-7)
1-0 O(6)	3.5007	2856.55	9	7584	1.50(-7)
1-0 O(7)	3.8075	2626.37	33	8365	1.06(-7)
1-0 O(8)	4.1625	2402.4	13	9286	0.74(-7)

APPENDIX 1 : H_2 VIBRATION/ROTATION LINES (continued)

TRAN	WAVELENGTH (um)	FREQ cm(-1)	G(J)	Eupper (K)	A sec(-1)
2-1 S(0)	2.3556	4245.15	5	12,095	3.68(-7)
2-1 S(1)	2.2477	4448.95	21	12,550	4.98(-7)
2-1 S(2)	2.1542	4642.04	9	13,150	5.60(-7)
2-1 S(3)	2.0649	4842.74	33	13,890	5.77(-7)
2-1 S(4)	2.0041	4989.84	13	14,764	5.57(-7)
2-1 S(5)	1.9449	5143.73	45	15,763	5.05(-7)
2-1 S(6)	1.8947	5277.8	17	16,880	4.30(-7)
2-1 S(7)	1.8528	5397.3	57	18,107	3.38(-7)
2-1 S(8)	1.8183	5499.6	21	19,434	2.41(-7)
2-1 S(9)	1.7904	5585.2	69	20,853	1.49(-7)
2-1 O(2)	2.7862	3589.11	1	11,635	12.9(-7)
2-1 O(3)	2.9741	3362.40	9	11,789	6.40(-7)
2-1 O(4)	3.1899	3134.93	5	12,095	4.41(-7)
2-1 O(5)	3.4379	2908.75	21	12,550	3.18(-7)
2-1 O(6)	3.7236	2685.58	9	13,150	2.28(-7)
2-1 O(7)	4.0540	2466.7	33	13,890	1.62(-7)
3-2 S(0)	2.5014	3997.73	5	17,389	3.88(-7)
3-2 S(1)	2.3864	4190.33	21	17,818	5.14(-7)
3-2 S(2)	2.2870	4372.49	9	18,386	5.63(-7)
3-2 S(3)	2.2014	4542.57	33	19,086	5.63(-7)
3-2 S(4)	2.1280	4699.32	13	19,912	5.22(-7)
3-2 S(5)	2.0656	4841.3	45	20,856	4.50(-7)
3-2 S(6)	2.0130	4967.7	17	21,911	3.57(-7)
3-2 S(7)	1.9692	5078.1	57	23,069	2.54(-7)
3-2 O(2)	2.9620	3376.07	1	16,952	14.1(-7)
3-2 O(3)	3.1637	3160.81	9	17,098	6.86(-7)
3-2 O(4)	3.3958	2944.80	5	17,387	4.87(-7)
3-2 O(5)	3.6630	2729.99	21	17,818	3.52(-7)
3-2 O(6)	3.9721	2517.58	9	18,386	2.53(-7)

APPENDIX 1 : H_2 VIBRATION/ROTATION LINES (continued)

TRAN	WAVELENGTH (um)	FREQ cm(-1)	G(J)	Eupper (K)	A sec(-1)
0-0 S(0)	28.221	354.35	5	510	2.94(-11)
0-0 S(1)	17.035	587.04	21	1015	4.76(-10)
0-0 S(2)	12.279	814.43	9	1682	2.76(-9)
0-0 S(3)	9.6649	1034.67	33	2504	9.84(-9)
0-0 S(4)	8.0258	1245.98	13	3474	2.64(-8)
0-0 S(5)	6.9091	1447.36	45	4586	5.88(-8)
0-0 S(6)	6.1088	1636.97	17	5829	1.14(-7)
0-0 S(7)	5.5115	1814.40	57	7197	2.00(-7)
0-0 S(8)	5.0529	1979.08	21	8677	3.24(-7)
0-0 S(9)	4.6947	2130.06	69	10,263	4.90(-7)
0-0 S(10)	4.4096	2267.80	25	11,940	7.03(-7)
0-0 S(11)	4.1810	2391.79	81	13,703	9.64(-7)
0-0 S(12)	3.9947	2503.0	29	15,549	1.27(-6)
0-0 S(13)	3.8464	2599.0	93	17,458	1.62(-6)
0-0 S(14)	3.724	2685.3	33	19,402	2.00(-6)
0-0 S(15)	3.625	2758.9	105	21,400	2.41(-6)
0-0 S(16)	3.547	2819.3	37	23,459	2.83(-6)
0-0 S(17)	3.485	2869.5	117	25,539	3.26(-6)
0-0 S(18)	3.438	2908.3	41	27,643	3.68(-6)
0-0 S(19)	3.404	2937.8	129	29,765	4.10(-6)
0-0 S(20)	3.380	2959	45	31,895	4.51(-6)
0-0 S(21)	3.369	2968	141	34,036	4.9 (-6)
0-0 S(22)	3.366	2971	49	36,173	5.3 (-6)
0-0 S(23)	3.372	2966	153	37,728	5.7 (-6)

APPENDIX 1 : H_2 VIBRATION/ROTATION LINES (continued)

TRAN	WAVELENGTH (um)	FREQ cm(-1)	G(J)	Eupper (K)	A sec(-1)
2-0 S(0)	1.1896	8406.3	5	12,095	1.27(-7)
2-0 S(1)	1.1622	8604.2	21	12,550	1.90(-7)
2-0 S(2)	1.1382	8785.5	9	13,150	2.38(-7)
2-0 S(3)	1.1175	8948.6	33	13,890	2.77(-7)
2-0 S(4)	1.0998	9092.4	13	14,764	3.07(-7)
2-0 S(5)	1.0851	9215.5	45	15,763	3.28(-7)
2-0 Q(1)	1.2383	8075.3	9	11,789	1.94(-7)
2-0 Q(2)	1.2419	8051.9	5	12,095	1.38(-7)
2-0 Q(3)	1.2473	8017.2	21	12,550	1.29(-7)
2-0 Q(4)	1.2545	7971.1	9	13,150	1.25(-7)
2-0 Q(5)	1.2636	7913.9	33	13,890	1.23(-7)
2-0 Q(6)	1.2745	7846.4	13	14,764	1.21(-7)
2-0 Q(7)	1.2873	7768.1	45	15,763	1.20(-7)
2-0 Q(8)	1.3020	7680.4	17	16,880	1.18(-7)
2-0 Q(9)	1.3188	7582.8	57	18,106	1.17(-7)
2-0 O(2)	1.2932	7732.6	1	11,635	3.47(-7)
2-0 O(3)	1.3354	7488.3	9	11,789	1.61(-7)
2-0 O(4)	1.3817	7237.5	5	12,095	1.03(-7)
2-0 O(5)	1.4322	6982.5	21	12,550	6.98(-8)
2-0 O(6)	1.4870	6725.1	9	13,150	4.72(-8)
2-0 O(7)	1.5464	6466.6	33	13,890	3.15(-8)
2-0 O(8)	1.6104	6209.5	13	14,764	2.05(-8)
2-0 O(9)	1.6796	5953.7	45	15,763	1.31(-8)
2-0 Q(3)	1.247	8017	21	12,550	1.29(-7)
3-1 Q(3)	1.324	7553	21	17,818	3.34(-7)
4-2 Q(3)	1.409	7096	21	23,295	5.60(-7)
5-3 Q(3)	1.502	6660	21	27,500	7.65(-7)
6-4 Q(3)	1.61	6210	21	31,700	9.16(-7)
7-5 Q(3)	1.74	5750	21	35,700	9.77(-7)

REFERENCES

Abbott, D.C., 1982. Ap.J., 263, 723.

Abbott, D.C., Bieging, J.H., & Churchwell,E., 1981. Ap.J., 250, 645.

Allison, A.C., & Dalgarno, A., 1970. At.Data, 1, 289.
Appenzeller, I., 1982. Fundam. Cosmic Phys., 7, 313.
Bally, J., 1982. Ap.J., 261, 558.

Bally, J., & Langer, W.D., 1982. Ap.J., 255, 143.

Bally, J., & Lada, C.J., 1983. Ap.J., 265, 824.

Bally, J., & Scoville, N.Z., 1982. Ap.J., 255, 497.

Bally, J., & Stark, A.A., 1983. Ap.J., 266, L61.

Bally, J., & Lane, A.P., 1985. Ap.J., in press.

Barral, J.F., & Canto, J., 1981. Rev.Mexicana Astron.Astrof., 5, 101.

Beck, S.C., & Beckwith, S., 1983. Ap.J., 271, 175.

Beck, S.C., 1984. Ap.J., 281, 205.

Beckwith, S.W.V., Persson, S.E., Neugebauer, G., & Becklin, E.E., 1978. Ap.J., 223, 464.

Beckwith, S., Evans, N.J.II, Gatley, I., Gull, G., & Russell, R.W., 1983. Ap.J., 264, 152.
Belcher, J.W. & Mac Gregor, K.B., 1976. Ap.J., 210, 498.
Beckwith, S., Natta, A., & Salpeter, E.E., 1983. Ap.J., 267, 596.
Bieging, J.H., 1984. Ap.J., 286, 591.
Black, H.J., & Dalgarno, A., 1976, Ap.J., 203, 132.

Blandford, R.D., & Rees, M., 1974. M.N.R.A.S., 169, 395.
Blandford, R.D. & Konigl, A., 1979. Ap. Letters, 20, 15.
Blitz, L., 1979. in "Giant Molecular Clouds in the Galaxy", p.211, ed. P.M. Solomon & M.G.Edwards (Oxford:Permagon)

Blitz, L., & Shu, F.H., 1980. Ap.J., 238, 148.

Brocklehurst, M., & Seaton, M.J., 1972. M.N.R.A.S., 157, 179.

Brown, R.L., Lockman, F.J., & Knapp, G.R., 1978. Ann.Rev.Astron.Astrophys., 16, 445.

Burton, M.G., 1986. Thesis (Edinburgh University).

Burton, M.G., Geballe, T.R., Brand, P., & Webster, A., 1986. preprint.

Canto, J., & Rodriguez, L.F., 1980. Ap.J., 239, 982.

Cartwright, D.C., & Drapatz, S., 1970. A.&A., 4, 443.

Castor, J., McCray, R.A., & Weaver, R., 1975. Ap.J., 200, L107.

Chackerian, C., & Tipping, R.H., 1983. J.Molec.Spec., 99, 431.

Chernoff, D.F., Hollenbach, D.J., & McKee, C.F., 1982. Ap.J., 259, L97.

Chevalier, R.A., 1975. Ap.J., 195, 53.

Chevalier, R.A., 1980. Astrophys. Lett., 21, 57.

Cohen, R.J., Rowland, P.R., & Blair, M.M., 1984. M.N.R.A.S., 210, 425.

Cohen, R.S., & Thaddeus, P., 1977. Ap.J., 217, L155.

Dabrowski, I., 1984. Can.J.Phys., 62, 1639.

Dalgarno, A., & Wright, E.L., 1972. Ap.J., 174, L49.

Dalgarno, A., Black, J.H. & Weisheit, J.C., 1973. Ap.Lett., 14, 17.

Dalgarno, A., 1975. in "Atomic & Molecular Processes in Astrophysics", ed. M.C.E. Hauber & N. Nussbaumer (Geneva Observatory).

Davis, D.S., Larson, H.P., & Smith, H.A., 1982. Ap.J., 259, 166.

Davis, D.S., Larson, H.P., & Hofmann, R., 1986. Ap.J., 304, 481.

Dickel, J.R., Dickel, H.R., & Wislon, W.J., 1978. Ap.J., 223, 840.

Dickel, H.R., Lubenow, A.F., Goss, W.M., Forster, J.R., & Rots, A.H., 1983. A.&A., 120, 74.

Dickel, H.R., Ho, P.T.P., & Wright, M.C.H., 1985. Ap.J., 290, 256.

Dickel, H.R., Goss, W.M., Rots, A.H., & Blout, H.M., 1986 (preprint).

Dickman, R.L.A., 1975. Ap.J., 202, 50.

Dickman, R.L., 1978. Ap.J.Supp., 37, 407.

Downes, D., & Rinehart. R., 1966. Ap.J., 144, 937.

Downes, D., Genzel, R., Becklin, E.E., & Wynn-Williams, C.G., 1981. Ap.J., 244, 869.

Draine, B.T., & Roberge, W.G., 1982. Ap.J., 259, L91.

Draine, B.T., & Roberge, W.G., 1984. Ap.J., 282, 491.

Draine, B.T., Roberge, W.G., & Dalgarno, A., 1983. Ap.J., 264, 485.

Draine, B.T., 1983. Ap.J., 270, 519.

Draine, B.T., 1980. Ap.J., 241, 1021.

Drapatz, S., 1979. A.&A., 75, 26.
Dyson, J.E., 1983. Astrophys.Space Sci., 106, 181.

Elmegreen, D.M., & Lada, C.J., 1976. Ap.J., 81, 1089.

Elmegreen, D.M., & Lada, C.J., 1977. Ap.J., 214, 725.

Elmegreen, D.M., & Elmegreen, B.G., 1979. Astron.J., 84, 615.

Field, G.B., Sommerville, W.B., & Dressler, K., 1966. Ann.Rev.Astr.Astrophys., 4, 207.

Field, G.B., Rather, J.D., Aannestad, P.A., & Orszag, S.A., 1968. Ap.J., 151, 953.

Fischer, J., Righini-Cohen, G., & Simon, M., 1981. Ap.J.Lett., 238, L155.

Fischer, J., Sanders, D.B., Simon, M., & Solomon, P.M., 1985. Ap.J., 293, 508.

Forster, J.R., Goss, W.M., Dickel, H.R., & Habing, H.J., 1981. M.N.R.A.S., 197, 513.

Frerking, M.A., Langer, W.D., & Wilson, R.W., 1982. Ap.J., 262, 590.

Fukue, J., & Yokoo, T., 1986. Nature, 321, 841.

Garay, G., Reid, M.J., & Moran, J.M., 1985. Ap.J., 289, 681.

Garden, R.P. 1986. in IAU Symposium No.115 : "Star Forming Regions", ed. M.Peimbert & J.Jugaku (Reidel Press).

Garden, R.P. & Geballe, T.R., 1986. M.N.R.A.S., 220, 611.

Garden, R.P., Geballe, T.R., Gatley, I., & Nadeau, D., 1986. M.N.R.A.S., 220, 203.

Garmany, C.D., & Conti, P.S. 1984. Ap.J., 284, 705.

Garmany, C.D., Olson, G.L., Conti, P.S., & van Steenberg, M.E., 1981. Ap.J., 250, 660.

Gatley, I., Hasegawa, T., Garden, R., & Brand, P.W.J.L., 1987. Ap.J., in press.

Geballe, T.R., Persson, S.E., Simon, T., Lonsdale, C.J., & McGregor, P.J., 1986. Ap.J., 302, 693.

Genzel, R., & Downes, D., 1977. A.&A.Supp., 30, 145.

Genzel, R., Watson, D.M., Crawford, M.K., & Townes, C.H., 1985. Ap.J., 297, 766.

Goldsmith, P.F., Snell, R.L., Hemeon-Heyer, M., & Langer, W.D., 1984. Ap.J., 286, 599.

Godreich, P., & Kwan, J., 1974. Ap.J., 189, 441.

Gordon, M.A., & Burton, W.B., 1976. Ap.J., 208, 346.

Green, S., & Chapman, S., 1978. Ap.J.Suppl., 37, 169.
Hasegawa, T., et al., Ap. J. 1984., 283, 117.
Hardee, P.E., 1982. Ap.J., 257, 509.

Hardee, P.E., 1983. Ap.J., 269, 94.

Hartmann, J., & Lazarus, F., 1941. Phil.Mag., 31, 35.

Hartmann, L., & McGregor, K.B., 1982. Ap.J., 259, 180.

Harris, S., 1973. M.N.R.A.S., 162, 5p.

Hartquist, T.W., Oppenhimer, M., & Dalgarno, A., 1980. Ap.J., 236, 182.

Harvey, P.M., Campbell, M.F., & Hoffmann, W.F., 1977. Ap.J., 211, 786.

Harvey, P.M., Joy, M., Lester, D.F., & Wilking, B.A., 1986. Ap.J., 300, 737.

Hasegawa, T., Gatley, I., Garden, R., & Brand, P.W.J.L., 1987. Ap.J., in press.

Hayashi, M., Hasegawa, T., Gatley, I., Garden, R.P., & Kaifu, N., 1985. M.N.R.A.S., 215, 31p.

Henkel, C., Walmsley, C.M., & Wilson, T.L., 1980. A.&A., 82, 41.

Herzberg, G., 1950. "Spectra of Diatomic Molecules", Pub. D. Van Nostrand Co.

Ho, P.T., Martin, R.N., & Barrett, A.H., 1981. Ap.J., 246, 761.

Hollenbach, D.J., 1982. Symposium on the Orion Nebula to Honor Henry Draper, Annals of New York Academy of Sciences, Vol.395, p.242, eds Glassgold,A.E., Huggins,P.J. & Schucking,E.L.

Hollenbach, D.J., & McKee, C.F., 1979. Ap.J.Supp., 41, 555.

Hollenbach, D.J., & McKee, C.F., 1980. Ap.J., 241, L47.

Hollenbach, D.J., & Shull, J.M., 1977. Ap.J., 216, 419.

Huber, K.P., & Herzberg, G., 1979. "Constants of Diatomic Molecules", Pub. Van Nostrand Reinhold Co.

Iglesias, E.R., & Silk, J., 1978. Ap.J., 226, 851.

Kaifu, N., Suzuki, S., Hasegawa, T., & Oishi, M., 1985. in IAU Symposium No.115 : " Star Forming Regions", ed. M.Peimbert & J.Jugaku (Reidel Press).

Kawabe, R., Ogawa, H., Fukui, Y., Takano, T., & Takaba, H., 1984. Ap.J., 282, L73.

Konigl, A., 1982. Ap.J., 261, 115.

Kuiper, T.B.H., Kuckerman, B., & Rodriguez Kuiper, E.N., 1981. Ap.J., 226,

851.

Kundt, W., 1984. Astrophys. Space Sci., 98, 275.

Kutner, M.L., & Ulich, B.L., 1981. Ap.J., 250, 341.

Kwan, J., 1977. Ap.J., 216, 713.

Kwok, S., & Volk, K., 1986. Ap.J., 299, 191.

Lada, C.J., & Wilking, B.A., 1984. Ap.J., 287, 610.

Lada, C.J., 1985. "Annual Rev. of Astr. & Astroph.", vol.23, p.267.

Lada, C.J., 1986. in IAU Symposium No.115 : "Star Forming Regions", ed. M.Peimbert & J.Jugaku (Reidel Press).

Landini, M., Natta, A., Oliva, E., Salinari, P., & Moorwood, A.F.M., 1984. A.&A., 134, 284.

Langer, W.D., 1977. Ap.J., 212, L39.

Langer, W.D., Goldsmith, P.F., Carlson, E.R., & Wilson, R.W., 1980. Ap.J., 235, L39.

Langer, W.D., Graedel, T.E., Frerking, M.A., & Armentrout, P.B., 1984. Ap.J., 277, 581.

Larson, R.B., 1973., MNRAS, 161, 133.

Lattanzio, J.C., Monaghan, J.J., Pongrcic, H., & Schwartz, M.P., 1985. M.N.R.A.S., 215, 125.

Lepp, S., & Shull, J.M., 1983. Ap.J., 270, 578.

Linke, R.A., & Goldsmith, P.F., 1980. Ap.J., 235, 437.

London, R., McCray, R., & Chu, S-I., 1977. Ap.J., 217, 442.

London, R., 1978. Ap.J., 225, 405.

Margulis, M., & Lada, C.J., 1985. Ap.J., 299, 925.

Martin, H.M., Sanders, D.B., & Hills, R.E., 1984. M.N.R.A.S., 208, 35.

Martin, R.N., & Barrett, A.H., 1978. Ap.J.Suppl., 1978, 36, 1.

Matsakis, D.N., Brandshaft, D., Chui, M.F., Cheung, A.C., Yngvesson, K.S., Cardiasmenos, A.G., Shanley, J.,F., & Ho, P.T.P., 1977. Ap.J.Lett., 214, L67.

Matsakis, D.N., Hjalmarson, A., Palmer, P., Cheung, A.C., & Townes, C.H., 1981. Ap.J.Lett., 250, L85.

McKee, C.F., & Hollenbach, D., 1980. Ap.J., 241,L47.

McKee, C.F., Chernoff, D.F., & Hollenbach, D.J., 1984. in "Galactic and Extragalactic Infrared Spectroscopy", ed. M.F.Kessler & J.P.Phillips (Reidel Press).

Mestel, L., 1985. in "Protostars & Planets II", ed: Black,D.C.

Mezger, P.G., Altenhoff, W., Schraml, J., Borke, B.F., Reifenstein, E.C., &

Mockler, R.C., & Bird, G.R., 1953. Phys.Rev., 98, 1837.

Morris, M., Palmer, P., Turner, B.E., & Zuckermann, B., 1974. Ap.J., 191, 349.
Moneti, A. et al. 1984. Ap.J., 282, 508.
Mullan, D.J., 1971. M.N.R.A.S., 153, 145.
Mundt, R., 1986. preprint., Ap.J. Suppl.
Mouschovias, T.,Ch., 1976. Ap.J., 207, 141.

Nadeau, D., Geballe, T.R., & Neugebauer, G., 1982. Ap.J., 253, 154.

Norman, C., & Silk, J., 1980. Ap.J., 238, 158.

Norman, M.L., Smarr, L., Wilson, J.R., & Smith, M.D., 1981. Ap.J., 247, 52.

Norman, M.L., Smarr, L., Winkler, K.H.A., & Smith, M.D., 1982. A.&A., 113, 285.

Norman, M.L., Smarr, L., & Winkler, K.A., 1986. in "Numerical Astrophysics", ed: Centrella,J.M., LeBlanc,J.M. & Bowers,R.L., pub: Jones & Bartlett Inc., Boston.
Okuda, T. & Ikeuchi, S, 1986. Publ. Astron. Soc. Japan., 38, 199.
Prandtl, M., 1904. Phys.Zs., 5, 599.

Persson, S.E., Geballe, T.R., McGregor, P.J., Edwards, S., & Lonsdale, C.J., 1984. Ap.J., 286, 289.

Phillips, T.G., Knapp, G.R., Huggins, P.J., Werner, M.W., & Wannier, P.G., 1981. Ap.J., 245, 512.

Plambeck, L.R., & Williams, D.R.W., 1979. Ap.J., 227, L43.

Plambeck, L.R., Snell, R.L., & Loren, R.B., 1983. Ap.J., 266, 321.
Pudritz, R.E., 1985, Ap.J., 293, 216
Pudritz, R.E., & Norman, C.A., 1983. Ap.J., 274, 677.
Pudritz, R.E. & Norman, C.A., 1986. Ap.J., 301, 571.
Reevs, R.R., & Harteck, P., 1979. Z.Naturforsh, 349, 163.

Richardson, K.J., White, G.J., Avery, L.W., Lesurf, J.C.G., & Harten, R.H., 1985. Ap.J., 290, 637.

Richardson, K.J., White, G.J., Gee, G., Griffin, M.J., Cunningham, C.T., & Ade, P.A.R., 1985b. M.N.R.A.S., 216, 713.

Richardson, K.J., White, G.J., Phillips, J.P., & Avery, L.W., 1986. M.N.R.A.S., 219, 167.

Righini-Cohen, G., Simon, M., & Young, E.T., 1979. Ap.J., 232, 782.

Rozyczka, M., & Tenorio-Tagle, G., 1985. A.&A., 147, 209.

Ryle, M., & Downes, D., 1967. Ap.J.Lett., 148, L17.
Sanders, R.H., 1983. Ap.J., 266, 73.

Schwartz, R.D., 1983. Ann.Rev.Astr.Astrophys., Vol.21, p.209.

Scilling, J., & Bryan, R.K., 1984. M.N.R.A.S., 211, 111.

Scoville, N.Z., & Solomon, P.M., 1975. Ap.J., 199, 105.

Scoville, N.Z., Irvine, W.M., Wannier, P.G., & Predmore, C.R., 1977. Ap.J., 216, 320.

Scoville, N.Z., Hall, D.N.B., Kleinmann, S.G., & Ridgweay, S.T., 1982. Ap.J., 253, 136.

Scoville, N.Z., Sargent, A.I., Sanders, D.B., Claussen, M.J., Masson, C.R., Lo, K.Y., & Phillips, T.G. 1986. Ap.J., 303, 416.

Sedov, L.I., 1959. "Similarity & Dimensional Methods In Mechanics", Pub: Academic Press, London.

Shu, F.H., 1977. Ap.J., 214, 488.

Shull, J.M., 1977. Ap.J., 215, 805.

Shull, J.M., & Hollenbach, D.J., 1978. Ap.J., 220, 525.

Shull,J.M., 1978a. Ap.J., 219, 877.

Shull, J.M., 1978b. Ap.J., 224, 841.

Shull,J.M., 1980a. Ap.J., 237, 769.

Shull,J.M., 1980b. Ap.J., 238, 860.

Shull, J.M., & Beckwith, S., 1982. Ann.Rev.Astr.Astrophys., 20, 163.

Simon, M., Felli, M., Cassar, L., Fischer, J., & Massi, M., 1983. Ap.J., 266, 623.

Snell, R.L., Langer, W.D., & Ferking, M.A., 1982. Ap.J., 255, 149.

Snell, R.L., Scoville, N.Z., Sanders, D.B., & Erickson, N.R., 1984. Ap.J., 284, 176.

Snell, R.L., & Schloerb, F.P., 1985. Ap.J., 295, 490.

Solomon, P.M., & Sanders, D.B., 1979. in "Giant Molecular Clouds in the Galaxy", ed. P.M.Solomon & M.G.Edwards (Oxford:Permagon).

Spitzer, L., 1978. "Physical Processes in the Interstellar Medium", pub: Wiley-Interscience.

Stahler, W.S., Shu, F.H., Taam, R.E., 1980. Ap.J., 241, 637.

Stahler, W.S. 1986. Ap.J., 308, 697.

Steigman, G., Strittmatter, P.A., & Williams, R.E., 1975. Ap.J., 198, 575.

Takano, T., Fukui, Y., Ogawa, H., Takaba, H., & Kawabe, R., 1984. Ap.J., 282, L69.

Tenorio-Tagle, G., 1979. A.&A., 71, 59.

Thronson, H.A., & Lada, C.J., 1984. Ap.J., 284, 135.

Tielens, A.G.G.M., & Hollenbach, D., 1985a, Ap.J., 291, 722.

Tielens, A.G.G.M., & Hollenbach, D., 1985b, Ap.J., 291, 747.

Torrelles, J.M., Rodriguez, L.F., Canto, J., Carral, P., & Marcaide, J., 1983. Ap.J., 274, 214.

Turner, J., Kirby-Docken, K., & Dalgarno, A., 1977. Ap.J.Suppl., 35, 281.

Uchida, Y., & Shibata, K., 1985. Publ.Astron.Soc.Japan, 37, 515.

Ulich, B.L., Cogdell, J.R., & Davis, J.H., 1973. Icarus, 19, 59.

Ulich, B.L., Davis, J.H., Rhodes, P.J., & Hollis, J.M., 1980. IEEE, AP-28, 367.

Wannier, P.G., 1980. Ann.Rev.Astr.Ap., 18, 399.

Watson, D.M., Genzel, R., Townes, C.H., & Storey, J.M.V., 1985. Ap.J.

Weaver, R., McCray, R., & Castor, J., 1977. Ap.J., 218, 377.

Werner, M.W., Elias, J.H., Gezari, D.Y., Hauser, M.G., & Westbrook, W.E., 1975. Ap.J.Lett., 199, L185.

Wheeler, J.C., Mazurek, T.J., & Sivaramakrishnan, C., 1980. Ap.J., 237, 781.

White, R.E., 1977. Ap.J., 211, 744.

Willingale, R., 1981. M.N.R.A.S., 194, 359.

Wilson, R.W., Langer, W.D., & Goldsmith, P.F., 1981. Ap.J., 243, L47.

Wilson, T.L., 1967. Ap.J.Lett., 150, L157.

Wilson, T.L., Martin-Pintado, J., Gardner, F.F., & Henkel, C., 1982. A.&A., 107, L10.

Wilson, M.J., & Falle, A.E.G., 1985. M.N.R.A.S., 216, 971.

Wootten, H.A., 1977. Ap.J., 216, 440.

Wootten, A., Loren, R.B., & Snell, R.L., 1982. Ap.J., 255, 160.

Wootten, A., Loren, R.B., Sandqvist, A., Friberg, P., & Hjalmrson, A., 1984. Ap.J., 279, 633.

Wright, A.E. & Barlow, M.J., 1975. MNRAS, 170, 41.

Wynn-Williams, C.G., Becklin, E.E., & Neugebauer, G., 1974. Ap.J., 187, 473.

Zuckerman, B., Kuiper, T.B.H., Rodriguez Kuiper, E.N., 1976. Ap.J., 209, 758.

ACKNOWLEDGEMENTS

I should particularily like to thank my supervisor, Dr. Peter W.J.L. Brand (Edinburgh University), and my friends and tutors, Dr. Ian Gatley (UKIRT) and Dr. Tom R. Geballe (UKIRT), for their invaluable advice and enthusiastic support of this and other projects undertaken during my graduate career. I am greatful to both Ian and Tom for teaching me how best to organise and conduct an observational project, and to Peter for persistently bringing me back to earth to face the grim realities of student life. I should also like to thank Cathy Gatley for entertaining and generally taking care of me during my extended visits to Hawaii; the friendship shown by both Ian and Cathy is sincerely appreciated.

In addition to those mentioned above, I have actively collaborated with several astronomers and fellow students on the different investigations described in this work. Of special mention, are my Japanese colleagues, Dr. Tetsuo Hasegawa, Dr. Masa Hayashi and Dr. Norio Kaifu, of the Nobeyama Radio Observatory, who enthusiastically introduced me to the new world of millimeter-wave astronomy. Their support and active interest was vital for the success of these observations. I thank all of them for their friendly collaboration; long may it last. When in Edinburgh, I spent a considerable amount of time discussing and debating current issues in astrophysics with Dr. Hans Zinnecker; these discussions significantly broadened my knowledge of physics and brought forth many new and often novel ideas that otherwise would not have emerged. At UKIRT, I must also thank Dr. Andy Longmore, Dr. Perry Williams and Dr. Malcolm Smith, and their families, for their friendship and assistance during my long and often lonely stays in Hawaii.

Some of the observations described in this Thesis were made using the UKIRT telescope on Mauna Kea. The efforts of all the staff in Hawaii, which led to a steady improvement in the operating system and instrumentation during the last three years, are greatly appreciated. Thanks go to, Kevin Krisciunas, Alan Pickup, Len Lawrence, Bernard McNally, David Beattie and the entire day-crew who were always at hand with their excellent support. I am especially greatful to the telescope operators, Dolores Walther, Joel Aycock and Thor Wold, who patiently sat through many a night of cloudy skies.

I learnt much from my fellow Research Students, but particularly would like to thank Michael Burton, who shares many of my own interests, for his friendship during hard times.

I acknowledge financial support from the UK SERC in the form of a Research Studentship and other grants.